Design and applications of shear/extension mode PFC actuators in vibration control of annular plates

A
Thesis Submitted in
Partial Fulfillment of the Requirements
for the Degree of

DOCTOR OF PHILOSOPHY

by

Manish Kumar Dubey
(Roll No: 136103010)

DEPARTMENT OF MECHANICAL ENGINEERING
INDIAN INSTITUTE OF TECHNOLOGY GUWAHATI,
GUWAHATI-781039, INDIA

February, 2020

Department of Mechanical Engineering
Indian Institute of Technology Guwahati
Guwahati-781039 INDIA

CERTIFICATE

It is certified that the work contained in the thesis entitled "**DESIGN AND APPLICATIONS OF SHEAR / EXTENSION MODE PFC ACTUATORS IN VIBRATION CONTROL OF ANNULAR PLATES**" submitted by **Manish Kumar Dubey (Reg. No. 136103010)** to the Indian Institute of Technology Guwahati for the award of the degree of Doctor of Philosophy has been carried out under my supervision in the Department of Mechanical Engineering, Indian Institute of Technology Guwahati. This work has not been submitted elsewhere for the award of any other degree or diploma.

(Dr. Satyajit Panda)
Associate Professor
Department of Mechanical Engineering
Indian Institute of Technology Guwahati
Guwahati-781039
INDIA

Declaration

I Manish Kumar Dubey (Roll no: 136103010) declare that the present written submission is my thoughts in my own words. I have adequately cited and referenced the original sources, where other's ideas have been involved. I also declare that I have adhered to all principles of academic honesty and integrity and have neither fabricated nor falsified any idea/data/fact/source in my submission. I understand that any violation of the above will be cause for disciplinary action by the Institute and can also evoke penal action from the sources which have thus not been properly cited or from whom proper permission has not been taken when needed.

(**Manish Kumar Dubey**)

Date: **Roll No: 136103010**

Dedication

This thesis is dedicated to my grandfather

Late Shri Indra Pal Dubey

Acknowledgments

The work presented in this thesis would not have been possible without my close association with several people I came across with. I would like to express my sincere gratitude and appreciation towards all those who made this Ph.D. thesis possible.

First and foremost, I would like to express my sincere appreciation and thanks to my thesis supervisor Dr. Satyajit Panda, who has been a remarkable mentor to me. His continuous support, enthusiasm, inspiration, encouragement and never give-up attitude has made a deep impression on me. During the course of interaction for last five years and six months at IIT Guwahati, I had learned a lot from him including how to approach a problem in a systematic way and specially in a situation when things do not work in your way. I am really pleased to be associated with a mentor like Dr. Satyajit Panda in my life.

Besides my thesis supervisor, I would like to thank Prof. D. Chakraborty, Dr. Poonam Kumari and Dr. A. Chakraborty for their insightful review and suggestions as doctoral committee members which helped me to widen my research. I am also grateful to past and present departmental heads Prof. P. Mahanta, Prof. A. K. Dass and Prof. S. K. Dwivedy for providing me enough facilities and support during my Doctoral program.

The financial support provided by the Ministry of Human Resources and Development, Government of India for research work at IIT Guwahati is gratefully acknowledged. I greatly acknowledge the Department of Mechanical Engineering, IIT Guwahati for providing the financial support for last six months.

I express my deep gratitude to my parents Smt. Kamal Dubey (mother) and Sri Om Prakash Dubey (father) for their infallible love, encouragement and moral support. I would like to thank my wife Neha and son Vashishth for their precious much needed patience and support during my research period.

Last but not the least, I would be grateful to my fellow lab mates Shashi and Abhay for their continuous sleepless, unfatigued, energetic, and fruitful discussions.

Date: **(Manish Kumar Dubey)**

Abstract

This dissertation deals with the active and active-passive control of annular plates through the design of two new piezoelectric fiber composite (PFC) actuators and a shear actuated hybrid damping treatment. The first PFC actuator is an extension-mode PFC actuator with the cylindrically periodic microstructure and designed for active control of plane structures of revolution. It is in the form of a thin annular disc where the continuous piezoelectric fibers are periodically distributed along the circumferential direction to yield the directional actuation in the radial coordinate of the cylindrical principal material coordinate system. This kind of microstructure of the annular PFC actuator yields its radially varying electromechanical properties that are determined through the segmentation of its (PFC) volume into a large number of micro-volumes of different fiber volume fractions. The closed-form expressions for the effective electromechanical coefficients of the micro-volumes are derived, and the corresponding verification is carried out through the numerical homogenization using the finite element (FE) procedure. The results reveal an indicative magnitude of an effective piezoelectric coefficient that quantifies the directional actuation in radial coordinate. But, the magnitude of this coefficient decreases indicatively with the increasing radius, and thus the annular PFC actuator is redesigned in a special manner for the improved magnitude of that piezoelectric coefficient at any radius. With these improved properties of the annular PFC actuator, its indicative actuation capability in control of flexural vibration of an annular plate is observed, and thus it may be a potential PFC actuator for active control of plane structures of revolution specifically where the actuation in radial coordinate is the major requirement.

The second PFC actuator is a new shear-mode PFC actuator by the name of balanced laminate of PFC (BL-PFC). It is developed through the analysis of shear actuation mechanism of an obliquely reinforced 1-3 PFC, where the main shortcoming arises due to the adverse effect of the transverse normal actuation force on the shear actuation force in the 1-3 PFC. In a quest of modified constructional features of the 1-3 PFC for the elimination of the unwanted transverse actuation force, the BL-PFC is designed. A micromechanics formulation is first presented for the determination of its (BL-PFC) effective electromechanical properties, and then its actuation capability is investigated in shear actuated bending deformation of a sandwich beam. The results reveal indicatively higher shear actuation capability of this BL-PFC over that of the obliquely reinforced 1-3 PFC as well as the monolithic shear piezoelectric actuators.

This BL-PFC is further used for shear-mode control of flexural vibration of annular plates where its effectiveness is compared with that of the available shear-mode actuators namely Shear Actuated Fiber Composite (SAFC) and monolithic shear piezoelectric actuator (PZT5H). Every actuator is used in the form of an actuator laminate that is inserted at the core of the annular sandwich plate in the form of patches. A fruitful arrangement of patches and a shear-based feedback control strategy are presented for effective vibration control of the annular sandwich plate according to the velocity feedback control law. First, the effective properties of the actuator laminate are determined using the Uniform Field Method. Next, a closed-loop FE model of the sandwich plate is developed. Subsequently, the suitability of the present arrangement of shear actuator patches and the shear-based control strategy are substantiated. This arrangement of the actuator patches is further optimized for every shear actuator, and the corresponding shear actuated resonant displacement amplitudes of the sandwich plate are evaluated. These results reveal lesser actuation capability of the SAFC than that of the PZT5H while the BL-PFC is the best one for shear-based attenuation of vibration of the annular plates.

Finally, a shear actuated hybrid active-passive damping treatment is designed for vibration control of annular plates using the BL-PFC and a 0-3 viscoelastic composite (VEC). A layered annular plate is composed with the stack of the active layer, passive damping layer and the layers of substrate material. The active layer is comprised of BL-PFC patches optimally embedded within the foam layer with 2-2 phase connectivity. The passive damping layer is initially made of a viscoelastic material (VEM); however, the graphite wafers are inserted within it (VEM) in an optimal manner with 0-3 phase connectivity resulting in a 0-3 VEC layer. On the basis of prioritising shear actuation over passive damping and vice versa, two different layered configurations of the hybrid damping treatment are designed in an optimal manner. The corresponding active-passive damping characteristics are investigated by developing a closed-loop FE model where the aforesaid shear-based feedback control strategy is utilized for activating the shear actuators according to the velocity feedback control law. The results reveal indicative active-passive control of vibration of the annular plate using BL-PFC actuator, and it could further be enhanced by the inclusion of graphite wafers (VEC) where the configuration of the layered annular plate would be based on the priority of shear actuation.

Table of Contents

Abstract
List of Figures
List of Tables
List of Symbols

Chapter 1 **Introduction**

1.1 Introduction 1

1.2 Piezoelectric materials 2

1.3 Piezoelectric fiber composite (PFC) 5

1.3.1 Extension-mode PFC 6

1.3.1.1 Analytical studies on the electromechanical properties of extension-mode PFCs 7

1.3.1.2 Numerical studies on the electromechanical properties of extension-mode PFCs 9

1.3.1.3 Experimental studies on the electromechanical properties of extension-mode PFCs 10

1.3.2 Shear-mode PFCs 11

1.4 Smart structures 12

1.4.1 Smart beams with extension-mode PFC actuator 13

1.4.2 Smart plates with extension-mode PFC actuator 14

1.4.3 Smart shells with extension-mode PFC actuator 15

1.4.4 Other smart structures with extension-mode PFC actuator 16

1.4.5 Smart structures with shear-mode PFC actuator 16

1.5 Hybrid active-passive damping 17

1.5.1 ACLD treatment of beams using extension-mode monolithic piezoelectric actuator 19

1.5.2 ACLD treatment of plates using extension-mode monolithic piezoelectric actuator 20

1.5.3 ACLD treatment of shells using extension-mode monolithic piezoelectric actuator 21

1.5.4 ACLD treatment of beams using shear-mode monolithic piezoelectric actuator 21

1.5.5 ACLD treatment of beams using extension-mode PFC actuator 22
1.5.6 ACLD treatment of plates using extension-mode PFC actuator 23
1.5.7 ACLD treatment of shells using extension-mode PFC actuator 24
1.6 Motivation and objectives of present research 24
1.7 Contributions 27
1.8 Organization of the thesis 28

Chapter 2 **Design of an extension mode piezoelectric fiber composite actuator with cylindrically periodic microstructure**

2.1 Introduction 31
2.2 Present annular PFC actuator 32
2.3 Effective properties of the annular PFC actuator 34
2.3.1 Effective properties of a typical sub-volume 36
2.3.2 Numerical homogenization of a typical sub-volume 43
2.4 Smart annular plate 51
2.5 Results and discussions 59
2.5.1 Verification of effective properties of a typical sub-volume 59
2.5.2 Varying electro-elastic properties of the annular PFC actuator 61
2.5.3 Actuation capability of the present annular PFC actuator 64
2.6 Summary 71

Chapter 3 **Shear actuation mechanism and shear-based actuation capability of an obliquely reinforced PFC in active control of annular plates**

3.1 Introduction 73
3.2 Present annular sandwich plate with shear actuators 74
3.3 Properties of constituent materials in the annular sandwich plate 78
3.4 FE model of the annular sandwich plate 80
3.5 Shear-based control strategy 87

3.6 Results and discussions 88
3.6.1 Verification of present FE formulation 89
3.6.2 Analysis of shear/extension mode actuation of the annular sandwich plate 91
3.6.2.1 Extension-mode actuation of the annular sandwich plate 93
3.6.2.1 Shear-mode actuation of the annular sandwich plate 93
3.6.3 Shear-based active control of vibration of the annular sandwich plate 95
3.7 Summary 101

Chapter 4 **A balanced laminate of piezoelectric fiber composite for improved shear piezoelectric actuation of beams**

4.1 Introduction 103
4.2 Present balanced laminate of PFC 103
4.2.1 Effective properties of PFC 106
4.2.2 Effective properties of 2-2 PFC layer and balanced laminate of PFC 108
4.3 Smart sandwich beam 112
4.4 Results and discussions 116
4.4.1 Verification of effective properties of the laminate of PFC 116
4.4.2 Verification of FE model of smart sandwich beam 119
4.4.3 Analysis of electro-elastic properties of BL-PFC 120
4.4.4 Shear actuation capability of balanced laminate of PFC 121
4.5 Summary 127

Chapter 5 **Shear-based vibration control of annular sandwich plates using different piezoelectric fiber composites: a comparative study**

5.1 Introduction 128
5.2 Shear actuator laminate and effective properties 130
5.3 Smart annular sandwich plate 134
5.4 Properties of constituent materials in the annular sandwich plate 135
5.5 FE model of the annular sandwich plate 136
5.6 Results and discussions 138
5.6.1 Effective properties of the shear actuator 138

laminate
5.6.2 Verification of the FE formulation 139
5.6.3 Analysis of shear-based active control of the annular sandwich plate 140
5.6.4 Optimal arrangement of shear actuator patches 142
5.6.5 Comparative study 145
5.7 Summary 148

Chapter 6 **A design of shear actuated hybrid damping treatment for annular plates using balanced laminate of PFC and 0-3 viscoelastic composite**

6.1 Introduction 150
6.2 Annular piezo-foam composite disc using BL-PFC patches 152
6.3 Design of an annular disc of 0-3 VEC 153
6.4 Design of a layered annular plate for shear actuated hybrid damping treatment 155
6.5 Properties of the constituent materials in the layered annular plate 157
6.6 FE model of the overall annular plate 160
6.7 Shear-based active control strategy 169
6.8 Results and discussions 170
6.8.1 Verification of present FE formulation 172
6.8.2 Shear-based active control of annular plates 176
6.8.3 Active-passive control of the annular plate using active and VEM layers 178
6.8.4 Active-passive control of the annular plate using active and VEC layers 181
6.8.5 Comparative study 184
6.9 Summary 188

Chapter 7 **Conclusions and scope of future work**

7.1 Conclusions 191
7.2 Scope for future work 197

References 198
List of Publications 230

List of Figures

Fig. 1.1	Schematic diagrams of the domain of piezoelectric material, (a) before polarization, (b) polarization under applied electric field, (c) remanent polarization after the removal of the applied electric field.	2
Fig. 1.2	(a) polarization (P)-electric field (E)) hysteresis loop, (b) strain (ε)-electric field (E)) hysteresis loop (butterfly curve.	3
Fig. 1.3	Piezoelectric actuators, (a) extension-mode actuator and (b) shear-mode actuator (P indicates the axis of poling and E_z is the applied electric field).	5
Fig. 1.4	Schematic diagram of a smart structure	12
Fig. 2.1	Schematic diagrams of 2-2 PFC lamina in (a) Cartesian coordinate system, (b)-(c) cylindrical coordinate system.	32
Fig. 2.2	(a) Stacking sequence of different layers within the annular PFC actuator, (b) laminated PFC actuator.	33
Fig. 2.3	Schematic diagrams of (a) the RV of the annular PFC actuator (Fig. 2.2(b)), (b) the top surface of the RV with the radial boundaries of sub-volumes, (c) a typical sub-volume of the RV.	35
Fig. 2.4	Schematic diagram of (a) the 2-2 PFC layer of sub-volume (Fig. 2.3(c)), (b) the unit normal and its components at a typical point (G) on θ -interface.	38
Fig. 2.5	A typical sub-volume of RV comprised of homogenized 2-2 PFC layer and epoxy layer.	41
Fig. 2.6	Schematic diagram of an annular plate integrated with the patches of the annular PFC actuator.	51
Fig. 2.7	Variations of FVF for (1) one RV within the overall radial span (r_i = 0.2 m, r_o = 1 m) of the annular PFC actuator and (2)-(5) four RVs corresponding to four equal radial divisions (S1, S2, S3, S4) of the same radial span.	62
Fig. 2.8	Variations of (a) $\bar{C}_{11}$, (b) $\bar{e}_{31}$ and (c) $\bar{e}_{32}$ for (1)one RV within the overall radial span (r_i = 0.2 m, r_o = 1 m) of the annular PFC actuator and (2)-(5) four RVs corresponding to four equal radial divisions of the same radial span.	63
Fig. 2.9	Verification of the present FE formulation in handling the electro-elastic coupling within the piezoelectric actuator (Pres.: Present FE results).	68
Fig. 2.10	(a) Variations of the maximum transverse displacement-amplitude ($W_{\max}$) of the smart annular plate with the operating frequency, (b) the corresponding variations of the maximum control-voltage ($V_{\max}$) (material for the patches: PFC2, $m=1$, p_o = 1 N/m^2, ω_o is the fundamental natural frequency).	69
Fig. 2.11	(a) Variations of the maximum transverse displacement-amplitude ($W_{\max}$) of the smart annular plate with frequency,	70

(b) the corresponding variations of the maximum control-voltage (V_{max}) for the material of the patches as PFC1/PFC2/PZT5H ($k_d = 100$, $p_o = 1$ N/m^2).

Fig. 3.1 Schematic diagrams of (a) vertically and (b) obliquely reinforced 1-3 PFC. 74

Fig. 3.2 Schematic diagram of the annular sandwich plate with the embedded shear actuator patches. 75

Fig. 3.3 A block of the obliquely reinforced 1-3 PFC (Figure 1(b)) used for making actuator patches in the shape of the annular sector within the core of the annular sandwich plate. 76

Fig. 3.4 Two bending mode shapes and the corresponding distributions of transverse shear stress (τ_{rz}) at the middle plane of a simply-supported isotropic annular plate; (a), (b) mode: $m=1$, $n=2$; (c), (d) mode: $m=1$, $n=4$ (m and n are the radial and circumferential mode numbers, respectively, W is the transverse deflection of the plate). 77

Fig. 3.5 Schematic diagram of a typical row of actuator patches in the $r\theta$-plane of the annular plate. 78

Fig. 3.6 Two different elemental stacking sequences. 84

Fig. 3.7 A part of the middle plane of the annular sandwich plate for illustrating the in-plane locations of velocity sensors. 88

Fig. 3.8 (a) Schematic diagram of a typical cross-section of the axisymmetric annular sandwich plate, (b) bending deflection of the axisymmetric annular sandwich plate across its radial span. 90

Fig. 3.9 Variation of maximum transverse deflection (w_{max}/h) of the annular sandwich plate with the fiber orientation angle (ϕ with the z-axis) of the patches of obliquely reinforced 1-3 PFC. 94

Fig. 3.10 (a) Variation of the maximum nodal transverse displacement-amplitude (w_{max}/h) of the annular sandwich plate with the operating frequency (ω), (b) the corresponding variations of the maximum control voltage ($p_o = 1.6$ N/m^2, $n_r = 2$, $n_\theta = 8$). 96

Fig. 3.11 Resonant transverse displacement amplitudes at the first three bending modes ($n=0,1,2$; $m=1$) of vibration of the annular sandwich plate for different values of n_θ ($p_o = 1.6$ N/m^2, $k_d = 40e4$). 97

Fig. 3.12 Variations of (a) the resonant transverse displacement amplitudes and (b) the corresponding maximum control voltages with the control gain (k_d) at the first and second bending modes of vibration of the annular sandwich plate ($p_o = 1.6$ N/m^2, $n_\theta = 8$). 99

Fig. 3.13 Variations of (a) the resonant displacement amplitude and (b) the corresponding maximum control voltage at the 100

fundamental bending mode of vibration of the annular sandwich plate within a two-dimensional domain of control gain (k_d) and load-amplitude ($n_\theta = 8$).

Fig. 4.1 (a) Balanced laminate of PFC and (b) the corresponding component layers. 104

Fig. 4.2 (a) Vertically reinforced 2-2 PFC lamina and (b) the corresponding representative volume element (denoted by RVE1). 105

Fig. 4.3 Representative volume element (denoted by RVE2) of the balanced laminate of PFC (Fig. 4.1). 106

Fig. 4.4 Schematic diagram of the smart sandwich beam. 112

Fig. 4.5 (a) Schematic diagram of a beam made of balanced laminate of PFC with two pairs of 2-2 PFC layers, (b) a typical cross-section of the beam made of balanced laminate of PFC. 118

Fig. 4.6 Bending deflection of the beam made of the BL-PFC due to the applied electric fields over two halves of the same beam in the opposite direction. 119

Fig. 4.7 Bending deflection of a smart sandwich beam with two segments of actuator patches for the uniform applied transverse electric field to the monolithic shear piezoelectric actuator patches. 120

Fig. 4.8 (a) Variation of maximum transverse deflection of the smart sandwich beam with the fiber orientation angle (ϕ with the z-axis) of the obliquely reinforced 1-3 PFC or balanced laminate of PFC ($|E_z| = 50$ V/mm). 122

Fig. 4.9 Bending deflection of the smart sandwich beam for the material of actuator patches as either of the monolithic piezoelectric ceramic (PZT 5H), obliquely reinforced 1-3 PFC and balanced laminate of PFC. 124

Fig. 4.10 Variations of the maximum deflection of the smart sandwich beam with the angle (ϕ) of the BL-PFC for different FVFs of its 2-2 PFC layers. 125

Fig. 4.11 Variations of the maximum deflection of the smart sandwich beam with the number of segments of patches for different values of coverage (L_p / L_s) of a typical patch in its segment. 126

Fig. 5.1 Schematic diagrams of (a) SAFC and (c) monolithic shear piezoelectric actuators. 129

Fig. 5.2 (a) Laminate of shear piezoelectric actuator (active) layers and (b) the corresponding Representative Volume Element (RVE) ($+\phi / -\phi$ is the positive/negative electric potential). 130

Fig. 5.3 Bending deflection (w) of the axisymmetric annular sandwich plate for an applied electric field across the thickness of the shear piezoelectric actuators in the core. 139

Fig. 5.4 Variations of (a) the maximum transverse displacement-amplitude ($w_{\max} / h$) of the annular sandwich plate and (b) the 141

corresponding maximum control voltage with the operating frequency (ω) ($p_o = 1.6$ N/m^2).

Fig. 5.5 Contour plot of resonant displacement-amplitude (w_{max}/h) at the fundamental mode of vibration of the annular plate within a two-dimensional domain of n_θ and ϕ where the patches are made of the BL-PFC laminate ($p_o = 5$ N/m^2, $k_d = 40e4$). 143

Fig. 5.6 Variation of the resonant displacement-amplitude (w_{max}/h) at the fundamental mode of vibration of the annular plate with n_θ where the patches are made of the SAFC/PZT-5H laminate ($p_o = 5$ N/m^2, $k_d = 40e4$). 144

Fig. 5.7 Variations of the resonant displacement-amplitude (w_{max}/h) and the corresponding maximum control voltage (V_{max}) with the control-gain (k_d); w_{max}/h for (a) mode: $m=1$, $n=0$ and (c) mode: $m=1$, $n=1$; V_{max} for (b) mode: $m=1$, $n=0$ and (d) mode: $m=1$, $n=1$ ($p_o = 5$ N/m^2). 145

Fig. 5.8 Contour plots of (a) the resonant displacement-amplitude (w_{max}/h) at the fundamental mode and (b) the corresponding maximum control voltage (V_{max}) in the two-dimensional domain of the load-amplitude (p_o) and control-gain (k_d) for the patches of the BL-PFC laminate. 146

Fig. 6.1 (a) Schematic diagram of active layer, (b) a block of BL-PFC used for making a typical row of actuator patches in the active layer. 153

Fig. 6.2 Schematic diagrams of (*a*) a rectangular 0-3 VEC layer and (*b*) an annular disc of 0-3 VEC. 154

Fig. 6.3 Cross-section of the layered annular plate with (*a*) a VEM layer at the core or (*b*) two identical VEM layers symmetrically located with respect to the middle plane of the overall plate. 156

Fig. 6.4 Cross-section of the layered annular plate with (*a*) a VEM layer at the core and two identical active layers or (*b*) an active layer at the core and two identical VEM layers. 156

Fig. 6.5 Cross-section of the layered annular plate with (*a*) a VEC layer at the core and two identical active layers or (*b*) an active layer at the core and two identical VEC layers. 157

Fig. 6.6 Elemental stacking sequences in the FE mesh of the layered annular plate with the VEC core and two piezo-foam layers (Fig.6(a)). 163

Fig. 6.7 Actuator zones and the corresponding locations of the velocity sensors over the plane of the annular plate. 171

Fig. 6.8 Bending deflection comparison of the axisymmetric annular sandwich plate across its radial span (w is the transverse deflection). 174

Fig. 6.9 Distributions of transverse shear strain (γ_{rz}) over the top surfaces of the (a) active (piezo-foam layer) and (b) VEC layer of the layered annular plate (Fig. 6.5(b)); (c) bending deflection of the overall annular plate (Fig. 6.5(b)) for a transversely applied electric field over the actuator patches. 175

Fig. 6.10 Resonant transverse displacement amplitudes at the first four bending modes ($n=0,1,2,3;\ m=1$) of the annular sandwich plate for different values of n_θ ($p_o = 5$ N/m^2, $k_d = 50e4$) 177

Fig. 6.11 (*a*)Frequency responses of the layered annular plate (Fig. 6.4(b), $h_d \approx 0$)with the active (piezo-foam) layer at the core and (*b*) the corresponding variations of the maximum control voltage (V_{max}) for different values of the control gain (k_d) (p_o = 5 N/m^2) 179

Fig. 6.12 (*a*) Variations of the resonant displacement-amplitude (w_{max}/h, $m=0$, $n=1$) with the thickness (h_s^1) of the inner substrate layers in the configurations (PFC-VEM#1 and PFC-VEM#2) of the layered annular plate; (*b*) corresponding variations of the maximum control voltage (V_{max}) ($p_o = 40$ N/m^2) 180

Fig. 6.13 Contour plots of (w_{max}/h) in the two-dimensional domains of (*a*) n_{rg} and $n_{\theta g}$, (*b*) r_c and Δr_v. 182

Fig. 6.14 Variation of (w_{max}/h) with the thickness (h_s^1) of the inner substrate layers 183

Fig. 6.15 Variations of (a) the resonant displacement-amplitude (w_{max}/h) and (b) the maximum control voltage (V_{max}) with the control gain (k_d) for the configurations PFC-VEM#1 and PFC-VEC#2 of the overall annular plate ($p_o = 40$ N/m^2) 185

Fig. 6.16 Frequency responses ($w_{max}/h, m=0, n=1$) of the layered annular plate for its different configurations (*a*) PFC-VEM#1 (Fig. 6.4(a)) and (*b*) PFC-VEC#2 (Fig. 6.5(b))($p_o = 40$ N/m^2, $k_d = 40\times10^4$) 187

List of Tables

Table 2.1	Verification of effective coefficients (Eq. (2.9)) of 2-2 PFC layer ($v_f = 0.86$) in a typical sub-volume.	60
Table 2.2	Effective electro-elastic coefficients for a sub-volume ($v_f = 0.72$).	60
Table 2.3	Effective elastic coefficients ($\bar{C}_{ij}^l = ae^{br} + ce^{dr}$, in GPa) of the annular PFC actuator (the unit of r is m)	65
Table 2.4	Effective piezoelectric coefficients ($\bar{e}_{ij}^l = ae^{br} + ce^{dr}$, in C/m^2) of the annular PFC actuator (the unit of r is m)	66
Table 2.5	Effective density ($\bar{\rho}_c^l = ae^{br} + ce^{dr}$, in kg/m^3) of the annular PFC actuator (the unit of r is m)	66
Table 2.6	Verification of the present FE formulation for an annular plate (BC: boundary condition, CC: fully clamped boundary, SS: simply-supported boundary, $\lambda_i = \omega_i r_o^2 \sqrt{\rho h/D}$, $D = Eh^3/12\left(1-\nu^2\right)$, $h_p \approx 0$, $k_d = 0$, ω_i (i =1,2,3,.....) are the natural frequencies).	67
Table 3.1	Comparison of dimensionless ($\lambda = \omega r_o^2 \sqrt{\rho h / D}$, $D = Eh^3/12(1-\nu^2)$) natural frequency for the isotropic annular plate.	91
Table 3.2	Attenuation of the resonant displacement amplitude and the corresponding increase of the control voltage for an increase of control gain at different values of the load-amplitude.	101
Table 4.1	Verification of the present formulation for effective properties of 2-2 PFC lamina.	117
Table 4.2	Effective properties of the balanced laminate of PFC (BL-PFC, $\phi = 35^o$).	120
Table 4.3	Effective properties of vertically reinforced 1-3 PFC.	121
Table 5.1	Effective properties of the PZT5H, BL-PFC and SAFC laminates.	138
Table 5.2	Mode-based optimum values of the design variables (n_θ, ϕ) for the actuator patches of BL-PFC/SAFC/PZT5H laminate.	144
Table 5.3	Decrease of the resonant displacement-amplitude ($\Delta W(\%)$) at the fundamental mode and the corresponding increase of the maximum control voltage ($\Delta V(\%)$) for a change (from 30×10^4 to 90×10^4) of control gain (k_d) at different loadamplitudes (p_o).	148
Table 6.1	Comparison of dimensionless ($\lambda = \omega r_o^2 \sqrt{\rho h / D}$,	173

$D = Eh^3/12(1-\nu^2)$) natural frequency for the isotropic annular plate (CC/SS implies clamped/simply-supported inner and outer edges of the isotropic annular plate)

Table 6.2 Attenuation ($\Delta W(\%)$) of the resonant displacement-amplitude ($w_{\max}/h$, $m=0$, $n=1$) and the corresponding increase ($\Delta V(\%)$) of the control voltage for an increase (from 10×10^4 to 500×10^4) of control gain (k_d) at different load-amplitude (p_o) 188

List of Symbols

List of symbols used throughout the thesis are listed. List of symbols less frequently used, or that have different meaning or different forms at different contexts, are defined where they are used.

ε	Strain vector
$\boldsymbol{\sigma}$	Stress vector
$\boldsymbol{E}$	Electric field vector
E_z	Electric field along z direction
$\boldsymbol{D}$	Electrical displacement field vector
D_z	Electrical displacement along z direction
P	Poling direction
r, θ, z	Cylindrical coordinate system
x, y, z	Cartesian coordinate system
r_i, r_o	Inner and outer radius of an annular plate
$\boldsymbol{C} / \boldsymbol{e} / \in$	Stiffness/ piezoelectric coefficient/permittivity matrix
$\sigma_r / \sigma_\theta / \sigma_z$	Normal stress along $r / \theta / z$ direction
$\varepsilon_r / \varepsilon_\theta / \varepsilon_z$	Normal strain along $r / \theta / z$ direction
$\varepsilon_{r\theta} / \sigma_{r\theta}$	In-plane shear strain/stress in the $r\theta$ - plane
$\tau_{rz} / \tau_{\theta z}$	Transverse shear stress in $rz / \theta z$ - plane
$\gamma_{rz} / \gamma_{\theta z}$	Transverse shear strain in $rz / \theta z$ - plane
n_r / n_θ	Number of patches in radial and circumferential direction
θ_f / θ_c	Circumferential span of fiber and composite in sub-volume
Δr	Radial span of the sub-volume/annular-sector
$\Delta\theta$	Circumferential span of the annular-sector
$\Delta r_p, \Delta\theta_p$	Radial and circumferential span of the annular patches
$\Delta r_F, \Delta\theta_F$	Radial and circumferential gap b/w annular patches
$\boldsymbol{d}$	Global general displacement field vector
$\boldsymbol{d}^e$	Elemental nodal displacement vector
D	Bending rigidity of plate
p_O	Load amplitude

$\boldsymbol{N}$	Shape function matrix
E / ν	Young's modulus/Poisson's ratio
h	Thickness of substrate beam/plate
$\boldsymbol{I}$	Identity matrix
k	Number of layers
k_d	Feedback control gain
$\boldsymbol{K}$	Stiffness matrix
$\boldsymbol{L}$	Linear Operator matrices
$\bar{m}$	Mass per unit area
$\boldsymbol{M}$	Mass matrix
ρ	Mass density
$\boldsymbol{T}_t / \boldsymbol{T}_r$	Transformation vector
$\boldsymbol{P}_M^e$	Element mechanical load vector
$\boldsymbol{P}_E^e$	Electro-elastic coefficient vector
N_T	Transformation row matrix
δT_K	Variation of total kinetic energy
δT_P	Variation of total potential energy
u , v , w	Displacements components in coordinate directions
$u_0 / v_0 / w_0$	Displacement along $r / \theta / z$ direction at any point on reference surface
V	Applied voltage across the electrode surfaces
$w_{\max} / h$	Maximum resonant transverse amplitude
$V_{\max}$	control voltage at peak point
$\dot{w}$	Sensing point velocity
$\dot{\varphi}_r^s$	Time-rate of change of slope (in the rz - plane)
$\boldsymbol{X}$	Global nodal displacement vector
$\Delta W(\%)$	Percentage attenuation of resonant amplitude
$\Delta V(\%)$	Percentage increase of control voltage at peak point
ω	Circular frequency
ω_0	Fundamental frequency of vibration
m / n	Longitudinal/circumferential mode number
ω	Operating frequency

$p(r,\theta,t)$	Transverse (radial) harmonic distributed load
$\otimes$	Kronecker product

Superscript:

e	Element
i	A State of deformation
s	Sensing point
v	Velocity
a	Active layer
T	Transpose
E	Electrical load

Subscript:

b	Bending
L	Linear
f	Fiber
m	matrix
p	Phase of material
U	Uniform
N	Non-uniform

Symbols with the *overbar* denotes the average values.

Abbreviations:

RVE	Representative volume element
AFC	Active fiber composite
MFC	Macro fiber composite
SAFC	Shear actuated fiber composite
PFC	Piezoelectric fiber composite
BL-PFC	Balanced laminate of PFC
UFM	Uniform field method
UCLD	Unconstrained layer damping
FVF	Fiber volume fraction
CLD	Constrained layer damping
FE	Finite element
VEC	Viscoelastic composite
VEM	Viscoelastic material

Chapter 1

Introduction

1.1 Introduction

In the past few decades, piezoelectric ceramics are widely utilized as materials for distributed actuators in active control of vibration of flexible structures mainly because of their capability in providing a good shear or extension mode actuation force within a wide range of frequency. These ceramics are also available at low cost. Besides these advantages, the main drawbacks with these actuators are their high stiffness, poor conformability and incapability in providing directional actuation. These shortcomings have motivated researchers to develop shear-mode and extension-mode piezoelectric fiber composite (PFC) actuators, and the same have also been utilized extensively in active vibration control of flexible structures. However, studies on these piezoelectric actuators indicate their low actuation capability that is not usually compatible with the mechanically induced stresses in a structure of high rigidity. In view of this shortcoming, the utilization of piezoelectric actuators along with the viscoelastic materials has been recommended in a good number of studies in the literature. The low stiffness of viscoelastic materials is compatible with the actuation force of piezoelectric actuator resulting in a fruitful utilization of piezoelectric actuators in enhancement of viscoelastic (passive) damping of structural vibration. This kind of damping of structural vibration is commonly known as active-passive damping or hybrid damping or hybrid active-passive damping that is now available in different arrangements of viscoelastic and piezoelectric materials.

In this introductory chapter, first, a brief introduction on the piezoelectric ceramics and piezoelectric composites is presented. Next, a literature review on the applications of these materials in the active control and active-passive damping treatment of vibration of thin-walled flexible structures is presented. On the basis of this literature review, the scope of the present research is identified, and the objectives of the present thesis are furnished. The contributions in the field of piezoelectric actuators and their applications in active/active-passive control of structural vibration made towards the preparation of this dissertation are delineated thereafter. In the end, the organization of the thesis is outlined.

1.2 Piezoelectric materials

Piezoelectricity is a property of certain ceramics to generate electrical charge or voltage in response to an applied mechanical stress and vice-versa, and these reversible properties of piezoelectric ceramics are commonly known as the converse and direct piezoelectricity effects. Curie brothers (Jacques and Pierre) discovered the direct piezoelectricity effect in 1880. Subsequently, in 1881, converse piezoelectric effect was proposed theoretically by Gabriel Lippmann. In the same year, Curie brothers confirmed experimentally the existence of converse piezoelectric effect in piezoelectric crystals. Later, during World War II, isolated groups of researchers in US, Japan, and Soviet Union discovered a new class of synthetic materials named as ferroelectrics. They found that synthetically prepared materials had piezoelectric and dielectric properties, and these synthetic materials possess superior piezoelectric properties than natural piezoelectric materials. The synthetic piezoelectric materials include lead zirconate titanate (PZT), barium titanate, lead niobrate, lead lanthanum zirconate titanate (PLZT), ammonium dihydrogen phosphate, lithium sulfate, polyvinylidene fluoride (PVDF or PVF_2). [1].

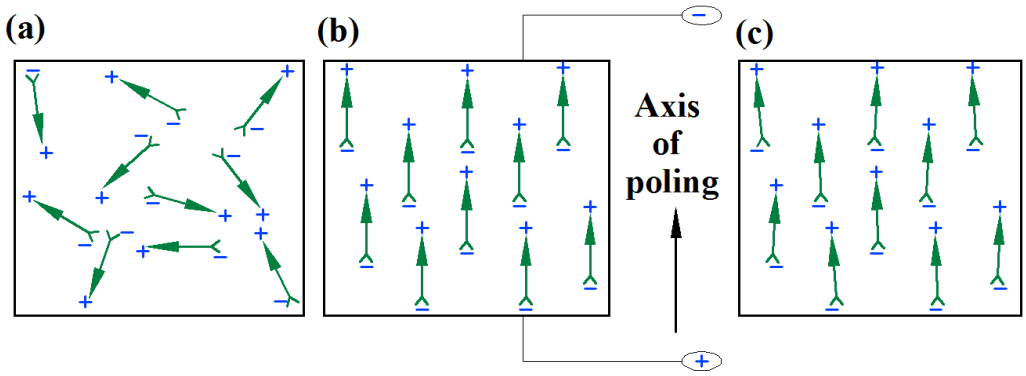

Fig. 1.1 Schematic diagrams of the domain of a piezoelectric material, (a) before polarization, (b) polarization under applied electric field, (c) remanent polarization after the removal of the applied electric field.

The raw synthetic piezoelectric ceramics are usually isotropic materials. Their dipoles are randomly oriented (Fig. 1.1 (a)) with zero dipole density or polarization. In order to achieve their piezoelectric properties, a poling treatment is needed where the piezoelectric material is first heated, and then an intense electric field (>2000 V/mm) is applied along the required poling direction for forcing the molecular dipoles to align along the same direction that is commonly

called the poling axis (Fig. 1.1 (b)). On removal of the applied electric field, the material possesses a permanent polarization (Fig. 1.1 (c)) leading to its piezoelectric properties. This phenomenon of polarization (P) is usually described by a hysteresis loop as shown in Fig. 1.2 (a). As the applied electric field increases from its zero value, the polarization increases linearly (segment AB in Fig. 1.2 (a).

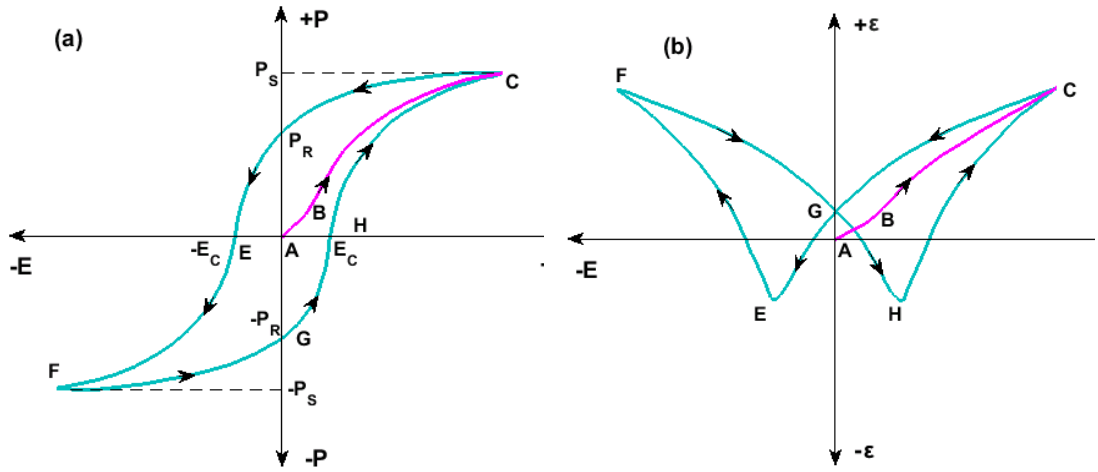

Fig. 1.2 (a) polarization (P)-electric field (E)) hysteresis loop, (b) strain (ε)-electric field (E)) hysteresis loop (butterfly curve).

Subsequently, as the electric field continues to increase, the polarization of molecular dipoles in the domain starts to switch towards the direction of the applied electric field leading to the nonlinear polarization response (segment BC in Fig. 1.2 (a)) and a point (C in Fig. 1.2(a)) of saturation of polarization (P_s) is reached. If the electric field decreases from this point (C), some molecular dipoles in the domain switch back but the polarization will not reach to its zero value for the complete removal of the applied electric field leading to a permanent polarization (P_R, Fig. 1.2(a)). In order to achieve zero polarization, a finite negative electric field is to be applied that is usually called as coercive electric field ($-E_c$). A further decrease of electric field causes a new alignment of dipoles as well as saturation of polarization ($-P_R$, Fig. 1.2(a)). The complete cycle is shown in Fig. 1.2 (a). However, in parallel to this polarization-electric field hysteresis loop, the corresponding polarization switching effect leads to the strain-electric field hysteresis loop as shown in Fig. 1.2(b). The strain-electric field hysteresis loop resembles the shape of a butterfly, and thus it is commonly known as butterfly curve. The strain increases with the increase of electric field following the path ABC (Fig. 1.2(b)) and reaches the saturation point (C). For the decrease of the

electric field from this point (C), the crystal contracts till point E (Fig. 1.2(b)) corresponding to the coercive electric field. Further decrease of the electric field causes the material to expand until a practical strain limit (F, Fig. 1.2 (b)). However, in practical applications of the piezoelectric ceramics as materials of sensors and actuators, the applied electric field is usually kept below the coercive electric field (point E or H in Fig. 1.2 (a)).

Moreover, the linear constitutive behavior of piezoelectric materials is preferred, that lies at well below the coercive electric field. In the case where the applied electric field exceeds the coercive electric field, the depoling takes place and the material behaves differently. It is also required that the operating temperature would not exceed a certain limit that is usually known as the Curie temperature [2]. The aforesaid constitutive behavior of a piezoelectric ceramic under a constant temperature can be described through four field quantities namely six components of stress (σ), six components of strain (ε), three components of electric displacement (D) and three components of electric field (E). Based on these field quantities, four different thermodynamic potentials can be obtained as given in Eq. (1.1) [3], where U, H, F and G represent internal energy, enthalpy, Helmholtz free energy and Gibbs free energy, respectively.

$$dH = \sigma d\varepsilon - DdE,\ dU = EdD + \sigma d\varepsilon,$$
$$dF = EdD - \varepsilon d\sigma,\ dG = -\varepsilon d\sigma - DdE, \tag{1.1}$$

These piezoelectric constitutive formulations (Eq. (1.1)) are utilized depending on the natural variables in an application of the material. In structural applications of piezoelectric materials, the natural variables usually appear as the strain ($\boldsymbol{\varepsilon}$) and electric field ($\boldsymbol{E}$). The corresponding linear constitutive relations of the piezoelectric material are defined from the thermodynamic potential H as follows [3],

$$\boldsymbol{\sigma} = \boldsymbol{C}\boldsymbol{\varepsilon} - \boldsymbol{e}\boldsymbol{E} \tag{1.2}$$

$$\boldsymbol{D} = \boldsymbol{e}^{\mathrm{T}}\boldsymbol{\varepsilon} + \in \boldsymbol{E} \tag{1.3}$$

where, $\boldsymbol{C}$, $\boldsymbol{e}$ and $\in$ are known as the stiffness, piezoelectric and permittivity matrices, respectively. It may be noted here that Eqs. (1.2) and (1.3) are mathematical representations of the converse and direct constitutive behavior of a linear piezoelectric material, respectively, at a constant temperature.

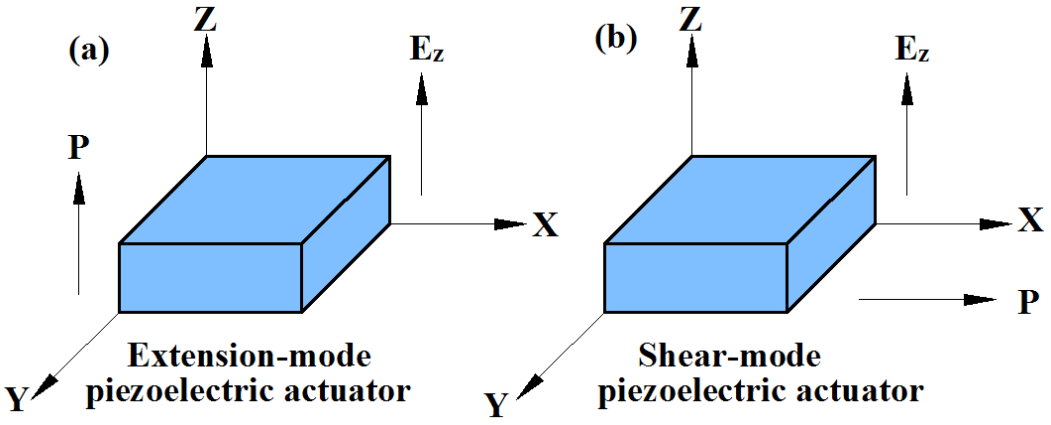

Fig. 1.3 Piezoelectric actuators, (a) extension-mode actuator and (b) shear-mode actuator (P indicates the axis of poling and E_z is the applied electric field).

These direct and converse constitutive behaviors of a linear piezoelectric ceramic are exploited to develop piezoelectric sensors and actuators, respectively. However, in applications of a piezoelectric actuator, its poling axis and the direction of the externally applied electric field are important in order to have either shear or extensional actuation force within the actuator. For having extensional actuation force in the piezoelectric actuator, the external electric field (E_z) is applied in the direction of poling (P) axis as demonstrated in Fig. 1.3(a). In contrast, the application of the external electric field (E_z) perpendicular to the axis of poling (P) results in the shear actuation force in the actuator as shown in Fig. 1.3(b). Depending on the kind of actuation force in a piezoelectric actuator, it is generally identified either as a shear-mode piezoelectric actuator or as an extension-mode piezoelectric actuator. Moreover, if an actuator is made of a monolithic piezoelectric material, then it is usually named as monolithic shear-mode piezoelectric actuator or monolithic extension-mode piezoelectric actuator. These monolithic piezoelectric actuators are extensively utilized in active control of flexible structures and a detailed review is presented in section 1.4.

1.3 Piezoelectric fiber composite (PFC)

Piezoelectric sensors and actuators have been widely utilized over the last three decades for active control of deformation/vibration of a variety of flexible structures (section 1.4). In most of these applications of the piezoelectric sensors and actuators, the monolithic piezoelectric materials are utilized, and it may be due to their availability at low cost. However, the piezoelectric sensors and

actuators are usually attached to or embedded in the host structures for achieving active control of their (host structures) deformation/vibration. These kinds of integration of the piezoelectric sensors/actuators require their sufficient flexibility and conformability especially for a host structure with highly curved boundary surface or complex geometry. In addition to these properties, a piezoelectric actuator should have a high strain energy density and also be capable of providing directional actuation. With reference to these required properties of a piezoelectric actuator, monolithic piezoelectric actuators possess high brittleness, high stiffness and low strain energy density. In view of these shortcomings, the piezoelectric fiber composites (PFCs) emerged as materials for the piezoelectric sensors/actuators. A typical PFC is made of piezoelectric fibers and a polymer matrix. The polymer constituent provides sufficient flexibility and conformability of a PFC while the inclusion of piezoelectric fibers yields the electro-elastic properties of the PFC.

The PFCs available in the literature may be classified as extension-mode and shear-mode PFCs. The extension-mode PFCs are capable of providing extensional actuation force along the axes of the material principal coordinate system, while the shear-mode PFCs provide transverse shear actuation force in planes of principal axes of the material coordinate system. In the following subsections, a literature review on the development of these shear and extension mode PFCs is presented.

1.3.1 Extension-mode PFC

Newnham et al. [4] proposed the classification of piezoelectric composites based on the connectivity of a piezoelectric fiber and a polymer matrix. According to this classification, for instance, the particulate piezoelectric composite is named as 0-3 piezoelectric composite where 0 and 3 indicate the phase connectivity of piezoelectric particles and the matrix phase, respectively. Similarly, the unidirectional piezoelectric fiber-reinforced composite is named as 1-3 PFC where 1 and 3 indicate the phase connectivity of the piezoelectric fiber and the matrix phase. However, concerning the development of PFCs, 1-3 PFC was first used as the material for transducers for pulse echo medical imaging technique [5–12]. Later, Smith and Auld [13] presented a 1-3 PFC consisting of vertically reinforced piezoelectric fibers embedded in an epoxy matrix. This 1-3 PFC is commonly known as a material of thickness mode piezoelectric actuator, where the extension

mode piezoelectric actuation appears in the thickness/transverse direction for an externally applied transverse electric field. Subsequently, a horizontally reinforced PFC was proposed by Hagood and Bent [14]. The fibers of this PFC are transversely poled, and it (PFC) provides in-plane actuation force for a transversely applied electric field. Bent and Hagood [15] proposed a similar PFC by the name of Active Fiber Composite (AFC). The piezoelectric fibers of AFC are poled along their longitudinal direction and it provides in-plane actuation force by means of a special arrangement of electrodes (Interdigitated Electrodes (IDEs)). The AFC was further modified by High and Wilkie [16] to improve upon its actuation capability. This modified AFC is known as the Macro-Fiber Composite (MFC), and it is the most popular PFC for active control of flexible structures. Mallik and Ray [17] and Ray [18] proposed a 1-3 PFC that has the constructional features similar to those of an earlier PFC [14] but every layer of piezoelectric fibers in the PFC can be activated by a uniform electric field [18] leading to the improved actuation capability of the 1-3 PFC actuator.

1.3.1.1 Analytical studies on the electromechanical properties of extension-mode PFCs

Apart from the design of the aforesaid popular extension-mode PFCs, many other studies have also been reported in the literature where the main objective is to analyze the electromechanical behavior of extension-mode PFCs by evaluating their effective electro-elastic properties through available micromechanics methods. Among many others, Benveniste and Dvorak [19] and Wang [20] studied the electromechanical behavior of a PFC by developing its micromechanics model in continuum approach. Dunn and Taya [21] presented the uncoupled behavior of a PFC by evaluating its effective properties using the classical micromechanics theories. Benveniste [22] derived the electro-elastic properties of the binary and multiphase piezoelectric composites using concentric cylinder assemblage approach. Benveniste [23] also investigated the exact constitutive relations for binary piezoelectric composites with arbitrary geometry. Huang and Kuo [24,25] presented a micromechanics model of a PFC having spatially oriented piezoelectric fibers. Yu [26] developed a micromechanics model for evaluating effective properties of two-phase PFC using the equivalent inclusion method and Fourier series expansion. Sabina et al. [27] utilized asymptotic homogenization method (AHM) to obtain effective properties of PFC having a hexagonal symmetry.

Tan and Tong [28,29] proposed the rectangular as well as the rectangular-cylinder model of PFC and derived the closed-form expressions for its effective electro-elastic constants using linear piezoelectricity and iso-field assumption. Bowen et al. [30,31] investigated the influence of pore anisotropy, fiber volume fraction and polymer phase on the hydrostatic properties of 3-3 PFC. Ruan et al. [32] developed a three-dimensional connectivity model of PFC and reported that the effective piezoelectric properties heavily depend on the fiber orientation angle. They also observed severe influence of dielectric permittivity of the matrix on the effective properties of the PFC.

Kar-Gupta and Venkatesh [33–35] investigated effects of the poling direction and fiber distribution on the electromechanical behavior of a 1-3 PFC and reported that the effective properties are not sensitive to the fiber distribution in the matrix. Della and Shu [36,37] investigated the electromechanical behavior of a 1-3 PFC with active, passive and porous non-piezoelectric matrix phases and reported that the active polymer matrix can significantly improve the effective properties of a PFC in comparison to the active piezoelectric matrix. They also found that the porosity can significantly enhance the effective hydrostatic performance of 1-3 PFC. Challagulla and Venkatesh [38] presented the effective electro-elastic properties of 2-2 layered PFC using an asymptotic homogenization method (AHM). Deraemaeker et al. [39] presented a micromechanics model for evaluating the effective properties d_{31} and d_{33} of an MFC. Sakthivel and Arockiarajan [40] estimated the effective thermo-electromechanical properties of a 1-3 PFC where both the constituent phases are piezoelectrically active, and it is reported that the effective pyroelectric coefficients are strongly dependent on the active polymer matrix. Nasser et al. [41] presented a micromechanics model of a MFC using the UFM. Brenner et al. [43] obtained the electromechanical behavior of a 2-1-2 PFC using the double asymptotic homogenization method (DAH) and a numerical Fourier transform, and reported that the DAH overestimates the out-of-plane effective piezoelectric properties.

Sakthivel and Arokiarajan [44, 45] proposed an analytical model for estimating the effective properties of the 1-3-2 piezoelectric composite. The matrix and fiber materials of this piezoelectric composite are considered as piezoelectrically active materials. The effects of the poling characteristics of the individual fiber and matrix phases on the effective properties of the 1-3-2

piezoelectric composite are reported in these studies [44, 45]. Kalamkarov and Savi [46] presented a micromechanical model of a smart grid composite structure. Prasath and Arockiarajan [47] proposed a micromechanics model for estimating the effective properties, d_{31} and d_{33} MFC using the equivalent layered approach. Kar-Gupta and Venkatesh [48] investigated effects of the poling direction and the phase volume fraction of the piezoelectric fibers on the electromechanical behavior of 2-2 multilayered PFC and observed that the effective electro-elastic properties are greatly influenced by the softer constituent. Iyer and Venkatesh [49] derived closed-form expressions for the effective electro-elastic constants of a 3-1 PFC with anisotropic constituent materials. Eynbeygi and Aghdam [50] presented a generalized plane strain micromechanics model based on the element-free Galerkin method (EFG) to study the electromechanical behaviour of a PFC with the reinforcement of the elliptical piezoelectric fibers.

1.3.1.2 Numerical studies on the electromechanical properties of extension-mode PFCs

The aforesaid literature review shows a good number of analytical studies on estimation of electromechanical behavior of different kinds of PFCs. However, in parallel, a good number of numerical studies on the same area are also available in the literature. Among many others, Poizat and Sester [51] evaluated the effective properties of 1-3 PFC using 3D solid element in ABAQUS where they studied effects of the fiber volume fraction and the fiber aspect ratio on the longitudinal and transverse piezoelectric coefficients. Pettermann and Suresh [52] presented a unit cell model of a 1-3 PFC with periodic hexagonal or square distribution of continuous fibers. Qin [53] used the boundary element method (BEM) to compute the effective properties of a PFC having inclusions or voids of various shapes. Berger et al., [54–57] developed a FE-based methodology to evaluate effective electro-elastic properties of 1-3 PFCs. Kari et al. [58] carried out a numerical study on the effective properties of PFC having randomly oriented piezoelectric fibers and found that the effective properties are dependent on both the fiber volume fraction and the fiber diameter. Deraemaeker et al. [59] proposed a FE procedure to estimate the effective electro-elastic properties of a MFC. Kar-Gupta and Venkatesh [60] numerically studied the electromechanical behaviour of five types of piezoelectric composites namely, particulate, short-fiber, long-fiber, laminate and networked composites. They reported effects of the geometrical

connectivity, the grain size distribution, the volume fraction and the poling direction of piezoceramic fibers on the electromechanical behavior of the piezoelectric composites. Deraemaeker and Nasser [61] developed a FE based homogenization technique for finding d_{31} and d_{33} of a MFC. Li et al. [62] carried out a FE based numerical study to investigate the effect of piezoelectric fiber shape on the effective properties of a 1-3 PFC and reported that the shape of fibers has negligible effect on the effective properties of a 1-3 PFC. Trindade and Benjeddou [63] presented a numerical study to estimate the effective electro-elastic property, d_{31} of a MFC considering it (MFC) as a composite package including the electrode and the protective layers.

1.3.1.3 Experimental studies on the electromechanical properties of extension-mode PFCs

Although it is in a limited number, the experimental studies on the electromechanical behavior of extension-mode PFCs are also available in the literature. Zhen et al. [64] fabricated a 1-3 PFC using dice-fill technique and obtained the effective elastic and piezoelectric properties experimentally for 10-35% of piezoceramic fiber content. Shindo et al. [65] carried out an experimental study on the polarization switching in 1-3 PFC. Zhou et al. [66] fabricated a 1-3-2 PFC using dice and fill technique for experimental demonstration of its electromechanical coupling behavior. Jayendiran and Arockiarajan [67] conducted an experimental study on the nonlinear electro-elastic behavior of 1-3 PFC for its different fiber volume fraction (under cyclic loading and compressive stress). They reported significant influence of fiber volume fraction and compressive stress on the electromechanical response of 1-3 PFC. Xu et al. [68] developed three types of 1-3 PFCs with the Gaussian distribution of piezoelectric fibers. Geng et al. [69] fabricated a multi-element 1-3 PFC that is comprised of piezoelectric ceramic, epoxy matrix and decoupling material (silica gel and polyurethane), and they observed that the multi-element 1-3 PFC has higher piezoelectric voltage than that of the monolithic piezoelectric material. Mi et al. [71] fabricated a 1-1-3 ceramic/rubber/resin PFC using dice & fill technique and studied experimentally the effect of percentage volume of ceramic on the 1-1-3 PFC. They found that the variation of ceramic fiber volume fraction has only effect on the acoustic impedance whereas the same parameter has no effect on the electromechanical coupling coefficient of the PFC. Yi et al. [72] experimentally

studied the electromechanical coupling in a 2-2-2 PFC comprised of uniform or Gaussian distribution of piezoelectric fibers and addressed that 2-2-2 PFC possesses high electromechanical coupling in the thickness mode actuation.

1.3.2 Shear-mode PFCs

The aforesaid analytical, numerical and experimental studies show a great deal of research on the development of extension-mode PFCs, whereas a few studies on the development of shear-mode PFCs are available in the literature till the date. Raja and Ikeda [73] proposed a shear-mode PFC by the name of Shear Actuated Fiber Composite (SAFC). It is basically a 2-2 PFC lamina that is composed of the longitudinally poled piezoelectric fibers and epoxy matrix so that the electrically induced transverse shear actuation force arises in response to an externally applied transverse electric field. This electromechanical behavior of SAFC is demonstrated in [73] by deriving its effective electro-elastic properties using UFM where the proposed SAFC is taken in the form of a composite laminate of SAFC layer, protective layer of acrylic, Kapton layer and electrode layer. Benjeddou and Al-Ajmi [74] derived the closed-form expressions of effective material constants of a similar PFC named as d_{15} shear-mode MFC. Apart from these theoretical works, Trindade and Benjeddou [75] developed FE based homogenization technique for seven-layered d_{15} MFC and addressed its electromechanical behavior through numerical estimation of the effective material constants. Here, the d_{15} shear-mode MFC is taken in a composite package so that the effective electromechanical coupling reduces notably resulting in lesser shear piezoelectric actuation. Trindade and Benjeddou [76] carried out further study and reported the effects of fiber volume fraction, active layer thickness, elastic modulus of epoxy and thickness of electrodes on the effective properties of the d_{15} MFC. They recommended relatively thicker piezoelectric fibers and stiffer epoxy binder for better electromechanical coupling in d_{15} shear-mode MFC. Kranz et al. [77,78] estimated the effective properties of the d_{15} shear-mode MFC using enthalpy based homogenization method in conjunction with the FE procedure. The experimental study on the electromechanical behavior of this d_{15} shear-mode MFC was also carried out by Trindade and Benjeddou [79]. Yuan et al. [80] fabricated a shear piezoelectric fiber composite (SPFC) that is comprised of transversely poled

piezoelectric fibers embedded in the epoxy matrix where shear actuation appears for an applied electric field along the length of the fibers through IDEs. For a fiber volume fraction of 56.6%, the effective shear piezoelectric coefficient (d_{35}) of SAFC appears with the value of 320 pm/V whereas the same coefficient for SPFC arises with the value of 400 pm/V.

1.4 Smart structures

The piezoelectric sensors and actuators are usually attached to or built in a host structure for achieving self-sensing and self-controlling capabilities of the overall structure. A structure having these capabilities is commonly called as a smart or intelligent structure [81–85]. Figure 1.4 demonstrates the schematic diagram of a smart structure, where the substrate structure is attached to a piezoelectric actuator and a sensor at its top and bottom surfaces, respectively. The deformation of the overall structure is sensed by the piezoelectric sensor, and it is fed back to the piezoelectric actuator through a controller for an appropriate action in controlling the deformation of the overall structure (Fig. 1.4).

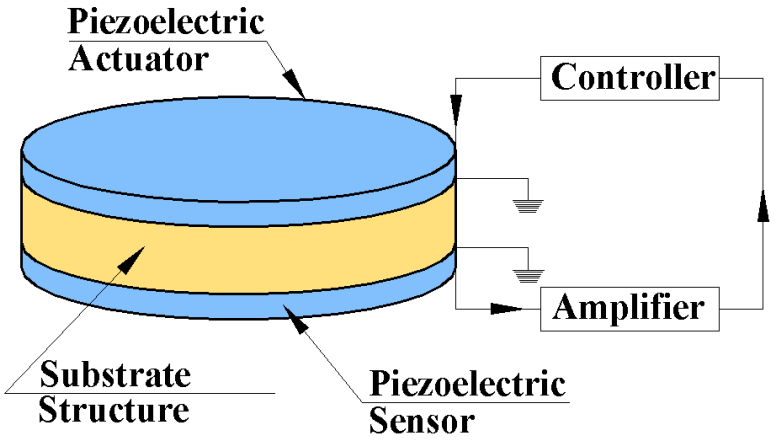

Fig. 1.4 Schematic diagram of a smart structure.

A great deal of research on the development of smart structures has been reported in the literature especially for the active control of deformation/vibration of the basic structural elements namely beams [86-127], plates [128-161] and shells [162-179]. Besides, the concept of smart structure has also been implemented for active control of other kinds of flexible structures [180-183]. Although the extension-mode monolithic piezoelectric actuators are utilized in these studies [86-183], the applications of the shear-mode monolithic

piezoelectric actuators have also been addressed in a good number of available studies on the active control of beams [184-208], plates [209-219], shells [220-224] and other kinds of structural elements [225-227]. These studies infer the significance of extension and shear mode monolithic piezoelectric actuators in the active control of flexible structures. However, the monolithic piezoelectric actuators possess some indicative drawbacks in their structural applications as mentioned in section 1.3. So, the polymer-based PFC actuators are developed (section 1.3), and the same have also been utilized widely for the active control of different kinds of flexible structures. In the following subsections, a literature review on the utilization of the shear/extension mode PFC actuators in active control of beams, plates, shells and other kinds of flexible structures are furnished.

1.4.1 Smart beams with extension-mode PFC actuator

Aldraihem and Wetherhold [228] demonstrated the active control of laminated beams integrated with distributed 1-3 PFC actuators. Mahut et al. [229] studied the performance of a PFC actuator in active control of cantilever beams, and reported that the actuation capability of the PFC reduces after a certain value of the fiber volume fraction. Cesnik and Shin [230] developed an asymptotic formulation for analysis of a multi-cell box beam element integrated with the AFC actuator. Sodano et al. [231] experimentally studied the attenuation of vibration and structural health monitoring of beams using MFC actuator. Wickramasinghe and Hagood [232,233] experimentally investigated the usefulness of AFC actuator in control of helicopter blades. Park and Kim [234] studied the performance of single crystal MFC (single piezoelectric crystal material) actuator for active twisting actuation of rotor blades and found superior actuation performance of MFC compared to that of AFC. Brockmann and Lammering [235] developed the FE model of a rotating thin-walled beam integrated with PFC considering shear flexibility and out-of-plane torsional warping. Guennam and Luccioni [236] presented the FE model of a single cell thin-walled smart box-beam that is designed with two different control configurations namely inclined pairs of PFC patches at the top and bottom surfaces of the host structure and independent control patches, and reported that the later configuration (independent control patches) provides better control of the box-beam. Nguyen and Kornmann [237] performed a comparative study on the actuation capabilities of AFC, MFC and

conventional monolithic piezoelectric actuators in control of flexural vibration of a cantilever beam and found that PFC actuators possess higher actuation capability than that of the monolithic piezoelectric actuators. Choi et al. [238,239] studied the vibration suppression of rotating thin-walled beams integrated with MFC actuators and PVDF sensor and reported that the rotation of beam and fiber orientation angle of MFC have significant influence on the smart damping in beams through the negative velocity feedback control law. Cook and Vel [240] carried out the multi-scale analysis of a laminated composite beam integrated with the segmented extension-mode PFC actuators and found that transverse shear stress is maximum at the interface of the PFC segment and substrate layer while longitudinal stress is higher in PFC actuator than that in the substrate layer.

1.4.2 Smart plates with extension-mode PFC actuator

Azzouz et al. [241] presented an FE analysis of cantilever square and triangular plates integrated with MFC or PZT5A actuator, and reported excellent actuation capability of MFC actuator in comparison to that of the PZT5A actuator. Mallik and Ray [242] presented the exact solution for flexural deformation of a laminated plate integrated with a 1-3 PFC actuator [17]. The same authors [243] also presented the FE analysis of symmetric and anti-symmetric laminated plates integrated with the 1-3 PFC actuator. Park and Kim [244] studied the large aero-thermal deflection of plates embedded with the MFC actuators and reported the snap-through behavior of the smart plates under the actuation force in the MFC actuators. Panda and Ray [245], Ray and Sachade [246,247], Reddy and Ray [248] and Panda and Ray [249] presented the static/dynamic behavior of a functionally graded plate integrated with a 1-3 PFC [17]. Zhang and Shen [250] developed a three dimensional analytical model to study the active vibration control of laminated plates utilizing 1-3 PFC actuator layers equipped with interdigitated electrodes (IDE). Dano and Julliere [251] proposed a control algorithm for active control of thermally induced deflection of a cantilever plate integrated with MFC actuators. Mahato and Maiti [252] studied the aeroelastic flutter response of a laminated composite plate integrated with AFC actuators. They reported that the change in the stiffness of the composite plate under hygro-thermal condition causes reduced flutter velocity and frequency but those regain under the activated AFC actuators. Panda [253] and Panda and Sopan [254] presented the

performance of a cylindrically orthotropic annular PFC actuator in active control of nonlinear deformation of a functionally graded annular sector plate. Kapuria and Yasin [255] developed a FE model for active vibration control of flexible laminated skew plate bonded with PFC actuators and sensors. Kumar et al. [256] carried out a nonlinear frequency response analysis of a heated functionally graded plate integrated with a layer of PFC actuator and reported the effect of temperature on the actuation capability of the PFC actuator in control of the heated plate. Zhang et al. [257] presented a comparative study on the actuation capabilities of d_{31} MFC and d_{33}MFC in active control of a laminated composite plate and reported that the actuation capability of d_{33} MFC is greater than that of d_{31} MFC. Zippo et al. [258] demonstrated the active vibration control of free-edge sandwich plate using MFC actuator and PPF controller. Kumar et al. [259] performed a comparative study on the control capabilities of four different types of cylindrically orthotropic PFC actuators in active control of an isotropic annular plate, and addressed the best one (PFC actuator) for effective actuation of the annular plate. Pandey and Arockiarajan [260] studied the performance of d_{31} and d_{33} MFC actuators in active control of a composite plate subjected to the thermal loading and suggested appropriate fiber thickness and fiber orientation angle in MFC for efficient actuation of the plate. Wang et al. [261] presented the vibration suppression of morphing wing and the smooth continuous morphing motion of the wing using MFC actuator. Recently, Rouzegar and Abbasi [262] proposed a new four-node nonconforming rectangular plate element for the FE analysis of cross-ply and angle-ply laminated composite plates integrated with PFC actuators.

1.4.3 Smart shells with extension-mode PFC actuator

Kwak et al. [263] experimentally investigated the attenuation of vibration of a circular cylindrical shell glued with two MFC actuators. They used multi-input-multi-output (MIMO) PPF controller for activating the MFC actuators and demonstrated the actuation capability of MFC actuator in active control of the shell. Sohn et al. [264,265] presented the vibration control of hull structures using surface bonded MFC actuator patches that are activated through the design of a LQG (Linear Quadratic Gaussian) controller. Kim et al. [266] investigated the active vibration suppression of end-capped cylindrical shell integrated with MFC

actuators and reported an indicative control capability of MFC actuator in vibration control of the shell. Panda [267] investigated the control capability of a short piezoelectric fiber reinforced composite (SPFRC) [268] for active vibration control of functionally graded circular cylindrical shell and reported its (SPFRC) actuation capability in comparison to that of the 1-3 PFC actuator [17] and the monolithic piezoelectric actuators. Guo et al. [269] presented the nonlinear vibration control of a doubly curved shell using d_{31} MFC actuator where they addressed efficient vibration control, as well as the dynamic stability, of the structure using the MFC actuator.

1.4.4 Other smart structures with extension-mode PFC actuator

Tarazaga et al. [270] experimentally demonstrated the active vibration suppression of a space inflatable boom structure embedded with MFC actuators. The PPF controller with the feedback of velocity, strain and acceleration signals is used to attenuate the fundamental mode of vibration and they observed that velocity and acceleration feedback controller provides efficient vibration reduction in expense of a low control voltage. Park et al. [271] presented the damage detection of railway tracks utilizing MFC impedance based wireless structural health monitoring (SHM) systems. Barkanov et al. [272] presented a methodology for the optimal placement of MFC actuators in active control of helicopter blades. Bilgen et al. [273,274] studied the actuation of a variable chamber airfoil using MFC actuator and observed a significant lift coefficient due to the peak-to-peak actuation voltage. Wang et al. [275] reported that the roll maneuver of unmanned air vehicle (UAV) can be achieved effectively via the active shape control of morphing wings utilizing multiple MFC actuators.

1.4.5 Smart structures with shear-mode PFC actuator

The aforesaid studies indicate a good deal of research on the utilization of extension-mode PFC actuators for active control of different kinds of flexible structures. In parallel, a few studies on the utilization of the shear-mode PFC actuators have been addressed in the literature. Raja et al. [276] numerically investigated the shear actuation capability of SAFC [73] in active vibration control of a laminated plate. The SAFC actuator is embedded within the laminated plate and used to provide smart damping, where they observed a promising smart damping capacity of SAFC in attenuation of vibration of the thin laminated plate.

Gopinath et al. [277,278] studied the active control of aero-elastic flutter of a plate using the shear-mode PFC (SAFC) actuator along with an extension-mode (MFC) PFC actuator, where they observed improved active control of the plate due to the incorporation of the shear PFC actuator.

1.5 Hybrid active-passive damping

Viscoelastic materials (VEMs) have long been utilized for passive damping of structural vibration due their ability to dissipate energy under dynamic loads. Generally, these materials are attached to or embedded in a host structure [279–281] for vibration attenuation of the overall structure. In a particular case of passive damping of flexural vibration of thin-walled structures, VEMs are usually employed in the form of layer that is freely attached to the host structure-surface or constrained between the host structure-surface and a constraining layer. The damping treatment of structural vibration through these arrangements are commonly known as the unconstrained layer damping (UCLD) [279] and constrained layer damping (CLD) [281] treatments. The passive damping through the UCLD treatment appears by means of extensional strain of the unconstrained VEM layer whereas the same (damping) in the CLD treatment arises due to the transverse shear strain of the constrained VEM layer. The CLD treatment is also known as the passive constrained layer damping (PCLD) treatment. These damping treatments are usually effective at high operating frequency but incapable to provide notable damping at low operating frequency [282]. Moreover, these passive damping treatments are not adaptive to the change of vibration characteristics of a structure. Besides, the piezoelectric actuators can provide adaptive control of a flexible structure within a wide range of frequency. So, the utilization of piezoelectric actuators along with the viscoelastic materials has been addressed in a good number of research papers [283–292] especially for having efficient adaptive control or damping of vibration of flexible structures within a wide range of operating frequency. This kind of damping treatment of structural vibration is commonly called as active-passive or hybrid or hybrid active-passive damping treatment, and it is now available in different arrangements of VEM and piezoelectric actuator namely Active Constrained Layer Damping (ACLD) [288], Electromechanical Surface Damping (EMSD) [289,290], Conventional Active Piezoelectric Damping Composite (CAPDC) [291], Active Piezoelectric Damping Composite (APDC) [292]. Among these different kinds of hybrid active-passive

damping treatments, the most popular one is the ACLD treatment for its indicative active-passive damping capability, and thus its wide application for vibration control of different kinds of flexible structures have been addressed in the literature after the proposition of the concept. Figure 1.5(a) shows a substrate structure integrated with an ACLD layer where the viscoelastic layer is sandwiched between the substrate-surface and a piezoelectric constraining layer (active layer). It is similar to the PCLD treatment except the active constraining layer instead of the passive one. As the overall structure undergoes bending deformation (Fig. 1.5(b)), the viscoelastic layer experiences transverse shear strain that induces passive damping in the overall structure according to the usual concept of the PCLD treatment. However, when the piezoelectric constraining layer (active layer) is activated by means of some control strategy, it (active layer) enhances the shear deformation of the viscoelastic layer and also imparts direct actuation of the overall structure resulting in an improved vibration control of the overall structure over that in the use of the PCLD treatment. In the following subsections, a detailed review on the development of this ACLD treatment is furnished.

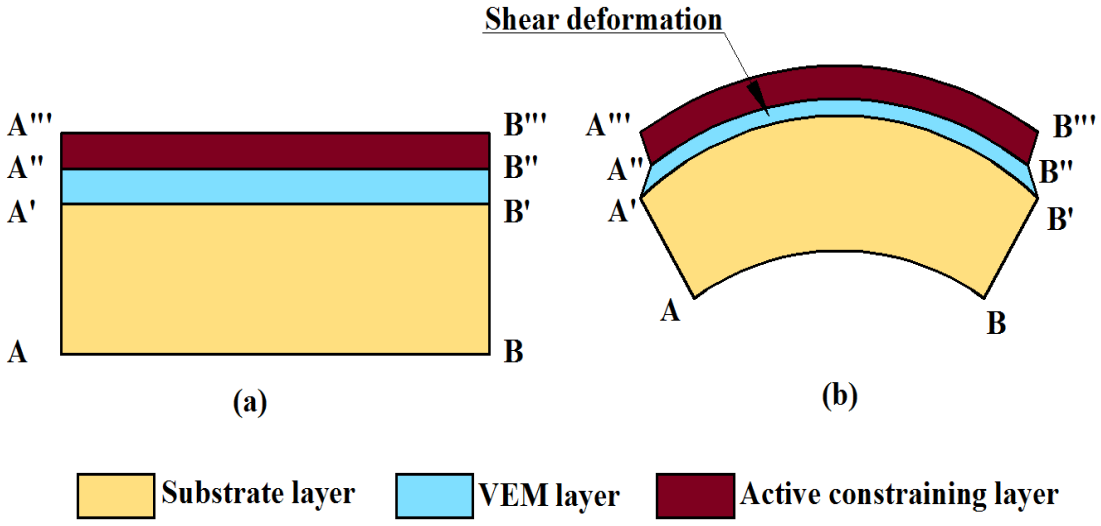

Fig. 1.5 Schematic diagram of a substrate structure integrated with a ACLD layer, (a) unreformed and (b) deformed.

1.5.1 ACLD treatment of beams using extension-mode monolithic piezoelectric actuator

Agnes and Napolitano [293] and Yellin and Shen [294] demonstrated ACLD treatment of a beam where the same piezoelectric constraining layer acts as the sensor as well as actuator element. Baz and Ro [295,296] proposed an ACLD treatment using a VEM layer sandwiched between piezoelectric actuator and sensor layers in order to avoid the complex arrangements of self-sensing actuators. Further analysis of this arrangement of ACLD treatment was carried out by Veley and Rao [297] and Baz [298] and they observed significant collocalization between the actuator and sensor. A segmented configuration of active and passive layers for ACLD treatment of beams was presented by Kapadia and Kawiecki [299]. Azvine et al. [300] demonstrated Active–Passive Constrained Layer Damping (APCLD) treatment of beams using piezoelectric patch instead of layer. Similar APCLD treatment was also analyzed by Rongong et al. [301]. However, a drawback in the aforesaid ACLD treatment was identified as the active action of actuator does not transfer to the host structure in an effective manner due to the intermediate soft viscoelastic layer. So, the piezoelectric actuators remain underutilized [302]. In this consequence, Liao and Wang [302] suggested an edge element in the ACLD treatment to improve the transmissibility of active action from actuator layer to host structure, and this active-passive damping treatment is named as Enhanced Active Constrained Layer Damping (EACLD) treatment. Subsequently, Varadan et al. [303] studied the optimal placement of edge elements in the ACLD treatment of structural vibration. Badre-Alam et al. [304] analyzed the damping capacity of EACLD in control of a substrate beam by locating the treatment symmetrically over the top and bottom surfaces of the host beam. Liu and Wang [305] also utilized the EACLD treatment in control of beams but they used self-sensing piezoelectric actuators. Crassidis et al. [306] and Chen and Baz [307] introduced a configuration of the ACLD treatment to improve the transmissibility of active action by separately using the active and passive damping treatments, and this damping treatment was termed as Active Control/Passive Constrained Layer Damping (AC/PCLD) treatment. Lam et al. [308] also worked on the similar AC/PCLD treatment of beams where the piezoelectric actuator patch and PCLD layer are either attached to the same (top/bottom) surface or attached to the different (top and bottom) surfaces of the host beam. They reported the requirement of small control voltage for this

AC/PCLD treatment in comparison to that for the conventional configuration of ACLD treatment. Lam et al. [309] also developed Active Control/Passive Stand-Off Layer Damping (AC/PSOLD) treatment by placing piezoelectric actuator layer directly in contact with substrate beam in order to have simultaneous active actuation and elevated PCLD treatment.

1.5.2 ACLD treatment of plates using extension-mode monolithic piezoelectric actuator

Baz and Ro [310] investigated the ACLD treatment of flexural vibration of plates and reported superior performance of ACLD treatment over PCLD treatment. Ray and Baz [311] studied the optimal ACLD treatment in control of plate vibration and observed better ACLD treatment in case of a viscoelastic core with low loss factor. Park and Baz [312] carried out FE analysis of ACLD (viscoelastic layer sandwiched between two monolithic piezoelectric layers) treatment for plates and reported that the damping improves five times for the use of active constraining layer (ACLD) instead of the passive one (PCLD). Ro and Baz [313] addressed the optimal locations of ACLD patches over the flat plate-surface for effective damping of plate vibration. Liu et al. [314] proposed H_∞ robust vibration control of plates treated with segmented ACLD treatment. Boudaoud et al. [315] developed a FE model for a five-layered plate where a viscoelastic layer is sandwiched between two elastic layers that are further stacked between two piezoelectric actuator layers. Araujo et al. [316], Moita et al. [317,318] and Araujo et al. [319] presented FE analysis of the active-passive damping treatment of multilayered laminated plates where viscoelastic layer is sandwiched between piezoelectric actuator layers that are further covered by two elastic face layers. Plattenburg et al. [320] presented the analytical model for thin plate structures integrated with the active and passive damping patches side-by-side and verified this analytical model with experimental results. For the partial ACLD treatment of plates, Lu et al. [321] developed a corresponding FE formulation based on the GHM model and reported superior performance of VEM at high frequency range while piezoelectric actuator works well at low frequency range. Luis et al. [322] presented the multi-objective optimization problem based on the direct multi-search algorithm for the vibration control of laminated composite plates using ACLD treatment. Moita et al. [323] carried out an FE analysis of hybrid active-passive damping of multilayered functionally graded plates, and found that the active-passive damping treatment

with embedded piezoelectric layer provides lesser damping in comparison to that when the same active layer is bonded to the top/bottom surface of the overall plate structure. Lu et al. [324] presented a numerical model with updating methodology for superior estimation of damping in a clamped-clamped plate integrated with ACLD patches. Kumar et al. [325] proposed a new 0-3 VEC composite layer instead of the conventional VEM layer for improved ACLD treatment of plates.

1.5.3 ACLD treatment of shells using extension-mode monolithic piezoelectric actuator

Shen [326] utilized the ACLD treatment for active vibration control of deep shells where basically the energy dissipation from the overall structure is analyzed to ensure the stability of the ACLD treated shell structures. Baz and Chen [327] presented the axisymmetric vibration control of simply supported circular cylindrical shells using ACLD treatment and reported efficient vibration control with low control voltage. Ray et al. [328] presented FE analysis of active-passive vibration control of thin cylindrical shell integrated with two ACLD patches and observed significant attenuation of shell vibration by activating the actuator layer of ACLD patches according to the derivative feedback control law. Ray and Reddy [329] presented the vibration control of a thin circular cylindrical shell using ACLD patches with their optimum size and locations at the inner surface of the shell and reported that the efficient performance of the ACLD patches can be achieved by locating them at 180 degree apart from each other. Zheng et al. [330] investigated the performance of segmented ACLD patches in vibration control of cylindrical shells and reported that the performance of ACLD treatment mainly relies on the topology of ACLD patches, control action in activating actuator, control gain and thickness of the shell. Kumar and Singh [331] experimentally studied the multimode vibration control of a curved panel integrated with the partial ACLD treatment and observed that ACLD patches located at the edges and middle span can significantly control the first four bending modes of vibration of the curved panel.

1.5.4 ACLD treatment of beams using shear-mode monolithic piezoelectric actuator

Batra and Geng [332] presented a comparative study where the effectiveness of a hybrid active-passive damping treatment using monolithic shear-mode

piezoelectric actuator is compared with that for the use of monolithic extension-mode piezoelectric actuator. They observed that the energy dissipation through the hybrid damping treatment using shear piezoelectric actuator is higher than that for the similar damping treatment using extension-mode piezoelectric actuator. Trindade et al. [333] experimentally analyzed the vibration characteristics of a sandwich beam with the viscoelastic core where also a monolithic shear piezoelectric actuator is located at the core. They reported indicative hybrid active-passive damping treatment of the overall sandwich beam using the shear piezoelectric actuator at the core. Apart from these studies, further investigation on the shear based active-passive damping treatment of structural vibration has not been observed by this author.

1.5.5 ACLD treatment of beams using extension-mode PFC actuator

Although most of the studies on the active-passive damping treatment of structural vibration have been carried out using monolithic piezoelectric actuators, the utilization of the PFC actuators for the same has also been addressed in the literature. Ray and Mallik [334] used an extension-mode 1-3 PFC actuator for ACLD treatment of beams and reported superior performance of the treatment due to the replacement of the monolithic piezoelectric actuator by the PFC actuator. Ray and Pradhan [335] presented the actuation capability of a vertically reinforced 1-3 PFC in ACLD treatment of a laminated beam. A similar study was also carried out by Sarangi and Ray [336] where the vertically/obliquely reinforced 1-3 PFC actuator is utilized as the active layer of ACLD treatment in control of geometrically nonlinear vibration of laminated composite beams. Biswas and Ray [337] analyzed the active-passive damping of geometrically nonlinear vibration of a rotating beam using vertically/obliquely reinforced 1-3 PFC actuator as the active constraining layer. They observed that ACLD treatment performs better when the vertically reinforced 1-3 PFC is used instead of the obliquely reinforced 1-3 PFC. Ghosh et al. [338] investigated the vibration control of a sandwich beam using the ACLD patches where the vertically reinforced 1-3 PFC actuator is utilized, and they reported an indicative actuation capability of the vertically reinforced 1-3 PFC in the ACLD treatment. Sahoo and Ray [339] analyzed the ACLD treatment of a laminated composite beam using the triangular or rectangular ACLD patches and reported that triangular ACLD patch shows

better active vibration control of the beam in comparison to that for the rectangular ACLD patch.

1.5.6 ACLD treatment of plates using extension-mode PFC actuator

Ray and Reddy [340] presented the structural-acoustic control of symmetric and antisymmetric laminated plates integrated with ACLD patches using a 1-3 PFC actuator. Ray [341] studied the utility of two ACLD patches in the vibration attenuation of FG plates where the ACLD patches are separately made using horizontally and obliquely reinforced PFC actuator. He observed that the improvement in damping can be achieved by integrating the ACLD patches on the softer surface of FG plate. Panda and Ray [342,343] presented the active control of geometrically nonlinear vibration of FG laminated plates using ACLD patches attached to the top surface of the graded laminated plate. Ray and Faye [344] presented the structural-acoustic control of laminated composite plates using vertically/obliquely reinforced 1-3 PFC in the ACLD patches. Kumar and Ray [345] and Li and Narita [346] studied the hybrid active-passive damping of a sandwich plate bonded with the ACLD patches having the active layer of vertically/obliquely reinforced 1-3 PFC. Kanasogi et al. [347, 348] presented linear and nonlinear vibration control of laminated skew plates using vertically/obliquely reinforced 1-3 PFC actuator in the corresponding ACLD treatment. Kumar and Ray [349] studied the active-passive damping of geometrically nonlinear vibration of laminated composite plates using vertically/obliquely reinforced 1-3 PFC through the ACLD arrangement. Kumar et al. [350] investigated the ACLD treatment of geometrically nonlinear vibration of a heated FG plate using 1-3 PFC actuator. Kattimani and Ray [351] presented the geometrically nonlinear vibration control of magneto-electro-elastic (MEE) composite plate integrated with the segmented ACLD patch that is made up of VEM and 1-3 PFC layer. The substrate MEE plate consists of three layers where the top and bottom layers are made of piezoelectric material while middle layer is made of magnetostrictive material. Later on, Kattimani and Ray [352,353] investigated the geometrically nonlinear vibration control of multiferroic fibrous composite plate (FRMEE) integrated with the similar ACLD patches. The FRMEE layer is comprised of piezoelectric fibers embedded in the piezomagnetic matrix. Sahoo and Ray [354] studied the vibration suppression of a laminated plate utilizing the ACLD patch in different shapes namely square, ellipse and circle. A

1-3 PFC actuator is utilized with its different fiber orientation angles, and it is observed that the ACLD patch provides maximum damping when it is in elliptic shape. Vinyas [355] investigated the active-passive damping of skew MEE plates integrated with ACLD patches that are comprised of VEM and 1-3 PFC actuator. This study reveals feasible vibration suppression of skew plates for the higher skew angles.

1.5.7 ACLD treatment of shells using extension-mode PFC actuator

Ray and Reddy [356] analyzed the vibration control of a laminated circular cylindrical shell integrated with the ACLD patches where a horizontally reinforced 1-3 PFC actuator is utilized and the effect of its (PFC) fiber orientation angle on the damping capacity of the treatment is addressed. Ray and Balaji [357] and Ray [358] presented structural-acoustic control of symmetric/anti-symmetric composite panels using two ACLD patches comprised of a 1-3 PFC and the VEM. Ray and Pradhan [359,360] presented the performance of a vertically/obliquely reinforced 1-3 PFC in the partial ACLD treatment of laminated composite cylindrical shells. Further investigations on the utilization of the same PFC (vertically/obliquely reinforced 1-3 PFC) in the ACLD treatment of shells are available in [361–365]. In [366-368], the theoretical studies on the ACLD treatment of stationary or rotary truncated laminated conical shell are presented using vertically/obliquely reinforced 1-3 PFC. Li and Narita [369] analyzed the attenuation of vibration of a laminated panel using horizontally reinforced 1-3 PFC in the ACLD patch. Shivakumar et al. [370] utilized the same 1-3 PFC for partial ACLD treatment of nonlinear vibration of shallow shells. However, these available studies indicate an extensive utilization of the extension-mode PFC actuators in the ACLD or active-passive damping treatment of structural vibration, whereas an application of the shear-mode PFC actuator in the similar damping treatment is not yet reported in the literature to the best knowledge this author.

1.6 Motivation and objectives of present research

The aforesaid literature review on the design, development and applications of different kinds of shear and extension mode PFCs reveals only one shear-mode PFC actuator (SAFC) [73] till the date, whereas a good number of extension-mode PFC actuators have been developed [13-17, 37, 42, 45, 46, 48, 69, 70]. These

shear and extension mode PFC actuators are substantially utilized for active control of deformation/vibration of the thin-walled flexible structures like beams, rectangular plates, plate strips, singly/doubly curved shells, circular cylindrical shells, airfoils, etc. [230-232, 236, 238, 243, 248, 260, 264, 273, 371]. Besides these structures, the plane structures of revolution like annular and circular plates may be treated as the basic structural elements as those are often used in micro-valves, implantable medical devices, micro-switches, micro-pumps, oil storage tanks, brakes in vehicles, airfoil cascades, oceanographic applications, etc. [372-378]. However, it is observed from the available literature that a few studies on the active control of annular/circular plates have been reported in the literature utilizing extension-mode monolithic piezoelectric actuators [151, 160]. Moreover, the utilization of any of the available PFCs or shear-mode monolithic piezoelectric actuator for active control of annular/circular plates has not yet been reported in the literature. So, the primary objective of this research is decided as the design and application of PFC actuators towards the advancement of active, as well as active-passive, vibration control of annular plates.

The existing PFCs are designed in the Cartesian material coordinate system so that these PFCs may not be well-qualified materials for the distributed actuators in active control of annular plates where the mechanically induced stresses/strains usually arise in the cylindrical coordinates. It infers the requirement of the design of microstructure of PFC in the cylindrical material coordinate system for effective active control of annular plates. The research in this concern is not yet addressed in the literature. So, the first objective of this dissertation is decided as the design of a new annular PFC actuator with the cylindrically periodic microstructure in particular to achieve the directional/maximum extensional actuation force along the radial direction in the cylindrical principal material coordinate system. The verification of its (annular PFC actuator) performance in active vibration control of annular plates is also included in the same objective.

The vertically reinforced 1-3 PFC [13] is commonly known as a material of thickness mode piezoelectric actuator, where the extension-mode piezoelectric actuation appears in the thickness/transverse direction for an externally applied transverse electric field. If the vertically oriented fibers in this 1-3 PFC are considered to be obliquely oriented at an angle with the thickness coordinate, then the transverse shear actuation force arises along with the thickness mode

actuation force. This shear actuation force may be utilized for active control of deformation/vibration of flexible structures. However, if it is applied for the shear actuated bending deformation of thin annular plates, then the corresponding effectiveness of the obliquely reinforced 1-3 PFC actuator is in doubt mainly because of the anisotropic properties of this PFC in the reference cylindrical coordinate system for the host annular plate. In this view, the second objective of this dissertation is decided for investigating the shear actuation mechanism and shear-based actuation capability of the obliquely reinforced 1-3 PFC in active control of vibration of annular plates.

The aforesaid obliquely reinforced 1-3 PFC possesses anisotropic material properties so that the transverse shear actuation force within it is coupled with the extensional strain components, and this coupling poses detrimental effect on the shear actuation capability of the PFC. The elimination of this coupling effect through the microstructural change of the PFC may result a new shear mode PFC having superior shear actuation capability. This development of a new shear mode PFC is taken as the third objective of this dissertation. In order to verify the utility of this new shear mode PFC in shear-based vibration control of annular plates, it is required to compare its actuation capability with that of the existing shear-mode piezoelectric actuators namely SAFC and shear-mode monolithic piezoelectric actuators. This comparative study is identified as the fourth objective of the present research.

The passive damping of flexural vibration of annular plates can simply be achieved using the pure viscoelastic materials (VEMs) through UCLD/CLD treatment as the same has been reported in the literature. However, the advanced damping materials like 1-3/0-3 viscoelastic composites (VECs) [325,400] can be used instead of VEM for improved passive damping of the same (annular) plates. But, the geometry of these plates requires certain changes in the constructional features of the available 1-3/0-3 VECs so that the passive damping may not be augmented in a fruitful manner. The additional issues may arise in implementation of the adaptive control of the annular plates by means of adding a shear-mode PFC or monolithic piezoelectric actuator, where the main difficulty arises in deciding appropriate locations of the VEC layer and the shear actuator since the shear actuation and viscoelastic damping mainly appear through the same field quantity i.e. transverse shear strain. In order to investigate these

issues, another objective of this research is decided as the active-passive control of vibration of annular plates using the shear-mode PFC and VECs.

In order to fulfil the aforesaid objectives in this research, the following theoretical studies have been carried out.

(a) Electromechanical properties and actuation capability of an extension-mode piezoelectric fiber composite actuator with cylindrically periodic microstructure.

(b) Shear actuation mechanism and shear-based actuation capability of an obliquely reinforced PFC in active control of annular plates.

(c) Design of a balanced laminate of piezoelectric fiber composite.

(d) Shear-based vibration control of annular sandwich plates using different piezoelectric fiber composites: a comparative study.

(e) A design of shear actuated hybrid damping treatment for annular plates using balanced laminate of PFC and 0-3 viscoelastic composite.

1.7 Contributions

The following contributions in the field of smart structures have been made towards the preparation of this dissertation.

1. A novel extension-mode PFC actuator with cylindrically periodic microstructure is proposed for directional (radial direction) actuation of plane structures of revolution.
2. A fruitful strategy for effective utilization of this extension-mode PFC in active control of annular plates is presented.
3. An obliquely reinforced 1-3 PFC is introduced for shear-based active control of annular plates.
4. A shear-based feedback control strategy is proposed for effective utilization of shear piezoelectric actuators in active control of vibration of annular plates according to the velocity feedback control law.
5. A novel balanced laminate of PFC (BL-PFC) is proposed for improved shear-mode piezoelectric actuation of flexible structures.
6. Among the available shear-mode piezoelectric actuators namely SAFC, BL-PFC and monolithic piezoelectric (PZT5H) actuators, the best one for

shear-based attenuation of flexural vibration of annular plates is addressed.

7. A fruitful layered arrangement of shear-mode piezoelectric actuator and viscoelastic damping material is presented for effective active-passive control of vibration of annular plates.
8. The performance of the BL-PFC in active-passive control of annular plates is presented.
9. The performance of a 0-3 VEC layer in augmentation of active-passive control of vibration of annular plates is presented.

1.8 Organization of the thesis

A brief introduction and a review of the literature on the smart structures are presented in Chapter 1. The review of the literature on the design and utilization of various PFCs towards the development of smart structures are also presented within the same chapter (Chapter 1). The literature on the ACLD treatment of structural vibration is also presented. Consequently, the motivation of the present research and objectives of this dissertation are outlined.

Chapter 2 deals with the design of an extension-mode annular PFC actuator with the cylindrically periodic microstructure. The radially varying effective electro-elastic properties of this PFC are estimated by deriving the closed-form expressions of its effective electro-elastic coefficients, and an analysis of these effective properties are presented to illustrate the electro-mechanical behavior of the annular PFC actuator. Subsequently, the performance of this annular PFC actuator in active control of annular plates is investigated where also a fruitful geometric configuration of the annular PFC actuator is presented towards the effective control of annular plates.

An obliquely reinforced 1-3 PFC is introduced in Chapter 3 for shear-based active control of annular plates. The study is carried out by constructing an annular sandwich plate where the patches of the 1-3 PFC in the shape of the annular sector are embedded within the core of foam. First, an electro-elastic FE analysis of the annular sandwich plate is carried out in a special manner for investigating the shear actuation mechanism of the annular sandwich plate having the embedded patches of the obliquely reinforced 1-3 PFC actuator. Next, the controlled frequency responses of the annular sandwich plate are evaluated

to estimate the shear-based actuation capability of the obliquely reinforced 1-3 PFC actuator in attenuation of vibration of annular plates.

In Chapter 4, a novel balanced laminate of PFC (BL-PFC) is designed as a material of shear-mode PFC and its electro-elastic properties are estimated through a micromechanics formulation. Subsequently, the BL-PFC is utilized as a material of shear actuator patches at the core of a sandwich beam, and its shear actuation capability is assessed by evaluating the shear actuated deflection of the sandwich beam. The shear actuation capability of BL-PFC is also compared with that of the traditional monolithic shear-mode piezoelectric actuators.

Chapter 5 is concerned with the shear-based attenuation of vibration of an annular sandwich plate using two different shear-mode PFC actuators namely SAFC and BL-PFC. A conventional shear-mode monolithic piezoelectric (PZT5H) actuator is also used, and a comparative study on the shear actuation capabilities of all three shear actuators is performed to address the best one for shear-based control of the annular sandwich plate. Every actuator is used in the form of an actuator laminate that is inserted at the core of the sandwich plate in the form of the patches, where a fruitful arrangement of the patches and a shear-based control strategy are presented for effective attenuation of vibration of the sandwich plate according to the velocity feedback control law. First, the effective properties of the actuator laminate are determined. Next, a closed-loop FE model of the sandwich plate is developed. Subsequently, the suitability of the present arrangement of shear actuator patches and the shear-based control strategy are substantiated. This arrangement of the actuator patches is further optimized for every shear actuator, and the corresponding shear actuated resonant displacement-amplitudes of the sandwich plate are evaluated for the comparative study on the shear actuation capabilities of three different shear-mode piezoelectric actuators.

In Chapter 6, a shear actuated hybrid active-passive damping treatment is designed for vibration control of annular plates using BL-PFC and a 0-3 VEC. A layered annular plate is designed with the stack of active layer, passive damping layer and the layers of substrate material. The active layer is comprised of BL-PFC patches embedded within the foam layer in an optimal manner with 2-2 phase connectivity. The passive damping layer is initially made of a viscoelastic material (VEM), however, the graphite wafers are inserted within it (VEM) in an optimal

manner with 0-3 phase connectivity resulting in a 0-3 VEC layer. On the basis of prioritizing shear actuation over passive damping and vice versa, two different layered configurations of the hybrid damping treatment are designed in an optimal manner. The corresponding active-passive damping characteristics are investigated by developing a closed-loop FE model of the overall annular plate where the aforesaid shear-based closed-loop control strategy (in Chapter 5) is utilized for activating the actuator patches.

Finally, the important conclusions from work carried out, and the future scope of the present thesis work are outlined in Chapter 7. The list of references is provided at the end of the thesis.

Chapter 2

Design of an extension mode piezoelectric fiber composite actuator with cylindrically periodic microstructure

2.1 Introduction

In the design of the existing PFCs, the principal material coordinate system is taken as the Cartesian coordinate system. The primary or directional actuation in these PFCs appears following an axis or a plane of orthogonal axes of the Cartesian principal material coordinate system. So, these PFCs may not provide effective actuation in a structural application where the maximum/directional actuation is required along the radial direction in a reference cylindrical coordinate system. This kind of radial piezoelectric actuation may be useful in many practical applications as mentioned in the introductory chapter (section 1.6). However, a similar PFC actuator capable to provide primary/directional actuation along the radial direction in the reference cylindrical coordinate system is not yet addressed in the available literature to the best knowledge of this author. It is attempted in this chapter where a new annular PFC actuator with the cylindrically periodic microstructure is designed especially for achieving the directional/maximum actuation force along the radial direction in the cylindrical principal material coordinate system. The application of this annular PFC disc in active control of annular plates is also demonstrated with the main objective of its (PFC) effective utilization, and it leads to a special design of the same annular PFC actuator on the basis of the nature of its radially varying properties.

In the following sections, first, the design of the present annular PFC disc is presented, and its radially varying effective electro-elastic properties are determined through analytical as well as numerical homogenization. Next, its utilization for active vibration control of annular plates is demonstrated through the design of a smart annular plate where the PFC actuator is integrated on the top surface of an annular substrate plate and also activated according to the velocity feedback control strategy. Subsequently, a closed-loop FE model of the smart annular plate is derived for its analysis through the evaluation of numerical results. In the numerical results, the radially varying properties of the

annular PFC disc are first presented, and then an analysis of these properties is carried out especially for its effective utilization in control of annular plates. From this analysis, a fruitful arrangement of the annular PFC actuator over the top surface of the annular substrate plate is decided, and its (PFC actuator) control capability is assessed by evaluating the controlled frequency responses of a smart annular plate. Finally, the salient features in the design and control capability of the present annular PFC actuator are concluded at the end of the chapter.

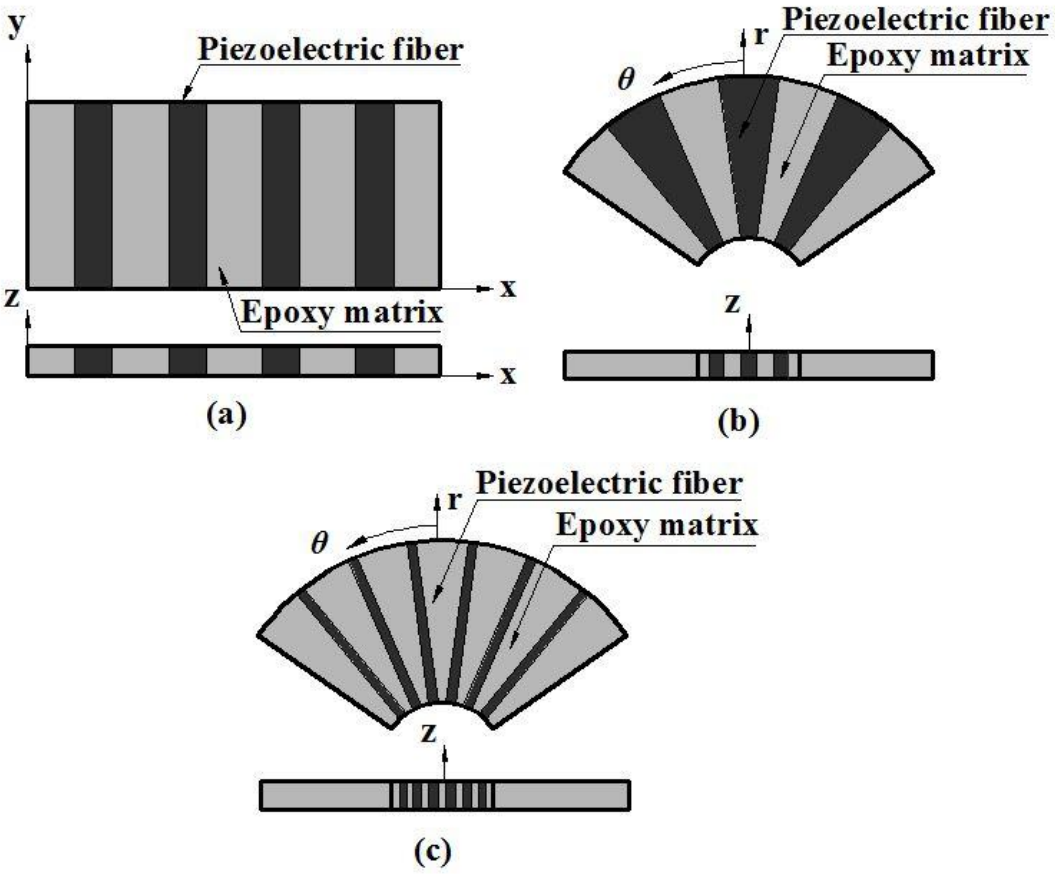

Fig. 2.1 Schematic diagrams of 2-2 PFC lamina in (a) Cartesian coordinate system, (b)-(c) cylindrical coordinate system.

2.2 Present annular PFC actuator

The active layer of the conventional d_{31} MFC is a 2-2 PFC lamina as shown in Fig. 2.1(a). The poling direction of the piezoelectric fibers within this 2-2 PFC is the thickness direction, and the electrically induced actuation force mainly arises along the longitudinal direction of the fibers when an electric field is

applied across the thickness of the lamina. Now, for achieving similar actuation force along the radial direction in a cylindrical coordinate system, the PFC lamina (Fig. 2.1(a)) can be constructed in the shape of the annular-sector as shown in Fig. 2.1(b). In this modification of the 2-2 PFC lamina, the width of the fibers (in the circumferential direction) increases gradually with the increasing radius, and thus the flexibility of the PFC lamina decreases especially for a large radial span of the lamina. In view of this shortcoming, the 2-2 PFC lamina (Fig. 2.1(b)) is presently constructed using the conventional shape of the fibers as shown in Fig. 2.1(c). The fibers are reinforced along the radial direction within the epoxy matrix while the angle between them is kept constant. With this construction of the 2-2 PFC lamina, the cross-sectional area (in the θz plane) of the 2-2 PFC lamina varies along the radial direction while the cross-sectional area of any of the fibers remains constant along the same (radial) direction. So, the effective electro-elastic properties of the 2-2 PFC lamina vary along the radial direction.

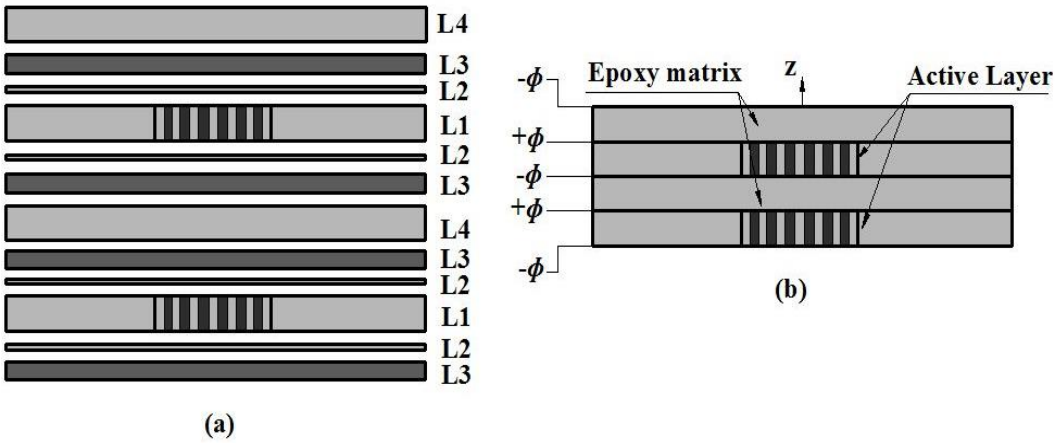

Fig. 2.2 (a) Stacking sequence of different layers within the annular PFC actuator, (b) laminated PFC actuator.

For a specified electric field across the thickness of the 2-2 PFC lamina, the required voltage increases with the increase of the thickness of the lamina. Also, the structural rigidity of the 2-2 PFC lamina increases with the increase of its thickness. So, the 2-2 PFC lamina would be of small thickness. Because of this small thickness, the control force may not be achieved sufficiently in its (2-2 PFC) structural applications, and thus a number of 2-2 PFC layers may be used in the form of a laminate. Presently, two identical 2-2 PFC layers (Fig. 2.1(c)) are utilized to form an annular PFC actuator, and the corresponding stacking

sequence of different layers is shown in Fig. 2.2(a). The component layers within this stacking sequence (Fig. 2.2(a)) are, 2-2 PFC layer (L1), thin epoxy layer (L2), electrode layer (L3) and thick epoxy layer (L4). A thin epoxy layer (L2) binds an electrode layer (L3) and a 2-2 PFC layer (L1). Similarly, a thick epoxy layer (L4) binds two consecutive electrode layers (L3). The external electric field across the thickness of every active layer (L1) is applied by means of the corresponding top and bottom electrode layers. The electric potentials of these top and bottom electrode layers are presently denoted by $+\phi$ and $-\phi$, respectively. It is important to note here that the magnitude of the electric field within any active (2-2 PFC) layer is lesser than the magnitude of the applied electric field across the corresponding top and bottom electrode layers. This discrepancy arises due to the thin epoxy layer (L2) that possesses the dielectric coefficients of small magnitudes. In view of this discrepancy, the lamination may be carried out at high pressure and high temperature [379] so that the thin epoxy layer (L2) becomes an extremely thin layer. Concurrently, it is to be ensured that the thick epoxy layer (L4) would have sufficient thickness after lamination since the electrodes at its (L4) top and bottom surfaces are of different electric potentials. As per these aspects of the lamination, a negligibly small thickness of the thin epoxy layer (L2) is considered in the present analysis. Also, the elastic effects of the electrode layers on the effective properties of the overall laminate are not accounted since the thickness of the electrode layers is very small in comparison to the thickness of the active layers. According to these considerations, the overall laminate is shown in Fig. 2.2(b), and the corresponding representative volume (RV) is shown in Fig. 2.3(a) for determination of the effective electro-elastic coefficients.

2.3 Effective properties of the annular PFC actuator

According to the constructional features of the RV (Fig. 2.3(a)), the cross-sectional area (in the θz plane) of the RV varies along the radial direction while the cross-sectional area of the fiber remains constant along the same direction. So, the effective properties of the RV would vary along the radial direction. Presently, these radially varying effective properties are estimated using a concept of homogenization for the functionally graded materials [380]. Following this concept, the radial span $(r_o - r_i)$ of the RV is divided asymptotically into a

number (N) of segments ($\Delta r = (r_o - r_i)/N$, $\Delta r << (r_o - r_i)$) as shown in Fig. 2.3(b). Corresponding to these radial segments, the sub-volumes within the domain of

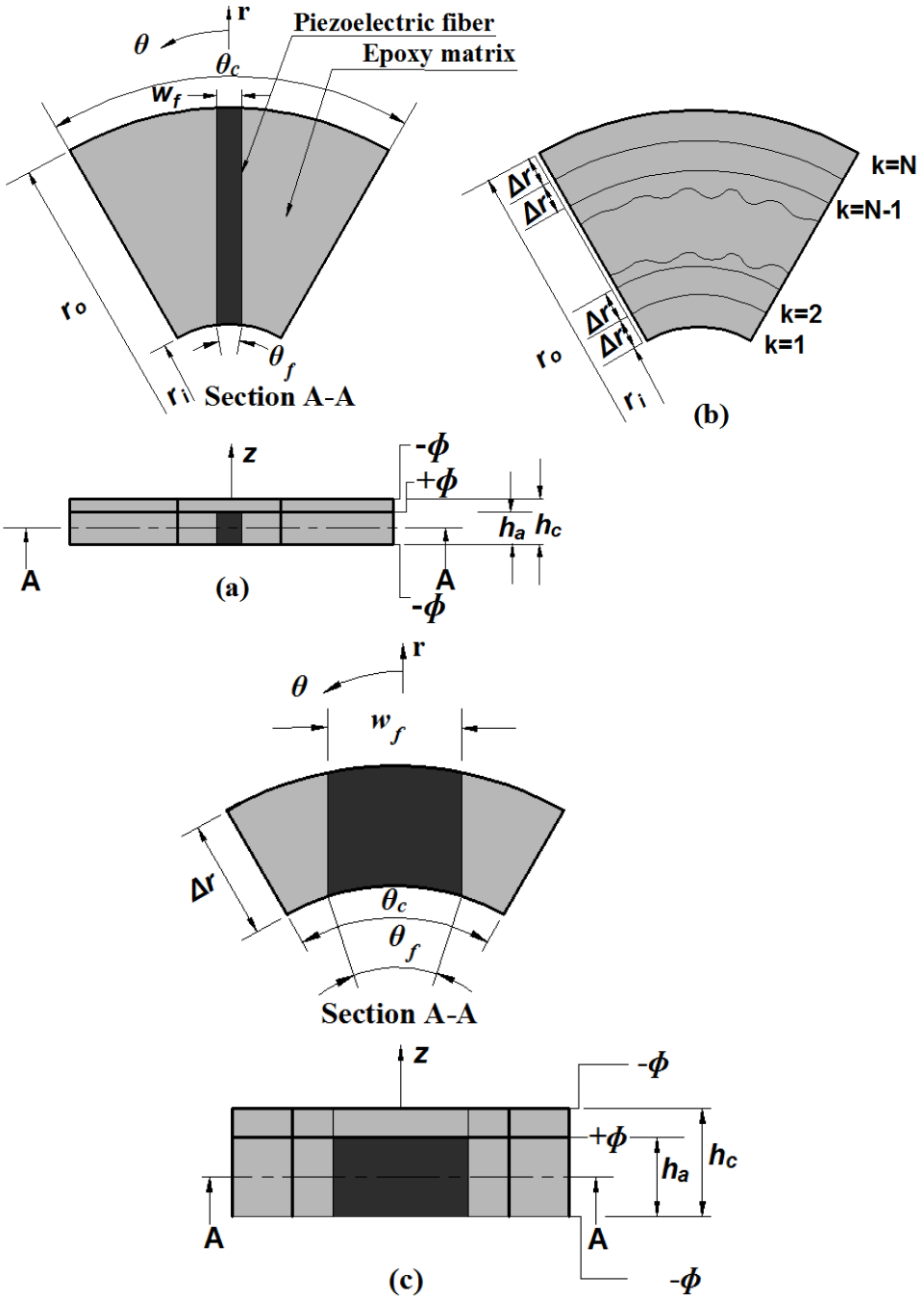

Fig. 2.3 Schematic diagrams of (a) the RV of the annular PFC actuator (Fig. 2.2 (b)), (b) the top surface of the RV with the radial boundaries of sub-volumes, (c) a typical sub-volume of the RV.

the RV are identified, and the volume of the RV is assumed to be comprised of these sub-volumes. A typical sub-volume is shown in Fig. 2.3(c). As the sub-

volumes contain the fibers of uniform shape and size, the fiber volume fraction (FVF) varies over the sub-volumes. The physical dimensions of every sub-volume are taken in micro-scale, and it is considered as an homogeneous volume. The effective properties of the RV at a radial location are identified as the effective properties of the sub-volume at that radial location. So, the radially varying properties of the RV can be obtained by computing the effective properties of every sub-volume as is done in the following section.

2.3.1 *Effective properties of a typical sub-volume*

The linear constitutive relations of a piezoelectric material can be written in the cylindrical coordinate system ($r\theta z$) as [381],

$$\boldsymbol{\sigma} = \mathbf{C}\boldsymbol{\varepsilon} - \boldsymbol{e}^{\mathrm{T}}\boldsymbol{E},$$

$$\boldsymbol{D} = \boldsymbol{e}\boldsymbol{\varepsilon} + \boldsymbol{\epsilon}\,\boldsymbol{E},$$

$$\boldsymbol{\sigma} = \left\{\sigma_r \quad \sigma_\theta \quad \sigma_z \quad \tau_{\theta z} \quad \tau_{rz} \quad \tau_{r\theta}\right\}^{\mathrm{T}},$$

$$\boldsymbol{\varepsilon} = \left\{\varepsilon_r \quad \varepsilon_\theta \quad \varepsilon_z \quad \gamma_{\theta z} \quad \gamma_{rz} \quad \gamma_{r\theta}\right\}^{\mathrm{T}},$$

$$\boldsymbol{E} = \left\{E_r \quad E_\theta \quad E_z\right\}^{\mathrm{T}},\ \boldsymbol{D} = \left\{D_r \quad D_\theta \quad D_z\right\}^{\mathrm{T}},$$

$$\boldsymbol{C} = \begin{bmatrix} C_{11} & C_{12} & C_{13} & 0 & 0 & 0 \\ C_{12} & C_{11} & C_{13} & 0 & 0 & 0 \\ C_{13} & C_{13} & C_{22} & 0 & 0 & 0 \\ 0 & 0 & 0 & C_{44} & 0 & 0 \\ 0 & 0 & 0 & 0 & C_{44} & 0 \\ 0 & 0 & 0 & 0 & 0 & C_{66} \end{bmatrix},$$

$$\boldsymbol{e} = \begin{bmatrix} 0 & 0 & 0 & 0 & e_{15} & 0 \\ 0 & 0 & 0 & e_{24} & 0 & 0 \\ e_{31} & e_{32} & e_{33} & 0 & 0 & 0 \end{bmatrix},$$

$$\boldsymbol{\epsilon} = \begin{bmatrix} \epsilon_{11} & 0 & 0 \\ 0 & \epsilon_{22} & 0 \\ 0 & 0 & \epsilon_{33} \end{bmatrix} \qquad (2.1)$$

where, σ_r / ε_r, $\sigma_\theta / \varepsilon_\theta$ and σ_z / ε_z are the normal stresses/strains along the r, θ and z directions, respectively; $\tau_{r\theta} / \gamma_{r\theta}$, τ_{rz} / γ_{rz} and $\tau_{\theta z} / \gamma_{\theta z}$ are the shear stresses/strains in the $r\theta$, rz and θz planes, respectively; the direction of poling is along the z-direction; D_r / E_r, D_θ / E_θ and D_z / E_z are the electric

displacements/electric fields along the r, θ and z directions, respectively; $\boldsymbol{C}$ is the stiffness matrix that is defined at zero/constant electric field; $\boldsymbol{\epsilon}$ is the dielectric matrix that is defined at zero/constant strain; $\boldsymbol{e}$ is the piezoelectric matrix; C_{ij} $(i, j = 1,2,\ldots,6)$ are the stiffness coefficients; e_{kj} $(k = 1,2,3;$ and $j = 1,2,\ldots,6)$ are the piezoelectric coefficients; ϵ_{kl} $(k = 1,2,3;$ and $l = 1,2,3)$ are the dielectric coefficients.

As per the present design of the annular PFC actuator (Fig. 2.2(b)), a dominant electric field (E_z) or electric displacement (D_z) is imposed along the thickness (z) direction. So, an assumption of $E_r = E_\theta \approx 0$ can be made [382], and the constitutive relations for two different phases of the composite can be written as,

$$\begin{Bmatrix} \boldsymbol{\sigma}^p \\ D_z^p \end{Bmatrix} = \boldsymbol{C}^p \begin{Bmatrix} \boldsymbol{\varepsilon}^p \\ -E_z^p \end{Bmatrix},$$

$$\boldsymbol{C}^p = \begin{bmatrix} C_{11}^p & C_{12}^p & C_{13}^p & 0 & 0 & 0 & e_{31}^p \\ C_{12}^p & C_{22}^p & C_{23}^p & 0 & 0 & 0 & e_{32}^p \\ C_{13}^p & C_{23}^p & C_{33}^p & 0 & 0 & 0 & e_{33}^p \\ 0 & 0 & 0 & C_{44}^p & 0 & 0 & 0 \\ 0 & 0 & 0 & 0 & C_{55}^p & 0 & 0 \\ 0 & 0 & 0 & 0 & 0 & C_{66}^p & 0 \\ e_{31}^p & e_{32}^p & e_{33}^p & 0 & 0 & 0 & -\epsilon_{33}^p \end{bmatrix} \tag{2.2}$$

where, the superscript p indicates the piezoelectric fiber or the matrix phase as per its value as 1 or 2, respectively. Also, the magnitudes of the piezoelectric coefficients (e_{ij}^p) for the matrix phase ($p = 2$) are equal to zero as the matrix phase is made of piezoelectrically inactive material. Equation (2.2) can also be written in terms of the volume-average field quantities in phases as follows,

$$\begin{Bmatrix} \bar{\boldsymbol{\sigma}}^p \\ \bar{D}_z^p \end{Bmatrix} = \boldsymbol{C}^p \begin{Bmatrix} \bar{\boldsymbol{\varepsilon}}^p \\ -\bar{E}_z^p \end{Bmatrix},$$

$$\bar{\boldsymbol{\sigma}}^p = \frac{1}{V^p} \int_{V^p} \boldsymbol{\sigma}^p dV^p,$$

$$\bar{\boldsymbol{\varepsilon}}^p = \frac{1}{V^p}\int_{V^p} \boldsymbol{\varepsilon}^p dV^p \,,$$

$$\bar{D}_z^p = \frac{1}{V^p}\int_{V^p} D_z^p dV^p \,, \qquad (2.3)$$

$$\bar{E}_z^p = \frac{1}{V^p}\int_{V^p} E_z^p dV^p$$

where, the over-bar indicates the volume-average field quantity over the volume

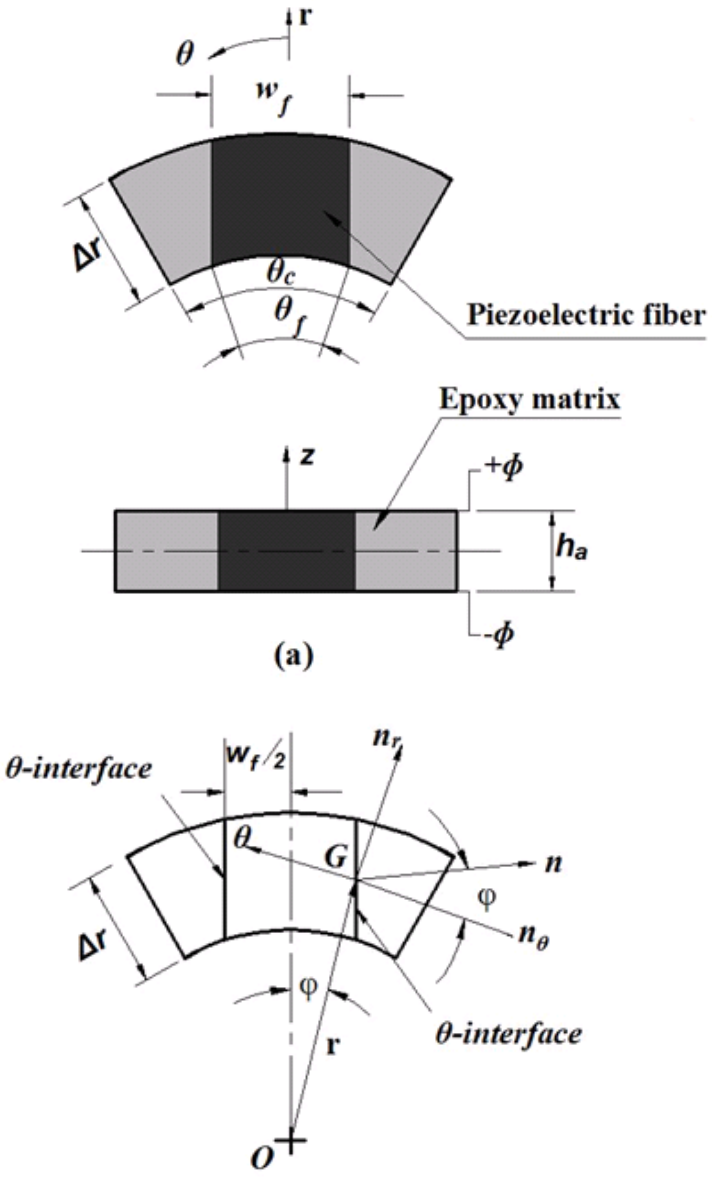

Fig. 2.4 Schematic diagram of (a) the 2-2 PFC layer of sub-volume (Fig. 2.3 (c)), (b) the unit normal and its components at a typical point (G) on θ-interface.

(V^p) of fiber ($p=1$) or matrix ($p=2$) phase. Presently, the closed-form expressions for the effective coefficients of the homogeneous sub-volume (Fig. 2.3(c)) are derived on the basis of the constitutive relations in Eq. (2.3). First, the closed-form expressions for the effective coefficients of homogenized 2-2 PFC layer (Fig. 2.4(a)) of the sub-volume are derived. From the geometry of this 2-2 PFC layer (Figs. 2.4(a) and 2.4(b)), the components (n_r, n_θ and n_z) of the unit normal (n) at a typical point (G) on the θ-interphase surface are, $n_r = \sin(\varphi)$, $n_\theta = \cos(\varphi)$ and $n_z = 0$ where $\varphi = \sin^{-1}(w_f / 2r)$. The width ($w_f$) of the fiber is very small in comparison to the radius (r) at any point on the θ-interphase surface ($w_f << r$). So, the angle (φ) appears with a very small value ($\varphi \approx 0$), and it yields, $n_r \approx 0$, $n_\theta \approx 1$ and $n_z = 0$. Accordingly, the tractions at any point on the θ-interphase surface can be written as,

$$\overset{\theta}{T}_r = \bar{\tau}_{\theta r}, \ \overset{\theta}{T}_\theta = \bar{\sigma}_\theta, \ \overset{\theta}{T}_z = \bar{\tau}_{\theta z} \tag{2.4}$$

Since tractions at the interphase surfaces of a composite are to be continuous field quantities for equilibrium. We assume that (composite) asymptotic homogenization [383], the stress components ($\bar{\tau}_{\theta r}, \bar{\sigma}_\theta, \bar{\tau}_{\theta z}$) would be uniform field quantities throughout the volume of the 2-2 PFC (Fig. 2.4(a)). In the 2-2 PFC layer (Fig. 2.4(a)), the constituent phases are continuously distributed on the rz-plane and thus the strain components ($\bar{\varepsilon}_r$, $\bar{\varepsilon}_z$, $\bar{\gamma}_{rz}$) are assumed to be uniform field quantities over both the phases of the 2-2 PFC layer. As the top and bottom surfaces of the 2-2 PFC layer are fully electrode-surfaces, the applied electric field ($\bar{E}_z$) across these electrodes is assumed to be uniformly distributed over the volume of the 2-2 PFC. These uniform field components over the volume of the 2-2 PFC layer can be written as,

$$\Upsilon^1 = \Upsilon^2 = \Upsilon, \ \Upsilon = \left\{ \bar{\varepsilon}_r \quad \bar{\varepsilon}_z \quad \bar{\gamma}_{rz} \quad \bar{\sigma}_\theta \quad \bar{\tau}_{\theta z} \quad \bar{\tau}_{r\theta} \quad \bar{E}_z \right\}^{\mathrm{T}},$$

$$\Upsilon^p = \left\{ \bar{\varepsilon}_r^p \quad \bar{\varepsilon}_z^p \quad \bar{\gamma}_{rz}^p \quad \bar{\sigma}_\theta^p \quad \bar{\tau}_{\theta z}^p \quad \bar{\tau}_{r\theta}^p \quad \bar{E}_z^p \right\}^{\mathrm{T}}, \ p = 1,2 \tag{2.5}$$

The volume averages of the remaining field components over the volumes of the matrix and fiber phases within the 2-2 PFC layer can be written as,

$$\Gamma_p = \left\{ \bar{\varepsilon}_\theta^p \quad \bar{\gamma}_{r\theta}^p \quad \bar{\gamma}_{\theta z}^p \quad \bar{\sigma}_r^p \quad \bar{\sigma}_z^p \quad \bar{\tau}_{rz}^p \quad \bar{D}_z^p \right\}^{\mathrm{T}}, \ p = 1,2 \tag{2.6}$$

Using the constitutive relations (Eq. (2.3)), the field vectors ($\mathbf{\Gamma}_p$, $p=1,2$) are expressed in terms of the uniform field quantities (Υ) as,

$$\mathbf{\Gamma}_1 = \boldsymbol{A}_1 \Upsilon$$
$$\mathbf{\Gamma}_2 = \boldsymbol{A}_2 \Upsilon \tag{2.7}$$

According to the rule of mixture, the field vectors ($\mathbf{\Gamma}_1, \mathbf{\Gamma}_2$) for fiber and matrix phases can be combined into an equivalent field vector ($\mathbf{\Gamma}$) for the volume-averages of the field components ($\bar{\tau}_{rz}, \bar{\sigma}_r, \bar{\sigma}_z, \bar{\varepsilon}_\theta, \bar{\gamma}_{\theta z}, \bar{\gamma}_{r\theta}, \bar{D}_z$) over the volume of the 2-2 PFC layer as,

$$\mathbf{\Gamma} = \left(v_1 \mathbf{\Gamma}_1 + v_2 \mathbf{\Gamma}_2\right),$$
$$\mathbf{\Gamma} = \left\{\bar{\varepsilon}_\theta \quad \bar{\gamma}_{r\theta} \quad \bar{\gamma}_{\theta z} \quad \bar{\sigma}_r \quad \bar{\sigma}_z \quad \bar{\tau}_{rz} \quad \bar{D}_z\right\}^{\mathrm{T}} \tag{2.8}$$

In Eq. (2.8), v_1 and v_2 are the volume fractions of the fiber ($p=1$) and matrix ($p=2$) phases, respectively, within the 2-2 PFC layer (Fig. 2.4(a)). Equation (2.7) is introduced in Eq. (2.8), and then the resulting expressions are arranged in the form of Eq. (2.3) in order to obtain the closed-form expressions for the effective coefficients of the 2-2 PFC layer as,

$$C_{22}^a = C_{22}^2 C_{22}^1 \Big/ \left(C_{22}^1 v_2 + v_1 C_{22}^2\right),$$
$$C_{12}^a = C_{22}^a \left(v_1 C_{12}^1 / C_{22}^1 + v_2 C_{12}^2 / C_{22}^2\right),$$
$$C_{23}^a = C_{22}^a \left(v_2 C_{23}^2 / C_{22}^2 + v_1 C_{23}^1 / C_{22}^1\right),$$
$$e_{32}^a = v_1 C_{22}^a \, e_{32}^1 / C_{22}^1 ,$$
$$C_{11}^a = \left(C_{12}^a\right)^2 \Big/ C_{22}^a + v_1 \left(C_{11}^1 - \left(C_{12}^1\right)^2 \Big/ C_{22}^1\right) + v_2 \left(C_{11}^2 - \left(C_{12}^2\right)^2 \Big/ C_{22}^2\right),$$
$$e_{31}^a = e_{32}^a C_{12}^a / C_{22}^a + v_1 \left(e_{31}^1 - C_{12}^1 e_{32}^1 / C_{22}^1\right),$$
$$C_{44}^a = C_{44}^1 C_{44}^2 \Big/ \left(C_{44}^1 v_2 + C_{44}^2 v_1\right),$$
$$C_{55}^a = \left(C_{55}^1 v_1 + C_{55}^2 v_2\right),$$
$$C_{66}^a = C_{66}^1 C_{66}^2 \Big/ \left(C_{66}^1 v_2 + C_{66}^2 v_1\right) ,$$
$$C_{13}^a = \left(C_{12}^a C_{23}^a\right) \Big/ C_{22}^a + v_1 \left(C_{13}^1 - \left(C_{12}^1 C_{23}^1\right) \Big/ C_{22}^1\right) + v_2 \left(C_{13}^2 - \left(C_{12}^2 C_{23}^2\right) \Big/ C_{22}^2\right),$$

$$C_{33}^{a}=\left(C_{23}^{a}\right)^{2}\Big/C_{22}^{a}+v_1\left(C_{33}^{1}-\left(C_{23}^{1}\right)^{2}\Big/C_{22}^{1}\right)+v_2\left(C_{33}^{2}-\left(C_{23}^{2}\right)^{2}\Big/C_{22}^{2}\right),$$

$$e_{33}^{a}=\left(e_{32}^{a}C_{23}^{a}\right)\Big/C_{22}^{a}+v_1\left(e_{33}^{1}-C_{23}^{1}e_{32}^{1}/C_{22}^{1}\right),$$

$$\epsilon_{33}^{a}=-\left(e_{32}^{a}\right)^{2}\Big/C_{22}^{a}+v_1\left(\epsilon_{33}^{1}+\left(e_{32}^{1}\right)^{2}\Big/C_{22}^{1}\right)+v_2\,\epsilon_{33}^{2} \qquad (2.9)$$

In Eq. (2.9), the superscript a denotes the effective coefficients of the 2-2 PFC layer; the superscripts 1 and 2 indicate the coefficients (C_{ij}, ϵ_{ij}, e_{ij}) for fiber ($p=1$) and matrix ($p=2$) phases, respectively.

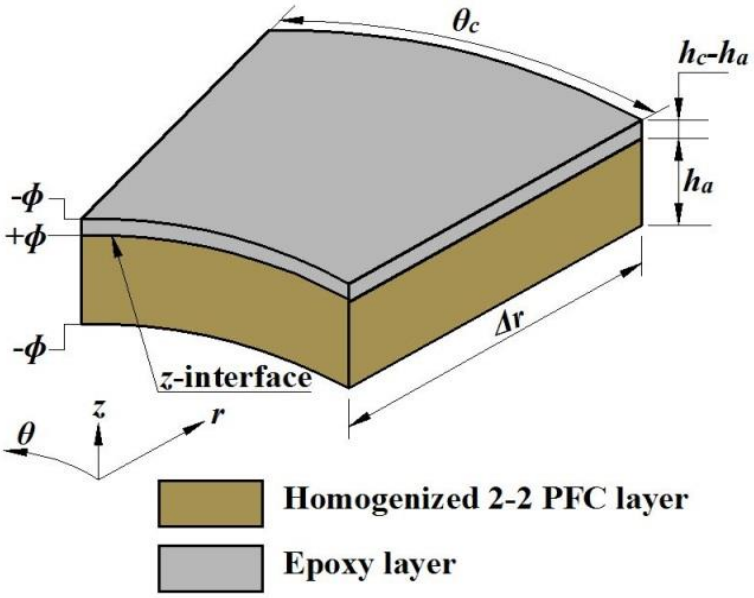

Fig. 2.5 A typical sub-volume of RV comprised of homogenized 2-2 PFC layer and epoxy layer.

According to the homogenized properties (Eq. (2.9)) of the 2-2 PFC layer, the geometrical features of the sub-volume (Fig. 2.3) can be simplified in the form of a laminate of homogenized 2-2 PFC and epoxy layers as shown in Fig. 2.5. The piezoelectric actuation within this sub-volume (Fig. 2.5) appears due to the externally applied electric field (E_z^a) across the thickness of the 2-2 PFC layer, and this actuation is characterized by deriving the effective converse piezoelectric constitutive relations of the sub-volume (Fig. 2.5). The converse piezoelectric constitutive relations for the homogenized 2-2 PFC layer and the similar constitutive relation for the epoxy layer can be written as,

$$\boldsymbol{\sigma}^{a}=\boldsymbol{C}^{a}\boldsymbol{\varepsilon}^{a}-\boldsymbol{e}^{a}E_z^{a},$$

$$\boldsymbol{\sigma}^m = \boldsymbol{C}^m \boldsymbol{\varepsilon}^m \tag{2.10}$$

where, the superscript a or m indicates a quantity for active (2-2 PFC) or epoxy layer, respectively; the elements of the property matrices $\boldsymbol{C}^a$ and $\boldsymbol{e}^a$ are given in Eq. (2.9); $\boldsymbol{C}^m$ is the stiffness matrix of the epoxy layer. For the homogenized volume of the sub-volume (Fig. 2.5), the tractions or phase volume-average stress components ($\bar{\tau}_{rz}$, $\bar{\tau}_{\theta z}$, $\bar{\sigma}_z$) at the z-interface are to be uniform field quantities over both the phases (layers) of the two-layered sub-volume (Fig. 2.5) [383]. Further, the homogenized 2-2 PFC and epoxy layers of the sub-volume (Fig. 2.5) are continuously distributed on the $r\theta$-plane, and thus the strain components ($\bar{\varepsilon}_r, \bar{\varepsilon}_\theta, \bar{\gamma}_{r\theta}$) are assumed as uniform field quantities over both the layers. Apart from these uniform field quantities ($\bar{\tau}_{rz}, \bar{\tau}_{\theta z}, \bar{\sigma}_z, \bar{\varepsilon}_r, \bar{\varepsilon}_\theta, \bar{\gamma}_{r\theta}$), the remaining components of the stress and strain fields within the layers can be written as,

$$\mathfrak{I}_\ell = \left\{ \bar{\varepsilon}_z^\ell \quad \bar{\gamma}_{z\theta}^\ell \quad \bar{\gamma}_{rz}^\ell \quad \bar{\sigma}_r^\ell \quad \bar{\sigma}_\theta^\ell \quad \bar{\tau}_{r\theta}^\ell \right\}^{\mathrm{T}}, \ \ell = 1,2 \tag{2.11}$$

where, ℓ indicates the homogenized 2-2 PFC layer or epoxy layer in the two-layered sub-volume (Fig. 2.5) as per its value as 1 or 2, respectively. Using Eq. (2.11) and the uniform stress/strain components ($\bar{\tau}_{rz}$, $\bar{\tau}_{\theta z}$, $\bar{\sigma}_z, \bar{\varepsilon}_r$, $\bar{\varepsilon}_\theta$, $\bar{\gamma}_{r\theta}$), the constitutive relations in Eq. (2.10) can be rewritten as,

$$\begin{aligned} \mathfrak{I}_1 &= \boldsymbol{B}_1 \mathfrak{R} - \boldsymbol{H}_1 E_z^a, \\ \mathfrak{I}_2 &= \boldsymbol{B}_2 \mathfrak{R}, \\ \mathfrak{R} &= \left\{ \bar{\varepsilon}_r \quad \bar{\varepsilon}_\theta \quad \bar{\gamma}_{r\theta} \quad \bar{\sigma}_z \quad \bar{\tau}_{\theta z} \quad \bar{\tau}_{rz} \right\}^{\mathrm{T}} \end{aligned} \tag{2.12}$$

where, the matrices $\boldsymbol{B}_1$ and $\boldsymbol{H}_1$ are comprised of the elements of the property matrices ($\boldsymbol{C}^a, \boldsymbol{e}^a$) of the homogenized 2-2 PFC layer; the matrix $\boldsymbol{B}_2$ is comprised of the elements of the stiffness matrix ($\boldsymbol{C}^m$) of the epoxy layer. Using the mixing rule, the phase volume-average vector quantities ($\mathfrak{I}_1$, $\mathfrak{I}_2$) can be combined into an equivalent volume-average vector quantity ($\mathfrak{I}$) over the volume of the two-layered sub-volume (Fig. 2.5) as,

$$\begin{aligned} \mathfrak{I} &= \left(q_1 \mathfrak{I}_1 + q_2 \mathfrak{I}_2 \right), \\ \mathfrak{I} &= \left\{ \bar{\varepsilon}_z \quad \bar{\gamma}_{z\theta} \quad \bar{\gamma}_{rz} \quad \bar{\sigma}_r \quad \bar{\sigma}_\theta \quad \bar{\tau}_{r\theta} \right\}^{\mathrm{T}} \end{aligned} \tag{2.13}$$

where, q_1 and q_2 are the volume fractions of the homogenized 2-2 PFC layer and epoxy layer, respectively. Using Eq. (2.12) in Eq. (2.13) and then expressing the resulting equations in the form of Eq. (2.10), the following closed-form expressions for the elements of the effective stiffness ($\bar{\boldsymbol{C}}$) and piezoelectric ($\bar{\boldsymbol{e}}$) matrices of the homogenized sub-volume (Fig. 2.5) can be obtained,

$$\bar{C}_{33} = C_{33}^a C_{33}^m \Big/ \left(q_2 C_{33}^a + q_1 C_{33}^m\right),$$

$$\bar{C}_{23} = \bar{C}_{33}\left(q_1 C_{23}^a / C_{33}^a + q_2 C_{23}^m / C_{33}^m\right),$$

$$\bar{C}_{13} = \bar{C}_{33}\left(q_1 C_{13}^a / C_{33}^a + q_2 C_{13}^m / C_{33}^m\right),$$

$$\bar{e}_{33} = \bar{C}_{33}\left(q_1 e_{33}^a / C_{33}^a\right),$$

$$\bar{C}_{22} = \left(\bar{C}_{23}\right)^2 / \bar{C}_{33} + q_1\left(C_{22}^a - \left(C_{23}^a\right)^2 / C_{33}^a\right) + q_2\left(C_{22}^m - \left(C_{23}^m\right)^2 / C_{33}^m\right),$$

$$\bar{C}_{11} = \left(\bar{C}_{13}\right)^2 / \bar{C}_{33} + q_1\left(C_{11}^a - \left(C_{13}^a\right)^2 / C_{33}^a\right) + q_2\left(C_{11}^m - \left(C_{13}^m\right)^2 / C_{33}^m\right),$$

$$\bar{C}_{12} = \left(\bar{C}_{13}\bar{C}_{23}\right)/\bar{C}_{33} + q_1\left(C_{12}^a - \left(C_{13}^a C_{23}^a\right)/C_{33}^a\right) + q_2\left(C_{12}^m - \left(C_{13}^m C_{23}^m\right)/C_{33}^m\right),$$

$$\bar{C}_{44} = C_{44}^a C_{44}^m \Big/ \left(q_1 C_{44}^m + q_2 C_{44}^a\right),$$

$$\bar{C}_{55} = C_{55}^a C_{55}^m \Big/ \left(q_2 C_{55}^a + q_1 C_{55}^m\right),$$

$$\bar{C}_{66} = \left(q_1 C_{66}^a + q_1 C_{66}^m\right), \bar{e}_{32} = \left(\bar{e}_{33}\bar{C}_{23}\right)/\bar{C}_{33} + q_1\left(e_{32}^a - C_{23}^a e_{33}^a / C_{33}^a\right),$$

$$\bar{e}_{31} = \left(\bar{e}_{33}\bar{C}_{13}\right)/\bar{C}_{33} + q_1\left(e_{31}^a - \left(C_{13}^a e_{33}^a\right)/C_{33}^a\right) \tag{2.14}$$

In Eq. (2.14), the superscripts a and m denote the homogenized 2-2 PFC and epoxy layers, respectively, within the two-layered sub-volume (Fig. 2.5). It may be noted here that the effective piezoelectric actuation in the sub-volume for an applied electric field (E_z^a) across the thickness of the 2-2 PFC layer can be obtained through the effective coefficients as presented in Eq. (2.14).

2.3.2 Numerical homogenization of a typical sub-volume

In order to verify the effective coefficients (Eq. (2.14)) of a typical sub-volume (Fig. 2.3(a)) of the RV of annular PFC actuator, the same effective coefficients are also computed through the numerical homogenization of the sub-volume (Fig.

2.3(a)) by means of deriving its electro-elastic FE model. The strain-displacement and electric field-potential relations at any point within the sub-volume (Fig. 2.3(a)) can be written as,

$$\{\boldsymbol{\varepsilon} \quad -E_z\}^{\mathrm{T}} = \boldsymbol{L}\boldsymbol{d} \,,$$

$$\boldsymbol{d} = \{u \quad v \quad w \quad \phi\}^{\mathrm{T}} \tag{2.15}$$

where, u, v and w are the displacements at any point within the sub-volume along the r, θ and z directions, respectively; ϕ is the electric potential at any point within the sub-volume; $\boldsymbol{L}$ is an operator matrix as given in Eq. (2.16).

$$\boldsymbol{L} = \begin{bmatrix} (\partial/\partial r) & 0 & 0 & 0 \\ (1/r) & (1/r)(\partial/\partial\theta) & 0 & 0 \\ 0 & 0 & (\partial/\partial z) & 0 \\ 0 & (\partial/\partial z) & (1/r)(\partial/\partial\theta) & 0 \\ (\partial/\partial z) & 0 & (\partial/\partial r) & 0 \\ (1/r)(\partial/\partial\theta) & (\partial/\partial r)-(1/r) & 0 & 0 \\ 0 & 0 & 0 & (\partial/\partial z) \end{bmatrix} \tag{2.16}$$

According to the constitutive relations (Eq. (2.2)), the first variation of the electro-elastic internal energy of the sub-volume can be written as [384],

$$\delta U = \sum_{p=1}^{2} \left(\int_{V^p} \left\langle \{\delta\boldsymbol{\varepsilon} \quad -\delta E_z\} \boldsymbol{C}^p \{\boldsymbol{\varepsilon} \quad -E_z\}^{\mathrm{T}} \right\rangle dV^p \right) \tag{2.17}$$

where, δ is an operator for the first variation; V^p is the volume of the fiber phase ($p=1$) or the matrix phase ($p=2$). The volume of the sub-volume is discretized by 27-node isoparametric elements. The edges of any element are in parallel to the axes of the reference cylindrical coordinate system, and a typical element is made of either fiber or matrix material. The electro-elastic state vector ($\boldsymbol{d}$) at any point within a typical element can be written in terms of the shape function matrix ($\boldsymbol{N}$) and the elemental nodal electro-elastic state vector ($\boldsymbol{d}^e$) as,

$$\boldsymbol{d} = \boldsymbol{N}\boldsymbol{d}^e \tag{2.18}$$

Using Eqs. (2.15) and (2.18) in Eq. (2.17), the first variation of the internal energy (δU^e) of a typical element can be obtained as,

$$\delta U^e = (\delta \boldsymbol{d}^e)^{\mathrm{T}} (\boldsymbol{K}^e \boldsymbol{d}^e) \,,$$

$$\boldsymbol{K}^e = \int_{V_e^p} \left(\boldsymbol{N}^{\mathrm{T}} \boldsymbol{L}^{\mathrm{T}} \boldsymbol{C}^p \boldsymbol{L} \boldsymbol{N} \right) dV_e^p \tag{2.19}$$

In Eq. (2.19), V_e^p is the elemental volume within the fiber phase ($p=1$) or the matrix phase ($p=2$). Assembling the elemental equations (Eq. (2.19)), the following expression for the first variation of the internal energy of the sub-volume can be obtained,

$$\delta U = (\delta \boldsymbol{X})^{\mathrm{T}} \langle \boldsymbol{K}\, \boldsymbol{X} \rangle \tag{2.20}$$

where, $\boldsymbol{K}$ and $\boldsymbol{X}$ are the global electro-elastic coefficient matrix and the global nodal electro-elastic state vector, respectively. For a specified nodal displacement or electric potential (say, X_q) over the boundary surface of the sub-volume, its (X_q) first variation is equal to zero ($\delta X_q = 0$). So, the q^{th} row of $\boldsymbol{K}$ is to be removed while the corresponding column ($\boldsymbol{P}_q$) of $\boldsymbol{K}$ forms the load vector as,

$$\delta U = (\delta \boldsymbol{X}_r)^{\mathrm{T}} (\boldsymbol{K}_r\, \boldsymbol{X}_r + \boldsymbol{P}_q X_q) \tag{2.21}$$

where, the subscript r denotes the reduced vector or matrix after the implementation of the boundary condition. According to the principle of virtual displacements, Eq. (2.21) can be written for a number (Q) of specified elements of $\boldsymbol{X}$ over the boundary surface of the sub-volume as,

$$\boldsymbol{K}_r\, \boldsymbol{X}_r = -\sum_{q=1}^{Q} \boldsymbol{P}_q X_q \tag{2.22}$$

The solution of Eq. (2.22) provides the nodal electro-elastic state vector ($\boldsymbol{X}$) corresponding to a specified kinematic boundary condition over the boundary surface of the sub-volume. This nodal electro-elastic state vector can then be utilized for computation of the volume-average field quantities ($\bar{\boldsymbol{\sigma}}, \bar{\boldsymbol{\varepsilon}}, \bar{D}_z, \bar{E}_z$) over a volume ($V$) within the domain of the sub-volume according to the following expressions,

$$(\bar{\boldsymbol{\sigma}}, \bar{\boldsymbol{\varepsilon}}, \bar{D}_z, \bar{E}_z) = (1/V) \sum_{e=1}^{Q_v} \int_{V^e} (\boldsymbol{\sigma}^e, \boldsymbol{\varepsilon}^e, D_z^e, E_z^e)\, dV^e \tag{2.23a}$$

where, Q_v is the number of elements within the volume (V); V^e is the elemental volume and the superscript e denotes elemental quantities.

In practice, the macroscopic properties of a large composite are predicted by means of computing the average behaviour of the corresponding RVE. In this computation of the average behaviour of RVE, the volume-average stresses and strains over the volume of the RVE are computed by applying homogeneous

boundary conditions either in terms of displacements or in terms of tractions over the boundary surface of the RVE [405]. Presently, the homogeneous displacement boundary conditions are followed. The general form of the homogeneous displacement and electric potential boundary conditions in the Cartesian coordinate system (xyz) can be written as [383],

$$u_i(s) = \varepsilon_{ij}^0 x_j\,,\ \phi(s) = -E_j^0 x_j\,;\ i,j = 1,2,3 \tag{2.23b}$$

where, s represents the boundary surface of RVE; 1, 2 and 3 denote the x, y and z directions of the Cartesian coordinate system, respectively; x_j is the coordinate along j^{th} axis; u_i is the displacement along i^{th} direction; ε_{ij}^0 and E_j^0 are the specified strain and electric field components, respectively. If one writes Eq. (2.23b) explicitly, then the following expressions can be obtained,

$$\begin{aligned} &u_1(s) = \varepsilon_{11}^0 x_1 + \varepsilon_{12}^0 x_2 + \varepsilon_{13}^0 x_3\,,\ u_2(s) = \varepsilon_{12}^0 x_1 + \varepsilon_{22}^0 x_2 + \varepsilon_{23}^0 x_3\,, \\ &u_3(s) = \varepsilon_{13}^0 x_1 + \varepsilon_{23}^0 x_2 + \varepsilon_{33}^0 x_3\,,\ \phi(s) = -(E_1^0 x_1 + E_2^0 x_2 + E_3^0 x_3) \end{aligned} \tag{2.23c}$$

Now, let the RVE be in the shape of a rectangular parallelepiped and its six boundary planes are denoted by +1, -1, +2, -2, +3 and -3 where a boundary plane is denoted by its outward normal direction. The strain-displacement and electric field-electric potential relations at any point within the RVE can be written as,

$$\begin{aligned} &\varepsilon_{11} = \frac{\partial u_1}{\partial x_1}\,,\ \varepsilon_{22} = \frac{\partial u_2}{\partial x_2}\,,\ \varepsilon_{33} = \frac{\partial u_3}{\partial x_3}\,,\ \varepsilon_{23} = \frac{\partial u_2}{\partial x_3} + \frac{\partial u_3}{\partial x_2}\,, \\ &\varepsilon_{13} = \frac{\partial u_1}{\partial x_3} + \frac{\partial u_3}{\partial x_1}\,,\ \varepsilon_{12} = \frac{\partial u_1}{\partial x_2} + \frac{\partial u_2}{\partial x_1}\,,\ E_1 = -\frac{\partial \phi}{\partial x_1}\,, E_2 = -\frac{\partial \phi}{\partial x_2}\,, E_3 = -\frac{\partial \phi}{\partial x_3} \end{aligned} \tag{2.23d}$$

The elastic and piezoelectric constituent materials of the RVE are arranged with respect to the reference coordinate system in such a manner that the normal strains ($\varepsilon_{11}, \varepsilon_{22}, \varepsilon_{33}$) are not coupled with the shear strains ($\varepsilon_{12}, \varepsilon_{23}, \varepsilon_{13}$). The shear strains ($\varepsilon_{12}, \varepsilon_{23}, \varepsilon_{13}$) are not also coupled with each other, but the normal strains ($\varepsilon_{11}, \varepsilon_{22}, \varepsilon_{33}$) are coupled with each other. Also, there is a dominant electric field component (E_3) with the assumption ($E_1 \approx 0$ and $E_2 \approx 0$). The shear strains are not coupled with this dominant electric field (E_3), but the normal strains are coupled with the same electric field (E_3). Under this circumstance, if one wishes to achieve the volume-average strain and electric field components in

a manner as, $\bar{\varepsilon}_{11}=\varepsilon_{11}^{0}, \bar{\varepsilon}_{22}=0, \bar{\varepsilon}_{33}=0, \bar{\varepsilon}_{23}=0, \bar{\varepsilon}_{13}=0, \bar{\varepsilon}_{12}=0, \bar{E}_3=0$; then the corresponding homogeneous displacement and electric potential boundary conditions can be obtained from Eqs. (2.23c)-(2.23d) as,

$$u_1^{\pm1}=\varepsilon_{11}^{0}x_1^{\pm1};\ u_1^{\pm2}=\varepsilon_{11}^{0}x_1^{\pm2};\ u_1^{\pm3}=\varepsilon_{11}^{0}x_1^{\pm3};\ \ u_2^{\pm1}=0;\ u_2^{\pm2}=0;\ u_2^{\pm3}=0;$$
$$u_3^{\pm1}=0;\ u_3^{\pm2}=0;\ u_3^{\pm3}=0;\ \phi^{\pm1}=0;\ \phi^{\pm2}=0;\ \phi^{\pm3}=0 \qquad (2.23e)$$

where, the superscript +1/-1/+2/-2/+3/-3 indicates the quantity over the boundary surface that is denoted by +1/-1/+2/-2/+3/-3. Here, the pairs of displacement boundary conditions like $(u_1^{\pm2}, u_2^{\pm1})$, $(u_1^{\pm3}, u_3^{\pm1})$ and $(u_2^{\pm3}, u_3^{\pm2})$ ensure the applied normal strain (ε_{11}^{0}) without any shear strain. But, as mentioned above, the normal strains are not coupled with shear strains and thus the boundary conditions for these surface displacements are the redundant ones. Similarly, the boundary conditions for the surface electric potentials like $\phi^{\pm1}$ and $\phi^{\pm2}$ are also the redundant ones because of the assumption ($E_1\approx0, E_2\approx0$). Consequently, the boundary conditions (2.23e) can be reduced as,

$$u_1^{\pm1}=\varepsilon_{11}^{0}x_1^{\pm1};\ u_2^{\pm2}=0;\ u_3^{\pm3}=0;\ \ \phi^{\pm3}=0 \qquad (2.23f)$$

Now, the applied homogeneous boundary conditions (Eq. (2.23f)) and the corresponding volume-average strain and electric field components ($\bar{\varepsilon}_{11}=\varepsilon_{11}^{0}$, $\bar{\varepsilon}_{22}=0, \bar{\varepsilon}_{33}=0, \bar{\varepsilon}_{23}=0, \bar{\varepsilon}_{13}=0, \bar{\varepsilon}_{12}=0, \bar{E}_3=0$) imply the average strain theorem, and thus the computation of the corresponding volume-average stress ($\bar{\sigma}_{ij}$) and electric displacement ($\bar{D}_j$) components yields the effective properties of the RVE [383]. However, the same strain condition ($\bar{\varepsilon}_{11}=\varepsilon_{11}^{0}, \bar{\varepsilon}_{22}=0, \bar{\varepsilon}_{33}=0, \bar{\varepsilon}_{23}=0, \bar{\varepsilon}_{13}=0$, $\bar{\varepsilon}_{12}=0, \bar{E}_3=0$) can also be achieved by applying the homogeneous boundary conditions with respect to the middle point of the RVE as,

$$u_1^{\pm1}=\pm\varepsilon_{11}^{0}(\Delta x/2);\ u_2^{\pm2}=0;\ u_3^{\pm3}=0;\ \phi^{\pm3}=0 \qquad (2.23g)$$

where, Δx is the span of the RVE along 1-direction. In similar way, the homogeneous displacement and electric potential boundary conditions can be obtained for the other normal strain condition like $\bar{\varepsilon}_{22}=\varepsilon_{22}^{0}$ ($\bar{\varepsilon}_{11}=0, \bar{\varepsilon}_{33}=0$, $\bar{\varepsilon}_{23}=0, \bar{\varepsilon}_{13}=0, \bar{\varepsilon}_{12}=0, \bar{E}_3=0$) or $\bar{\varepsilon}_{33}=\varepsilon_{33}^{0}$ ($\bar{\varepsilon}_{11}=0, \bar{\varepsilon}_{22}=0, \bar{\varepsilon}_{23}=0, \bar{\varepsilon}_{13}=0, \bar{\varepsilon}_{12}=0$, $\bar{E}_3=0$). For achieving the shear strain condition like $\bar{\varepsilon}_{12}=\varepsilon_{12}^{0}$ ($\bar{\varepsilon}_{11}=0, \bar{\varepsilon}_{22}=0$,

$\bar{\varepsilon}_{33}=0, \bar{\varepsilon}_{23}=0, \bar{\varepsilon}_{13}=0, \bar{E}_3=0$), the corresponding homogeneous displacement boundary conditions can be obtained from Eqs. (2.23c)-(2.23d) as,

$$u_1^{\pm 2}=(1/2)\varepsilon_{12}^0 x_2^{\pm 2},\ u_2^{\pm 1}=(1/2)\varepsilon_{12}^0 x_1^{\pm 1} \tag{2.23h}$$

For deriving Eq. (2.23h), it may be recalled that a shear strain component is not coupled with any normal strain component and also the shear strain components are not coupled with each other. Further, a shear strain component is not coupled with the dominant electric field (E_3). Following the form of Eq. (2.23g), Eq. (2.23h) can be written as,

$$u_1^{\pm 2}=\pm\varepsilon_{12}^0(\Delta y/4),\ u_2^{\pm 1}=\pm\varepsilon_{12}^0(\Delta x/4) \tag{2.23i}$$

where, Δx and Δy are the spans of the RVE along 1 and 2 directions, respectively. The same procedure can be followed in deriving the homogeneous displacement boundary conditions for the other shear strain condition like $\bar{\varepsilon}_{23}=\varepsilon_{23}^0$ ($\bar{\varepsilon}_{11}=0, \bar{\varepsilon}_{22}=0, \bar{\varepsilon}_{33}=0, \bar{\varepsilon}_{12}=0, \bar{\varepsilon}_{13}=0, \bar{E}_3=0$) or $\bar{\varepsilon}_{13}=\varepsilon_{13}^0$ ($\bar{\varepsilon}_{11}=0, \bar{\varepsilon}_{22}=0, \bar{\varepsilon}_{33}=0, \bar{\varepsilon}_{23}=0, \bar{\varepsilon}_{12}=0, \bar{E}_3=0$). It may be noted here that similar boundary conditions are also illustrated in [406] for the estimation of the effective properties of a fibre-reinforced composite, where the effective elastic properties of the composite are evaluated using the displacement-based FEM and the corresponding results are verified with the analytical and experimental results.

The aforesaid homogeneous displacement and electric potential boundary conditions are illustrated for the RVE in the Cartesian coordinate system. But, the same boundary conditions cannot be applied for an RVE in the cylindrical coordinate system mainly because of the corresponding strain-displacement relations (Eqs. (2.15)-(2.16)). However, the physical dimensions of the present sub-volume are taken in micro-scale while it is located at a large radius within the annular PFC actuator. This radius for location of the sub-volume appears in macro-scale since the inner and outer radii of the annular PFC actuator are in the same scale (macro-scale). Thus, the radial span (Δr) and circumferential span (θ_c) of the sub-volume are very small in comparison to its inner/outer radius. With these dimensions of the sub-volume, its geometry in the shape of the annular sector becomes very close to the shape of a rectangle. Consequently, the strain-displacement relations (Eq. (Eqs. (2.15)-(2.16))) can be assumed as,

$$\varepsilon_r \approx \frac{\partial u}{\partial r},\ \varepsilon_\theta \approx \frac{1}{r_c}\frac{\partial v}{\partial \theta},\ \varepsilon_z \approx \frac{\partial w}{\partial z},\ \gamma_{\theta z} \approx \left(\frac{1}{r_c}\frac{\partial w}{\partial \theta} + \frac{\partial v}{\partial z}\right),$$
$$\gamma_{rz} \approx \left(\frac{\partial w}{\partial r} + \frac{\partial u}{\partial z}\right),\ \gamma_{r\theta} \approx \left(\frac{1}{r_c}\frac{\partial u}{\partial \theta} + \frac{\partial v}{\partial r}\right) \quad (2.23j)$$

where, r_c is the radial coordinate at the middle point of the sub-volume. On the basis of this assumed strain-displacement relations (Eq. (2.23j)), the aforesaid procedure for deriving the homogeneous boundary conditions is followed, and six sets of displacement and electric potential boundary conditions are decided as given in the following points (a)-(f) on next page. Every set of boundary conditions is separately applied over the FE model (Eq. (2.22)) of the sub-volume and the effective properties of the sub-volume are estimated. Here, the effective elastic and piezoelectric coefficients are estimated for the zero value of the electric field (E_z) throughout the volume of the sub-volume. It is achieved by assigning the zero value of the electric potential over the electrode surfaces, where ϕ_t, ϕ_b and ϕ_a denote the electric potentials over the top, bottom and intermediate electrode surfaces, respectively. In points (a)-(f), a boundary surface of the sub-volume is denoted by its outward normal direction so that the six sides of the sub-volume are denoted by, $\pm r$, $\pm\theta$ and $\pm z$. However, it should be noted here that the displacement boundary conditions ((a)-(f)) are presently decided on the basis of the assumed strain-displacement relations (Eq. (2.23j)) due to the physical dimensions of the sub-volume. Therefore, the applicability of these boundary conditions is to be verified first as per the physical dimensions of the sub-volume, and then the effective material constants of the sub-volume can be computed. It is carried out at present as described below considering the first set of the boundary conditions.

Under the zero value of the electric field (E_z), the applied strain component in the first set of the boundary condition is ε_r^0. For this applied strain component, the volume-average strain components ($\bar{\varepsilon}_r, \bar{\varepsilon}_\theta, \bar{\varepsilon}_z, \bar{\gamma}_{\theta z}, \bar{\gamma}_{rz}, \bar{\gamma}_{r\theta}$) in the sub-volume are computed using Eq. (2.23a). Subsequently, the values of the volume-average strain components are verified. If it is found that ε_r^0 is equal to $\bar{\varepsilon}_r$ and the value of ε_r^0 is remarkably higher ($10^4/10^5$ times) than that of any other volume-average strain component ($\bar{\varepsilon}_\theta, \bar{\varepsilon}_z, \bar{\gamma}_{\theta z}, \bar{\gamma}_{rz}, \bar{\gamma}_{r\theta}$), then it is considered that the set of the boundary conditions results in one strain

component that is the applied one ($\bar{\varepsilon}_r = \varepsilon_r^0, \bar{\varepsilon}_\theta \approx 0, \bar{\varepsilon}_z \approx 0, \bar{\gamma}_{\theta z} \approx 0, \bar{\gamma}_{rz} \approx 0, \bar{\gamma}_{r\theta} \approx 0$). Accordingly, the average strain theorem can be followed for estimating the effective material constants through the computation of the corresponding volume-average stress and electric displacement components using Eq. (2.23a). It is obvious that a fully correct set of the boundary conditions for the applied strain (ε_r^0) would yield the volume-average strain components as $\bar{\varepsilon}_r = \varepsilon_r^0, \bar{\varepsilon}_\theta = 0$, $\bar{\varepsilon}_z = 0, \bar{\gamma}_{\theta z} = 0, \bar{\gamma}_{rz} = 0, \bar{\gamma}_{r\theta} = 0$. But, it is difficult to decide according to the strain-displacement relations (Eqs. (2.15)-(2.16)) in the cylindrical coordinate system. However, the present boundary conditions can provide close results according to the physical dimensions of the sub-volume, and a corresponding verification on the accuracy in the computed magnitudes of the effective material constants is presented in Table 2.2.

(a) Applied $\varepsilon_r : \bar{\varepsilon}_r = \varepsilon_r^0$;

BCs: $u\big|_{\pm r} = \pm\varepsilon_r^0 \Delta r/2$, $v\big|_{\pm\theta} = 0$, $w\big|_{\pm z} = 0$, $\phi_t = \phi_b = \phi_a = 0$;

Coefficients: $\bar{C}_{11} = \bar{\sigma}_r / \bar{\varepsilon}_r$, $\bar{C}_{21} = \bar{\sigma}_\theta / \bar{\varepsilon}_r$, $\bar{C}_{31} = \bar{\sigma}_z / \bar{\varepsilon}_r$, $\bar{e}_{31} = \bar{D}_z / \bar{\varepsilon}_r$.

(b) Applied ε_θ: $\bar{\varepsilon}_\theta = \varepsilon_\theta^0$;

BCs: $u\big|_{\pm r} = 0$, $v\big|_{\pm\theta} = \pm\varepsilon_\theta^0 r_c \theta_c/2$, $w\big|_{\pm z} = 0, \phi_t = \phi_b = \phi_a = 0$;

Coefficients: $\bar{C}_{12} = \bar{\sigma}_r / \bar{\varepsilon}_\theta$, $\bar{C}_{22} = \bar{\sigma}_\theta / \bar{\varepsilon}_\theta$, $\bar{C}_{32} = \bar{\sigma}_z / \bar{\varepsilon}_\theta$, $\bar{e}_{32} = \bar{D}_z / \bar{\varepsilon}_\theta$.

(c) Applied ε_z: $\bar{\varepsilon}_z = \varepsilon_z^0$;

BCs: $u\big|_{\pm r} = 0, v\big|_{\pm\theta} = 0, w\big|_{\pm z} = \pm\varepsilon_z^0 h_c/2, \phi_t = \phi_b = \phi_a = 0$;

Coefficients: $\bar{C}_{13} = \bar{\sigma}_r / \bar{\varepsilon}_z$, $\bar{C}_{23} = \bar{\sigma}_\theta / \bar{\varepsilon}_z$, $\bar{C}_{33} = \bar{\sigma}_z / \bar{\varepsilon}_z$, $\bar{e}_{33} = \bar{D}_z / \bar{\varepsilon}_z$.

(d) Applied $\gamma_{\theta z}$: $\bar{\gamma}_{\theta z} = \gamma_{\theta z}^0$;

BCs: $w\big|_{\pm\theta} = \pm\gamma_{\theta z}^0 r_c \theta_c/4$, $v\big|_{\pm z} = \pm\gamma_{\theta z}^0 h_c/4$;

Coefficients: $\bar{C}_{44} = \bar{\tau}_{\theta z} / \bar{\gamma}_{\theta z}$.

(e) Applied $\gamma_{rz} : \bar{\gamma}_{rz} = \gamma_{rz}^0$;

BCs: $w\big|_{\pm r} = \pm\gamma_{rz}^0 \Delta r/4$, $u\big|_{\pm z} = \pm\gamma_{rz}^0 h_c/4$;

Coefficients: $\bar{C}_{55} = \bar{\tau}_{rz} / \bar{\gamma}_{rz}$.

(f) Applied $\gamma_{r\theta} : \bar{\gamma}_{r\theta} = \gamma_{r\theta}^0$;

BCs: $v\big|_{\pm r} = \pm\gamma_{r\theta}^0 \Delta r / 4$, $u\big|_{\pm\theta} = \pm\gamma_{r\theta}^0 r_c \theta_c / 4$;

Coefficients: $\bar{C}_{66} = \bar{\tau}_{r\theta} / \bar{\gamma}_{r\theta}$.

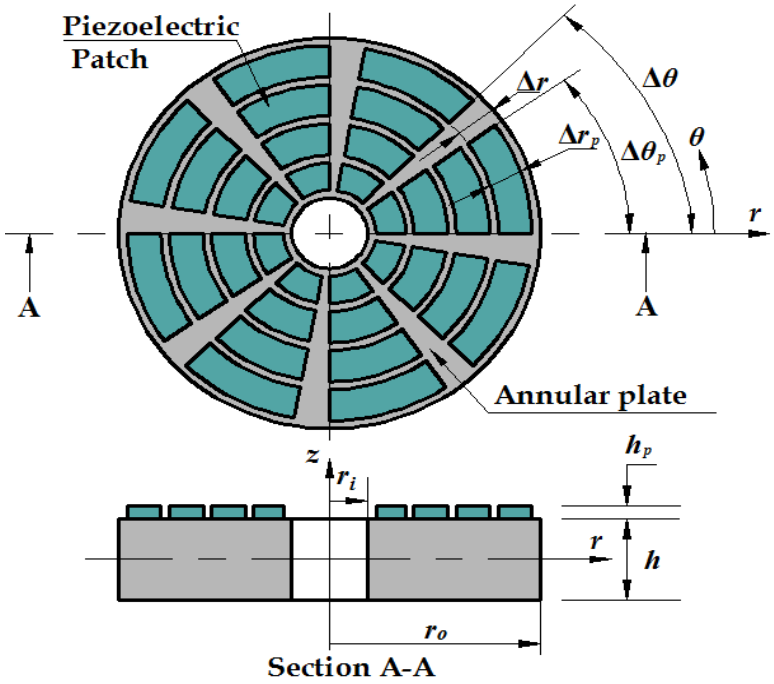

Fig. 2.6 Schematic diagram of an annular plate integrated with the patches of the annular PFC actuator.

2.4 Smart annular plate

The actuation capability of the present annular PFC actuator is investigated by utilizing it in control of vibration of an annular substrate plate. The patches of the PFC actuator with the shape of the annular-sector are attached to the top surface of the host annular plate as shown in Fig. 2.6. The radial span of the annular plate is equally divided into a number (N_r) of divisions where every division has a radial span of, Δr ($\Delta r = (r_o - r_i)/N_r$). Similarly, the circumferential span (2π) of the same plate is also equally divided into a number (N_θ) of divisions where every division has the circumferential span of $\Delta\theta$ ($\Delta\theta = 2\pi / N_\theta$). Corresponding to these divisions, annular-sectors are formed over the plane of the annular plate. The dimensions of every sector along the radial and circumferential directions are, Δr and $\Delta\theta$, respectively. In every annular-sector,

a patch of the present PFC actuator is located with the dimensions of Δr_p and $\Delta\theta_p$ along the radial and the circumferential directions, respectively, as shown in Fig. 2.6. The patches are considered to be spaced closely in any of the radial and circumferential directions ($(\Delta\theta - \Delta\theta_p) << \Delta\theta, (\Delta r - \Delta r_p) << \Delta r$). Generally, the extension mode piezoelectric actuators are located around the anti-nodes of a bending mode shape of plates. So, this arrangement is made to provide a large number of patches around every anti-node for any mode shape of vibration of the smart annular plate within a frequency-domain. Now, as the mechanically induced in-plane normal stresses at all anti-nodes do not appear with the same sign at any instant of time, every patch is activated by taking the feedback of local velocity, and it is achieved by locating the velocity sensors at the middle points of the patches.

The middle plane of the host annular plate (Fig. 2.6) is taken as the reference plane and the origin of the cylindrical coordinate system ($r\theta z$) is located at the center of the reference annular plane. The overall smart plate is considered as a thin plate. So, the displacement field within the overall plate is defined according to the first-order shear deformation theory (FSDT) as,

$$\begin{aligned} u_p(r,\theta,z,t) &= u_0(r,\theta,t) + z\psi_r(r,\theta,t), \\ v_p(r,\theta,z,t) &= v_0(r,\theta,t) + z\psi_\theta(r,\theta,t), \\ w_p(r,\theta,z,t) &= w_0(r,\theta,t) \end{aligned} \tag{2.24}$$

where, u_p, v_p and w_p are the displacements at any point within the overall plate along the r, θ and z directions, respectively; u_0, v_0 and w_0 are the displacements at any point over the reference plane along the r, θ and z directions, respectively; ψ_r and ψ_θ are the rotations of the normal to the reference plane with respect to the θ and r axes, respectively. According to the displacement field (Eq. (2.24)), the displacement vector ($\boldsymbol{d}_p$) and the generalized displacement vector ($\boldsymbol{d}_p^g$) are written as,

$$\begin{aligned} \boldsymbol{d}_p &= \{u_p \quad v_p \quad w_p\}^{\mathrm{T}}, \\ \boldsymbol{d}_p^g &= \{u_0 \quad v_0 \quad w_0 \quad \psi_r \quad \psi_\theta\}^{\mathrm{T}} \end{aligned} \tag{2.25}$$

The state of stress and the state of strain at any point within the plate can be written as,

$$\boldsymbol{\varepsilon}_b = \{\varepsilon_r \quad \varepsilon_\theta \quad \gamma_{r\theta}\}^{\mathrm{T}},$$

$$\boldsymbol{\varepsilon}_s = \{\gamma_{rz} \quad \gamma_{\theta z}\}^{\mathrm{T}},$$

$$\boldsymbol{\sigma}_b = \{\sigma_r \quad \sigma_\theta \quad \tau_{r\theta}\}^{\mathrm{T}},$$

$$\boldsymbol{\sigma}_s = \{\tau_{rz} \quad \tau_{\theta z}\}^{\mathrm{T}} \tag{2.26}$$

According to the displacement field (Eq. (2.24)), the strain-displacement relations and the displacement vector ($\boldsymbol{d}_p$) at any point within the overall annular plate can be written as,

$$\boldsymbol{\varepsilon}_b = (\boldsymbol{L}_{bt} + z\boldsymbol{L}_{br})\boldsymbol{d}_p^g,$$

$$\boldsymbol{\varepsilon}_s = \boldsymbol{L}_s \boldsymbol{d}_p^g,$$

$$\boldsymbol{d}_p = (\boldsymbol{T}_t + z\boldsymbol{T}_r)\boldsymbol{d}_p^g,$$

$$\boldsymbol{L}_{bt} = \begin{bmatrix} (\partial/\partial r) & 0 & 0 & 0 & 0 \\ (1/r) & (1/r)(\partial/\partial\theta) & 0 & 0 & 0 \\ (1/r)(\partial/\partial\theta) & (\partial/\partial r)-(1/r) & 0 & 0 & 0 \end{bmatrix},$$

$$\boldsymbol{L}_{br} = \begin{bmatrix} 0 & 0 & 0 & (\partial/\partial r) & 0 \\ 0 & 0 & 0 & (1/r) & (1/r)(\partial/\partial\theta) \\ 0 & 0 & 0 & (1/r)(\partial/\partial\theta) & (\partial/\partial r)-(1/r) \end{bmatrix},$$

$$\boldsymbol{L}_s = \begin{bmatrix} 0 & 0 & (\partial/\partial r) & 1 & 0 \\ 0 & 0 & (1/r)(\partial/\partial\theta) & 0 & 1 \end{bmatrix},$$

$$\boldsymbol{T}_t = \begin{bmatrix} 1 & 0 & 0 & 0 & 0 \\ 0 & 1 & 0 & 0 & 0 \\ 0 & 0 & 1 & 0 & 0 \end{bmatrix},$$

$$\boldsymbol{T}_r = \begin{bmatrix} 0 & 0 & 0 & 1 & 0 \\ 0 & 0 & 0 & 0 & 1 \end{bmatrix} \tag{2.27}$$

The constitutive relations for the host isotropic annular plate can be written as,

$$\boldsymbol{\sigma}_b^k = \boldsymbol{C}_b^k \boldsymbol{\varepsilon}_b,$$

$$\boldsymbol{\sigma}_s^k = \boldsymbol{C}_s^k \boldsymbol{\varepsilon}_s, \quad k = 1$$

$$\boldsymbol{C}_b^k = \frac{E}{1-\nu^2}\begin{bmatrix} 1 & \nu & 0 \\ \nu & 1 & 0 \\ 0 & 0 & \dfrac{1-\nu}{2} \end{bmatrix}, \qquad \boldsymbol{C}_s^k = \frac{E}{1+\nu}\begin{bmatrix} 1/2 & 0 \\ 0 & 1/2 \end{bmatrix} \tag{2.28}$$

where, $\boldsymbol{C}_b^k$ and $\boldsymbol{C}_s^k$ $(k=1)$ are the stiffness matrices; E and ν are Young's modulus and Poisson's ratio, respectively.

The electro-elastic properties of the present PFC actuator vary along the radial direction. These varying properties are evaluated by means of segmentation of its RV into the large number of micro-volumes/sub-volumes where the variation of properties along the radial direction appears over the radially distributed homogeneous micro-volumes of different FVFs. Presently, these varying properties across the radial span of the annular PFC actuator are expressed as functions of radial coordinate (r). Accordingly, the constitutive relations of the actuator for its application in active control of a thin annular plate under the assumption of $\sigma_z \approx 0$ can be written as,

$$\boldsymbol{\sigma}_b^k = \boldsymbol{C}_b^k(r)\boldsymbol{\varepsilon}_b - \boldsymbol{e}_b^k(r)^{\mathrm{T}} E_z ,$$

$$\boldsymbol{\sigma}_s^k = \boldsymbol{C}_s^k(r)\boldsymbol{\varepsilon}_s ,$$

$$D_z^k = \boldsymbol{e}_b^k(r)\boldsymbol{\varepsilon}_b + \in_{33}^k(r) E_z , k=2$$

$$\boldsymbol{C}_b^k(r) = \begin{bmatrix} \bar{C}_{11}^k(r) & \bar{C}_{12}^k(r) & 0 \\ \bar{C}_{12}^k(r) & \bar{C}_{22}^k(r) & 0 \\ 0 & 0 & C_{66}^k(r) \end{bmatrix},$$

$$\boldsymbol{C}_s^k(r) = \begin{bmatrix} C_{55}^k(r) & 0 \\ 0 & C_{44}^k(r) \end{bmatrix},$$

$$\boldsymbol{e}_b^k(r) = \begin{bmatrix} \bar{e}_{31}^k(r) & \bar{e}_{32}^k(r) & 0 \end{bmatrix},$$

$$\bar{C}_{11}^k(r) = C_{11}^k(r) - \left\langle C_{13}^k(r) \right\rangle^2 \Big/ C_{33}^k(r) ,$$

$$\bar{C}_{12}^k(r) = C_{12}^k(r) - \left\langle C_{13}^k(r) C_{23}^k(r) \right\rangle \Big/ C_{33}^k(r) ,$$

$$\bar{C}_{22}^k(r) = C_{22}^k(r) - \left\langle C_{23}^k(r) \right\rangle^2 \Big/ C_{33}^k(r) ,$$

$$\bar{e}_{31}^{k}(r) = e_{31}^{k}(r) - \left\langle C_{13}^{k}(r)\, e_{33}^{k}(r) \right\rangle \Big/ C_{33}^{k}(r),$$

$$\bar{e}_{32}^{k}(r) = e_{32}^{k}(r) - \left\langle C_{23}^{k}(r)\, e_{33}^{k}(r) \right\rangle \Big/ C_{33}^{k}(r) \qquad (2.29)$$

In Eqs. (2.28) and (2.29), the superscript k denotes the substrate annular plate or the PFC actuator patches according to its value as 1 or 2, respectively; $\boldsymbol{C}_b^k(r)$ and $\boldsymbol{C}_s^k(r)$ are the stiffness matrices; $\boldsymbol{e}_b^k(r)$ is the piezoelectric matrix; $C_{ij}^k(r)$, $e_{ij}^k(r)$ and $\in_{ij}^k(r)$ are the stiffness, piezoelectric and dielectric coefficients, respectively; D_z^k is the electric displacement along the transverse (z) direction; E_z is the applied electric field across the thickness (h_a) of the active layers of the annular PFC actuator, and it (E_z) can be expressed as, $E_z = -V/h_a$ for an applied voltage (V) across the top and bottom fully electrode surfaces of the active layers.

The overall annular plate is considered to be subjected to a transversely distributed harmonic mechanical load ($p(r,\theta,t)$). For the corresponding vibration of the overall plate, the first variations of its total potential energy (δT_p) and the total kinetic energy (δT_k) at any instant of time (t) can be written as [384],

$$\delta T_p = \int_{r_i}^{r_o}\int_0^{2\pi} \left\langle \sum_{k=1}^{2} \int_{h_k}^{h_{k+1}} \left(\delta\boldsymbol{\varepsilon}_b^{\mathrm{T}} \boldsymbol{\sigma}_b^k + \delta\boldsymbol{\varepsilon}_s^{\mathrm{T}} \boldsymbol{\sigma}_s^k \right) dz - \int_{h_k}^{h_{k+1}} \left(\delta E_z D_z \right)_{k=2} dz - Q_p \right\rangle r\, d\theta\, dr,$$

$$Q_p = \delta w_p \left(p(r,\theta,t) \right)_{z=-h/2} \qquad (2.30)$$

$$\delta T_k = \int_{r_i}^{r_o}\int_0^{2\pi} \left\langle \sum_{k=1}^{2} \int_{h_k}^{h_{k+1}} \left\{ \delta\dot{u}_p \quad \delta\dot{v}_p \quad \delta\dot{w}_p \right\} \rho^k \left\{ \dot{u}_p \quad \dot{v}_p \quad \dot{w}_p \right\}^{\mathrm{T}} dz \right\rangle r\, d\theta\, dr \qquad (2.31)$$

where, ρ^k is the mass density for the host plate ($k=1$) or the piezoelectric actuator ($k=2$); h_k and h_{k+1} are the thickness coordinates at the bottom and top surfaces of k^{th} layer, respectively. For deriving FE model of the overall annular plate, the plane of the plate is discretized using 9-node quadrilateral element. A typical element is in the shape of annular-sector with the edges parallel to the radial and circumferential directions of the overall plate. At any point within an element, the displacement vector ($\boldsymbol{d}_p$), generalized displacement vector ($\boldsymbol{d}_p^g$) and

generalized strains ($\boldsymbol{\varepsilon}_b, \boldsymbol{\varepsilon}_s$) can be written in terms of the shape function matrix ($\boldsymbol{N}_p$) and the elemental nodal displacement vector ($\boldsymbol{d}_p^e$) as follows,

$$\begin{aligned}
\boldsymbol{d}_p^g &= \boldsymbol{N}_p \boldsymbol{d}_p^e, \\
\boldsymbol{\varepsilon}_b &= \left(\boldsymbol{B}_{bt} + z\boldsymbol{B}_{br}\right)\boldsymbol{d}_p^e, \\
\boldsymbol{\varepsilon}_s &= \boldsymbol{B}_s \boldsymbol{d}_p^e, \\
\boldsymbol{d}_p &= \left(\boldsymbol{B}_t^m + z\boldsymbol{B}_r^m\right)\boldsymbol{d}_p^e, \\
\boldsymbol{B}_{bt} &= \boldsymbol{L}_{bt}\boldsymbol{N}_p, \\
\boldsymbol{B}_{br} &= \boldsymbol{L}_{br}\boldsymbol{N}_p, \\
\boldsymbol{B}_s &= \boldsymbol{L}_s \boldsymbol{N}_p, \\
\boldsymbol{B}_t^m &= \boldsymbol{T}_t \boldsymbol{N}_p, \\
\boldsymbol{B}_r^m &= \boldsymbol{T}_r \boldsymbol{N}_p
\end{aligned} \tag{2.32}$$

Substituting Eqs. (2.28), (2.29) and (2.27) in Eqs. (2.30) and (2.31) and then using Eq. (2.32), the first variations of the total potential energy (δT_p^e) and the total kinetic energy (δT_k^e) for a typical element can be obtained as,

$$\begin{aligned}
\delta T_p^e &= \left(\delta \boldsymbol{d}_p^e\right)^{\mathrm{T}} \left\langle \left(\boldsymbol{K}_b^e + \boldsymbol{K}_s^e\right)\boldsymbol{d}_p^e - \boldsymbol{P}_E^e V - \boldsymbol{P}_M^e(t) \right\rangle, \\
\delta T_k^e &= (\delta \dot{\boldsymbol{d}}_p^e)^{\mathrm{T}} \boldsymbol{M}^e \dot{\boldsymbol{d}}_p^e, \\
\boldsymbol{K}_b^e &= \int_{A_e} \left(\boldsymbol{B}_{bt}^{\mathrm{T}} \boldsymbol{A}_b(r) \boldsymbol{B}_{bt} + \boldsymbol{B}_{bt}^{\mathrm{T}} \boldsymbol{B}_b(r) \boldsymbol{B}_{br} + \boldsymbol{B}_{br}^{\mathrm{T}} \boldsymbol{B}_b(r) \boldsymbol{B}_{bt} + \boldsymbol{B}_{br}^{\mathrm{T}} \boldsymbol{D}_b(r) \boldsymbol{B}_{br} \right) dA_e, \\
\boldsymbol{K}_s^e &= \int_{A_e} \left(\boldsymbol{B}_s^{\mathrm{T}} \boldsymbol{A}_s(r) \boldsymbol{B}_s \right) dA_e, \\
\boldsymbol{P}_E^e &= \int_{A_e} \left(\boldsymbol{B}_{bt}^{\mathrm{T}} \boldsymbol{A}_{be}(r) + \boldsymbol{B}_{br}^{\mathrm{T}} \boldsymbol{B}_{be}(r) \right) dA_e, \\
\boldsymbol{P}_M^e(t) &= \int_{A_e} \left\langle \left(\boldsymbol{N}_p\right)^{\mathrm{T}} \{0 \quad 0 \quad p(r,\theta,\mathrm{t}) \quad 0 \quad 0\}^{\mathrm{T}} \right\rangle dA_e, \\
\boldsymbol{M}^e &= \int_{A_e} \left(\left(\boldsymbol{B}_t^m\right)^{\mathrm{T}} \bar{m}_1 \boldsymbol{B}_t^m + \left(\boldsymbol{B}_t^m\right)^{\mathrm{T}} \bar{m}_2 \boldsymbol{B}_r^m + \left(\boldsymbol{B}_r^m\right)^{\mathrm{T}} \bar{m}_2 \boldsymbol{B}_t^m + \left(\boldsymbol{B}_r^m\right)^{\mathrm{T}} \bar{m}_3 \boldsymbol{B}_r^m \right) dA_e
\end{aligned} \tag{2.33}$$

where, A_e is the elemental area. The rigidity matrices ($\boldsymbol{A}_b, \boldsymbol{A}_s, \boldsymbol{B}_b, \boldsymbol{D}_b$), electro-elastic coupling vectors ($\boldsymbol{A}_{be}, \boldsymbol{B}_{be}$) and mass parameters ($\bar{m}_1, \bar{m}_2, \bar{m}_3$) appearing in Eq. (2.33) are as follows,

$$\boldsymbol{A}_b(r) = \sum_{k=1}^{2} \int_{h_k}^{h_{k+1}} \boldsymbol{C}_b^k(r)\, dz\,,$$

$$\boldsymbol{A}_s(r) = \sum_{k=1}^{2} \int_{h_k}^{h_{k+1}} \boldsymbol{C}_s^k(r)\, dz\,,$$

$$\boldsymbol{B}_b(r) = \sum_{k=1}^{2} \int_{h_k}^{h_{k+1}} \boldsymbol{C}_b^k(r)\, z\, dz\,,$$

$$\boldsymbol{D}_b(r) = \sum_{k=1}^{2} \int_{h_k}^{h_{k+1}} \boldsymbol{C}_b^k(r)\, z^2 dz\,,$$

$$\boldsymbol{A}_{be}(r) = \int_{h_k}^{h_{k+1}} \frac{1}{h_a} \boldsymbol{e}_b^k(r)\Big|_{k=2} dz\,,$$

$$\boldsymbol{B}_{be}(r) = \int_{h_k}^{h_{k+1}} \frac{1}{h_a} \boldsymbol{e}_b^k(r)\Big|_{k=2} z\, dz\,,$$

$$\bar{m}_1(r) = \sum_{k=1}^{2} \int_{h_k}^{h_{k+1}} \rho^k(r)\, dz\,,$$

$$\bar{m}_2(r) = \sum_{k=1}^{2} \int_{h_k}^{h_{k+1}} \rho^k(r)\, z\, dz\,,$$

$$\bar{m}_3(r) = \sum_{k=1}^{2} \int_{h_k}^{h_{k+1}} \rho^k(r)\, z^2 dz \qquad (2.34)$$

In Eq. (2.34), the stiffness matrices ($\boldsymbol{C}_b^k(r), \boldsymbol{C}_s^k(r)$) and the mass density ($\rho^k(r)$) are constant quantities for the host isotropic annular plate ($k=1$). The governing equations of motion of the smart annular plate are derived employing Hamilton's principle as,

$$\int_{t_1}^{t_2} \left(\delta T_k^e - \delta T_p^e\right) dt = 0 \qquad (2.35)$$

Introducing the expressions of δT_p^e and δT_k^e in Eq. (2.35), the following governing equations of motion for a typical element of the smart annular plate can be obtained,

$$\boldsymbol{M}^e \ddot{\boldsymbol{d}}_p^e + \left(\boldsymbol{K}_b^e + \boldsymbol{K}_s^e\right) \boldsymbol{d}_p^e = \boldsymbol{P}_E^e V + \boldsymbol{P}_M^e(t) \qquad (2.36)$$

Assembling the elemental governing equations of motion (Eq. (2.36)), the following global equations of motion of the smart annular plate can be obtained,

$$\boldsymbol{M}\ddot{\boldsymbol{X}}_p + \left(\boldsymbol{K}_b + \boldsymbol{K}_s\right)\boldsymbol{X}_p = \sum_{q=1}^{n_p} \boldsymbol{P}_E^q V^q + \boldsymbol{P}_M(t) \tag{2.37}$$

In Eq. (2.37), $\boldsymbol{M}$ is the global mass matrix; $\boldsymbol{K}_b$ and $\boldsymbol{K}_s$ are the bending and shear counterparts of the global stiffness matrix; $\boldsymbol{P}_M(t)$ is the global nodal mechanical load vector; $\boldsymbol{X}_p$ is the global nodal displacement vector; $\boldsymbol{P}_E^q$ is the electro-elastic coefficient vector for the q^{th} patch and it is obtained through the assembly of elemental matrices ($\boldsymbol{P}_E^e$) for the elements within the q^{th} patch; V^q is the applied voltage to the q^{th} patch; n_p is the total number of actuator patches.

The external voltage (V^q) is supplied to the q^{th} patch according to the negative velocity feedback control strategy. The transverse velocity ($\dot{w}^q$) at the middle point of the q^{th} patch is sensed and it ($\dot{w}^q$) is fed back in the form of a voltage (V^q) as,

$$V^q = -k_d^q \dot{w}^q \tag{2.38}$$

where, k_d^q is the velocity feedback control-gain for the q^{th} patch. The transverse velocity ($\dot{w}^q$) can be expressed in terms of the global nodal velocity vector ($\dot{\boldsymbol{X}}_p$) as follows,

$$\dot{w}^q = \boldsymbol{N}_T^q \dot{\boldsymbol{X}}_p \tag{2.39}$$

where, N_T^q is a row matrix that indicates the element of $\dot{\boldsymbol{X}}_p$ corresponding to the transverse velocity at the middle point of the q^{th} patch. Using Eqs. (2.38) and (2.39) in Eq. (2.37), the following FE equations of motion of the smart annular plate can be obtained,

$$\boldsymbol{M}\ddot{\boldsymbol{X}}_p + \boldsymbol{C}\dot{\boldsymbol{X}}_p + \boldsymbol{K}\boldsymbol{X}_p = \boldsymbol{P}_M(t),\ \boldsymbol{K} = \left(\boldsymbol{K}_b + \boldsymbol{K}_s\right),\ \boldsymbol{C} = \sum_{q=1}^{n_p} \boldsymbol{C}^q,\ \boldsymbol{C}^q = (\boldsymbol{P}_E^q k_d^q N_T^q) \tag{2.40}$$

2.5 Results and discussions

2.5.1 Verification of effective properties of a typical sub-volume

In order to verify the effective properties (Eq. (2.14)) of the annular PFC actuator, first, the closed-form expressions (Eq. (2.9)) for the effective coefficients of the 2-2 PFC layer in a typical sub-volume are verified. A typical RVE (Fig. 2.4) of the 2-2 PFC layer in a sub-volume possesses the fiber of uniform cross-section. So, it is not an RVE of usual 2-2 PFC as shown in Figs. 2.1(a) and 2.1(b). However, the width (w_f) of the fiber, radial span (Δr) and circumferential span (θ_c) of a typical RVE (Fig. 2.4) of 2-2 PFC in sub-volume are taken in micro-scale with reference to its (RVE) large radial distance from the origin of the cylindrical principal material coordinate system. With these dimensions, the geometry of a typical RVE (Fig. 2.4) appears close to that for an RVE of the usual 2-2 PFC. Accordingly, the closed-form expressions of its effective coefficients are derived using Eq. (2.9). For verification of these effective coefficients (Eq. (2.9)), the material properties of constituents and FVF of the 2-2 PFC are taken from [385], and the magnitudes of the corresponding effective coefficients are computed using the closed-form expressions in Eq. (2.9). These results are illustrated in Table 2.1 along with the similar results for an RVE of usual 2-2 PFC as available in [385,386]. It may be observed from Table 2.1 that the present analytical results are in good agreement with the results available in [385,386], and this comparison verifies the present closed-form expressions in Eq. (2.9) for the effective coefficients of 2-2 PFC layer within a small volume of sub-volume.

For verification of the closed-form expressions (Eq. (2.14)) of the effective coefficients of a typical sub-volume, similar results for an identical PFC actuator are not available in the literature. So, this verification is presently carried out by computing the same effective coefficients through the numerical homogenization using the FE model of the sub-volume (section 2.3.2). The properties of the piezoelectric fiber (PZT5H) are taken as [17], C_{11} = 151 GPa, C_{12} = 98 GPa, C_{13} = 96 GPa, C_{33} = 124 GPa, C_{44} = 23 GPa, C_{66} = 26.5 GPa, e_{31} = -5.1 C/m^2, e_{33} = 27 C/m^2, e_{24} = 17 C/m^2, ϵ_{11}= 15.1e-9 C/V-m, ϵ_{33}= 13.27e-9 C/V-m, ρ = 7500 kg/m^3. The properties of the epoxy matrix are taken as, E = 1.8 GPa, ν = 0.4; ϵ = 0.079e-9 C/V-m; ρ = 1250 kg/m^3. The geometrical properties and fiber volume fraction (FVF, v_f) of a sub-volume are considered as, r_i = 0.2 m, Δr = 200

μm, $h_a = 200$ μm, $(h_c - h_a) =$ 20 μm, $w_f = h_a \times 0.8$, $\theta_f = 2\sin^{-1}\left(w_f / 2r_i\right)$, $\theta_c = h_a / r_i$ and $v_f =$ 0.72. According to these material and geometrical properties of the constituents, the effective coefficients of the sub-volume are computed using Eq. (2.14) as well as the FE procedure presented in section 2.3.2. These results are illustrated in Table 2.2, and it may be observed from this table that the results obtained from the analytical expressions (Eq. (2.14)) are close to the similar results obtained through the numerical homogenization using FE formulation.

Table 2.1 Verification of effective coefficients (Eq. (2.9)) of 2-2 PFC layer ($v_f =$ 0.86) in a typical sub-volume.

Effective coefficients	Present	Ref. [385]	Ref. [386]
E_1 (GPa)	46.89	47.17	46.89
E_2 (GPa)	16.53	16.98	17.92
G_{23} (GPa)	5.89	6.06	6.07
G_{13} (GPa)	16.91	17.00	16.91
G_{12} (GPa)	5.87	6.03	5.87
ν_{12} (GPa)	0.39	0.39	0.39
$\bar{e}_{31}$ (C/m^2)	-10.14	-10.23	-10.35
$\bar{e}_{32}$ (C/m^2)	-3.92	-4.05	-4.53
$\epsilon_{33}^T / \epsilon_0$	1567	1600	1609.9

Table 2.2 Effective electro-elastic coefficients for a sub-volume ($v_f =$ 0.72).

Effective coefficients	Mixing rule Eq. (2.14)	FEM
C_{11} (GPa)	61.50	61.15
C_{12} (GPa)	8.13	8.26
C_{13} (GPa)	15.31	14.56
C_{23} (GPa)	6.03	6.33
C_{22} (GPa)	15.56	15.84
C_{33} (GPa)	25.49	23.93
C_{44} (GPa)	2.19	2.26
C_{55} (GPa)	5.28	5.07
C_{66} (GPa)	2.71	2.82
e_{31} (C/m^2)	-8.75	-9.20
e_{32} (C/m^2)	-2.37	-2.32
e_{33} (C/m^2)	9.54	8.66

Although the effective properties of a sub-volume are presently computed through both the analytical and FE procedures for verification as presented in

Table 2.2, the FE procedure usually provides more realistic results [387]. So, further computation of effective properties of the sub-volumes is carried out using the FE procedure.

2.5.2 Varying electro-elastic properties of the annular PFC actuator

The cross-sectional area (in the θz plane) of RV (Fig. 2.3(a)) of the annular PFC actuator varies along the radial direction, but the cross-sectional area of the corresponding fiber remains constant along the same direction. So, the electro-elastic properties of the RV or the annular PFC actuator vary along the radial direction. These varying properties of the RV are estimated by assuming a number of homogeneous sub-volumes of different FVFs across the radial span of the RV where the electro-elastic properties of the RV at a radial location are identified as the effective properties of the sub-volume at that radial location. So, the varying properties of the RV are estimated by computing the effective properties of every sub-volume. Presently, the radial span (Δr) of the sub-volumes within the RV is taken as 200 μm while the geometrical properties of the RV are considered as, $r_i =$ 0.2 m, $r_o = 1$ m, $h_a = 200$ μm, $(h_c - h_a) =$ 20 μm, $w_f = h_a \times 0.8$, $\theta_f = 2\sin^{-1}\left(w_f / 2r_i\right)$, $\theta_c = h_a / r_i$. The variation of FVF over the sub-volumes across the radial span of RV is illustrated by the curve (1) in Fig. 2.7 where the FVF of a typical sub-volume is plotted against the radial coordinate of its middle point. For the same sub-volumes, their effective properties are evaluated using the FE procedure (section 2.3.2), and the corresponding magnitudes of the effective coefficients ($\bar{C}_{11}$, $\bar{e}_{31}$ and $\bar{e}_{32}$) are illustrated by the curve (1) in Figs. 2.8(a)-(c). Similar to the FVF, the magnitudes of the effective coefficients of a typical sub-volume are plotted against the radial coordinate of its (sub-volume) middle point. It may be observed from curve (1) in Fig. 2.7 that the FVF appears with its maximum value at the innermost sub-volume, but it (FVF) decreases significantly with the increasing radius. The effective coefficients ($\bar{C}_{11}$, $\bar{e}_{31}$, $\bar{e}_{32}$ by curve (1) in Figs. 2.8(a)-(c)) vary following the nature of variation of the FVF (curve (1) in Fig. 2.7). It may be observed from Figs. 2.8(b)-(c) that the magnitude of the coefficient $\bar{e}_{31}$ is significantly higher than that of the coefficient $\bar{e}_{32}$ at any radius. So, for the thin annular PFC actuator, it provides the primary or directional actuation along the radial direction, and this actuation is

quantified by the coefficient $\bar{e}_{31}$. It is important to observe from curve (1) in Fig. 2.8(b) that the magnitude of the effective piezoelectric coefficient ($\bar{e}_{31}$) decreases significantly with the increasing radius. As

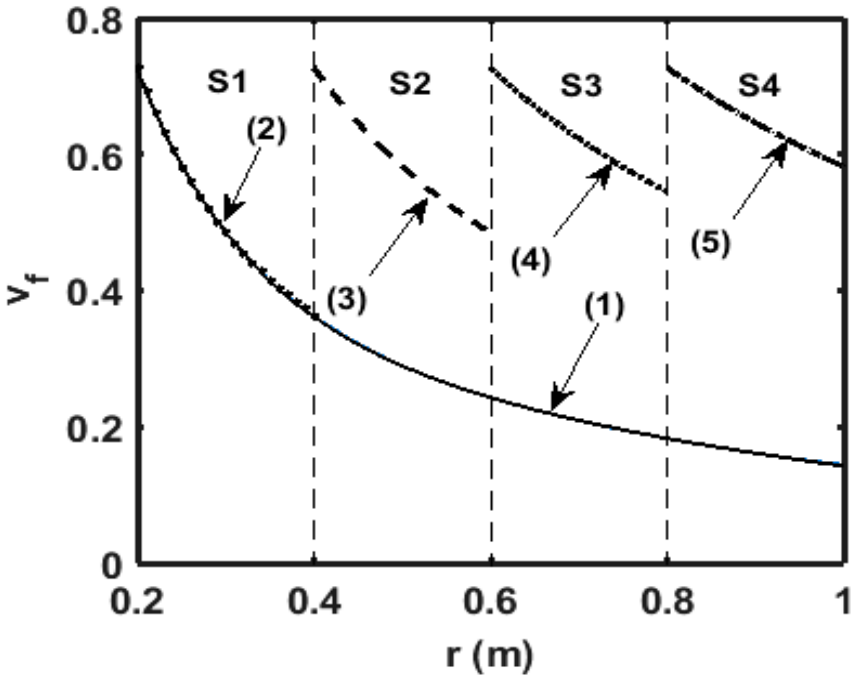

Fig. 2.7 Variations of FVF for (1) one RV within the overall radial span (r_i = 0.2 m, r_o = 1 m) of the annular PFC actuator and (2)-(5) four RVs corresponding to four equal radial divisions (S1, S2, S3, S4) of the same radial span.

this fact causes low actuation capability of the annular PFC actuator especially for its large radial span, presently the radial span (r_i = 0.2 m, r_o = 1 m) of RV is divided into four equal divisions having the radial length of 0.2 m, and the RV is redesigned for every radial division. These radial divisions are denoted by S1, S2, S3 and S4 following the outward radial direction. The RVs corresponding to these radial divisions are denoted by, RV^{S1}, RV^{S2}, RV^{S3} and RV^{S4}. Every RV is considered to have a maximum FVF of 0.72 at its inner radius, and the variation of the FVF over the sub-volumes in every radial division is shown by curves (2)--(5) in Fig. 2.7. Correspondingly, the variations of the effective coefficients ($\bar{C}_{11}$, $\bar{e}_{31}$, $\bar{e}_{32}$) for every RV (RV^{S1}, RV^{S2}, RV^{S3}, RV^{S4}) are illustrated by curves (2)-(5) in Figs. 2.8(a)-(c). It may be observed from the curves (2)-(5) in Fig. 2.7 that the FVF increases significantly in the last three radial divisions (S2, S3 and S4) for this redesign. Accordingly, the magnitude of the effective piezoelectric coefficient

($\bar{e}_{31}$) increases significantly for each of the RVs (RV^{S2}, RV^{S3}, RV^{S4}) within the last

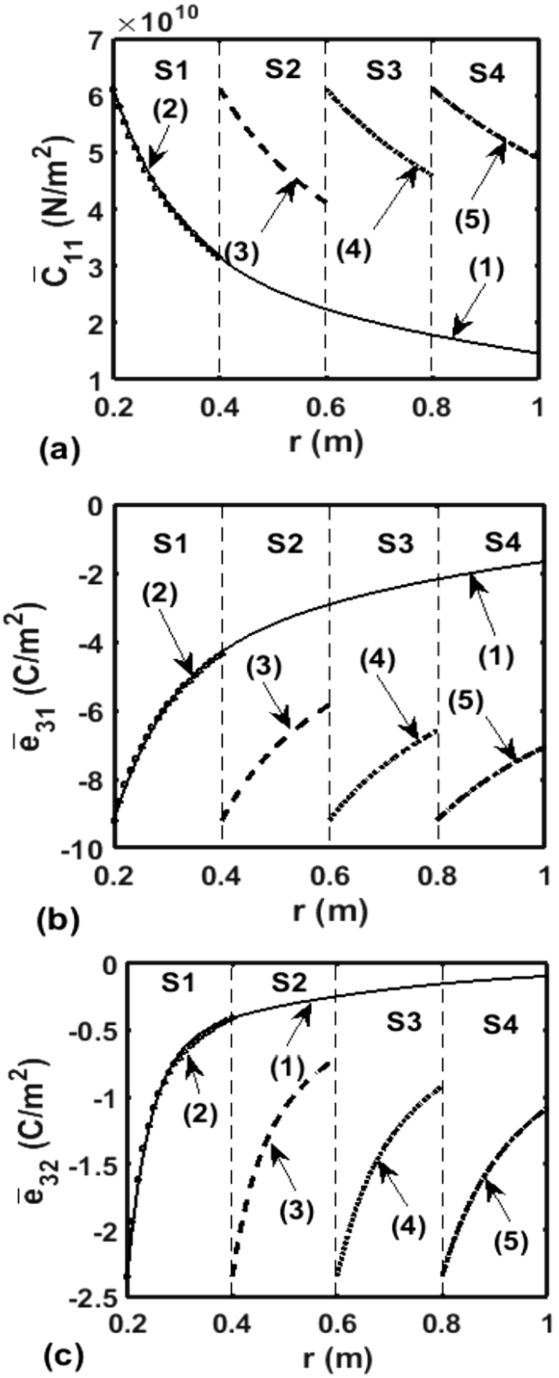

Fig. 2.8 Variations of (a) $\bar{C}_{11}$, (b) $\bar{e}_{31}$ and (c) $\bar{e}_{32}$ for (1) one RV within the overall radial span (r_i = 0.2 m, r_o = 1 m) of the annular PFC actuator and (2)-(5) four RVs corresponding to four equal radial divisions of the same radial span.

three radial divisions (S2, S3 and S4) (Fig. 2.8(b), curves (2)-(5)). So, the magnitude of the effective coefficient ($\bar{e}_{31}$) of the annular PFC actuator can be improved by designing it in small radial spans instead of single large radial span. Consequently, the control capability of the annular PFC actuator is expected to improve as it is investigated in the next section. For the mathematical modelling of the annular PFC actuator, its radially varying effective coefficients are expressed in a functional form as, $Y = (ae^{br} + ce^{dr})$ (a, b, c and d are the constants). The constants (a, b, c and d) for each of the effective coefficients are given in Tables 2.3 and 2.4. In these tables, an effective coefficient for RV^{S1}/ RV^{S2}/RV^{S3}/RV^{S4} is denoted by the superscript 1/2/3/4 while the superscript 0 indicates an effective coefficient for one RV within the whole radial span. The varying density of each of the RVs is also estimated by computing the density of every sub-volume using the rule of mixture. The constants (a, b, c and d) for the radially varying density of each of the RVs are presented in Table 2.5.

2.5.3 Actuation capability of the present annular PFC actuator

The control capability of the present annular PFC actuator is assessed by evaluating the controlled responses of the smart annular plate (Fig. 2.6) under a harmonic load of varying frequency. The geometrical properties of the smart annular plate (Fig. 2.6) are considered as, r_i = 0.2 m, $r_o = 1$ m, $h = 4$ mm, n_r = 4, $n_\theta = 8$, $\Delta r = 5$ mm, $\Delta\theta = 45^0$, $(\Delta r - \Delta r_p) = 5$ mm, $(\Delta\theta - \Delta\theta_p) = 5^0$. The thicknesses of the active layer (2-2 PFC) and the epoxy layer within the annular PFC actuator are 200 μm and 20 μm, respectively. The laminate of the annular PFC actuator is considered to be made of two active layers. So, the total thickness (h_p) of the actuator is 440 μm. As mentioned in the previous section, the annular PFC actuator is presently designed in its two geometric configurations, and the corresponding PFC actuators are denoted by PFC1 and PFC2. In the first one (PFC1), the annular PFC actuator possesses the same radial span as that is for the host annular plate. The uniform actuator patches over the top surface of the host plate are made from this annular PFC disc (PFC1). For the second geometric configuration of the PFC actuator (PFC2), the overall radial span of

Table 2.3 Effective elastic coefficients ($\bar{C}_{ij}^{l} = ae^{br} + ce^{dr}$, in GPa) of the annular PFC actuator (the unit of r is m).

$\bar{C}_{ij}^{l}$	a (×1e9)	b	c (×1e9)	d	$\bar{C}_{ij}^{l}$	a (×1e9)	b	c (×1e9)	d
$\bar{C}_{11}^{0}$	157	-8.358	37.87	-0.9554	$\bar{C}_{12}^{0}$	147.6	17.55	4.082	-0.3694
$\bar{C}_{13}^{0}$	42.98	-9.227	8.789	-0.6566	$\bar{C}_{22}^{0}$	37.19	-18.43	7.074	-0.4836
$\bar{C}_{23}^{0}$	73.02	-16.16	3.572	-0.2603	$\bar{C}_{33}^{0}$	59.94	-8.384	14.48	-0.665
$\bar{C}_{44}^{0}$	29.35	-15.85	1.108	-0.4218	$\bar{C}_{55}^{0}$	8.089	-5.671	2.807	-0.5746
$\bar{C}_{66}^{0}$	80.89	-19.27	1.207	-0.5123	$\bar{C}_{11}^{1}$	268.4	-14.04	66	-1.917
$\bar{C}_{12}^{1}$	807	-27.46	6.572	-1.437	$\bar{C}_{13}^{1}$	92.88	-15.75	14.55	-1.58
$\bar{C}_{22}^{1}$	2170	-28.64	12.56	-1.785	$\bar{C}_{23}^{1}$	347	-25.41	5.142	-1.062
$\bar{C}_{33}^{1}$	931.4	-12.94	22.64	-1.434	$\bar{C}_{44}^{1}$	127.3	-24.7	1.84	-1.528
$\bar{C}_{55}^{1}$	9.475	-4.123	0.7221	-1.362	$\bar{C}_{66}^{1}$	493.2	-29.64	2.204	-1.89
$\bar{C}_{11}^{2}$	433.6	-9.332	83.99	-1.256	$\bar{C}_{12}^{2}$	3726	-18.22	9.532	-1.28
$\bar{C}_{13}^{2}$	206.2	-11.05	19.23	-1.156	$\bar{C}_{22}^{2}$	11030	-19.05	19.53	-1.563
$\bar{C}_{23}^{2}$	1311	-16.69	6.831	-0.9545	$\bar{C}_{33}^{2}$	134.7	-8.433	29.22	-1.026
$\bar{C}_{44}^{2}$	401.7	-15.88	2.622	-1.285	$\bar{C}_{55}^{2}$	9.395	-1.529	0.000072	-11.72
$\bar{C}_{66}^{2}$	2707	-19.73	3.53	-1.666	$\bar{C}_{11}^{3}$	649.5	-7.391	94.76	-0.9532
$\bar{C}_{12}^{3}$	9362	-13.96	11.82	-1.1	$\bar{C}_{13}^{3}$	465.7	-9.344	22.59	-0.9361
$\bar{C}_{22}^{3}$	29090	-14.59	25.11	-1.332	$\bar{C}_{23}^{3}$	2941	-12.76	8.069	-0.8243
$\bar{C}_{33}^{3}$	230.7	-7.264	35.35	-0.8639	$\bar{C}_{44}^{3}$	801.7	-12.02	3.209	-1.081
$\bar{C}_{55}^{3}$	9.218	-0.986	0	0	$\bar{C}_{66}^{3}$	7486	-15.12	4.632	-1.426
$\bar{C}_{11}^{4}$	1014	-6.436	103.6	-0.7842	$\bar{C}_{12}^{4}$	17740	-11.42	13.65	-0.956
$\bar{C}_{13}^{4}$	1875	-9.309	26.18	-0.8278	$\bar{C}_{22}^{4}$	56940	-11.93	29.68	-1.152
$\bar{C}_{23}^{4}$	5148	-10.42	9.015	-0.7177	$\bar{C}_{33}^{4}$	1245	-8.496	43.3	-0.812
$\bar{C}_{44}^{4}$	1367	-9.846	3.71	-0.939	$\bar{C}_{55}^{4}$	9.272	-0.7462	0	0
$\bar{C}_{66}^{4}$	15260	-12.38	5.561	-1.238	-	-	-	-	-

Table 2.4 Effective piezoelectric coefficients ($\bar{e}_{ij}^{l} = ae^{br} + ce^{dr}$, in C/m²) of the annular PFC actuator (the unit of r is m).

$\bar{e}_{ij}^{l}$	a	b	c	d	$\bar{e}_{ij}^{l}$	a	b	c	d
$\bar{e}_{31}^{0}$	-30.77	-9.797	-6.245	-1.326	$\bar{e}_{32}^{0}$	-181.4	-23.37	-1.027	-2.364
$\bar{e}_{33}^{0}$	19.8	-7.453	5.299	-1.117	$\bar{e}_{31}^{1}$	-101	-19.33	-11.66	-2.5
$\bar{e}_{32}^{1}$	-992.6	-33.2	-2.659	-4.669	$\bar{e}_{33}^{1}$	21.2	-6.593	3.187	-0.2475
$\bar{e}_{31}^{2}$	-322.3	-13.7	-14.71	-1.57	$\bar{e}_{32}^{2}$	-6137	-21.83	-5.258	-3.388
$\bar{e}_{33}^{2}$	21.23	-2.27	0.01429	5.745	$\bar{e}_{31}^{3}$	-613.4	-10.56	-16.08	-1.142
$\bar{e}_{32}^{3}$	-17580	-16.59	-7.544	-2.679	$\bar{e}_{33}^{3}$	21.23	-2.27	0.01429	5.745
$\bar{e}_{31}^{4}$	-620.9	-7.937	-16.1	-0.8573	$\bar{e}_{32}^{4}$	-36210	-13.5	-9.53	-2.226
$\bar{e}_{33}^{4}$	19.99	-1.04	0	0	-	-	-	-	-

Table 2.5 Effective density ($\bar{\rho}_{c}^{l} = ae^{br} + ce^{dr}$, in kg/m³) of the annular PFC actuator (the unit of r is m).

$\bar{\rho}_{c}^{l}$	a	b	c	d	$\bar{\rho}_{c}^{l}$	a	b	c	d
$\bar{\rho}_{c}^{0}$	10980	-7.42	3654	-0.5412	$\bar{\rho}_{c}^{1}$	11610	-8.579	4262	0.758
$\bar{\rho}_{c}^{2}$	12170	-1.963	29.27	4.839	$\bar{\rho}_{c}^{3}$	9.4e-6	19.27	11290	-1.123
$\bar{\rho}_{c}^{4}$	2.77e-14	34.22	11280	-0.8411	-	-	-	-	-

the host annular plate is divided into four equal radial divisions, and the annular PFC actuator is designed for each of the radial segments as presented in the previous section. In every radial segment, the corresponding annular PFC disc is divided according to the geometrical properties of the uniform actuator patches within that radial segment.

The substrate plate is considered to be made of Aluminum ($E = 70$ GPa, $\nu = 0.3$, $\rho = 2700$ kg/m³; E, ν and ρ are Young's modulus, Poisson's ratio and mass density, respectively). The inner and outer edges of the overall annular plate are considered as the simply-supported edges ($w_o = 0, v_o = 0, \phi_\theta = 0$). The patches are considered to be activated with a uniform value of the control-gains ($k_d^q = k_d$, $q = 1,2,3,....,n_p$) while the overall plate is considered to operate under a transversely distributed harmonic mechanical load as,

$$p(r,\theta,t) = p_o(1+\cos\theta+\cos 2\theta+\cos 3\theta)e^{j\omega t} \tag{2.46}$$

where, p_0 is the load-amplitude; ω is the operating frequency and $j=\sqrt{-1}$.

In order to verify the present FE formulation for the smart annular plate, the natural frequencies of the host annular plate are first computed for two different boundary conditions. These results are presented in Table 2.6 together with the similar results available in [388]. It may be observed from Table 2.6 that the present FE results are in good agreement with the similar analytical results in [388]. This comparison verifies the present FE formulation of an annular plate.

Table 2.6 Verification of the present FE formulation for an annular plate (BC: boundary condition, CC: fully clamped boundary, SS: simply-supported boundary, $\lambda_i=\omega_i r_o^2\sqrt{\rho h/D}$, $D=Eh^3/12\left(1-\nu^2\right)$, $h_p\approx 0$, $k_d=0$, ω_i (i=1,2,3,.....) are the natural frequencies).

BC	Source	λ_1	λ_2	Total no. of elements	λ_1	λ_2	Total no. of elements
		$r_i/r_o=0.2$		(Mesh size)	$r_i/r_o=0.4$		(Mesh size)
CC	Present	34.61	36.11	(24X20=480)	61.86	62.99	(24X24=576)
	Ref. [388]	35.12	37.82	-	61.88	63.04	-
SS	Present	16.77	19.22	(24X12=288)	28.12	30.10	(24X20=488)
	Ref. [388]	16.86	20.47	-	28.08	30.09	-

For verification of the FE formulation in handling the piezoelectric actuators, the radial and circumferential gaps among the piezoelectric patches (Fig. 2.6) are removed to obtain a piezoelectric layer over the top surface of a circular host plate. The material and geometrical properties of this smart circular plate are taken from [389] and the transverse deflections of the smart circular plate are computed for two different values of the applied electric field across the thickness of the piezoelectric layer. The corresponding results are illustrated in Fig. 2.9 together with the similar results available in [389]. It may be observed from Fig. 2.9 that the present FE results are in good agreement with similar analytical results in [389]. Thus, the present FE formulation is verified for handling the electro-elastic coupling in the piezoelectric actuators.

The frequency responses of the smart annular plate are evaluated within a range of the operating frequency. Within this range of the operating frequency, all natural modes of the plate are of fundamental radial mode number $(m=1)$ while they (modes) are separated by the circumferential node number (n) as, 0,

1, 2 and 3. For the material of the PFC patches as PFC2, Fig. 2.10(a) illustrates variations of the maximum transverse displacement-amplitude ($W_{\max} = \left(w_{\mathrm{p}}\right)_{\max} / h$) with the operating frequency for two different values of the control-gain (k_d). The corresponding variations of the maximum control voltage ($V_{\max}$) are also illustrated in Fig. 2.10(b). The maximum voltage ($V_{\max}$) at an operating frequency is taken as the maximum one among all the voltage-amplitudes at the locations of the velocity sensors over the actuator patches.

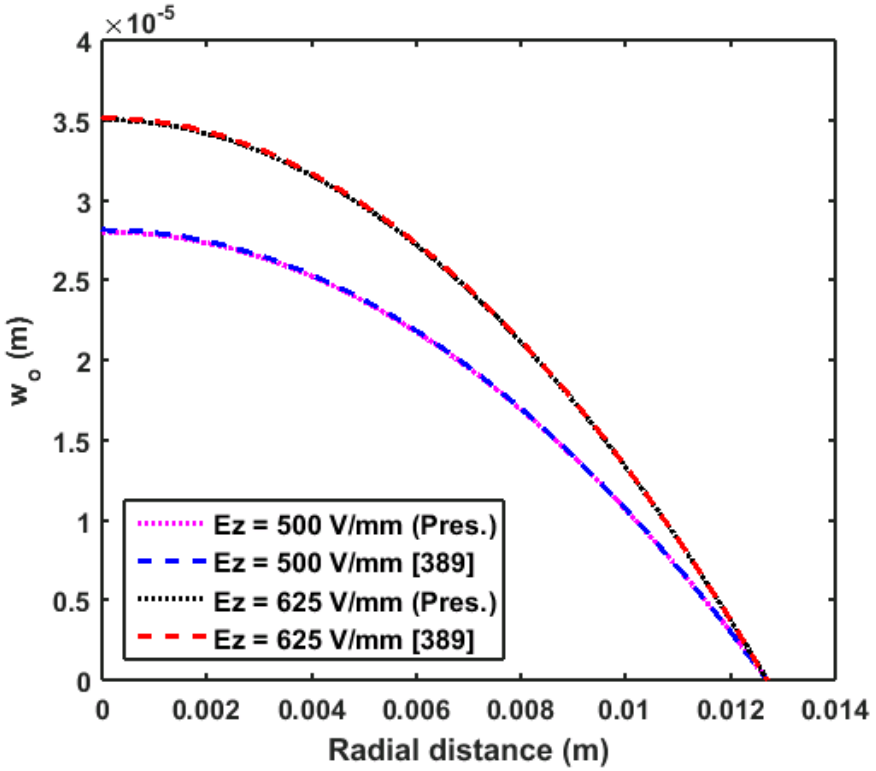

Fig. 2.9 Verification of the present FE formulation in handling the electro-elastic coupling within the piezoelectric actuator (Pres.: Present FE results).

It may be observed from Fig. 2.10 that the resonant transverse displacement-amplitudes are significantly attenuated by the present annular PFC actuator patches at the expense of reasonable control voltage. It may also be observed that all the resonant displacement-amplitudes are almost equally attenuated for an increase of the control-gain, and it infers the appropriateness of the present arrangement of the annular PFC actuator patches for control of all the modes of vibration of the smart annular plate using a single arrangement of the actuator patches.

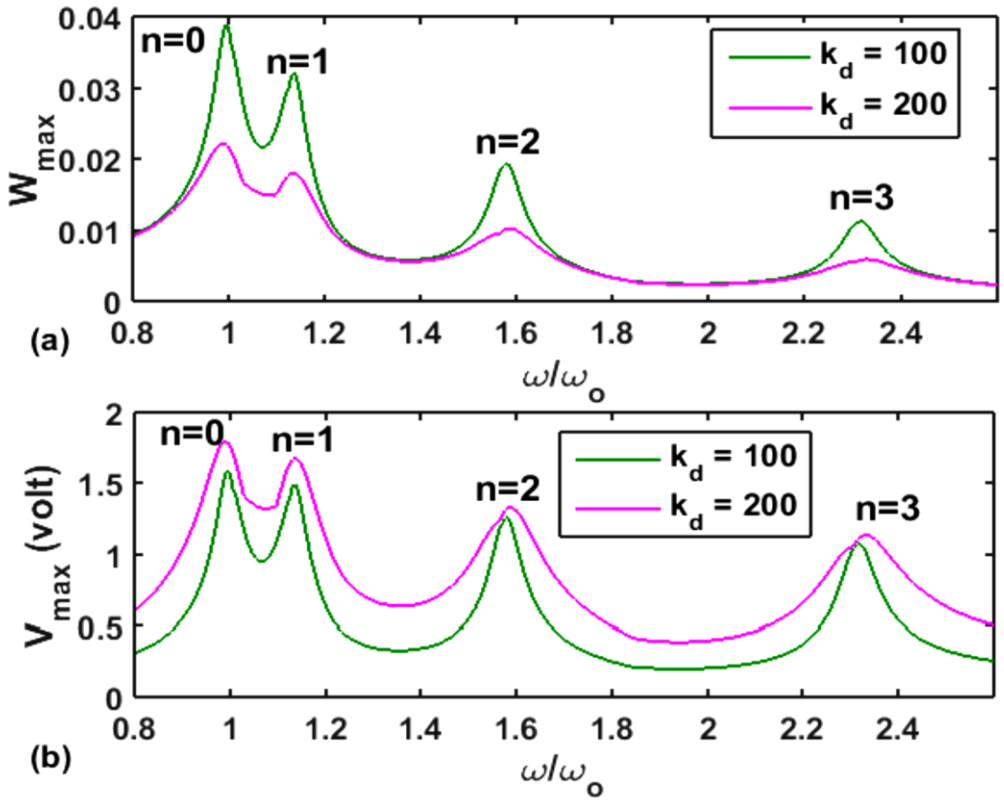

Fig. 2.10 (a) Variations of the maximum transverse displacement-amplitude ($W_{\max}$) of the smart annular plate with the operating frequency, (b) the corresponding variations of the maximum control-voltage ($V_{\max}$) (material for the patches: PFC2, $m=1$, $p_o=$ 1 N/m², ω_o is the fundamental natural frequency).

Figure 2.11(a) illustrates the variations of the maximum transverse displacement-amplitude ($W_{\max}$) of the smart annular plate with the operating frequency when the actuator patches are either made of PFC1 or made of PFC2. Figure 2.11(a) also illustrates a similar response of the smart annular plate when the actuator patches are made of a monolithic piezoelectric material (PZT5H) that is also used for the fibers of the annular PFC actuator. The corresponding variations of the maximum control-voltage ($V_{\max}$) are illustrated in Fig. 2.11(b). The results for PFC1 and PFC2 in Fig. 2.11 indicate that the actuation capability of the annular PFC actuator significantly improves with a decrease of the required control-voltage when it (PFC actuator) is designed with a small radial length by means of dividing the overall radial span of application into four equal divisions. It may also be observed from Fig. 2.11 that this

improved actuation capability of the present annular PFC actuator (PFC2) is close to that of the monolithic piezoelectric (PZT5H) actuator.

Although this observation shows almost equal control capability of PFC2 and monolithic PZT5H, the PFC2 or present PFC actuator may be preferred in structural applications due to the advantage of greater flexibility. In addition to the advantage of greater flexibility, the present annular PFC actuator is capable of providing in-plane directional actuation along the radial direction since an significant difference between the magnitudes of the effective coefficients $\bar{e}_{31}$ and $\bar{e}_{32}$ appears (Figs. 2.8(b)-(c)). Because of these advantages along with an significant actuation capability, the present annular PFC actuator may be utilized instead of the conventional monolithic piezoelectric actuators especially for active control of plane structures of revolution.

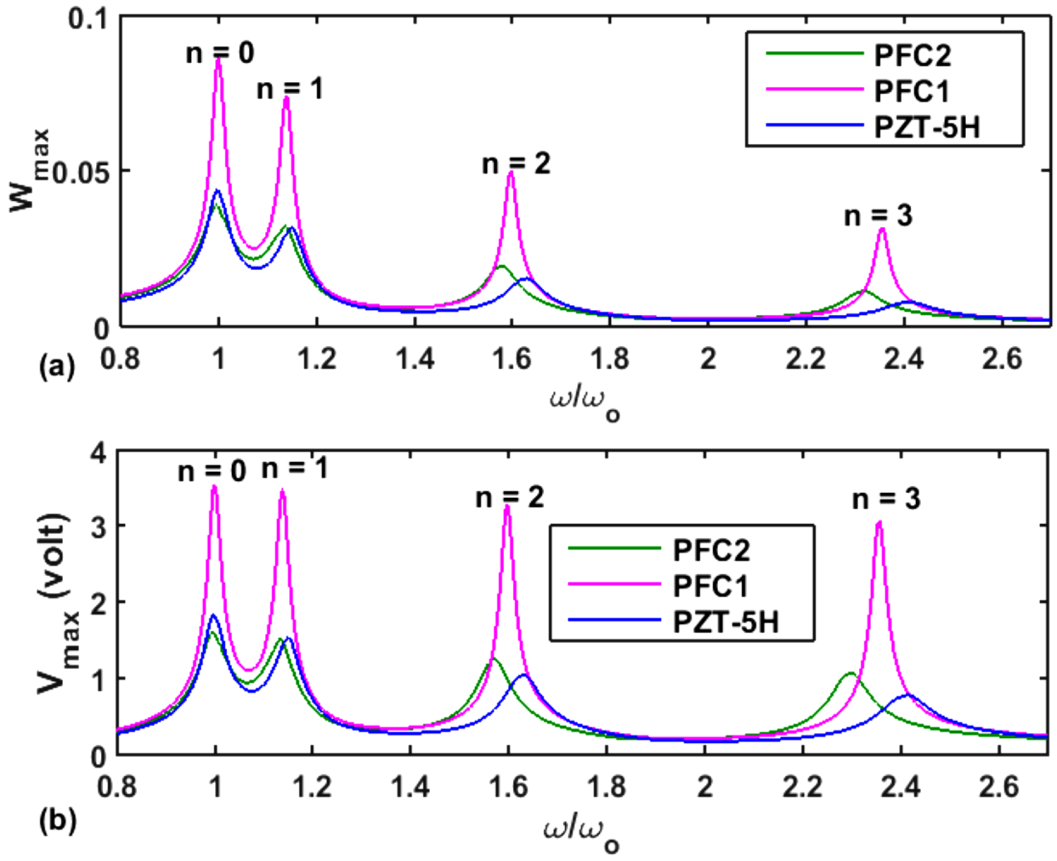

Fig. 2.11 (a) Variations of the maximum transverse displacement-amplitude ($W_{\max}$) of the smart annular plate with frequency, (b) the corresponding variations of the maximum control-voltage ($V_{\max}$) for the material of the patches as PFC1/PFC2/PZT5H ($k_d = 100$, $p_o = 1$ N/m²).

2.6 Summary

In this chapter, an extension mode annular PFC actuator with cylindrically periodic microstructure is designed for achieving primary/directional actuation along the radial direction in the cylindrical principal material coordinate system. This annular PFC actuator is a laminate of 2-2 PFC layers in the shape of a thin annular disc. The piezoelectric fibers in every annular 2-2 PFC disc are oriented along the radial direction while the fibers are periodically distributed along the circumferential direction. The cross-sectional area of the fibers remains constant throughout their length, and thus the effective electro-elastic properties of the laminated annular PFC disc vary along the radial direction. These radially varying electro-elastic properties are estimated by defining a representative volume (RV) that is assumed to be comprised of a large number of small sub-volumes of different FVFs. These sub-volumes are created in micro-scale through the equal divisions of the radial span of the RV. The micro-volumes/sub-volumes are assumed as macroscopically homogeneous volumes, and the electro-elastic properties at any radial location of the RV are identified as the effective properties of the micro-volume/sub-volume at that radial location. The closed-form expressions of the effective electro-elastic coefficients of the homogeneous sub-volumes/micro-volumes are derived, and these expressions for the effective coefficients are verified through the numerical homogenization of the sub-volumes using FE procedure.

The results for the radially varying effective electro-elastic properties of the present annular PFC actuator reveal an significant difference between the magnitudes of the effective piezoelectric coefficients ($\bar{e}_{31}$ and $\bar{e}_{32}, \bar{e}_{31} > \bar{e}_{32}$) that provide the actuation forces along the in-plane axes of the cylindrical principal material coordinate system. So, the annular PFC is capable of providing primary/directional actuation along the radial direction through the coefficient $\bar{e}_{31}$. This coefficient ($\bar{e}_{31}$) appears with an significant magnitude at the inner radius of the annular PFC disc, but this magnitude decreases significantly with the increasing radius. Since this characteristic of the coefficient ($\bar{e}_{31}$) may not provide a good actuation capability of the annular PFC actuator, it (PFC) is redesigned in small radial segments within a radial span of application. The corresponding results reveal significant improvement of the magnitude of the coefficient ($\bar{e}_{31}$) at any radius within the radial span of application. With these

improved electro-elastic properties of the annular PFC actuator, its actuation capability is investigated through the active control of vibration of a host annular plate under a transverse harmonic excitation. The corresponding results reveal a good actuation capability of the present annular PFC actuator. It is observed that the actuation capability of the present annular PFC actuator is close to that of the monolithic piezoelectric actuator. Although this equality in their actuation capability appears, the present annular PFC actuator may be preferred in active control of plane structures of revolution due to its advantages of greater flexibility and capability of directional actuation along the radial direction.

Chapter 3

Shear actuation mechanism and shear-based actuation capability of an obliquely reinforced PFC in active control of annular plates

3.1 Introduction

The literature survey in Chapter 1 shows a great deal of research on the development of extension mode PFC actuators. The study in the previous chapter (Chapter 2) is also in the same line where a new extension mode annular PFC actuator with the cylindrically periodic microstructure is designed for directional actuation of annular/circular plates. However, besides the extension mode PFC actuators, the research on the development of shear-mode PFC actuators is not yet matured as only one kind of PFC actuator by the name of SAFC [73] is found in the literature (till to date), and it infers the need of further research for the development of shear-mode PFC actuators. The study presented in this chapter is in this direction where an obliquely-reinforced PFC is addressed as a potential material of shear piezoelectric actuator, and it is obtained through the earlier concept of vertically reinforced 1-3 PFC [13].

The vertically reinforced 1-3 PFC [13], as shown in Fig. 3.1(a), is commonly known as a material of thickness mode piezoelectric actuator, where the extension mode piezoelectric actuation appears in the thickness/transverse direction for an externally applied transverse electric field. If the vertically oriented fibers in this 1-3 PFC are considered to be obliquely oriented at an angle (ϕ) with the thickness coordinate as shown in Fig. 3.1(b), then the transverse shear actuation force arises along with the thickness mode actuation force. This shear actuation force may be utilized for active control of deformation/vibration of flexible structures although a corresponding study on the shear actuation capability of the obliquely reinforced 1-3 PFC (Fig. 3.1(b)) is not yet addressed in the literature to the best knowledge of the author. It is presently carried out for shear-based active control of an annular plate following the primary objective of this dissertation. It may also be noted here that a study on the utilization of shear mode piezoelectric actuators for active control of annular/circular plates is not yet addressed in the literature. However, it is attempted in this Chapter in particular to investigate the shear actuation

mechanism and the shear-based active control capability of the obliquely reinforced 1-3 PFC (Fig. 3.1(b)) in attenuation of flexural vibration of annular plates.

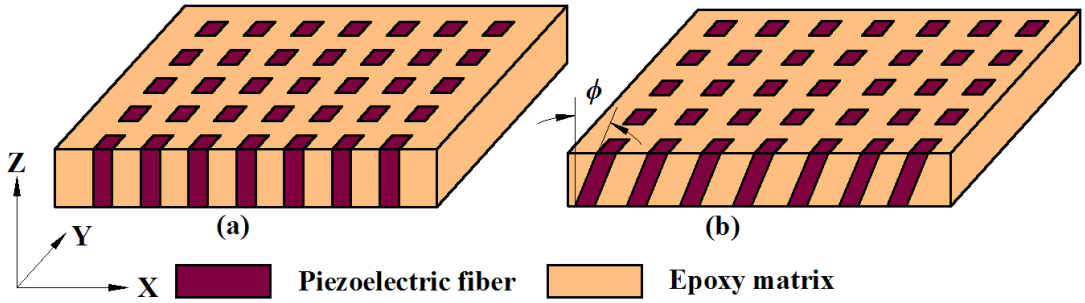

Fig. 3.1 Schematic diagrams of (a) vertically and (b) obliquely reinforced 1-3 PFC.

The obliquely-reinforced 1-3 PFC (Fig. 3.1(b)) is utilized here in the form of the patches that are embedded in a host annular plate through the construction of an annular sandwich plate. For effective utilization of the actuator patches in shear-mode control of vibration of the overall annular plate, a fruitful arrangement of the actuator patches at the core of the annular sandwich plate is presented, and also a shear-based control strategy is presented to activate the actuator patches according to the velocity feedback control law. The analysis of the overall smart annular sandwich plate is carried out by developing a closed-loop FE model based on the layer-wise deformation theory. Since the actuator patches are made with the Cartesian principal material coordinate system, their use in the cylindrical coordinate frame yields a little complex state of actuation force, and thus, first, an electro-elastic analysis of the smart annular sandwich plate is carried out in a special manner to identify the mechanism of shear actuation of the annular plate. Subsequently, the effectiveness of the patches of obliquely-reinforced 1-3 PFC in shear-mode active control of flexural vibration of the annular sandwich plate is investigated according to the present arrangement of the actuator patches and shear-based control strategy.

3.2 Present annular sandwich plate with shear actuators

For bending mode of deformation of annular plates, the mechanically induced transverse shear stress usually appears with its maximum magnitude around the middle plane of the plate. So, for shear mode actuation of the annular plate, it is presently taken in the form of an annular sandwich plate as shown in Fig. 3.2, where the actuator patches of the obliquely reinforced 1-3 PFC (Fig. 3.1(b))

are located at the core of foam. The inner and outer radii of the overall annular plate are denoted by r_i and r_o, respectively. The thicknesses of the face layers, core and overall plate are denoted by h_f, h_c and h, respectively.

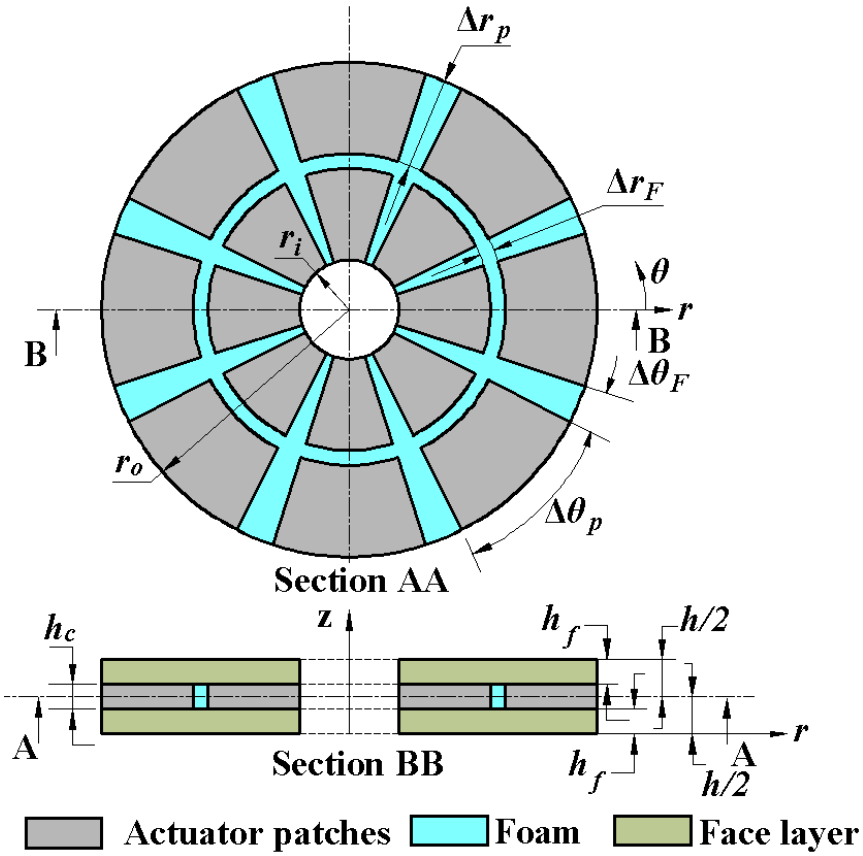

Fig. 3.2 Schematic diagram of the annular sandwich plate with the embedded shear actuator patches.

The radial and circumferential spans of the uniform patches in the shape of the annular sector are symbolized by Δr_p and $\Delta\theta_p$, respectively, while the corresponding gaps among the patches are denoted by Δr_F and $\Delta\theta_F$.

Since the obliquely reinforced 1-3 PFC (Fig. 3.1(b)) is made in the form of a rectangular block with the Cartesian principal material coordinate system (xyz), the patches in the shape of the annular sector (Fig. 3.2) can be cut out from a block of the 1-3 PFC as shown in Fig. 3.3, and the core layer of the sandwich plate (Fig. 3. 2) can be constructed using these patches. The top and bottom surfaces of every actuator patch are considered to be fully electrode surfaces, and the applied transverse electric field (E_z) through these electrodes results in

shear actuation force in the xz-plane of the Cartesian material coordinate system (xyz) of every patch. This shear actuation force is utilized mainly to counteract the mechanically induced transverse shear stress (τ_{rz}) in the plane of the radial (r) and transverse (z) coordinates of the annular plate according to the construction of the annular sandwich plate (Figs. 3.2 and 3.3) and the applied voltage. Now, the mechanically induced transverse shear stress (τ_{rz}) changes its sign over the in-plane coordinates of the plate as it is demonstrated in Figs. 3.4(a) and 3.4(c) for any two bending modes (Figs. 3.4(b) and 3.4(d)) of the annular plate. In accordance to this variation of sign of the mechanical stress (τ_{rz}), the sign of the applied transverse electric field (E_z) is to be varied over the plane of the annular plate for effective shear actuation, and it is presently achieved by taking the actuator in the form of the patches (Fig. 3.2) where the sign of the applied electric field for an actuator patch can be assigned as per its (patch) local requirement. But, the corresponding geometrical dimensions i.e., number (n_r) of patches along the radial direction, number (n_θ) of patches along the circumferential direction, radial gap (Δr_F) and circumferential gap $(\Delta\theta_F)$ are important factors for effective shear actuation of the annular sandwich plate.

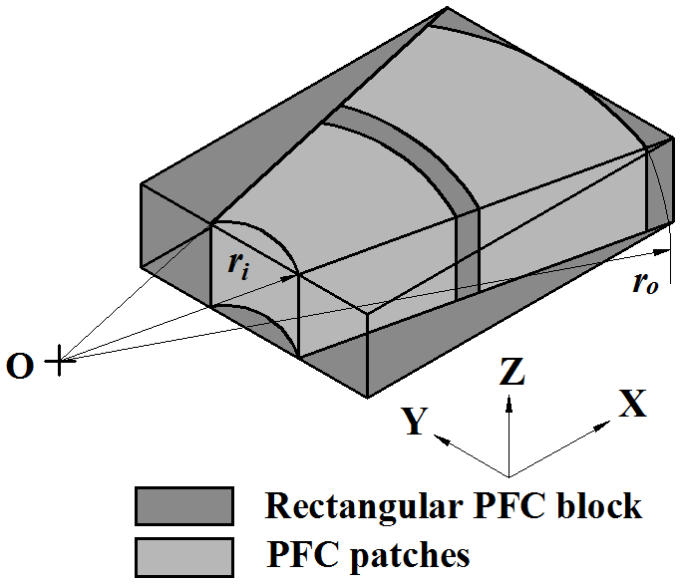

Fig. 3.3 A block of the obliquely reinforced 1-3 PFC (Figure 1(b)) used for making actuator patches in the shape of the annular sector within the core of the annular sandwich plate.

Presently, the gaps (Δr_F , $\Delta\theta_F$) are taken with their small values as an increase of these gaps results in lesser shear actuation of the annular plate. The number (n_r) of patches along the radial direction is taken as 2 (Fig. 3.2), where one of the radial edges of every patch is considered to be coincident with the inner/outer edge of the overall annular plate in particular to supply the external transverse electric field to the actuator patches through the edges of the overall sandwich plate. The number (n_θ) of patches along the circumferential direction mainly depends on the circumferential mode number (n) of bending mode-shape of vibration of the annular plate since the circumferential locations of alteration of sign of the stress (τ_{rz}) change with this mode number (n) (Fig. 3.4). So, the value of n_θ is presently taken on the basis of the bending modes of vibration of interest as it is illustrated in the later section.

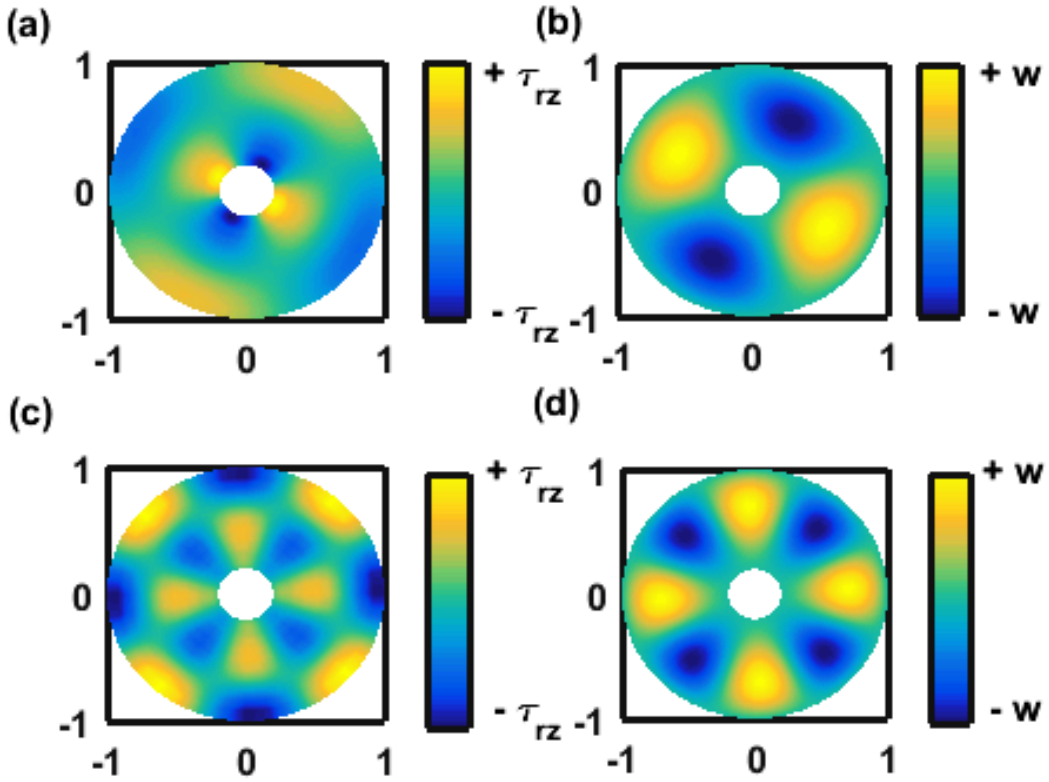

Fig. 3.4 Two bending mode shapes and the corresponding distributions of transverse shear stress (τ_{rz}) at the middle plane of a simply-supported isotropic annular plate; (a), (b) mode: $m=1$, $n=2$; (c), (d) mode: $m=1$, $n=4$ (m and n are the radial and circumferential mode numbers, respectively, W is the transverse deflection of the plate).

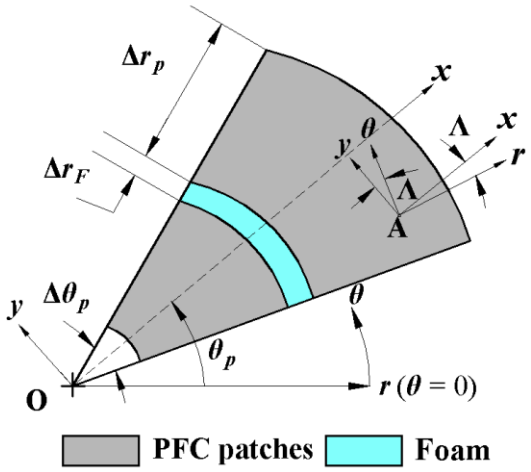

Fig. 3.5 Schematic diagram of a typical row of actuator patches in the $r\theta$-plane of the annular plate.

3.3 Properties of constituent materials in the annular sandwich plate

The fibers in the obliquely reinforced 1-3 PFC are aligned in the xz-plane in the Cartesian material coordinate system (xyz) while they (fibers) are oriented at an angle of ϕ with the vertical (z) axis. So, the properties of this obliquely reinforced 1-3 PFC can be obtained through the transformation of the properties of the vertically reinforced 1-3 PFC (Fig. 3.1(a)), with respect to the reference coordinate system (xyz). Again, this PFC is utilized as a material of actuator by applying an external transverse electric field (E_z) across its top and bottom fully electrode surfaces. So, the constitutive relations for this obliquely reinforced 1-3 PFC actuator with a dominant electric field (E_z)/displacement (D_z) can be written as,

$$\boldsymbol{\sigma} = (\boldsymbol{C}\boldsymbol{\varepsilon} - \boldsymbol{e}_z E_z),$$

$$D_z = (\boldsymbol{e}_z{}^{\mathrm{T}}\boldsymbol{\varepsilon} + \in_{33} E_z),$$

$$\boldsymbol{C} = \begin{bmatrix} C_{11} & C_{12} & C_{13} & 0 & C_{15} & 0 \\ C_{12} & C_{22} & C_{23} & 0 & C_{25} & 0 \\ C_{13} & C_{23} & C_{33} & 0 & C_{35} & 0 \\ 0 & 0 & 0 & C_{44} & 0 & 0 \\ C_{15} & C_{25} & C_{35} & 0 & C_{55} & 0 \\ 0 & 0 & 0 & 0 & 0 & C_{66} \end{bmatrix},$$

$$\boldsymbol{e}_z = \{e_{31} \quad e_{32} \quad e_{33} \quad 0 \quad e_{35} \quad 0\}^{\mathrm{T}} \tag{3.1}$$

where, $\boldsymbol{\sigma}$ and $\boldsymbol{\varepsilon}$ are the stress and strain vectors, respectively; E_z and D_z are the electric field and electric displacement along the thickness (z) direction, respectively; C_{ij}, e_{ij} and $\in_{ij}$ are the stiffness, piezoelectric and dielectric coefficients, respectively.

For a typical row of actuator patches within the core along the radial direction, the Cartesian material coordinate system (xyz) of PFC patches and the reference cylindrical coordinate system ($r\theta z$) for the overall annular plate are shown in Fig. 3.5. It may be noted from Fig. 3.5 that for any point (say, A) with the in-plane cylindrical coordinates of (r,θ), the angle between x and r axes or between y and θ axes can be obtained as, $\Lambda = (\theta_p - \theta)$, where θ_p is the circumferential coordinate of the middle points of the patches (Fig. 3.5). So, the material properties at any point (r,θ) of a PFC patch can be obtained in the cylindrical coordinate system ($r\theta z$) through a transformation of the properties (Eq. (3.1)) of PFC for a rotation of x/y axis with respect to the z-axis at an angle of $\Lambda = (\theta_p - \theta)$ as,

$$\boldsymbol{\sigma}^k = (\boldsymbol{C}^k \boldsymbol{\varepsilon}^k - \boldsymbol{e}_z^k E_z),$$

$$D_z^k = (\langle \boldsymbol{e}_z^k \rangle^{\mathrm{T}} \boldsymbol{\varepsilon}^k + \in_{33}^k E_z), k = 2$$

$$\boldsymbol{e}_z^k = \{e_{31}^k \quad e_{32}^k \quad e_{33}^k \quad e_{34}^k \quad e_{35}^k \quad e_{36}^k\}^{\mathrm{T}},$$

$$\boldsymbol{C}^k = \boldsymbol{T}\boldsymbol{C}\boldsymbol{T}^{\mathrm{T}},$$

$$\boldsymbol{e}_z^k = \boldsymbol{T}\boldsymbol{e}_z,$$

$$\in_{33}^k = \in_{33} \tag{3.2}$$

where, $\boldsymbol{T}$ is the transformation matrix of size (6×6). Besides the constitutive relations (Eq. (3.2)) of the PFC patches in the reference cylindrical coordinate system, similar relations for the isotropic face layers ($k = 1$, 3) and the foam at the core ($k = 2$) can be written as,

$$\boldsymbol{\sigma}^k = \boldsymbol{C}^k \boldsymbol{\varepsilon}^k, \; k = 1,2,3$$

$$\boldsymbol{C}=\begin{bmatrix} C_s(1-v^k) & C_s v^k & C_s v^k & 0 & 0 & 0 \\ C_s v^k & C_s(1-v^k) & C_s v^k & 0 & 0 & 0 \\ C_s v^k & C_s v^k & C_s(1-v^k) & 0 & 0 & 0 \\ 0 & 0 & 0 & \dfrac{E^k}{2(1+v^k)} & 0 & 0 \\ 0 & 0 & 0 & 0 & \dfrac{E^k}{2(1+v^k)} & 0 \\ 0 & 0 & 0 & 0 & 0 & \dfrac{E^k}{2(1+v^k)} \end{bmatrix},$$

$$C_s = E^k / \left\langle (1+v^k)(1-2v^k) \right\rangle \tag{3.3}$$

In Eq. (3.3), E^k and v^k are Young's modulus and Poisson's ratio, respectively. In Eqs. (3.2) and (3.3), k represents the bottom face layer, core layer and top face layer of the sandwich plate according to its (k) value as 1, 2 and 3, respectively.

3.4 FE model of the annular sandwich plate

The bottom plane of the overall annular plate (Fig. 3.2) is taken as the reference plane and the origin of the reference cylindrical coordinate system ($r\theta z$) is located at the centre of the reference annular plane. With respect to this reference cylindrical coordinate system, the kinematics of deformation of the overall annular plate is defined according to the layer-wise deformation theory as [390],

$$u^k(r,\theta,z,t) = u_0^k(r,\theta,t) + \sum_{i=1}^{3} z_i^k(z)\phi_i^k(r,\theta,t),$$

$$v^k(r,\theta,z,t) = v_0^k(r,\theta,t) + \sum_{i=1}^{3} z_i^k(z)\beta_i^k(r,\theta,t),$$

$$w^k(r,\theta,z,t) = w_0^k(r,\theta,t) + \sum_{i=1}^{3} z_i^k(z)\psi_i^k(r,\theta,t),$$

$$z_1^k = (z - z_0^k),$$

$$z_2^k = (z - z_0^k)^2,$$

$$z_3^k = (z - z_0^k)^3 \tag{3.4}$$

where, $u^k / u_0^k, v^k / v_0^k$ and w^k / w_0^k are the translational displacements at any point on the reference plane of k^{th} layer along the r, θ and z directions,

respectively; z_0^k is the thickness co-ordinate of reference plane of the k^{th} layer and it (z_0^k) is taken as the thickness coordinate of its (k^{th} layer) bottom surface; ϕ_i^k, β_i^k and ψ_i^k are the i^{th} order derivatives of u^k, v^k and w^k, respectively with respect to the thickness coordinate (z) and these derivatives are taken at the reference thickness co-ordinate (z_0^k) of k^{th} layer. Introducing the displacement continuity conditions at the interlayer surfaces, Eq. (3.4) can be written for every layer ($k = 1,2,3$) as,

$$
\begin{aligned}
u^1 &= u_0 + \sum_{i=1}^{3} z_i^1 \phi_i^1 , \\
u^2 &= u^1\Big|_{z=z_0^2} + \sum_{i=1}^{3} z_i^2 \phi_i^2 , \\
u^3 &= u^2\Big|_{z=z_0^3} + \sum_{i=1}^{3} z_i^3 \phi_i^3 , \\
v^1 &= v_0 + \sum_{i=1}^{3} z_i^1 \beta_i^1 , \\
v^2 &= v^1\Big|_{z=z_0^2} + \sum_{i=1}^{3} z_i^2 \beta_i^2 , \\
v^3 &= v^2\Big|_{z=z_0^3} + \sum_{i=1}^{3} z_i^3 \beta_i^3 , \\
w^1 &= w_0 + \sum_{i=1}^{3} z_i^1 \psi_i^1 , \\
w^2 &= w^1\Big|_{z=z_0^2} + \sum_{i=1}^{3} z_i^2 \psi_i^2 , \\
w^3 &= w^2\Big|_{z=z_0^3} + \sum_{i=1}^{3} z_i^3 \psi_i^3
\end{aligned}
\qquad (3.5)
$$

where, u_0, v_0 and w_0 are the translational displacements at any point on the reference plane ($z = 0$) along the r, θ and z directions, respectively. Equation (3.5) can also be written in a generalized form for k^{th} layer as,

$$
\begin{aligned}
\boldsymbol{d}^k &= (\boldsymbol{d}_t + \boldsymbol{Z}_k \boldsymbol{d}_r) , \\
\boldsymbol{d}^k &= \{u^k \quad v^k \quad w^k\}^{\mathrm{T}} , \\
\boldsymbol{d}_t &= \{u_0 \quad v_0 \quad w_0\}^{\mathrm{T}} ,
\end{aligned}
$$

$$\boldsymbol{d}_r = \left\{ (\boldsymbol{d}_r^1)^{\mathrm{T}} \quad (\boldsymbol{d}_r^2)^{\mathrm{T}} \quad (\boldsymbol{d}_r^3)^{\mathrm{T}} \right\}^{\mathrm{T}},$$

$$\boldsymbol{d}_r^k = \left\{ \phi_1^k \quad \beta_1^k \quad \psi_1^k \quad \phi_2^k \quad \beta_2^k \quad \psi_2^k \quad \phi_3^k \quad \beta_3^k \quad \psi_3^k \right\}^{\mathrm{T}},$$

$$\boldsymbol{Z}_k = \left[\boldsymbol{\zeta}_1^k \quad \boldsymbol{\zeta}_2^k \quad \boldsymbol{\zeta}_3^k \quad \boldsymbol{\zeta}_4^k \quad \boldsymbol{\zeta}_5^k \quad \boldsymbol{\zeta}_6^k \quad \boldsymbol{\zeta}_7^k \quad \boldsymbol{\zeta}_8^k \quad \boldsymbol{\zeta}_9^k \right],$$

$$\boldsymbol{\zeta}_s^k = (\boldsymbol{I}_{3\times 3} \otimes \xi_s^k), s = 1,2,\ldots,9. \tag{3.6}$$

where, $\boldsymbol{I}_{3\times 3}$ is the unit matrix of size (3×3); $\otimes$ represents Kronecker multiplication. The various thickness co-ordinates ($\boldsymbol{\xi}_s^k$, $s = 1,2,\ldots,9$) in Eq. (3.6) are,

$$\xi_1^1 = z,\ \xi_2^1 = z^2,\ \xi_3^1 = z^3,\ \xi_4^1 = 0,\ \xi_5^1 = 0,$$

$$\xi_6^1 = 0,\ \xi_7^1 = 0,\ \xi_8^1 = 0,\ \xi_9^1 = 0 \text{ for } k = 1 \tag{3.7a}$$

$$\xi_1^2 = h_f,\ \xi_2^2 = {h_f}^2,\ \xi_3^2 = {h_f}^3,\ \xi_4^2 = (z - h_f),$$

$$\xi_5^2 = (z - h_f)^2,\ \xi_6^2 = (z - h_f)^3,\ \xi_7^2 = 0,$$

$$\xi_8^2 = 0,\ \xi_9^2 = 0 \text{ for } k = 2 \tag{3.7b}$$

$$\xi_1^3 = h_f,\ \xi_2^3 = {h_f}^2,\ \xi_3^3 = {h_f}^3,\ \xi_4^3 = h_c,$$

$$\xi_5^3 = {h_c}^2,\ \xi_6^3 = {h_c}^3,\ \xi_7^3 = (z - h_c - h_f),$$

$$\xi_8^3 = (z - h_c - h_f)^2,\ \xi_9^3 = (z - h_c - h_f)^3 \text{ for } k = 3 \tag{3.7c}$$

Equation (3.6) can also be expressed in terms of the generalized displacement vector ($\boldsymbol{d}$) through the transformation matrices ($\boldsymbol{T}_t, \boldsymbol{T}_r$) as,

$$\boldsymbol{d}^k = (\boldsymbol{T}_t + \boldsymbol{Z}_k \boldsymbol{T}_r)\boldsymbol{d},$$

$$\boldsymbol{d}_t = (\boldsymbol{T}_t \boldsymbol{d}),$$

$$\boldsymbol{d}_r = (\boldsymbol{T}_r \boldsymbol{d}),$$

$$\boldsymbol{d} = \{(\boldsymbol{d}_t)^{\mathrm{T}} \ (\boldsymbol{d}_r)^{\mathrm{T}}\}^{\mathrm{T}} \tag{3.8}$$

The state of stress and state of strain at any point within the k^{th} layer of the overall annular plate can be written as,

$$\boldsymbol{\sigma}^k = \left\{ \sigma_r^k \quad \sigma_\theta^k \quad \sigma_z^k \quad \tau_{\theta z}^k \quad \tau_{rz}^k \quad \tau_{r\theta}^k \right\}^{\mathrm{T}},$$

$$\boldsymbol{\varepsilon}^k = \left\{ \varepsilon_r^k \quad \varepsilon_\theta^k \quad \varepsilon_z^k \quad \gamma_{\theta z}^k \quad \gamma_{rz}^k \quad \gamma_{r\theta}^k \right\}^{\mathrm{T}} \tag{3.9}$$

where, $\sigma_r^k / \varepsilon_r^k$, $\sigma_\theta^k / \varepsilon_\theta^k$ and $\sigma_z^k / \varepsilon_z^k$ are the normal stresses/strains at any point in the k^{th} layer along the r, θ and z directions, respectively; $\tau_{\theta z}^k / \gamma_{\theta z}^k$, $\tau_{rz}^k / \gamma_{rz}^k$ and $\tau_{r\theta}^k / \gamma_{r\theta}^k$ are the shear stress/strain at any point in the k^{th} layer on the θz, rz and $r\theta$ planes, respectively. According to the displacement field (Eq. (3.8)), the strain-displacement relations for the k^{th} layer can be written as,

$$\boldsymbol{\varepsilon}^k = (\boldsymbol{\varepsilon}_t + \mathbf{z}_r^k \boldsymbol{\varepsilon}_r),$$

$$\boldsymbol{\varepsilon}_t = (\partial_t \boldsymbol{T}_t \boldsymbol{d}),$$

$$\boldsymbol{\varepsilon}_r = (\partial_r \boldsymbol{T}_r \boldsymbol{d}),$$

$$\partial_r = \boldsymbol{I}_{9\times 9} \otimes \partial_\kappa,$$

$$\mathbf{z}_r^k = \begin{bmatrix} \mathbf{z}_{r1}^k & \mathbf{z}_{r2}^k & \mathbf{z}_{r3}^k & \mathbf{z}_{r4}^k & \mathbf{z}_{r5}^k & \mathbf{z}_{r6}^k & \mathbf{z}_{r7}^k & \mathbf{z}_{r8}^k & \mathbf{z}_{r9}^k \end{bmatrix}^{\mathrm{T}} \tag{3.10}$$

where, $\boldsymbol{I}_{9\times 9}$ is the unit matrix of size (9×9); ∂_t, ∂_κ and $\mathbf{z}_{ri}^k$ $(i = 1,2,.....9)$ are the matrices of size (6×3), (8×3) and (6×8), respectively. The nonzero elements of these matrices (∂_t, ∂_κ and $\mathbf{z}_{ri}^k$) are,

$$\partial_t = \begin{bmatrix} \frac{\partial}{\partial r} & 0 & 0 \\ \frac{1}{r} & \frac{1}{r}\frac{\partial}{\partial \theta} & 0 \\ 0 & 0 & 0 \\ 0 & 0 & \frac{1}{r}\frac{\partial}{\partial \theta} \\ 0 & 0 & \frac{\partial}{\partial r} \\ \frac{1}{r}\frac{\partial}{\partial \theta} & \left(\frac{\partial}{\partial r} - \frac{1}{r}\right) & 0 \end{bmatrix}, \quad \partial_\kappa = \begin{bmatrix} \frac{\partial}{\partial r} & 0 & 0 \\ \frac{1}{r} & \frac{1}{r}\frac{\partial}{\partial \theta} & 0 \\ 0 & 0 & 1 \\ 0 & 0 & \frac{1}{r}\frac{\partial}{\partial \theta} \\ 0 & 1 & 0 \\ 1 & 0 & 0 \\ 0 & 0 & \frac{\partial}{\partial r} \\ \frac{1}{r}\frac{\partial}{\partial \theta} & \left(\frac{\partial}{\partial r} - \frac{1}{r}\right) & 0 \end{bmatrix} \tag{3.11a}$$

$$\mathbf{z}_{ri}^k = \begin{bmatrix} \xi_i^k & 0 & 0 & 0 & 0 & 0 & 0 & 0 \\ 0 & \xi_i^k & 0 & 0 & 0 & 0 & 0 & 0 \\ 0 & 0 & \frac{\partial \xi_i^k}{\partial z} & 0 & 0 & 0 & 0 & 0 \\ 0 & 0 & 0 & \xi_i^k & \frac{\partial \xi_i^k}{\partial z} & 0 & 0 & 0 \\ 0 & 0 & 0 & 0 & 0 & \frac{\partial \xi_i^k}{\partial z} & \xi_i^k & 0 \\ 0 & 0 & 0 & 0 & 0 & 0 & 0 & \xi_i^k \end{bmatrix} \tag{3.11b}$$

For deriving the FE model of the overall annular plate, the plane of the plate is discretized by 9-node isoparametric quadrilateral elements such that every element is in the shape of the annular sector with its edges in parallel to the radial and circumferential axes of the reference cylindrical coordinate system. Since the core of the sandwich plate is comprised of two different materials (foam and PFC), the core layer of a typical element is considered to be made of either foam or PFC. So, two different elemental stacking sequences appear in the FE mesh as shown in Fig. 3.6.

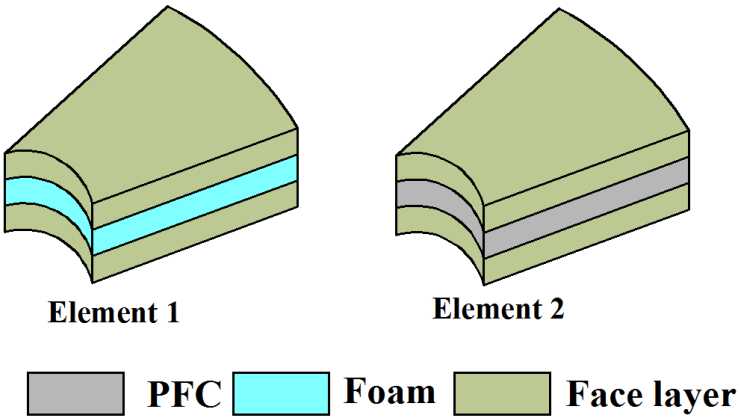

Fig. 3.6 Two different elemental stacking sequences.

The generalized displacement vector ($\boldsymbol{d}$) and generalized strain vectors ($\boldsymbol{\varepsilon}_t$, $\boldsymbol{\varepsilon}_r$) at any point within an element can be written in terms of the shape function matrix ($\boldsymbol{N}$) and the elemental nodal displacement vector ($\boldsymbol{d}_e$) as,

$$\begin{aligned} \boldsymbol{d} &= \boldsymbol{N}\boldsymbol{d}_e, \\ \boldsymbol{\varepsilon}_t &= \boldsymbol{B}_t\boldsymbol{d}_e, \\ \boldsymbol{\varepsilon}_r &= \boldsymbol{B}_r\boldsymbol{d}_e, \\ \boldsymbol{B}_t &= \partial_t\boldsymbol{T}_t\boldsymbol{N}, \\ \boldsymbol{B}_r &= \partial_r\boldsymbol{T}_r\boldsymbol{N} \end{aligned} \tag{3.12}$$

The overall annular plate is considered to be subjected to a transverse harmonic distributed load ($p(r,\theta,t)$) at its bottom surface ($z=0$). For the corresponding vibration of the plate, the first variations of the total potential energy (δT_p^e) and the total kinetic energy (δT_k^e) of a typical element at an instant of time (t) can be written similar to Eqs. (2.30) and (2.31) as,

$$\delta T_p^e = \int_{r_i^e}^{r_o^e}\int_{\theta_i^e}^{\theta_o^e}\left\{\sum_{k=1}^{3}\int_{h_k}^{h_{k+1}}\left[(\delta\boldsymbol{\varepsilon}^k)^{\mathrm{T}}\boldsymbol{\sigma}^k\right]dz - \int_{h_k}^{h_{k+1}}(\delta E_z)D_z^k\Big|_{k=2}dz - \left\langle(\delta w_0)\,p(r,\theta,t)\right\rangle\right\}rd\theta dr \qquad (3.13)$$

$$\delta T_k^e = \int_{r_i^e}^{r_0^e}\int_{\theta_i^e}^{\theta_0^e}\left\langle\sum_{k=1}^{3}\int_{h_k}^{h_{k+1}}\left\{\delta\dot{u}^k \quad \delta\dot{v}^k \quad \delta\dot{w}^k\right\}\rho^k\left\{\dot{u}^k \quad \dot{v}^k \quad \dot{w}^k\right\}^{\mathrm{T}}dz\right\rangle rd\theta dr \qquad (3.14)$$

where, h_k and h_{k+1} are the thickness coordinates at the bottom and top surfaces of k^{th} layer, respectively; ρ^k is the mass density of the k^{th} layer; r_i^e / θ_i^e and r_0^e / θ_0^e are the inner and outer radial/circumferential boundaries of an element, respectively. Using Eqs. (3.2), (3.3), (3.8), (3.10) and (3.12) in Eqs. (3.13) and (3.14), the simplified expressions for first variations of total potential energy (δT_p^e) and total kinetic energy (δT_k^e) for a typical element can be obtained as,

$$\delta T_p^e = \left(\delta\boldsymbol{d}_e\right)^{\mathrm{T}}\left\langle\boldsymbol{K}^e\boldsymbol{d}_e - \boldsymbol{P}_E^e E_z - \boldsymbol{P}_M^e\right\rangle,$$

$$\delta T_k^e = (\delta\dot{\boldsymbol{d}}_e)^{\mathrm{T}}\boldsymbol{M}^e\dot{\boldsymbol{d}}_e,$$

$$\boldsymbol{K}^e = \int_{r_i^e}^{r_o^e}\int_{\theta_i^e}^{\theta_i^e}\left\langle\boldsymbol{B}_t{}^{\mathrm{T}}\left(\boldsymbol{A}_b\boldsymbol{B}_t + \boldsymbol{B}_1\boldsymbol{B}_r\right) + \boldsymbol{B}_r{}^{\mathrm{T}}\left(\boldsymbol{B}_2\boldsymbol{B}_t + \boldsymbol{D}\boldsymbol{B}_r\right)\right\rangle rd\theta dr,$$

$$\boldsymbol{M}^e = \int_{r_i^e}^{r_o^e}\int_{\theta_i^e}^{\theta_i^e}\left\langle\boldsymbol{N}^{\mathrm{T}}\bar{\boldsymbol{m}}\boldsymbol{N}\right\rangle rd\theta dr,$$

$$\boldsymbol{P}_M^e = \int_{r_i^e}^{r_o^e}\int_{\theta_i^e}^{\theta_i^e}\left\langle\boldsymbol{N}^{\mathrm{T}}\boldsymbol{T}_p\,p\left(r,\theta,t\right)\right\rangle rd\theta dr,$$

$$\boldsymbol{P}_E^e = \int_{r_i^e}^{r_o^e}\int_{\theta_i^e}^{\theta_i^e}\left\langle\boldsymbol{B}_t^{\mathrm{T}}\boldsymbol{A}_E + \boldsymbol{B}_r^{\mathrm{T}}\boldsymbol{B}_E\right\rangle rd\theta dr \qquad (3.15)$$

where, $\boldsymbol{K}^e$ is the elemental stiffness matrix; $\boldsymbol{M}^e$ is the elemental mass matrix; $\boldsymbol{P}_E^e$ is the elemental nodal electro-elastic coefficient vector; $\boldsymbol{P}_M^e$ is the elemental nodal mechanical load vector; $\boldsymbol{T}_p$ is a row matrix that specifies the work-conjugate displacement (w_0) for the applied transverse distributed load ($p(r,\theta,t)$) at the bottom surface ($z=0$) of the overall plate. The rigidity matrices ($\boldsymbol{A}_b, \boldsymbol{B}_1, \boldsymbol{B}_2, \boldsymbol{D}$), electro-elastic coupling vectors ($\boldsymbol{A}_E, \boldsymbol{B}_E$) and mass matrix per unit area ($\bar{\boldsymbol{m}}$) are to be formed according to the elemental stacking sequences (Element 1 and Element 2 in Fig. 3.6) following the expressions in Eq. (3.16).

$$\boldsymbol{A}_b = \left(\sum_{k=1}^{3} \int_{h_k}^{h_{k+1}} \boldsymbol{C}^k \, dz \right),$$

$$\boldsymbol{B}_1 = \left(\sum_{k=1}^{3} \int_{h_k}^{h_{k+1}} \boldsymbol{C}^k \boldsymbol{z}_r^k \, dz \right),$$

$$\boldsymbol{B}_2 = \left(\sum_{k=1}^{3} \int_{h_k}^{h_{k+1}} \left(\boldsymbol{z}_r^k\right)^{\mathrm{T}} \boldsymbol{C}^k \, dz \right),$$

$$\boldsymbol{D} = \left(\sum_{k=1}^{3} \int_{h_k}^{h_{k+1}} \left(\boldsymbol{z}_r^k\right)^{\mathrm{T}} \boldsymbol{C}^k \, \boldsymbol{z}_r^k dz \right),$$

$$\boldsymbol{A}_E = \int_{h_k}^{h_{k+1}} \boldsymbol{e}_z^k \Big|_{k=2} dz \,,$$

$$\boldsymbol{B}_E = \int_{h_k}^{h_{k+1}} \left(\boldsymbol{z}_r^k\right)^{\mathrm{T}} \boldsymbol{e}_z^k \Big|_{k=2} dz \,,$$

$$\bar{\boldsymbol{m}} = \sum_{k=1}^{3} \int_{h_k}^{h_{k+1}} \left\langle \left(\boldsymbol{T}_t\right)^{\mathrm{T}} \rho^k \boldsymbol{T}_t + \left(\boldsymbol{T}_t\right)^{\mathrm{T}} \rho^k \boldsymbol{z}_r^k \boldsymbol{T}_r + \left(\boldsymbol{T}_r\right)^{\mathrm{T}} \left(\boldsymbol{z}_r^k\right)^{\mathrm{T}} \rho^k \boldsymbol{T}_t + \left(\boldsymbol{T}_r\right)^{\mathrm{T}} \left(\boldsymbol{z}_r^k\right)^{\mathrm{T}} \rho^k \boldsymbol{z}_r^k \boldsymbol{T}_r \right\rangle dz \quad (3.16)$$

In Eq. (3.16), the electro-elastic coupling vectors $(\boldsymbol{A}_E, \boldsymbol{B}_E)$ are the null vectors for the elements (Element 1) with the core of foam. The numerical integration to generate the elemental matrices and vectors (Eq. (3.15)) is carried out using 3 by 3 Gauss rule. In the case of Element 2, the material properties of the corresponding core layer of PFC are first computed at the Gauss points according to Eq. (3.2), and then the quantities in Eq. (3.16) are computed at the same (Gauss) points in order to generate the elemental matrices and vectors (Eq. (3.15)) as per 3 by 3 Gauss rule. For Element 1, the core layer is made of an isotropic material (foam), and thus the 3 by 3 Gauss rule is implemented in a straight forward manner. The governing equations of motion are derived employing Hamilton's principle (Eq. 2.35). Using Eq. (3.15) in Eq. (2.35), the elemental governing equations of motion for a typical element can be obtained, and the assemblage of these elemental equations in the global space yields the governing equations of motion for the annular sandwich plate as,

$$\boldsymbol{M}\ddot{\boldsymbol{X}} + \boldsymbol{K}\boldsymbol{X} = \boldsymbol{P}_M + \sum_{s=1}^{n_p} \boldsymbol{P}_E^s E_z^s \quad (3.17)$$

where, $\boldsymbol{M}$ and $\boldsymbol{K}$ are the global mass and stiffness matrices, respectively; $\boldsymbol{X}$ is the global nodal displacement vector; $\boldsymbol{P}_M$ is the global nodal mechanical load vector; n_p is the total number of PFC patches in the core layer; $\boldsymbol{P}_E^s$ is the global nodal electro-elastic coefficient vector for s^{th} PFC patch and it is obtained through the assemblage

of elemental nodal electro-elastic coefficient vectors $(\boldsymbol{P}_E^e)$ for the elements within the s^{th} PFC patch; E_z^s is the applied transverse electric field across the thickness of the s^{th} actuator patch.

3.5 Shear-based control strategy

The actuator patches made of the obliquely reinforced 1-3 PFC (Fig. 3.1(b)) are presently used mainly to counteract the mechanically induced transverse shear stress (τ_{rz}) in the annular sandwich plate. As this shear stress (τ_{rz}) changes its sign over the plane of the annular plate for its (plate) any bending mode-shape of vibration, the actuator is presently arranged in the form of the patches as demonstrated in Fig. 3.2, and the actuator patches are activated in accordance to the change of sign of the shear stress (τ_{rz}). In this consequence, the locations of change of sign of the shear stress (τ_{rz}) are coincident with that of the slope of bending deformation of the plate in the rz-plane. So, every actuator patch is presently activated by the feedback of the time-rate of change of the local slope of bending deformation of the plate in the rz-plane. Here, the time-rate of change of the slope is taken for activating the actuator patches according to the velocity feedback control law.

In order to implement this control strategy, the velocity-sensors are utilized, and these sensors are located over the top surface of the overall annular plate where the in-plane locations of the sensors are shown in Fig. 3.7 by taking a part of the middle plane of the overall annular plate. The transverse velocities sensed by these velocity-sensors are utilized to estimate the time-rate of change of slope (in the rz-plane) around an actuator patch as,

$$(\dot{\varphi}_r^s) = \frac{({}^o\dot{w}_0^s) - ({}^i\dot{w}_0^s)}{\Delta r^s},$$

$$\Delta r^s = (r_i^s - r_o^s) \tag{3.18}$$

In Eq. (3.18), the superscript s indicates an actuator patch; r_i^s and r_o^s are the radii of the locations of velocity sensors near the inner and outer radial ends of the s^{th} patch, respectively, and the corresponding transverse velocities sensed by the velocity-sensors are $({}^i\dot{w}_0^s)$ and $({}^o\dot{w}_0^s)$. The time-rate of change of slope (Eq. (3.18)) for an actuator patch is fed back in the form of the electric field

across the thickness of that patch according to the velocity feedback control law as follows,

$$E_z^s = -\frac{k_d^s}{\Delta r^s}\left\langle ({}^o\dot{w}_0^s) - ({}^i\dot{w}_0^s)\right\rangle \tag{3.19}$$

The transverse velocities at the sensing points can be expressed in terms of the global nodal velocity vector ($\dot{\boldsymbol{X}}$) through a transformation row matrix (N_T^s) as,

$$\left\langle ({}^o\dot{w}_0^s) - ({}^i\dot{w}_0^s)\right\rangle = N_T^s \dot{\boldsymbol{X}} \tag{3.20}$$

Using Eqs. (3.19) and (3.20) in Eq. (3.17), the FE equations of motion of the annular sandwich plate can be obtained as,

$$\boldsymbol{M}\ddot{\boldsymbol{X}} + \boldsymbol{C}\dot{\boldsymbol{X}} + \boldsymbol{K}\boldsymbol{X} = \boldsymbol{P}_M(t),$$

$$\boldsymbol{C} = \sum_{s=1}^{n_p}\left\langle \boldsymbol{P}_E^s k_d^s N_T^s \right\rangle \tag{3.21}$$

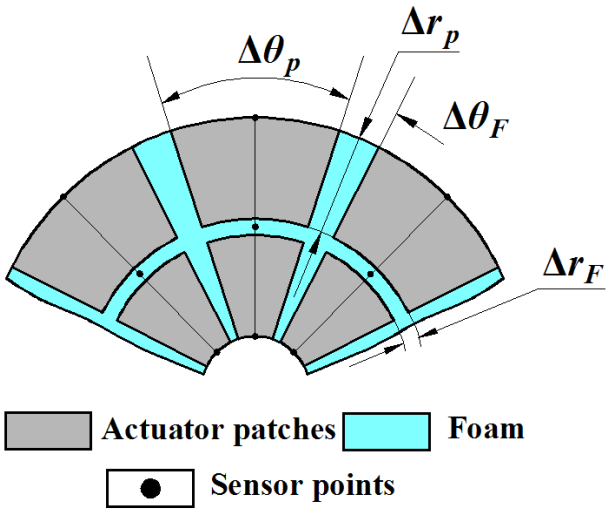

Fig. 3.7 A part of the middle plane of the annular sandwich plate for illustrating the in-plane locations of velocity sensors.

3.6 Results and discussions

In this section, first, the presently derived FE model of the annular sandwich plate is verified. Next, the mechanism of shear actuation of the annular sandwich plate using the patches of the obliquely reinforced 1-3 PFC is analysed. Subsequently, the fruitfulness of the present control strategy for shear-based active control of the annular plate is verified. Finally, the controlled

frequency responses of the overall annular plate are analysed to assess the shear actuation capability of the obliquely reinforced 1-3 PFC.

The face layers are considered to be made of Aluminium (E = 70 GPa, ν = 0.3, $\rho = 2700$ kg/m^3). The material properties of the foam at the core are considered as [195], E = 35.3 MPa, G = 12.76 MPa, ρ = 32 kg/m^3. Unless otherwise mentioned, the geometrical properties of the annular sandwich plate (Fig. 3.2) are considered as, r_i = 0.2 m, $r_o = 1$ m, $\Delta r_F = 5$ mm, $\Delta\theta_F = 2^o$, h_f = 2 mm, h_c = 2 mm, n_r = 2, n_θ = 8, and the edges of the overall annular plate are simply-supported edges ($w_0 = 0$; $v_0 = 0$; $\beta_i^k = 0$; $\psi_i^k = 0$ at $r = r_o$ and r_i). The fiber and matrix phases of the obliquely reinforced 1-3 PFC are considered to be made of PZT5H and epoxy, respectively, while the fiber volume fraction is considered as 0.7767. The material properties of the constituent material PZT5H are [391] , $C_{11} = 127$ GPa, $C_{33} = 117.84$ GPa, $C_{12} = 80.21$ GPa, $C_{13} = 84.67$ GPa, $C_{44} = 22.99$ GPa, $C_{66} = 23.47$ GPa, e_{31} = -6.6228 C/m^2, e_{33} = 23.24 C/m^2, e_{24} = 17.03 C/m^2, ϵ_{11}= 15.09e-9 F/m, ϵ_{33}= 12.69e-9 F/m, $\rho = 7500$ kg/m^3. The properties of the epoxy matrix are, $E = 2.9$ GPa, $\nu = 0.3$, ϵ_{11}= 3.763e-11 F/m, $\rho = 1250$ kg/m^3. According to these material properties of constituents and fiber volume fraction, first, the effective material constants of the vertically reinforced 1-3 PFC (Fig. 3.1(a)) are computed following the procedure given in [13]. These computed properties are subsequently transformed with respect to the reference coordinate system (xyz) for a given fiber orientation angle (ϕ) with the vertical (z) axis to obtain the properties of the obliquely reinforced 1-3 PFC (Fig. 3.1(b)). The density of this vertically/obliquely reinforced 1-3 PFC is computed according to the rule of mixture, and it is obtained as 6104 kg/m^3 for the aforesaid constituents and fiber volume fraction.

3.6.1 Verification of present FE formulation

Since a similar sandwich plate is not available in the literature, the verification of the present FE formulation is carried out considering the axisymmetric configuration of the overall annular plate with its fixed inner and outer edges. This axisymmetric configuration of the overall annular plate is achieved by removing the circumferential gaps ($\Delta\theta_F$) among the actuator patches so that the distributed actuators at the core appear in the form of the annular ring, while

the material of these actuators is considered as a radially poled monolithic piezoelectric material (PZT5H). For this poling direction of the monolithic piezoelectric ring, it possesses axisymmetric material properties and the axisymmetric shear actuation force appears in the rz-plane for a transversely applied electric field across its thickness. Two such annular rings of monolithic piezoelectric material are taken as shown in Fig. 3.8(a) through a typical cross-section of the axisymmetric annular sandwich plate. These actuators are considered to be activated by applying the external transverse electric fields with the identical magnitude, while the direction of the transverse electric field to the inner actuator is opposite to that for the outer actuator. With these applied electric fields, the corresponding electro-elastic deformation of the annular sandwich plate (Fig. 3.8(a)) is computed using the present FE formulation. This result shows the axisymmetric bending deformation of the overall annular plate, and it is presented in Fig. 3.8(b) by the legend as "Present FE".

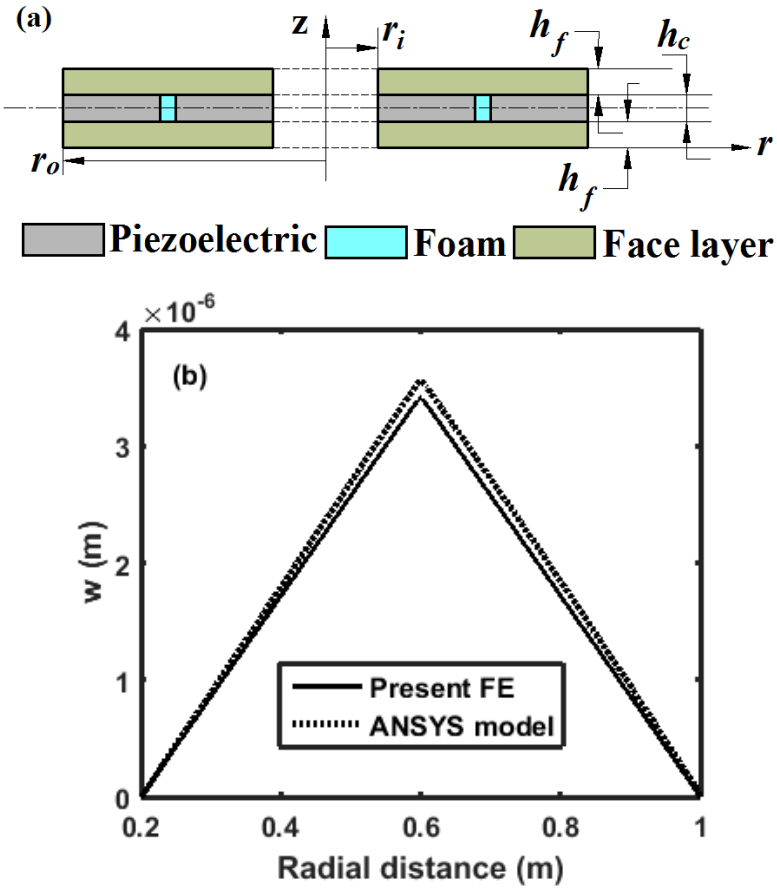

Fig. 3.8 (a) Schematic diagram of a typical cross-section of the axisymmetric annular sandwich plate, (b) bending deflection of the axisymmetric annular sandwich plate across its radial span.

In parallel to this result, similar bending response of the annular sandwich plate (Fig. 3.8(a)) is also evaluated by developing its (plate) axisymmetric FE model in ANSYS using PLANE223 element that has the nodal degrees of freedom as electric potential and two translational displacement components along the axes of the reference coordinate system. The corresponding result (from ANSYS model) is illustrated in Fig. 3.8(b) by the legend as "ANSYS model". It may be observed from Fig. 3.8(b) that the result obtained from the present FE formulation is in good agreement with the similar result obtained from the ANSYS model of the axisymmetric annular sandwich plate (Fig. 3.8(a)). The results in Fig. 3.8(b) verify the present FE formulation for handling the electrically induced shear actuation force in the actuators at the core of the annular sandwich plate.

For further verification of the present FE formulation, the overall annular plate is considered as an isotropic annular plate ($h_c \approx 0$), and its fundamental natural frequency is computed for different boundary conditions as well as different ratios of inner to outer radius. These results are illustrated in Table 3.1 together with the similar results for an identical isotropic annular plate in [388]. In Table 3.1, BCs indicates the type of boundary conditions where CC/SS implies clamped/simply-supported inner and outer boundary edges of the isotropic annular plate. It may be observed from Table 3.1 that the present results are in good agreement with the similar results available in [388]. The results in Table 3.1 verify the present FE formulation for handling the vibration of the annular plate.

Table 3.1 Comparison of dimensionless ($\lambda = \omega r_o^2 \sqrt{\rho h / D}$, $D = Eh^3/12(1-\nu^2)$) natural frequency for the isotropic annular plate.

Source	BCs	λ		
		$r_i / r_o = 0.2$	$r_i / r_o = 0.4$	$r_i / r_o = 0.6$
Present	CC	34.78	62.10	140.2
Ref. [388]		34.61	61.87	139.6
Present	SS	16.72	28.08	62.12
Ref. [388]		16.72	28.08	62.12

3.6.2 Analysis of shear/extension mode actuation of the annular sandwich plate

In association with the transverse electric field (E_z), the vertically reinforced 1-3 PFC (Fig. 3.1(a)) has three nonzero piezoelectric coefficients as, e_{31}, e_{32} and e_{33}.

For the inclination of the fibers in the obliquely reinforced 1-3 PFC (Fig. 3.1(b)), other nonzero piezoelectric coefficient associated with the transverse electric field arises as e_{35}. Now, if this obliquely reinforced 1-3 PFC having the Cartesian material coordinate system is taken in the form of patches within a reference cylindrical coordinate system (Figs. 3.2 and 3.3), then the corresponding transformation of its properties yields the nonzero values of all the piezoelectric coefficients (e_{31}, e_{32}, e_{33}, e_{34}, e_{35}, e_{36}) associated with the transverse electric field (E_z). Each of these coefficients provides in-plane and transverse extensional, as well as shear actuation, forces within the patches of 1-3 PFC for an externally applied transverse electric field. So, the actuation of the annular sandwich plate by the patches of obliquely reinforced 1-3 PFC does not appear in a straight forward manner. In order to make a clear understanding of the corresponding mechanism of actuation, presently an electro-elastic analysis of the overall annular plate is carried out in a special manner by applying the transverse electric field across the thickness of the patches of obliquely reinforced 1-3 PFC.

The geometrical properties, material properties and boundary conditions of the overall annular plate are taken as those mentioned at the beginning of the section (section 3.6). The actuator patches are primarily used to provide the shear actuation force in the rz-plane. So, for achieving the corresponding shear actuated bending deflection of the overall annular plate either in upward or in downward direction, the direction of the applied transverse electric field to the patches at the inner plate-edge is taken as opposite to that for the patches at the outer plate-edge, while these electric fields are taken with the uniform magnitude. Under this applied electric field, it is observed that the overall annular plate undergoes almost axisymmetric bending deformation similar to the bending-shape of the annular plate as obtained in the verification result (Fig. 3.8(b)). However, the mechanism of this actuation of the annular sandwich plate by the embedded patches of the obliquely reinforced 1-3 PFC is presently studied by computing the maximum bending deflection of the overall annular plate considering six cases as, (a) $e_{31} \neq 0\,(e_{3j} = 0,\ j \neq 1)$, (b) $e_{32} \neq 0\,(e_{3j} = 0,\ j \neq 2)$, (c) $e_{33} \neq 0\,(e_{3j} = 0,\ j \neq 3)$, (d) $e_{34} \neq 0\,(e_{3j} = 0,\ j \neq 4)$, (e) $e_{35} \neq 0\,(e_{3j} = 0,\ j \neq 5)$, (f) $e_{36} \neq 0\,(e_{3j} = 0,\ j \neq 6)$. For each of these cases under the aforesaid applied

electric field, the maximum bending deflections of the overall annular plate for different fiber orientation angles (ϕ with z-axis) of the patches of obliquely reinforced 1-3 PFC are presented in Fig. 3.9. Also, the total actuation of the overall annular plate through all the coefficients ($e_{3j} \neq 0$, $j = 1,2,...6$) is presented in the same figure (Fig. 3.9) by the legend as "Obliquely reinforced 1-3 PFC".

3.6.2.1 Extension mode actuation of the annular sandwich plate

Since the stiffness matrix of the patches of obliquely reinforced 1-3 PFC is fully populated (in the reference cylindrical coordinate system), any of the piezoelectric coefficients (e_{3j}, $j = 1,2,...6$) provides all the electrically induced extensional and shear stress components/actuation forces in the patches for the aforesaid applied transverse electric field. Among these actuation forces, the in-plane extensional ones through any coefficient (e_{3j}) are not effective to cause bending deformation of the overall annular plate since the actuator patches are located at the core of the symmetric annular sandwich plate. However, induced transverse extensional stress/actuation force through any coefficient (e_{3j}) causes thickness mode actuation that is usually not so effective in causing bending deformation of thin plates. So, rest of the actuation forces, i.e. shear actuation forces in the patches of obliquely reinforced 1-3 PFC mainly cause the bending deformation of the overall annular plate (Fig. 3.9) as it is described in the next section.

3.6.2.2 Shear mode actuation of the annular sandwich plate

The electrically induced shear stress components/shear actuation forces in the patches due to the coefficient (e_{31}/e_{32}) mainly appear through the shear-extension coupling stiffness coefficients as C_{14}/C_{24}, C_{15}/C_{25} and C_{16}/C_{26}. But these shear actuation forces through the coefficient (e_{31}/e_{32}) are not so effective to cause the bending deformation of the overall annular plate as it is observed from the curves in Fig. 3.9 for $e_{31} \neq 0$ ($e_{3j} = 0$, $j \neq 1$) and $e_{32} \neq 0$ ($e_{3j} = 0$, $j \neq 2$). The other coefficients like e_{34} and e_{36} directly induce the shear stresses/actuation forces in the θz and $r\theta$ planes of the patches of 1-3 PFC,

respectively. But, these coefficients (e_{34}, e_{36}) appear with very small magnitudes since the angle Λ (Fig. 3.5) at any point over the plane of a patch does not arise with indicative value for its (patch) small circumferential span ($\Delta\theta_p$, Fig. 3.2). So, these coefficients (e_{36} and e_{34}) do not have indicative effect on the bending deformation of the overall annular plate as it is observed from the curves in Fig. 3.9 for $e_{34} \neq 0\,(e_{3j} = 0,\ j \neq 4)$ or $e_{36} \neq 0\,(e_{3j} = 0,\ j \neq 6)$.

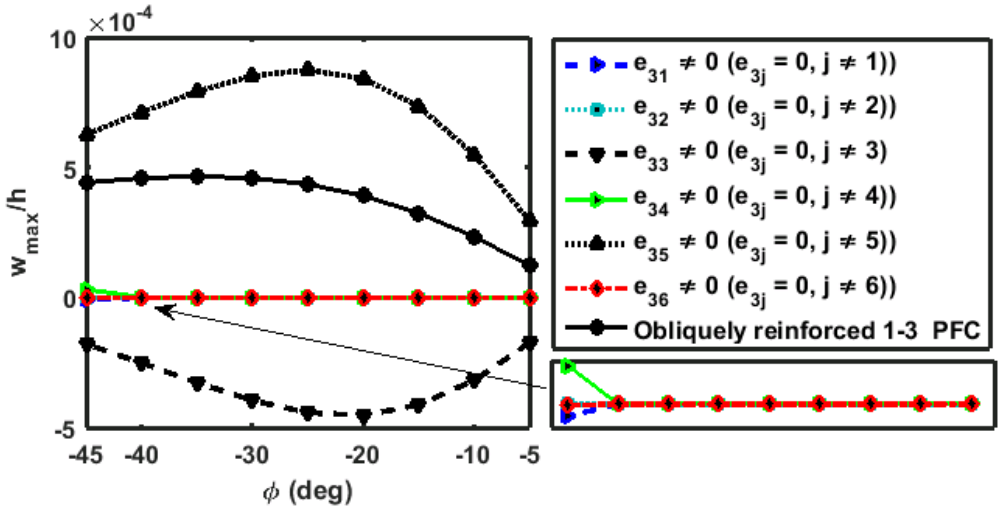

Fig. 3.9 Variation of maximum transverse deflection (w_{max}/h) of the annular sandwich plate with the fiber orientation angle (ϕ with the z-axis) of the patches of obliquely reinforced 1-3 PFC.

The shear actuation forces through the coefficient e_{33} appear due to the shear-extension coupling stiffness coefficients as C_{34}, C_{35} and C_{36}. Among these coefficients, C_{34} and C_{36} appear with the small magnitudes because of the small value of Λ (Fig. 3.5) at any point in a patch, while the other stiffness coefficient C_{35} appears with indicative magnitude because of the alignment of the obliquely oriented fibers of 1-3 PFC in the xz-plane of its (1-3 PFC) Cartesian material coordinate system. So, the shear actuation of the overall annular plate through the coefficient (e_{33}) appears mainly due to the corresponding shear actuation force in the rz-plane, and it occurs indicatively as shown in Fig. 3.9 by the curve for $e_{33} \neq 0\,(e_{3j} = 0,\ j \neq 3)$.

The coefficient e_{35} directly induces the transverse shear stress in the rz-plane of the patches although the other induced shear stresses in the θz and

$r\theta$ planes also appear through the same coefficient (e_{35}) due to the shear-shear coupling stiffness coefficients as C_{54} and C_{56}, respectively. But, the magnitudes of these stiffness coefficients (C_{54} and C_{56}) are very small in comparison to the magnitude of the stiffness coefficient C_{55} mainly because of the small value of Λ at any point in an actuator patch (Fig. 3.5). So, the shear actuation of the overall annular plate through e_{35} mainly arises due to the electrically induced transverse shear stress (τ_{rz}), and the corresponding maximum bending deflections of the overall annular plate for different fiber orientation angles of the patches of 1-3 PFC are shown in Fig. 3.9 by the curve for $e_{35} \neq 0$ ($e_{3j} = 0$, $j \neq 5$).

From the results in Fig. 3.9, it is clear that the actuation of the annular sandwich plate by the patches of obliquely reinforced 1-3 PFC mainly appears by means of shear actuation forces in the rz-plane through the coefficients e_{33} and e_{35}. But, the shear actuation force in the rz-plane through the coefficient e_{33} is opposite to that through the coefficient e_{35} (Fig. 3.9), and thus the total shear actuation of the annular sandwich plate decreases as it is shown in Fig. 3.9 by the curve for "Obliquely reinforced 1-3 PFC ". Despite this fact, it may be observed from Fig. 3.9 that the patches of obliquely reinforced 1-3 PFC cause an indicative shear actuated bending deformation of the annular sandwich plate.

3.6.3 Shear-based active control of vibration of the annular sandwich plate

The capability of the obliquely reinforced 1-3 PFC in shear-based attenuation of vibration of the annular sandwich plate is assessed in this section by means of evaluating the controlled frequency responses of the plate under a transversely distributed harmonic mechanical load (Eq. 2.46) at its bottom surface. Under this harmonic mechanical load, the frequency responses of the overall annular plate are evaluated within an operating frequency-range that includes its (plate) first three bending modes of vibration. All these bending modes of vibration are of fundamental radial mode member ($m = 1$) while those are separated by the circumferential-mode numbers (n) as 0, 1 and 2.

The shear actuator patches of the 1-3 PFC are taken with a fiber orientation angle (ϕ) of 35^{o} on the basis of the results in Fig. 3.9, and they (actuator patches) are activated according to the aforesaid shear-based active

control strategy where the feedback control gains (k_d^s, $s=1,2,....n_p$) are taken with a uniform value ($k_d^s = k_d$ for $s=1,2,....n_p$). In the following results for frequency responses of the annular sandwich plate, the maximum nodal transverse displacement-amplitude is presented at every operating frequency (ω), and it is denoted in the dimensionless form as, w_{max}/h. Besides, the required control voltage at every operating frequency is presented as the maximum one (V_{max}) among the control voltages over the actuator patches.

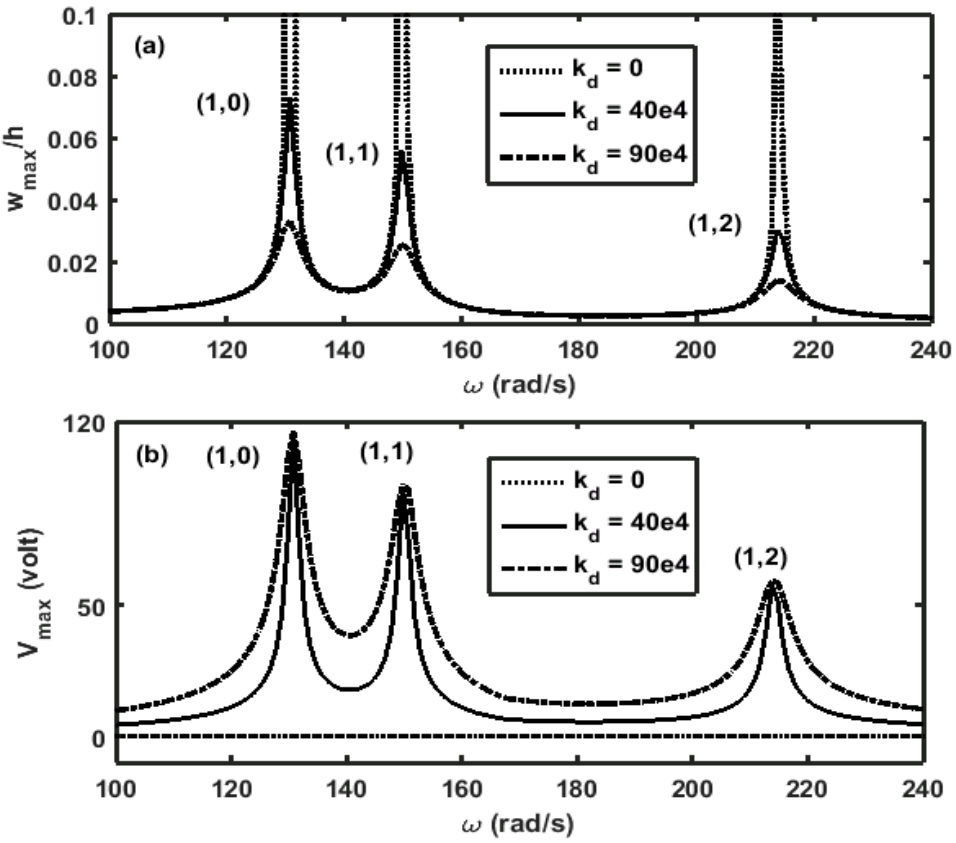

Fig. 3.10 (a) Variation of the maximum nodal transverse displacement-amplitude (w_{max}/h) of the annular sandwich plate with the operating frequency (ω), (b) the corresponding variations of the maximum control voltage ($p_0 = 1.6$ N/m², $n_r = 2$, $n_\theta = 8$).

Figure 3.10(a) illustrates the variation of the maximum nodal transverse displacement-amplitude (w_{max}/h) of the annular sandwich plate with the operating frequency (ω) for three different values of the control gain (k_d), where the bending mode at a resonant frequency is denoted by (m,n). The

corresponding variations of the maximum control voltage ($V_{\max}$) are also illustrated in Fig. 3.10(b). It may be observed from Fig. 3.10(a)-(b) that the actuator patches of the obliquely reinforced 1-3 PFC indicatively attenuate the resonant transverse displacement amplitudes of the overall annular plate in the expense of reasonable control voltage. It is interesting to observe at any resonant frequency that the maximum control voltage changes insignificantly for an increase of the control gain (k_d) while the resonant transverse displacement-amplitude decreases indicatively. It is an advantage of the present shear-based control strategy although this advantage can be achieved when the load-amplitude (p_o) remains constant. It may also be observed from Fig. 3.10(a) that all resonant transverse displacement amplitudes decrease almost in equal manner for an increase of the control gain (k_d). These observations infer the fruitfulness of the present arrangement of the shear actuator patches at the core of the annular plate and also the present shear-based control strategy based on the velocity feedback control law.

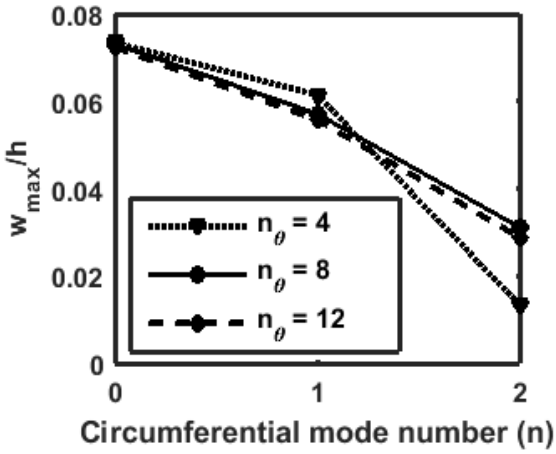

Fig. 3.11 Resonant transverse displacement amplitudes at the first three bending modes ($n=0,1,2;\ m=1$) of vibration of the annular sandwich plate for different values of n_θ ($p_o = 1.6$ N/m², $k_d = 40e4$).

For the results in Fig. 3.10, the number (n_θ) of circumferential segments in the arrangement of the actuator patches is taken as 8 while the patches are located at the inner and outer plate edges mainly for the convenience in the application of the external electric field to the actuator patches. However, as demonstrated in section 3.2, an appropriate value of n_θ is to be taken for effective control of all modes of vibration of interest ($m=1,\ n=0,\ 1,\ 2$). In order

to obtain it, the resonant displacement amplitudes are computed for different values of n_θ. The corresponding results in Fig. 3.11 show that all modes of vibration are attenuated effectively when the value of n_θ exceeds 8. So, a minimum number (n_θ) of circumferential segments is presently taken as 8.

For a constant value of the load-amplitude (p_o), the control gain (k_d) is gradually increased, and the corresponding variations of the resonant displacement amplitudes for the first and second bending modes of vibration of the annular sandwich plate are illustrated in Fig. 3.12(a). The corresponding variations of the maximum control voltage are also shown in Fig. 3.12(b). It may be observed from these results that the amplitude of vibration of the overall annular plate is significantly attenuated by the shear actuator patches of the obliquely reinforced 1-3 PFC in the expense of the reasonable control voltage. However, for an increase of the control gain, the corresponding attenuation of the resonant displacement-amplitude and the increase of required control voltage are quantified by defining the following parameters ($\Delta W(\%)$ and $\Delta V(\%)$),

$$\Delta W(\%) = \frac{\left(w_{\max}/h\right)_1 - \left(w_{\max}/h\right)_2}{\left(w_{\max}/h\right)_1} \times 100 \tag{3.22a}$$

$$\Delta V(\%) = \frac{\left(V_{\max}\right)_2 - \left(V_{\max}\right)_1}{\left(V_{\max}\right)_1} \times 100 \tag{3.22b}$$

where, the superscript 1/2 indicates the magnitudes of the parameters ($\left(w_{\max}/h\right), V_{\max}$) for a low/high value of the control gain (k_d). As the value of the control gain is increased from 10e4 to 90e4 (Fig. 3.12), the resonant displacement amplitudes at the first and second bending modes of vibration of the annular sandwich plate are attenuated ($\Delta W(\%)$) by, 88.72% and 88.73%, respectively, while the corresponding control voltage increases ($\Delta V(\%)$) by, 1.29% and 1.56%. These measures and the results in Figs. 3.12(a)-(b) infer an indicative shear actuation capability of the obliquely reinforced 1-3 PFC in attenuation of bending modes of vibration of the annular plate.

The results in Figs. 3.12(a)-(b) are illustrated considering a constant value of the load-amplitude (p_o). However, for different values of the control-gain (k_d) and load-amplitude (p_o), the corresponding variations of the resonant

displacement amplitude and control voltage are illustrated in Figs. 3.13(a) and 3.13(b), respectively at the fundamental bending mode.

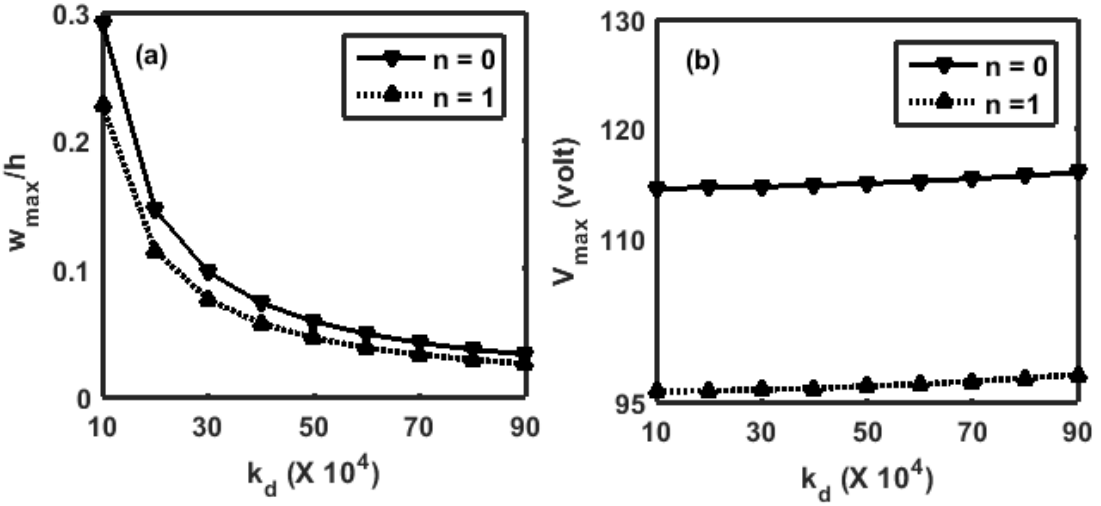

Fig. 3.12 Variations of (a) the resonant transverse displacement amplitudes and (b) the corresponding maximum control voltages with the control gain (k_d) at the first and second bending modes of vibration of the annular sandwich plate ($p_o = 1.6$ N/m², $n_\theta = 8$).

It may be observed from Fig. 3.13(b) that the required control voltage insignificantly changes with the control gain (k_d) for any value of the load-amplitude (p_o). But, the same parameter (control voltage) changes indicatively with the load-amplitude (p_o) for any value of the control gain (k_d). So, the application of the obliquely reinforced 1-3 PFC as a material of shear actuator is mainly limited to a certain value of the load-amplitude (p_o) where the applied control voltage exceeds its permissible value for this 1-3 PFC.

Table 3.2 illustrates the attenuation ($\Delta W(\%)$) of the resonant displacement amplitude and the corresponding increase of control voltage ($\Delta V(\%)$) for an increase of the control gain (k_d , from 10e4 to 100e4) at different load amplitudes (p_o). It may be observed from Table 3.2 that the resonant displacement-amplitude of the annular sandwich plate is indicatively attenuated by the actuator patches of the obliquely reinforced 1-3 PFC for any value of the load-amplitude (p_o). Moreover, the rate of attenuation of resonant displacement-amplitude or the corresponding increase of control voltage remain almost the same for any load amplitude (p_o). The results in Figs. 3.12-3.13 and Table 3.2

infer an significant shear actuation capability of the obliquely reinforced 1-3 PFC, and thus it may be a potential material of shear actuator in active control of annular plates.

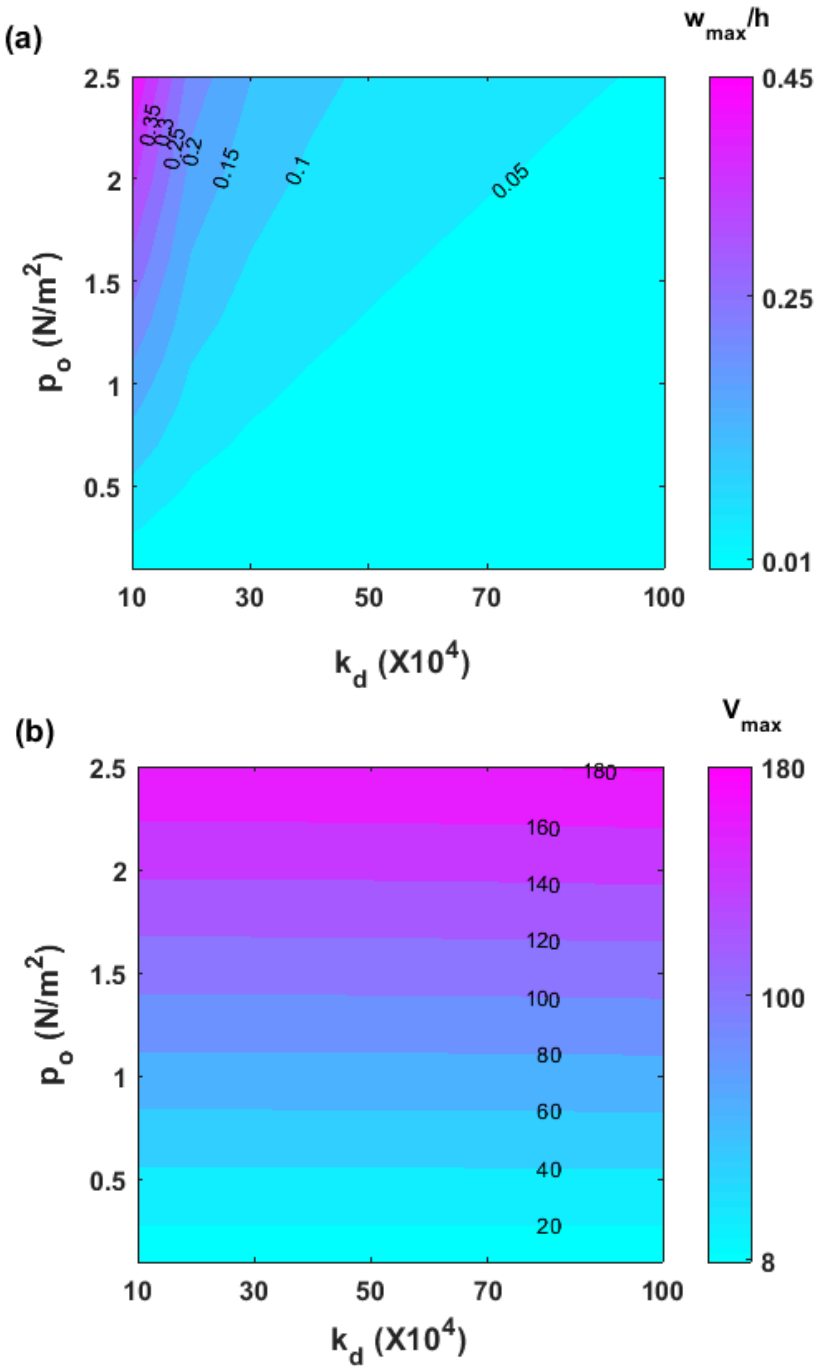

Fig. 3.13 Variations of (a) the resonant displacement amplitude and (b) the corresponding maximum control voltage at the fundamental bending mode of vibration of the annular sandwich plate within a two-dimensional domain of control gain (k_d) and load-amplitude ($n_\theta = 8$).

Table 3.2 Attenuation of the resonant displacement amplitude and the corresponding increase of the control voltage for an increase of control gain at different values of the load amplitude.

p_o (N/m^2)	ΔW(%)	ΔV(%)
2.5	89.82	1.54
2	89.81	1.58
1.6	89.81	1.54
1.3	89.82	1.55
0.9	89.82	1.54
0.5	89.82	1.54

3.7 Summary

In this chapter, an obliquely reinforced 1-3 PFC is introduced for shear-based active control of annular plates. The study is carried out by constructing an annular sandwich plate where the patches of the 1-3 PFC in the shape of the annular sector are embedded within the core of foam. A typical patch of the obliquely reinforced 1-3 PFC is comprised of longitudinally poled piezoelectric fibers that are obliquely reinforced in a vertical plane of the Cartesian material coordinate system for producing the shear actuation force in the same vertical plane in response to an applied transverse electric field. This shear actuation force is used in the plane of radial and transverse coordinates of the annular plate for actuation of its (plate) bending mode of deformation/vibration.

An electro-elastic FE model of the annular sandwich plate is developed based on the layer-wise deformation theory. Using this FE model, the mechanism of shear actuation of the annular sandwich plate with the embedded patches of the obliquely reinforced 1-3 PFC is first analysed. This analysis reveals that the shear actuated bending deformation of the annular plate appears through two main piezoelectric coefficients as e_{33} and e_{35}. Both the coefficients (e_{33} and e_{35}) provide the primary shear actuation forces in the same transverse plane of the annular plate. But, the shear actuation by e_{33} is opposite to that by e_{35}. So, the total actuation of the annular sandwich plate decreases, where the actuation through e_{35} is reduced by that through e_{33}. Despite this fact, a good shear actuated bending deformation of the annular sandwich plate is observed, and thus subsequent study on the effectiveness of the actuator patches of the obliquely reinforced 1-3 PFC in shear-based active

control of bending modes of vibration of the annular plate is carried out by developing a closed-loop FE model of the annular plate.

The closed-loop FE model is developed based on the velocity feedback control law where the feedback of the time-rate of change of local slope of bending deformation of the plate is introduced particularly for effective shear-based attenuation of vibration of the annular plate. The corresponding controlled frequency responses of the annular sandwich plate under a transverse harmonic load exhibit indicative shear mode actuation capability of the actuator patches made of the obliquely reinforced 1-3 PFC, where also the required control voltage remains within the reasonable range. It is observed that a higher attenuation of resonant displacement amplitude through an increase of the velocity feedback control gain does not require much increase of the control voltage. The increase of the required control voltage mainly appears for the higher amplitude of the applied harmonic load, and thus the application of the 1-3 PFC as a material of shear actuator is mainly limited to the load-amplitude where the applied electric field exceeds its permissible value. It is also observed that the rate of attenuation of the resonant displacement amplitude with the increase of the control gain is almost independent of the amplitude of the applied harmonic load. These observations infer an indicative shear mode actuation capability of the obliquely reinforced 1-3 PFC, and thus this PFC may be a potential material for shear-based actuation of flexible annular plates.

Chapter 4

A balanced laminate of piezoelectric fiber composite for improved shear piezoelectric actuation of beams

4.1 Introduction

An obliquely-reinforced 1-3 PFC is introduced in the previous chapter (Chapter 3) as a material of shear-mode piezoelectric actuator, and an analysis of its shear actuation capability in flexural vibration control of an annular plate is also presented. Although this analysis in the previous chapter shows an indicative shear actuation capability of the obliquely-reinforced 1-3 PFC, the main shortcoming arises due to the existence of thickness mode actuation force along with the transverse shear actuation force. The shear actuation force in this obliquely-reinforced 1-3 PFC mainly arises through the piezoelectric coefficient (e_{35}) but it (shear actuation force) is affected by the thickness mode actuation force through the coupling between the transverse normal stress and transverse shear strain. In this view, if this thickness mode actuation force is eliminated in some way, then the shear mode actuation capability of the PFC may be improved. In the quest of a way in this concern, a new balanced laminate of PFC is proposed in this chapter, and its shear-mode actuation characteristics are investigated considering the shear-mode actuation of bending deformation of a simple beam element.

In the subsequent sections, first, the geometrical features of this balanced laminate of PFC (BL-PFC) are presented, and its effective electromechanical properties are determined through a micromechanics formulation. Next, a sandwich beam is constructed where the BL-PFC actuator patches are embedded in the core, and an FE model of the overall beam is derived for its electro-elastic analysis. This analysis reveals the shear actuation capability of this BL-PFC actuator in comparison to that of the obliquely reinforced 1-3 PFC or the conventional monolithic shear piezoelectric actuator. This comparison study reveals the utility of the present concept of BL-PFC actuator for improved shear mode actuation of flexible structures.

4.2 Present balanced laminate of PFC

The present laminate of PFC is constructed using an even number of vertically reinforced 2-2 PFC laminae of identical thickness and properties, where the fiber

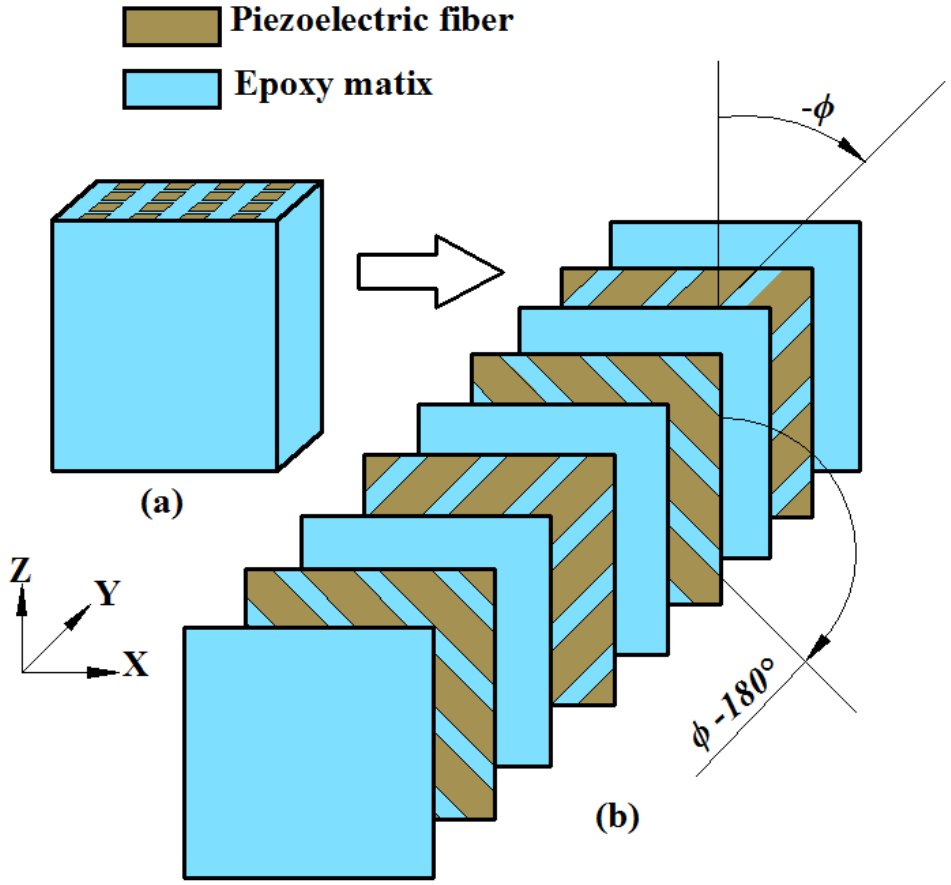

Fig. 4.1 (a) Balanced laminate of PFC and (b) the corresponding component layers.

orientation angles of every pair of consecutive 2-2 PFC layers are taken as $-\phi$ and $(\phi-180^{o})$ with respect to the vertical (z) axis of the laminate coordinate system as shown in Fig. 4.1. The PFC layers are considered to be perfectly bonded through the thin epoxy layers (Fig. 4.1). As per these fiber orientation angles in every pair of 2-2 PFC laminae, the in-plane (xz-plane) shear coupling stiffness coefficients of the laminate appear with zero value. Since it is a defined characteristic of a balanced laminate [392], the present laminate is called as a balanced laminate of PFC. For the sake of simplicity in the presentation, the fiber orientation angles ($-\phi$ and $(\phi-180^{o})$) of the 2-2 PFC laminae in the laminate are simply denoted as fiber orientation angle (ϕ) of balanced laminate of PFC (BL-PFC). If the uniform fiber orientation angle of the 2-2 PFC layers (Fig. 4.1) is taken as 0^{o} or other than 0^{o} with respect to the vertical (z) axis of the laminate coordinate system, then the PFC laminate appears as a vertically or obliquely

reinforced 1-3 PFC (Figs. 3.1(a) and 3.1(b)). Presently, the 2-2 PFC layers in the BL-PFC (Fig. 4.1) are taken with a very small thickness in micro-scale, and thus the investigation on its (PFC laminate) shear actuation capability is performed by computing its effective electromechanical properties.

This computation of effective electromechanical properties of the balanced laminate of PFC is carried out in two steps. In the first step, the effective properties of the vertically reinforced 2-2 PFC layer (Fig. 4.2(a)) are computed considering a corresponding representative volume element (denoted by RVE1) as shown in Fig. 4.2(b). These computed effective properties of the vertically reinforced 2-2 PFC lamina (Fig. 4.1(a)) are subsequently transformed with respect to the laminate coordinate system (Fig. 4.1) to obtain the electromechanical properties of the obliquely reinforced 2-2 PFC layers within the same laminate. Using these effective properties of the obliquely reinforced 2-2 PFC layers in the BL-PFC, the laminate (BL-PFC) is considered to be made of homogenized obliquely reinforced 2-2 PFC layers, and the effective properties of the laminate are computed (in the second step of homogenization) by defining a representative volume element (denoted by RVE2) as shown in Fig. 4.3.

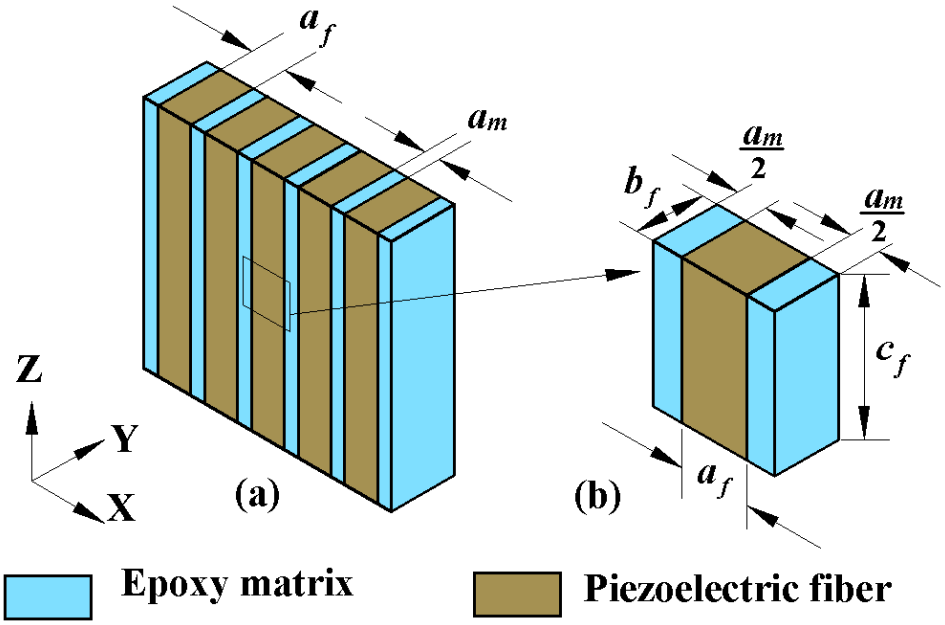

Fig. 4.2 (a) Vertically reinforced 2-2 PFC lamina and (b) the corresponding representative volume element (denoted by RVE1).

The RVE2 (Fig. 4.3) is comprised of a pair of obliquely reinforced 2-2 PFC laminae having the fiber orientation angles of $-\phi$ and $(\phi - 180^{o})$ with respect to

the vertical (z) axis. As these PFC layers in RVE2 (Fig. 4.3) possess dissimilar material properties due to their different fiber orientation angles, the RVE2 is basically comprised of homogeneous layers of three different materials that are the two homogenized 2-2 PFC with different fiber orientation angles and the epoxy. An analytical formulation for computation of effective properties of RVE1 and RVE2 is presented in the subsequent two sections.

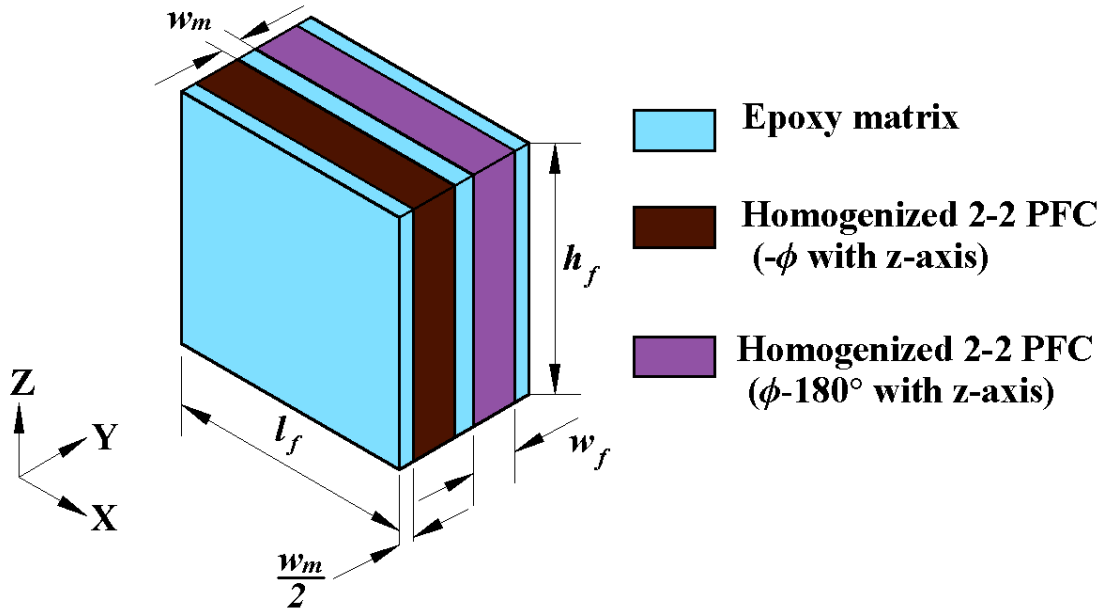

Fig. 4.3 Representative volume element (denoted by RVE2) of the balanced laminate of PFC (Fig. 4.1).

4.2.1 Effective properties of PFC

The constitutive behaviour (without thermal effect) of linear piezoelectric material can be described according to the piezoelectric stress formulation [393] as,

$$\begin{aligned} \boldsymbol{\sigma} &= (\boldsymbol{C}\boldsymbol{\varepsilon} - \boldsymbol{e}^{\mathrm{T}}\boldsymbol{E}), \\ \boldsymbol{D} &= (\boldsymbol{e}\boldsymbol{\varepsilon} + \in \boldsymbol{E}) \end{aligned} \tag{4.1}$$

where, $\boldsymbol{\sigma}$, $\boldsymbol{\varepsilon}$, $\boldsymbol{D}$ and $\boldsymbol{E}$ are the stress, strain, electric displacement and electric field vectors, respectively; $\boldsymbol{C}$ is the stiffness matrix defined at zero/constant electric field; $\boldsymbol{e}$ is the piezoelectric matrix defined either at zero/constant electric field or at zero/constant strain field; $\in$ is the permittivity matrix defined at zero/constant strain field. Equation (4.1) can also be written in a compact form [21] as,

$$\mathfrak{I} = \aleph \mathfrak{R},$$

$$\mathfrak{I} = \begin{Bmatrix} \boldsymbol{\sigma} \\ \boldsymbol{D} \end{Bmatrix}, \mathfrak{R} = \begin{Bmatrix} \boldsymbol{\varepsilon} \\ \boldsymbol{E} \end{Bmatrix},$$

$$\aleph = \begin{bmatrix} \boldsymbol{C} & -\boldsymbol{e}^{\mathrm{T}} \\ \boldsymbol{e} & \boldsymbol{\epsilon} \end{bmatrix} \tag{4.2}$$

Equations (4.1)-(4.2) describe the linear piezoelectric constitutive behaviour (without thermal effect) of a homogeneous piezoelectric material. Analogues to this homogeneous material, the present PFC is also considered as a macroscopically homogeneous piezoelectric material, and its (PFC) effective properties can be estimated by evaluating the average field quantities ($\bar{\boldsymbol{\varepsilon}}$, $\bar{\boldsymbol{E}}$, $\bar{\boldsymbol{\sigma}}$, $\bar{\boldsymbol{D}}$) over the volume of the composite under the homogenous displacement-electric potential boundary conditions [21]. The resulting effective stiffness ($\bar{\boldsymbol{C}}$), piezoelectric ($\bar{\boldsymbol{e}}$) and permittivity ($\bar{\boldsymbol{\epsilon}}$) matrices of the composite (PFC) can be obtained as [21], [383], [394],

$$\bar{\mathfrak{I}} = \bar{\aleph} \bar{\mathfrak{R}} \tag{4.3a}$$

$$\bar{\mathfrak{I}} = \begin{Bmatrix} \bar{\boldsymbol{\sigma}} \\ \bar{\boldsymbol{D}} \end{Bmatrix}, \bar{\mathfrak{R}} = \begin{Bmatrix} \bar{\boldsymbol{\varepsilon}} \\ \bar{\boldsymbol{E}} \end{Bmatrix}, \bar{\aleph} = \begin{bmatrix} \bar{\boldsymbol{C}} & -\bar{\boldsymbol{e}}^{\mathrm{T}} \\ \bar{\boldsymbol{e}} & \bar{\boldsymbol{\epsilon}} \end{bmatrix} \tag{4.3b}$$

$$\bar{\aleph} = \sum\nolimits_p \left(v_p \aleph^p \boldsymbol{A}^p \right) \tag{4.3c}$$

$$\bar{\mathfrak{R}}^p = \boldsymbol{A}^p \bar{\mathfrak{R}}, \ \bar{\mathfrak{R}}^p = \begin{Bmatrix} \bar{\boldsymbol{\varepsilon}}^p \\ \bar{\boldsymbol{E}}^p \end{Bmatrix} \tag{4.3d}$$

$$\sum\nolimits_p \boldsymbol{A}^p = \boldsymbol{I} \tag{4.3e}$$

where, v_p is the volume fraction of the p^{th} phase of the composite (PFC); $\aleph^p$ is of similar form of $\aleph$ (Eq. (4.2)) but it ($\aleph^p$) is for the p^{th} phase of the composite (PFC); $\boldsymbol{A}^p$ is the phase average strain-electric field concentration matrix that relates (Eq. (4.3d)) average strain ($\bar{\boldsymbol{\varepsilon}}^p$) and electric field ($\bar{\boldsymbol{E}}^p$) in the p^{th} phase to that ($\bar{\boldsymbol{\varepsilon}}$, $\bar{\boldsymbol{E}}$) of the composite (PFC); $\boldsymbol{I}$ is the unity matrix with the same size of $\boldsymbol{A}^p$.

In order to determine effective properties of a PFC according to Eqs. (4.3a)-(4.3e), the phase average concentration matrices ($\boldsymbol{A}^p$) are to be estimated, and it

can be done through any of the available micromechanics models like Mori-Tanaka approach, self-consistent method, differential scheme, etc. [21,383]. Presently, for simplicity in the geometrical features of the 2-2 PFC (Fig. 4.2) and the BL-PFC (Fig. 4.3), their effective properties are determined by estimating the phase average concentration matrices ($\boldsymbol{A}^p$) in Uniform Field approach [14,15].

According to the reference coordinate system for these PFCs (RVE1 and RVE2, Figs. 4.2(b) and 4.3), the average field vectors ($\bar{\mathfrak{I}}, \bar{\mathfrak{R}}$, Eq. (4.3b)) over the volume of composite (RVE1/RVE2) can be written as,

$$\bar{\mathfrak{I}} = \left\{ \bar{\sigma}_x \quad \bar{\sigma}_y \quad \bar{\sigma}_z \quad \bar{\tau}_{yz} \quad \bar{\tau}_{xz} \quad \bar{\tau}_{xy} \quad \bar{D}_x \quad \bar{D}_y \quad \bar{D}_z \right\}^{\mathrm{T}},$$

$$\bar{\mathfrak{R}} = \left\{ \bar{\varepsilon}_x \quad \bar{\varepsilon}_y \quad \bar{\varepsilon}_z \quad \bar{\gamma}_{yz} \quad \bar{\gamma}_{xz} \quad \bar{\gamma}_{xy} \quad \bar{E}_x \quad \bar{E}_y \quad \bar{E}_z \right\}^{\mathrm{T}} \tag{4.4}$$

where, $\bar{\sigma}_x / \bar{\varepsilon}_x / \bar{E}_x / \bar{D}_x$, $\bar{\sigma}_y / \bar{\varepsilon}_y / \bar{E}_y / \bar{D}_y$ and $\bar{\sigma}_z / \bar{\varepsilon}_z / \bar{E}_z / \bar{D}_z$ are the average normal stress/normal strain/electric field/electric displacement components over the volume of composite (RVE1/RVE2) along the x, y and z directions, respectively; $\bar{\tau}_{yz} / \bar{\gamma}_{yz}$, $\bar{\tau}_{xz} / \bar{\gamma}_{xz}$ and $\bar{\tau}_{xy} / \bar{\gamma}_{xy}$ are the average shear stress/strain components over the volume of composite (RVE1/RVE2) on the yz, xz and xy planes, respectively. As per the number of field components (Eq. (4.4)), the phase average concentration matrix ($\boldsymbol{A}^p$, Eq. (4.3d)) appears with the size of (9×9). So, for the two-phase ($p=1,2$) PFC (RVE1, Fig. 4.2(b)), a total of 162 elements of the concentration matrices (${}^{RVE1}\boldsymbol{A}^p$, $p=1,2$) are to be determined. Similarly, for the three-phase ($p=1,2,3$) PFC (RVE2, Fig. 4.3), a total of 243 elements of the phase average concentration matrices (${}^{RVE2}\boldsymbol{A}^p$, $p=1,2,3$) are to be determined. The estimation of these elements by recognizing the uniform fields in the PFCs is the subject in the next section.

4.2.2 Effective properties of 2-2 PFC layer and balanced laminate of PFC

According to the geometry of the vertically reinforced 2-2 PFC or RVE1 in Fig. 4.2(a)-(b), two different constituent phases are alternately stacked along the x-direction. Corresponding to this kind of geometry of a PFC, the pertinent studies on series and parallel models of piezoelectric composites in Uniform Field approach [14,15] are followed to recognize the uniform fields in RVE1, and every

phase average strain/electric field component in the yz-plane of RVE1 is assumed as equal to the same field component averaged over the volume of entire composite (RVE1). It can be expressed as,

$$\bar{\varepsilon}_y^1 = \bar{\varepsilon}_y^2 = \bar{\varepsilon}_y \,,$$

$$\bar{\varepsilon}_z^1 = \bar{\varepsilon}_z^2 = \bar{\varepsilon}_z \,,$$

$$\bar{\gamma}_{yz}^1 = \bar{\gamma}_{yz}^2 = \bar{\gamma}_{yz} \,,$$

$$\bar{E}_y^1 = \bar{E}_y^2 = \bar{E}_y \,,$$

$$\bar{E}_z^1 = \bar{E}_z^2 = \bar{E}_z \tag{4.5}$$

In Eq. (4.5), the superscript p ($p = 1, 2$) denotes a phase average field component for p^{th} phase in RVE1. The BL-PFC is constructed in the layered form (RVE2 in Fig. 4.3). So, the series and parallel models of piezoelectric composites in Uniform Field approach [14,15] are also followed in this case, and the phase average strain and electric field components in the xz-plane of RVE2 (Fig. 4.3) are assumed as,

$$\bar{\varepsilon}_x^1 = \bar{\varepsilon}_x^2 = \bar{\varepsilon}_x^3 = \bar{\varepsilon}_x \,,$$

$$\bar{\varepsilon}_z^1 = \bar{\varepsilon}_z^2 = \bar{\varepsilon}_z^3 = \bar{\varepsilon}_z \,,$$

$$\bar{\gamma}_{xz}^1 = \bar{\gamma}_{xz}^2 = \bar{\gamma}_{xz}^3 = \bar{\gamma}_{xz} \,,$$

$$\bar{E}_x^1 = \bar{E}_x^2 = \bar{E}_x^3 = \bar{E}_x \,,$$

$$\bar{E}_z^1 = \bar{E}_z^2 = \bar{E}_z^3 = \bar{E}_z \tag{4.6}$$

In Eq. (4.6), the superscript p ($p = 1,2,3$) denotes a phase average field component for p^{th} phase in RVE2. Using Eq. (4.5) in Eq. (4.3d), the values of some elements of the phase average concentration matrices (${}^{RVE1}\boldsymbol{A}^p$, $p = 1,2$) for RVE1 can be obtained as,

$${}^{RVE1}A_{qj}^p = 1 \text{ for } j = q \text{ and } j,q = 2,3,4,8,9 \tag{4.7a}$$

$${}^{RVE1}A_{qj}^p = 0 \text{ for } q \neq j \,,\ q = 2,3,4,8,9 \text{ and } j = 1,2,3,4,5,6,7,8,9 \tag{4.7b}$$

Similarly, using Eq. (4.6) in Eq. (4.3d), the values of the following elements of the phase average concentration matrices (${}^{RVE2}\boldsymbol{A}^p$, $p = 1,2,3$) for RVE2 can be obtained,

$$^{RVE2}A_{qj}^{p}=1 \text{ for } j=q \text{ and } j,q=1,3,5,7,9 \tag{4.8a}$$

$$^{RVE2}A_{qj}^{p}=0 \text{ for } q\neq j,\ q=1,3,5,7,9 \text{ and } q=1,2,3,4,5,6,7,8,9 \tag{4.8b}$$

In Eqs. (4.7a), (4.7b), (4.8a) and (4.8b), the subscript qj indicates an element of $^{RVE1}\boldsymbol{A}^{p}$ or $^{RVE2}\boldsymbol{A}^{p}$ at its q^{th} row and j^{th} column. Now, following the continuity of tractions and normal component of electric displacement at the inter-phase surfaces in a piezoelectric composite [383], the phase average stress and electric displacement components ($\bar{\sigma}_x^p$, $\bar{\tau}_{xz}^p$, $\bar{\tau}_{xy}^p$, $\bar{D}_x^p$) for two different phases ($p=1,2$) of RVE1 (Fig. 4.2(a)) are assumed to be related by the following expressions,

$$\bar{\sigma}_x^1=\bar{\sigma}_x^2,\ \bar{\tau}_{xz}^1=\bar{\tau}_{xz}^2,\ \bar{\tau}_{xy}^1=\bar{\tau}_{xy}^2,\ \bar{D}_x^1=\bar{D}_x^2 \text{ for RVE1} \tag{4.9}$$

Similar assumption can also be made for RVE2 (Fig. 4.3) according to the geometric arrangement of its three different phases ($p=1,2,3$) as,

$$\bar{\sigma}_y^1=\bar{\sigma}_y^2=\bar{\sigma}_y^3,\ \bar{\tau}_{yz}^1=\bar{\tau}_{yz}^2=\bar{\tau}_{yz}^3,\ \bar{\tau}_{xy}^1=\bar{\tau}_{xy}^2=\bar{\tau}_{xy}^3,\ \bar{D}_y^1=\bar{D}_y^2=\bar{D}_y^3 \text{ for RVE2} \tag{4.10}$$

Using the constitutive relations of phases, each of the expressions in Eq. (4.9)/Eq. (4.10) can be expressed in terms of the phase average strain and electric field components. Subsequently, using Eqs. (4.3d) and (4.3e), the following expressions can be obtained for RVE1/RVE2,

$$\sum_{j=1}^{9}\left(^{RVE1}Q_{qj}\ ^{RVE1}A_{jk}^{1}\right)=\aleph_{qk}^{2} \text{ for RVE1,}$$

$$^{RVE1}Q_{qj}=(v_2\aleph_{qj}^{1}+v_1\aleph_{qj}^{2}) \text{ for } q=1,5,6,7 \text{ and } k=1,2,\ldots,9 \tag{4.11}$$

$$\sum_{j=1}^{9}\left(^{RVE2}P_{qj}\ ^{RVE2}A_{jk}^{1}+\ ^{RVE2}Q_{qj}\ ^{RVE2}A_{jk}^{2}\right)=\aleph_{qk}^{3} \text{ for RVE2,}$$

$$\sum_{j=1}^{9}\left(^{RVE2}R_{qj}\ ^{RVE2}A_{jk}^{1}+\ ^{RVE2}S_{qj}\ ^{RVE2}A_{jk}^{2}\right)=\aleph_{qk}^{3} \text{ for RVE2,}$$

$$^{RVE2}P_{qj}=(v_3\aleph_{qj}^{1}+v_1\aleph_{qj}^{3}),$$

$$^{RVE2}Q_{qj}=v_2\aleph_{qj}^{3} \text{ for } q=2,4,6,8 \text{ and } k=1,2,\ldots,9.$$

$$^{RVE2}R_{qj}=v_1\aleph_{qj}^{3} \text{ for } q=2,4,6,8 \text{ and } k=1,2,\ldots,9.$$

$$ {}^{RVE2}S_{qj} = (v_3 \aleph^2_{qj} + v_2 \aleph^3_{qj}) \text{ for } q = 2,4,6,8 \text{ and } k = 1,2,\ldots,9. \tag{4.12} $$

where, $\aleph^p_{qj}$ ($p = 1,2$ for RVE1 or $p = 1,2,3$ for RVE2) is an element of $\aleph^p$ at its q^{th} row and j^{th} column. Using the known elements of ${}^{RVE1}\boldsymbol{A}^1$ for RVE1 (from Eqs. (4.7a)-(4.7b)) in Eq. (4.11), the unknown elements of the same matrix (${}^{RVE1}\boldsymbol{A}^1$) can be expressed as,

$$ \sum_{j=1,\, j\neq 2,3,4,8,9}^{9} \left\langle {}^{RVE1}Q_{qj}\ {}^{RVE1}A^1_{jk} \right\rangle = \left\langle \aleph^2_{qk} - \sum_{j=1,\, j\neq 1,5,6,7}^{9} ({}^{RVE1}Q_{qj}\ {}^{RVE1}A^1_{jk}) \right\rangle $$
$$ \text{for } q = 1,5,6,7 \text{ and } k = 1,2,\ldots,9. \tag{4.13} $$

Similarly, using the known elements of ${}^{RVE2}\boldsymbol{A}^1$ and ${}^{RVE2}\boldsymbol{A}^2$ for RVE2 (from Eqs. (4.8a)-(4.8b)) in Eq. (4.12), the unknown elements of the same matrices can be expressed as,

$$ \sum_{j=1,\, j\neq 1,3,5,7,9}^{9} \left({}^{RVE2}P_{qj}\ {}^{RVE2}A^1_{jk} + {}^{RVE2}Q_{qj}\ {}^{RVE2}A^2_{jk} \right) = $$
$$ \left\langle \aleph^3_{qk} - \sum_{j=1,\, j\neq 2,4,6,8}^{9} \left({}^{RVE2}P_{qj}\ {}^{RVE2}A^1_{jk} + {}^{RVE2}Q_{qj}\ {}^{RVE2}A^2_{jk} \right) \right\rangle , $$

$$ \sum_{j=1,\, j\neq 1,3,5,7,9}^{9} \left({}^{RVE2}R_{qj}\ {}^{RVE2}A^1_{jk} + {}^{RVE2}S_{qj}\ {}^{RVE2}A^2_{jk} \right) = $$
$$ \left\langle \aleph^3_{qk} - \sum_{j=1,\, j\neq 2,4,6,8}^{9} \left({}^{RVE2}R_{qj}\ {}^{RVE2}A^1_{jk} + {}^{RVE2}S_{qj}\ {}^{RVE2}A^2_{jk} \right) \right\rangle \tag{4.14} $$
$$ \text{for } q = 2,4,6,8 \text{ and } k = 1,2,\ldots,9. $$

For RVE1, 45 elements of ${}^{RVE1}\boldsymbol{A}^1$ are known from Eqs. (4.7a)-(4.7b) and the remaining 36 elements of the same matrix (${}^{RVE1}\boldsymbol{A}^1$) can be obtained by the solution of 36 algebraic equations in Eq. (4.13). Subsequently, the other phase average concentration matrix (${}^{RVE1}\boldsymbol{A}^2$) can be obtained using Eq. (4.3e) for determination of effective electro-elastic properties of RVE1 according to Eq. (4.3c).

Similarly, for RVE2, 90 elements of the matrices ${}^{RVE2}\boldsymbol{A}^1$ and ${}^{RVE2}\boldsymbol{A}^2$ are obtained from Eqs. (4.8a)-(4.8b), and other 72 elements of these matrices (${}^{RVE2}\boldsymbol{A}^1$ and ${}^{RVE2}\boldsymbol{A}^2$) can be obtained by the solution of 72 algebraic equations in Eq. (4.14). Then, the other phase average concentration matrix (${}^{RVE2}\boldsymbol{A}^3$) can be

obtained using Eq. (4.3e). After computation of the elements of these phase average concentration matrices, the effective material constants of RVE2 can be obtained from Eq. (4.3c).

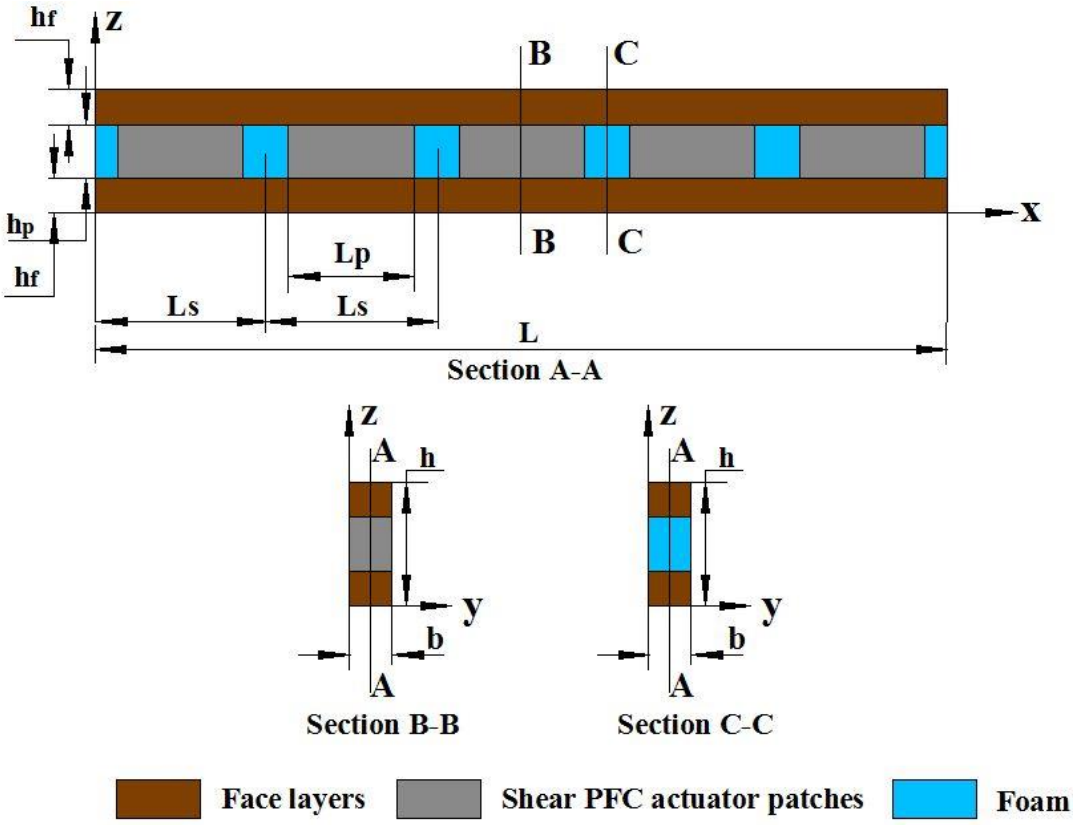

Fig. 4.4 Schematic diagram of the smart sandwich beam.

4.3 Smart sandwich beam

The shear actuation capability of the balanced laminate of PFC is investigated by utilizing it for actuation of bending deformation of a smart sandwich beam as shown in Fig. 4.4 where the shear actuator patches made of the balanced laminate of PFC are located at the core of foam. A number (n_p) of uniform segments with the length of L_s is considered over the length (L, $L=(n_p \times L_s)$) of the smart sandwich beam where every segment contains an actuator patch with the length of L_p at its (segment) centre (Fig. 4.4). The patches are considered to be closely spaced along the length of the smart sandwich beam ($(L_s - L_p) << L_s$), and the corresponding coverage of a patch within a segment is denoted by the ratio as, L_p / L_s. The other geometric dimensions of the smart sandwich beam

are shown in Fig. 4.4. The face layers and foam are considered to be made of the isotropic materials while the material properties of the actuator patches are considered as the homogenized material properties of the BL-PFC.

According to these constructional features of the smart sandwich beam (Fig. 4.4), the material properties do not vary along the y-direction at any point on the xz-plane. So, the rectangular cross-section of the overall beam has a vertical plane (xz-plane) of symmetry. The boundary conditions at the ends of the smart sandwich beam are considered symmetric with respect to this plane of symmetry. The patches of balanced laminate of PFC are activated by the external transverse electric field across their top and bottom fully electrode surfaces, and the corresponding shear actuation force in the xz-plane of any actuator patch can be assumed as uniformly distributed over its (patch) volume because of the homogenized material properties of the patches. So, the shear actuation force in the actuator patches is also symmetric with respect to the aforesaid plane of symmetry. Under these conditions, the smart sandwich beam has no tendency for twist and undergoes bending deformation in the vertical plane (xz-plane) of symmetry due to the shear actuation force. Now, the smart sandwich beam is taken with a narrow rectangular cross-section ($b < h$, Fig. 4.4). Also, there is no applied force on the boundary surfaces of the smart sandwich beam across its thickness (b, in y-direction). Under these geometrical properties, material properties, boundary conditions and applied load, the state of stress at any point in the smart sandwich beam can be assumed as the state of plane stress in the xz-plane. So, the analysis of the smart sandwich beam can be carried out by taking a typical xz-plane. Accordingly, the state of strain and the state of stress at any point in the xz-plane are,

$$\begin{aligned} \boldsymbol{\varepsilon} &= \{\varepsilon_x \quad \varepsilon_z \quad \gamma_{xz}\}^{\mathrm{T}}, \\ \boldsymbol{\sigma} &= \{\sigma_x \quad \sigma_z \quad \tau_{xz}\}^{\mathrm{T}} \end{aligned} \tag{4.15}$$

The linear strain-displacement relations at any point in the xz-plane can be written as,

$$\begin{aligned} \boldsymbol{\varepsilon} &= \boldsymbol{L}\boldsymbol{d}\,, \quad \boldsymbol{d} = \{u \quad w\}^{\mathrm{T}}, \\ \boldsymbol{L} &= \begin{bmatrix} \partial/\partial x & 0 & \partial/\partial z \\ 0 & \partial/\partial z & \partial/\partial x \end{bmatrix}^{\mathrm{T}} \end{aligned} \tag{4.16}$$

where, u and w are the displacements at any point on the xz-plane of the smart sandwich beam along the x and z directions, respectively; $\boldsymbol{d}$ is the displacement vector and $\boldsymbol{L}$ is the operator matrix. The constitutive relations for the isotropic face layers and foam at the core can be written as,

$$\boldsymbol{\sigma}^k = \boldsymbol{C}^k \boldsymbol{\varepsilon},$$

$$\boldsymbol{C}^k = \frac{E^k}{1-(\nu^k)^2}\begin{bmatrix} 1 & \nu^k & 0 \\ \nu^k & 1 & 0 \\ 0 & 0 & (1-\nu^k)/2 \end{bmatrix},\ k=1,2 \tag{4.17a}$$

where, E^k and ν^k are Young's modulus and Poisson's ratio, respectively for the k^{th} material. As the shear actuator patches are activated by applying the external voltage (V) across their top and bottom fully electrode surfaces, they are subjected to a dominant electric field (E_z) along their thickness direction. This electric field (E_z) can be assumed as, $E_z = -V/h_p$. Under this dominant electric field and the plane stress assumption, the constitutive relations for the actuator patches can be written as,

$$\boldsymbol{\sigma}^k = \boldsymbol{C}^k \boldsymbol{\varepsilon} - \boldsymbol{e}^k E_z,$$

$$D_z^k = (\boldsymbol{e}^k)^{\mathrm{T}} \boldsymbol{\varepsilon} + \in_{33}^k E_z,$$

$$\boldsymbol{C}^k = \begin{bmatrix} \tilde{C}_{11}^k & \tilde{C}_{13}^k & \tilde{C}_{15}^k \\ \tilde{C}_{13}^k & \tilde{C}_{33}^k & \tilde{C}_{35}^k \\ \tilde{C}_{15}^k & \tilde{C}_{35}^k & \tilde{C}_{55}^k \end{bmatrix},\ \boldsymbol{e}^k = \begin{Bmatrix} \tilde{e}_{31}^k \\ \tilde{e}_{33}^k \\ \tilde{e}_{35}^k \end{Bmatrix},\ k=3$$

$$\tilde{C}_{11}^k = C_{11}^k - (C_{12}^k)^2/C_{22}^k,\ \tilde{C}_{13}^k = C_{13}^k - (C_{12}^k C_{23}^k)/C_{22}^k,$$

$$\tilde{C}_{15}^k = C_{15}^k - (C_{12}^k C_{25}^k)/C_{22}^k,\ \tilde{C}_{33}^k = C_{33}^k - (C_{23}^k)^2/C_{22}^k,$$

$$\tilde{C}_{35}^k = C_{35}^k - (C_{23}^k C_{25}^k)/C_{22}^k,\ \tilde{C}_{55}^k = C_{55}^k - (C_{25}^k)^2/C_{22}^k,$$

$$\tilde{e}_{31}^k = e_{31}^k - (e_{32}^k C_{12}^k)/C_{22}^k,\ \tilde{e}_{33}^k = e_{33}^k - (e_{32}^k C_{23}^k)/C_{22}^k,$$

$$\tilde{e}_{35}^k = e_{35}^k - (e_{32}^k C_{25}^k)/C_{22}^k \tag{4.17b}$$

In Eqs. (4.17a) and (4.17b), the superscript k denotes the materials for the face layers, foam and actuator patches as per its value as 1, 2 and 3, respectively. The symbols C_{ij}^k, e_{ij}^k and $\in_{ij}^k$ in Eq. (4.17b) are the stiffness, piezoelectric and dielectric coefficients, respectively for the actuator patches ($k=3$).

For FE analysis of the smart sandwich beam by taking a typical xz-plane under the plane stress assumption, this plane (xz-plane) is discretized by nine-node quadrilateral element. The edges of any element are in parallel to the edges of the xz-section of the smart sandwich beam, and a typical element is made of either of the constituent materials within the xz-section. The displacement vector ($\boldsymbol{d}$, Eq. (4.16)) at any point in an element can be expressed by the elemental nodal displacement vector ($\boldsymbol{d}^e$) and the shape function matrix ($\boldsymbol{N}$),

$$\boldsymbol{d} = \boldsymbol{N}\boldsymbol{d}^e \tag{4.18}$$

For a deformation of the smart sandwich beam due to an applied electric field (E_z) across the thickness of the actuator patches, the first variation of its total potential energy (δT_P) can be written as,

$$\delta T_P = \sum_{k=1}^{3}\left[\int_{A_k}\left\langle(\delta\boldsymbol{\varepsilon})^{\mathrm{T}}\boldsymbol{\sigma}^k - (\delta E_z)D_z^k\right\rangle dA_k\right] \tag{4.19}$$

where, δ is an operator for the first variation; A_k is the area of the k^{th} material on the xz-plane of the smart sandwich beam. Using Eqs. (4.17a), (4.17b), (4.16) and (4.18) in Eq. (4.19), the following expression of δT_P for a typical element can be obtained,

$$\delta T_P = (\delta\boldsymbol{d}^e)^{\mathrm{T}}\left(\boldsymbol{K}^e\boldsymbol{d}^e - \boldsymbol{P}_E^e E_z\right),$$

$$\boldsymbol{K}^e = \int_{A_k^e}\left(\boldsymbol{N}^{\mathrm{T}}\boldsymbol{L}^{\mathrm{T}}\boldsymbol{C}^k\boldsymbol{L}\boldsymbol{N}\right)dA_k^e,$$

$$\boldsymbol{P}_E^e = \int_{A_k^e}\left(\boldsymbol{N}^{\mathrm{T}}\boldsymbol{L}^{\mathrm{T}}\boldsymbol{e}^k\right)dA_k^e \tag{4.20}$$

In Eq. (4.20), A_k^e is the area over an element within the k^{th} material on the xz-plane of the smart sandwich beam. According to the principle of minimum potential energy ($\delta T_P = 0$), the governing equations of a typical element can be obtained from Eq. (4.20) as,

$$\boldsymbol{K}^e\boldsymbol{d}^e = \boldsymbol{P}_E^e E_z \tag{4.21}$$

Assembling the elemental equations (Eq. (4.21)), the governing equations of the smart sandwich beam under the plane stress assumption can be obtained as,

$$\boldsymbol{K}\boldsymbol{X} = \sum_{i=1}^{n_p}\boldsymbol{P}_E^i E_z^i \tag{4.22}$$

where, $\boldsymbol{K}$ is the global stiffness matrix; $\boldsymbol{X}$ is the global nodal displacement vector; $\boldsymbol{P}_E^i$ is the electro-elastic coefficient vector that is obtained by assembling the elemental vectors ($\boldsymbol{P}_E^e$) for the elements in i^{th} actuator patch; E_z^i is the applied electric field to the i^{th} actuator patch; n_p is the number of actuator patches within the smart sandwich beam.

The ends of the smart sandwich beam are considered as fixed ends ($u = w = 0$ at $x = 0, L$). The applied electric field (E_z) to the actuator patches in the left half ($0 < x < (L/2)$) of the smart sandwich beam is taken in the opposite directionto that for the actuator patches in the right half ($(L/2) < x < L$) of the same beam. Accordingly, the positive ($+E_z$) and negative ($-E_z$) electric fields are applied to the actuator patches in ($0 < x < (L/2)$ and ($(L/2) < x < L$), respectively, and these applied electric fields are considered to be of equal magnitude. This kind of applied electric field to the actuator patches is considered to cause the bending deflection of the smart sandwich beam either in upward ($+z$) or in downward ($-z$) direction.

4.4 Results and discussions

4.4.1 Verification of effective properties of the laminate of PFC

As mentioned in section 4.2, the effective properties of the balanced laminate of PFC are presently computed in two steps. In the first step, the asymptotically homogenized material properties of the vertically reinforced 2-2 PFC layer are computed. Using these homogenized material properties of 2-2 PFC layers, the BL-PFC is assumed as a laminate of homogeneous layers, and the effective properties of this laminate of homogeneous layers are computed in the second step. For verification of the corresponding formulation (section 4.2.2), first, the presently computed effective properties of the 2-2 PFC layer are verified considering the material and geometrical properties of its (2-2 PFC) constituent phases as that are taken for a similar 2-2 PFC in [395]. These results are illustrated in Table 4.1 together with the similar results available in [395]. It may be observed from Table 4.1 that the present results are in good agreement with the available results [395], and this comparison verifies the present

formulation (section 4.2.2) for computation of effective properties of 2-2 PFC lamina.

Table 4.1 Verification of the present formulation for effective properties of 2-2 PFC lamina.

Parameters	UFM [395]	PHM [395]	Present
E_1 (GPa)	47.14	47.15	47.152
E_2 (GPa)	19.06	19.08	19.414
E_3 (GPa)	42.16	42.17	42.174
G_{12} (GPa)	6.011	6.015	5.982
G_{13} (GPa)	16.99	17.00	17.00
G_{23} (GPa)	6.664	6.216	6.6238
ν_{12}	0.3878	0.3878	0.3893
ν_{13}	0.4388	0.4388	0.4389
ν_{23}	0.1699	0.17	0.1737
d_{31} (pC/N)	-182.9	-182.9	-183
d_{32} (pC/N)	-173.4	-173.4	-174.2
d_{33} (pC/N)	435.8	435.8	435.9
$\in_{33}$ (nF/m)	6.068	6.069	6.070

In the next step, to verify the computation of effective properties of the balanced laminate of PFC using the material properties of the corresponding homogenized 2-2 PFC layers, there is no similar result available in the literature. So, presently a numerical study on the electromechanical deformation of this laminate of homogenized 2-2 PFC layers is performed, where the material properties of the laminate are either considered as the properties of individual layer (layer-wise properties) or considered as the computed effective properties of that laminate. This numerical study is carried out on the basis of the main objective of the shear actuated deformation of the laminate by considering it in the form of a laminated beam as shown in Figs. 4.5(a)-(b). The ends of the laminated beam are fixed ends, and two pairs of homogenized 2-2 PFC laminae are considered where the fiber orientation angles in every pair of homogenized 2-2 PFC laminae are taken as -35^o and $35^o - 180^o$ with respect to the vertical (z) axis. Other geometrical properties of the laminated beam (Fig. 4.5) are considered as, $a = 0.1$ m, $c = 500$ μm, $b = 412$ μm, $b_f = 100$ μm, $b_e = 3$ μm. The top and bottom surfaces of the laminated beam (Fig. 4.5) are electrode surfaces, but each of these electrodes is separated in two parts at the middle point of the same beam with a gap (Δa) of $a/20$ (Fig. 4.5) in particular to apply the

transverse electric fields (E_z) over the two halves ($0<x<a/2$ and $a/2<x<a$) of the beam (Fig. 4.5) in opposite direction ($+E_z$ on $0<x<(a-\Delta a)/2$ and $-E_z$ on $(a+\Delta a)/2<x<a$).

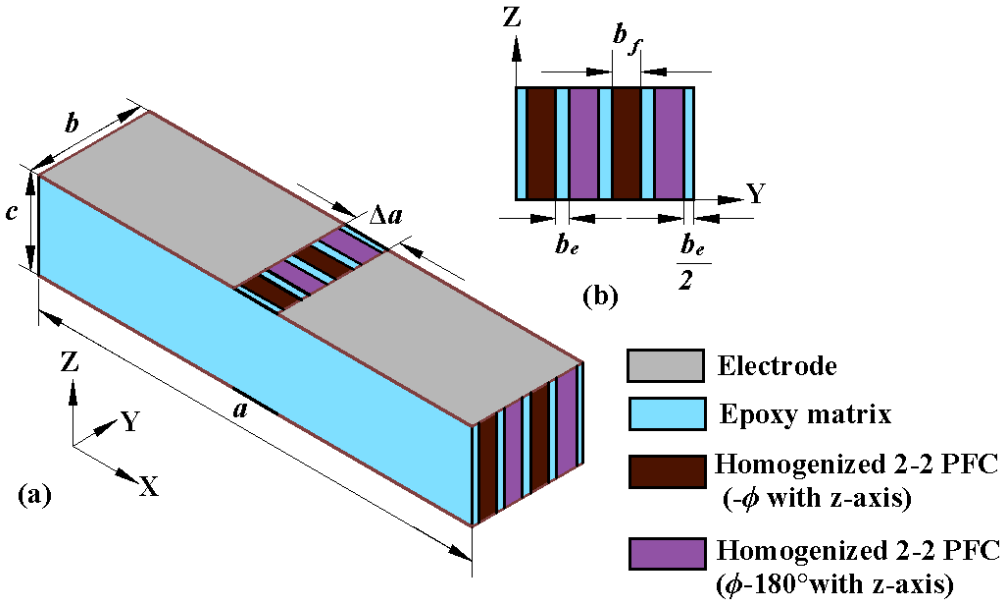

Fig. 4.5 (a) Schematic diagram of a beam made of balanced laminate of PFC with two pairs of 2-2 PFC layers, (b) a typical cross-section of the beam made of balanced laminate of PFC.

With this configuration of the laminated beam (Fig. 4.5) and applied transverse electric field, its three-dimensional FE model is developed in ANSYS simulation software using SOLID 226 element with the nodal degrees of freedoms as the electric potential and three translational displacements along the axes of the reference coordinate system. For consideration of layer-wise properties of the laminate, a typical element is considered to be made of either of the materials for layers in the laminate. In parallel, instead of the layer-wise properties of the laminate, its (laminate) computed effective properties are considered as the material properties for all elements in the FE mesh of the laminated beam. For each of these two cases of material properties of the laminated beam, the nodal displacements over the cross-sections at the ends of the laminated beam are set to zero value, and the nodal electric potentials over the electrode surfaces are assigned according to the aforesaid applied transverse electric fields. Subsequently, the FE mesh convergence study is performed for sufficient numerical accuracy in the result, and the corresponding FE mesh of

the laminated beam is used to obtain its deformation due to the applied transverse electric fields.

From these results, it is observed that the laminated beam (Fig. 4.5) mainly undergoes bending deformation in the vertical (xz) plane due to the applied transverse electric fields, and thus its (laminated beam) transverse deflection is plotted in Fig. 4.6 for each of the cases of its (laminated beam) "Layer-wise material properties" and "Homogenized material properties".

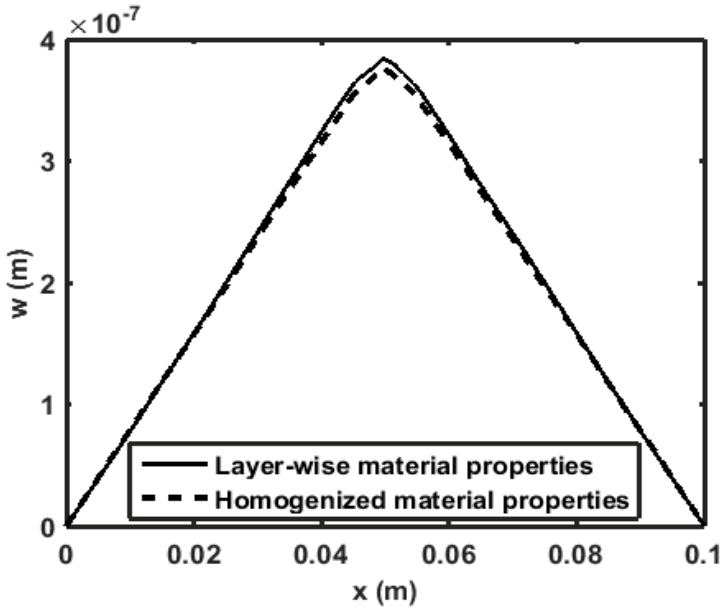

Fig. 4.6 Bending deflection of the beam made of the BL-PFC due to the applied electric fields over two halves of the same beam in the opposite direction.

It may be noted from Fig. 4.6 that the result for the layer-wise material properties of the laminate is very close to that for the computed effective properties of the same laminate. So, the present formulation (section 4.2.2) provides a good estimation of effective properties of the balanced laminate of PFC although this verification is presently carried out based on the shear actuated deformation of the laminate.

4.4.2 Verification of FE model of smart sandwich beam

In order to verify the present FE formulation of the smart sandwich beam (Fig. 4.4), two identical segments ($n_p = 2,\ L_s = L/2$) of actuator patches are considered where every segment contains a shear piezoelectric actuator patch ($L_p / L_s = 0.2$) made of a monolithic piezoelectric material (PZT5H). For an applied electric field across the thickness of the actuator patches, the bending shape of

this smart sandwich beam is computed using the present FE formulation, and this result is presented in Fig. 4.7 together with the similar result available in [196]. It may be observed from Fig. 4.7 that the present FE result is very close to the similar analytical result available in [196] and this comparison verifies the present FE formulation for a smart sandwich beam using shear piezoelectric actuator patches at the core.

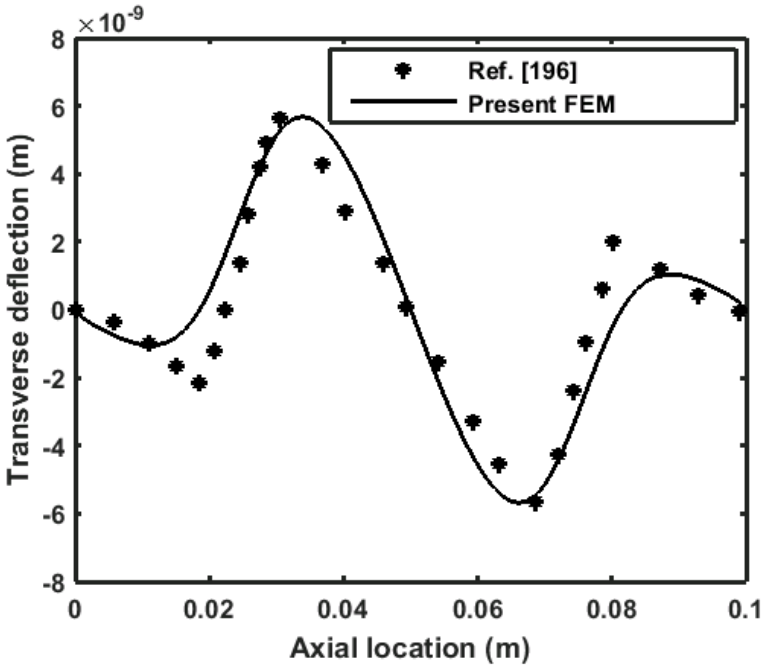

Fig. 4.7 Bending deflection of a smart sandwich beam with two segments of actuator patches for the uniform applied transverse electric field to the monolithic shear piezoelectric actuator patches.

Table 4.2 Effective properties of the balanced laminate of PFC (BL-PFC, $\phi = 35^{o}$).

Balanced laminate of PFC								
C_{11} (GPa)	C_{22} (GPa)	C_{33} (GPa)	C_{12} (GPa)	C_{13} (GPa)	C_{23} (GPa)	C_{44} (GPa)	C_{55} (GPa)	C_{66} (GPa)
21.246	45.998	32.743	11.915	15.669	16.669	8.814	10.313	5.715
e_{11} (C/m^2)	e_{12} (C/m^2)	e_{13} (C/m^2)	e_{26} (C/m^2)	e_{35} (C/m^2)	ϵ_{11} (nF/m)	ϵ_{22} (nF/m)	ϵ_{33} (nF/m)	
3.819	-0.898	8.103	0.129	8.643	3.45	1.21	6.89	

4.4.3 Analysis of electro-elastic properties of BL-PFC

Apart from the verification results (Fig. 4.6), the BL-PFC is presently considered to be made of PZT5H fibers and epoxy matrix as the same constituent materials

are considered for the obliquely-reinforced 1-3 PFC in the previous chapter (Chapter 3). Unless otherwise mentioned, the fiber volume fraction (FVF) of the 2-2 PFC layers within the balanced laminate is taken as 0.8. The thicknesses of the 2-2 PFC and epoxy binder layers in the balanced laminate are considered as, 100 μm and 3 μm, respectively. The corresponding computed effective properties of the BL-PFC are illustrated in Table 4.2 considering the fiber orientation angles of every pair of 2-2 PFC layers (FVF of 0.8) as -35^o and $35^o - 180^o$ with respect to the vertical (z) axis of the laminate coordinate system. This fiber orientation angle (35^o) for the BL-PFC is chosen typically for an illustration of its material properties (Table 4.2). Similar effective properties of the BL-PFC can also be obtained for any other fiber orientation angle using the same formulation (section 4.2.2). However, it may be observed from Table 4.2 that the BL-PFC possesses orthotropic material properties with only one non-zero piezoelectric coefficient (e_{35}) associated with the transverse electric field. As it (e_{35}) is a shear piezoelectric coefficient, the BL-PFC is capable to produce transverse shear actuation force for an applied transverse electric field. There is no other kind of actuation force in the BL-PFC. So, the layered arrangement of the obliquely-reinforced 1-3 PFC layers in the form of a balanced laminate eliminates the transverse normal actuation force although the individual obliquely reinforced 1-3 PFC layer produces both the transverse normal and shear actuation forces for an applied transverse electric field.

Table 4.3 Effective properties of vertically reinforced 1-3 PFC.

Vertically reinforced 1-3 PFC								
C_{11} (GPa)	C_{22} (GPa)	C_{33} (GPa)	C_{12} (GPa)	C_{13} (GPa)	C_{23} (GPa)	C_{44} (GPa)	C_{55} (GPa)	C_{66} (GPa)
16.631	45.998	50.245	7.313	9.226	21.301	17.873	4.809	4.286
e_{31} (C/m^2)	e_{32} (C/m^2)	e_{33} (C/m^2)	e_{24} (C/m^2)	e_{15} (C/m^2)	ϵ_{11} (nF/m)	ϵ_{22} (nF/m)	ϵ_{33} (nF/m)	
-0.602	-1.566	21.389	0.704	0.019	0.185	1.194	10.135	

4.4.4 Shear actuation capability of balanced laminate of PFC

The elimination of the transverse normal actuation force in the obliquely reinforced 1-3 PFC by means of constructing BL-PFC may result a shear mode PFC (BL-PFC) with the improved shear actuation capability. It is verified in this

section by comparing the shear actuation capability of the BL-PFC with that of the obliquely reinforced 1-3 PFC. For this comparison study, the 2-2 PFC layers and the epoxy binding layers are taken with the aforesaid geometrical and material properties while the fiber orientation angle of the 2-2 PFC layers in the PFC laminate is taken differently for obtaining the obliquely reinforced 1-3 PFC and BL-PFC from the same PFC laminate of 2-2 PFC layers. The properties of the BL-PFC are computed directly from the present micromechanics formulation (section 4.2.2). However, for computation of the properties of obliquely reinforced 1-3 PFC, first, the properties of the vertically reinforced 1-3 PFC are computed for the fiber orientation angle of the 2-2 PFC layers as 0^o as illustrated in Table 4.3. Subsequently, the properties of the vertically reinforced 1-3 PFC are transformed for a fiber orientation angle other than 0^o corresponding to the obliquely reinforced 1-3 PFC.

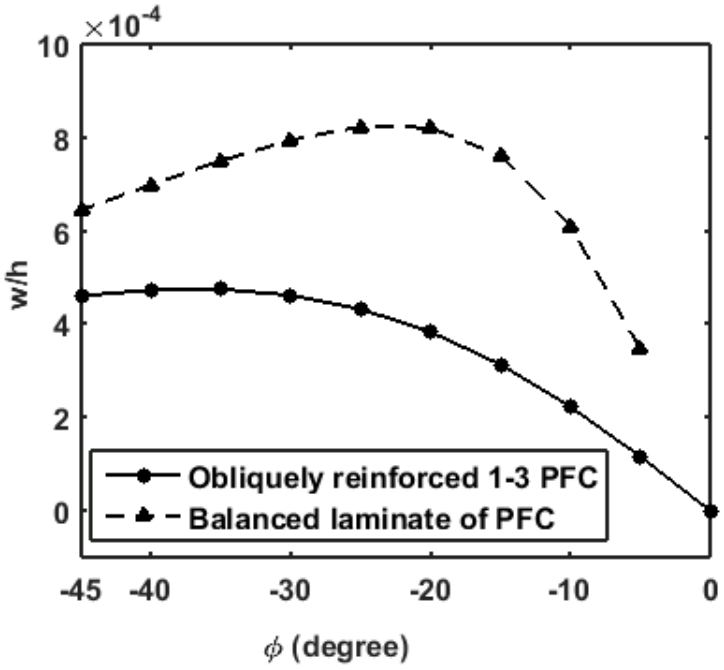

Fig. 4.8 (a) Variation of maximum transverse deflection of the smart sandwich beam with the fiber orientation angle (ϕ with the z-axis) of the obliquely reinforced 1-3 PFC or balanced laminate of PFC ($|E_z| = 50$ V/mm).

These BL-PFC and obliquely reinforced 1-3 PFC, made in a uniform manner, are used separately as the material of shear actuator patches at the core of the sandwich beam (Fig. 4.4), and their shear actuation capabilities are studied by means of activating the actuator patches in causing shear actuated

bending deformation of the sandwich beam. The sandwich beam (Fig. 4.4) is taken with two equal segments ($n_p = 2,\ L_s = L/2$) over its length (L), and every segment contains an actuator patch at its (segment) centre with a coverage (L_p / L_s) of 0.95. The other geometrical properties of the smart sandwich beam (Fig. 4.4) are considered as, h_f = 2 mm, h_p = 2 mm and L = 0.4 m. The material for the face layers is considered as Aluminium (E = 70 GPa, ν = 0.3), and the material properties of the foam at the core are taken as ([196]), E = 35.3 MPa, G = 12.76 MPa. The applied electric fields (E_z) to the actuator patches within the two segments ($n_p = 2$) are of equal magnitude, but they are in opposite sign ($+E_z$ for the patch in $0 < x < L/2$ and $-E_z$ for the patch in $L/2 < x < L$). Fixed-fixed boundary conditions constrain the ends of the sandwich beam.

With these geometrical properties, material properties, applied electric field to the actuator patches and boundary conditions at the ends of the beam; the variations of the maximum transverse deflection (w/h) of the smart sandwich beam with the fiber orientation angle (ϕ) is illustrated in Fig. 4.8 for every kind of actuator material (obliquely reinforced 1-3 PFC and BL-PFC). It may be observed from Fig. 4.8 that an indicative enhancement of the shear actuated bending deflection of the smart sandwich beam appears for the actuator patches of the BL-PFC instead of the patches of the obliquely reinforced 1-3 PFC. It may also be observed that the shear actuation capability of the actuator patches of BL-PFC is not uniform for all the angles (ϕ) because of the associated variations of its effective properties. So, there would be an optimum angle (ϕ) of the BL-PFC for its maximum actuation capability as it presently appears between -20^o and -25^o (Fig. 4.8).

Figure 4.9 shows the bending deflections of the smart sandwich beam (Fig. 4.4) for the applied electric field ($|E_z| = 50$ V/mm) when the actuator patches are made either of monolithic piezoelectric material (PZT5H), obliquely reinforced 1-3 PFC and BL-PFC. The geometric configuration of the smart sandwich beam is considered as that is for the previous results (Fig. 4.8). The fiber orientation angle (ϕ) of the obliquely reinforced 1-3 PFC is taken as 35^o corresponding to its

maximum actuation capability (Fig. 4.8). The angles ($-\phi$ and ($\phi - 180^o$)) for the BL-PFC are taken with $\phi = 20^o$ for its maximum actuation capability (Fig. 4.8).

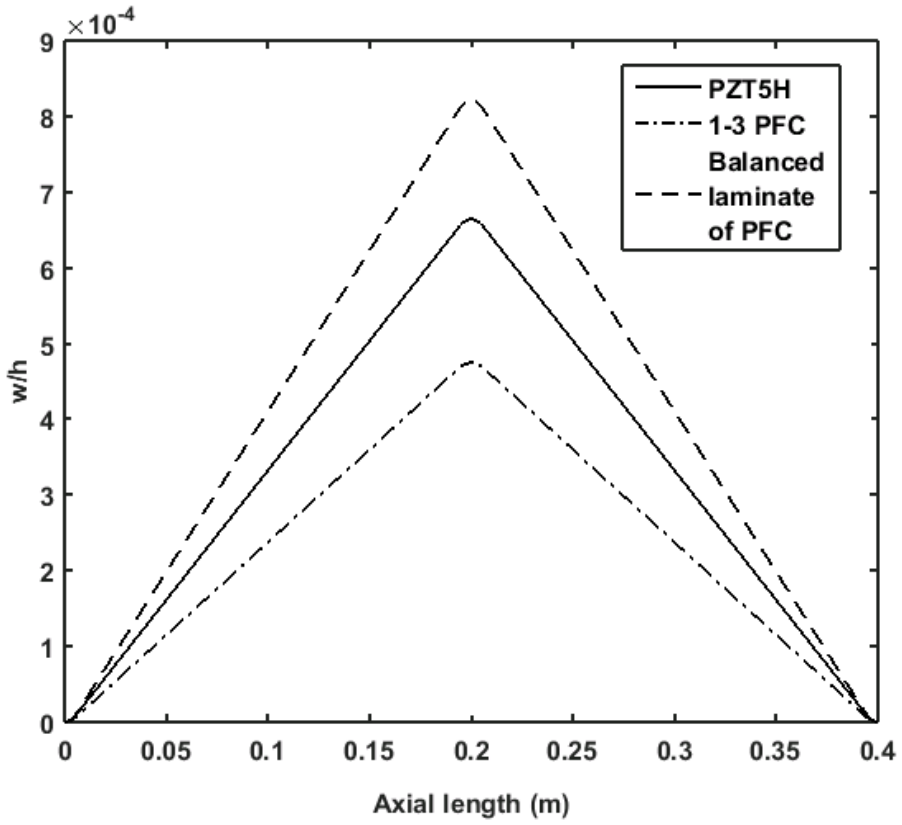

Fig. 4.9 Bending deflection of the smart sandwich beam for the material of actuator patches as either of the monolithic piezoelectric ceramic (PZT 5H), obliquely reinforced 1-3 PFC and balanced laminate of PFC.

The material of the monolithic piezoelectric actuator patches is the same material that is taken for the fibre phase of the obliquely reinforced 1-3 PFC and balanced laminate of PFC. The monolithic piezoelectric actuator patches are poled along the longitudinal (x) direction so that they provide shear actuation force in the xz-plane for a transversely applied electric field (E_z). It may be observed from this result (Fig. 4.9) that the actuation capability of the present BL-PFC is indicatively more than that for the monolithic shear piezoelectric actuator or the obliquely reinforced 1-3 PFC. So, the present BL-PFC may be recommended as a potential material for shear actuation of thin-walled flexible structures. Similar to the results in Fig. 4.8, the variations of the maximum deflection of the smart sandwich beam with the angle (ϕ) of the BL-PFC are illustrated in Fig. 4.10 for different values of FVF of the 2-2 PFC layers in the

BL-PFC. It may be observed from the results in Fig. 4.10 that the actuation capability of the BL-PFC increases with the increase of the FVF of the corresponding 2-2 PFC layers, but this increment of actuation capability occurs up to a certain value of FVF.

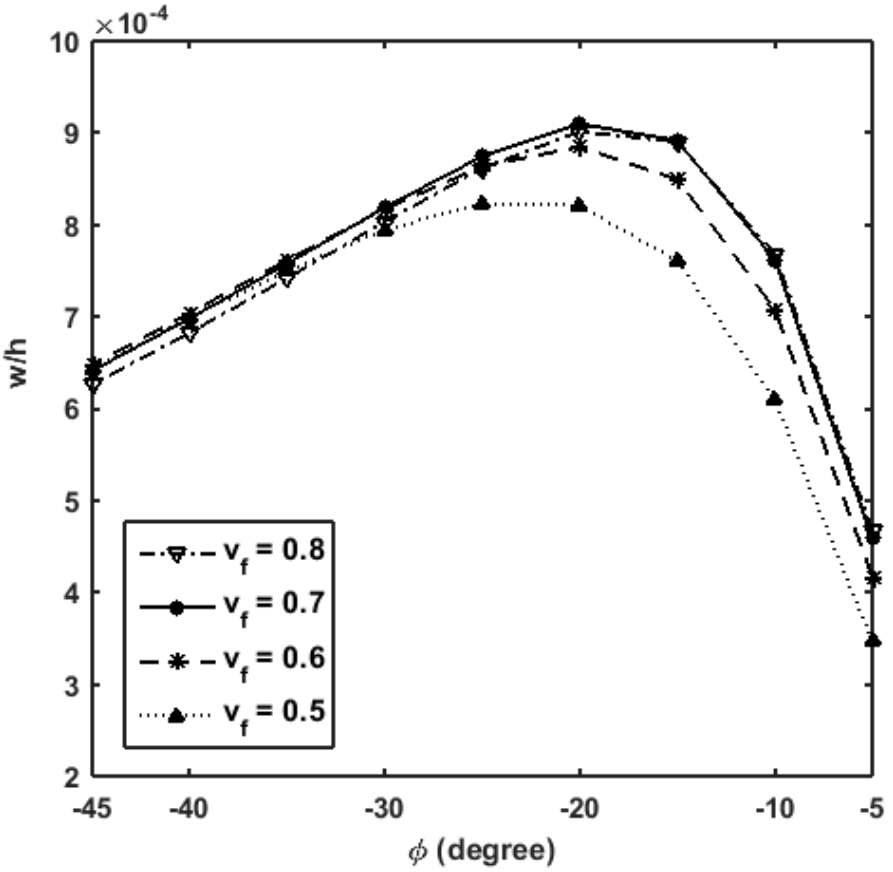

Fig. 4.10 Variations of the maximum deflection of the smart sandwich beam with the angle (ϕ) of the BL-PFC for different FVFs of its 2-2 PFC layers.

In the previous results (Figs. 4.8-4.10), two segments ($n_p = 2$) of actuator patches corresponding to the two halves ($0 < x < L/2$ and $L/2 < x < L$) of the smart sandwich beam are considered with a coverage (L_p / L_s) of 0.95. Now, if the number of segments of actuator patches is increased with the same strategy for the applied electric field ($+E_z$ on the patches in $0 < x < L/2$ and $-E_z$ on the patches in $L/2 < x < L$), then the corresponding variations of the maximum transverse deflection of the smart sandwich beam are illustrated in Fig. 4.11 for different values of the coverage (L_p / L_s) of a typical patch within its segment. The actuator patches are made of the balanced laminate of PFC that has the

pairs of 2-2 PFC layers (FVF of 0.8) with the fiber orientation angles of -20^o and $(20^o - 180^o)$. It may be observed from Fig. 4.11 that the bending deflection of the smart sandwich beam indicatively increases with the increase of the number (n_p) of segments of the actuator patches for any value of the coverage (L_p / L_s). But this increment of actuation occurs up to a certain number of segments. It may also be observed from Fig. 4.11 that for any number (n_p) of segments of actuator patches, the actuation of the smart sandwich beam increases for a higher value of the coverage (L_p / L_s) although the effect of the coverage (L_p / L_s) on the actuation does not appear indicatively for a higher number (n_p) of segments of actuator patches.

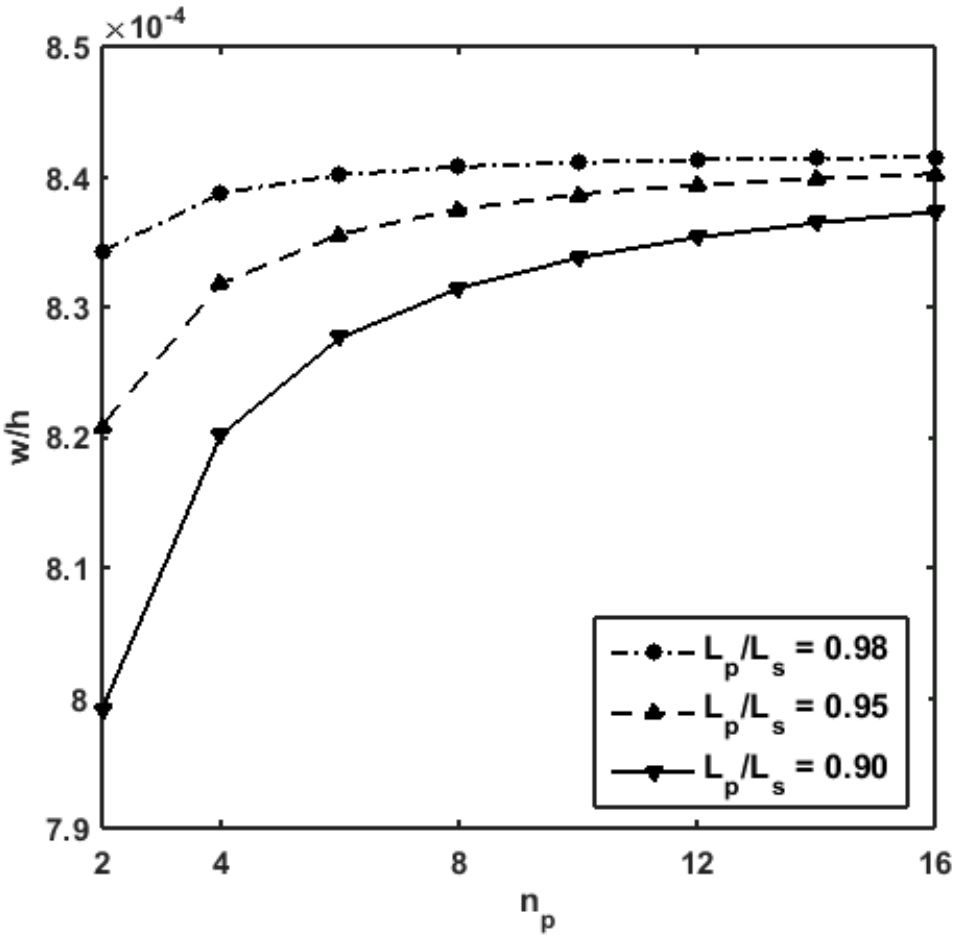

Fig. 4.11 Variations of the maximum deflection of the smart sandwich beam with the number of segments of patches for different values of coverage (L_p / L_s) of a typical patch in its segment.

4.5 Summary

In this chapter, a new balanced laminate of PFC is designed by taking an even number of obliquely reinforced 2-2 PFC layers. The 2-2 PFC layers in the BL-PFC are bonded through the epoxy binder layers while their thickness is taken in micro-scale. So, the investigation on the shear actuation capability of the BL-PFC is carried out by evaluating its (laminate) effective properties through a micromechanics formulation. With these effective properties, the balanced laminate of PFC is utilized as a material of the actuator patches at the core of a sandwich beam, and the corresponding results for shear actuated bending deflection of the beam are evaluated. These results reveal an indicative shear actuation capability of the BL-PFC. It is found that the shear actuation capability of the BL-PFC is indicatively higher than that of the traditional monolithic shear piezoelectric actuators. Apart from this improved shear actuation capability of the BL-PFC, it possesses greater flexibility due to the reinforcement of short-length piezoelectric fibers in the epoxy matrix. With reference to these advantages, the present BL-PFC may be recommended as a potential material for shear piezoelectric actuation of thin and flexible structures.

Chapter 5

Shear-based vibration control of annular sandwich plates using different piezoelectric fiber composites: a comparative study

5.1 Introduction

As it is observed from the literature survey (Chapter 1), advanced design of annular/circular plates is usually achieved by implementing the concept of the smart structure where the piezoelectric materials are used to incorporate the self-sensing and self-controlling capabilities of the plates. In this development of smart annular/circular plates, the extension mode piezoelectric actuators are utilized extensively (section 1.6). Besides, the shear mode piezoelectric actuators can also be used, where the available studies show the requirement of the sandwich configuration of a plate for its effective shear mode piezoelectric actuation. In this consequence, the shear piezoelectric actuators can be employed in active control of an annular/circular plate if the required sandwich configuration of the plate is compatible with the other requirements in its (plate) design for an application. However, a pertaining study on the utilization of a shear piezoelectric actuator in active control of annular/circular plates is not yet addressed in the literature to the best knowledge of the author. It is attempted in Chapter 3 for an investigation on the shear actuation capability of an obliquely reinforced 1-3 PFC in control of annular plates. The corresponding results in Chapter 3 show a good shear-based control of annular plates, but the shortcomings in the shear actuation mechanism in the obliquely reinforced 1-3 PFC lead to a new BL-PFC that is proposed in Chapter 4, where it is observed that the BL-PFC possesses indicatively superior shear actuation capability than that of the obliquely reinforced 1-3 PFC. So, the BL-PFC may be used in place of the obliquely reinforced 1-3 PFC for improved shear mode actuation of annular plates.

In this concern of shear mode actuation of annular plates, other available shear mode actuators namely Shear Actuated Fiber Composite (SAFC) [73] and monolithic shear piezoelectric actuator as shown in Figs. 5.1(a)-(b) can also be used. The SAFC (Fig. 5.1(a)) is basically a 2-2 PFC lamina constructed in the Cartesian material coordinate system (xyz), where the piezoelectric phase is

poled (P) along the x-direction and the externally applied external electric field (E_z) acts in the transverse (z) direction so that the 2-2 PFC lamina produces electrically induced shear actuation force in the xz-plane.

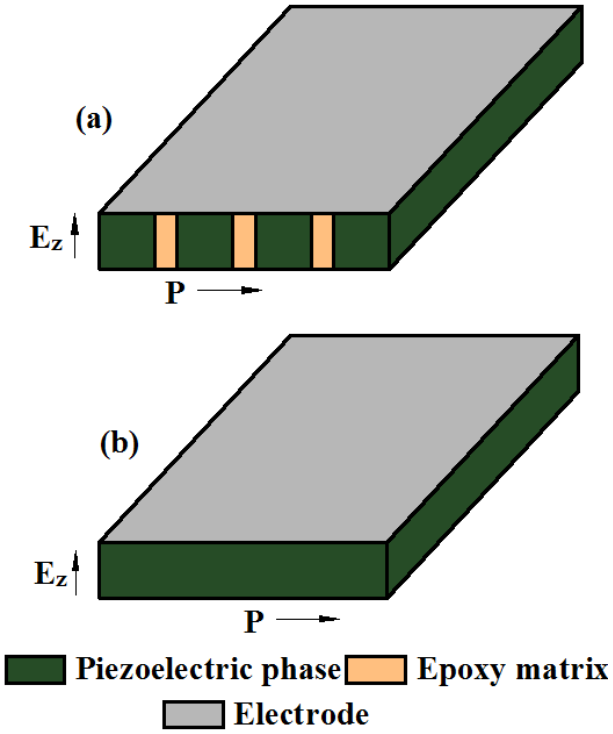

Fig. 5.1 Schematic diagrams of (a) SAFC and (b) monolithic shear piezoelectric actuators.

Besides this SAFC, the conventional shear mode piezoelectric actuator (Fig. 5.1(b)) is made of the monolithic piezoelectric material that is poled (P) along the x-direction in the Cartesian material coordinate system (xyz) so that it is capable to provide shear actuation force in the xz-plane for an applied electric field (E_z) along the transverse (z) direction. However, these existing shear-mode actuators (Figs. 5.1(a)-(b)) may provide better shear actuation than that of the present BL-PFC. In this view, the study in this chapter is concerned with a comparative study on the shear actuation capabilities of the BL-PFC (Fig. 4.1), SAFC (Fig. 5.1(a)) and monolithic shear piezoelectric actuator (Fig. 5.1(b)) in shear-based active control of an annular plate. The annular plate is taken here in the form of an annular sandwich plate similar to that considered in Chapter 3 (Fig. 3.2). The actuator patches in the shape of the annular sector are embedded in the core and are activated according to a shear-based control strategy as that is presented in section 3.5. However, the patches of a shear actuator are now

made from an actuator laminate that is comprised of a number of identical layers of that actuator. The actuator laminate is considered here to achieve greater shear actuation force in the expense of lesser applied voltage.

For the analysis of the smart annular sandwich plate, first, the effective electro-elastic properties of the actuator laminate are determined through a micromechanics formulation based on the Uniform Field Method (UFM). Next, a closed-loop FE model of the annular sandwich plate is developed on the basis of the layer-wise shear deformation theory. Using this FE model, the mode-based optimal arrangement of the actuator patches in the core is determined for each of the BL-PFC, SAFC and monolithic shear piezoelectric actuators. On the basis of this optimal arrangement of actuator patches, the actuation capabilities of the three different shear actuators are evaluated in attenuation of bending modes of vibration of the annular sandwich plate. Finally, a comparative study on the actuation capabilities of the shear actuators is performed to address the best one in attenuation of vibration of the annular sandwich plate.

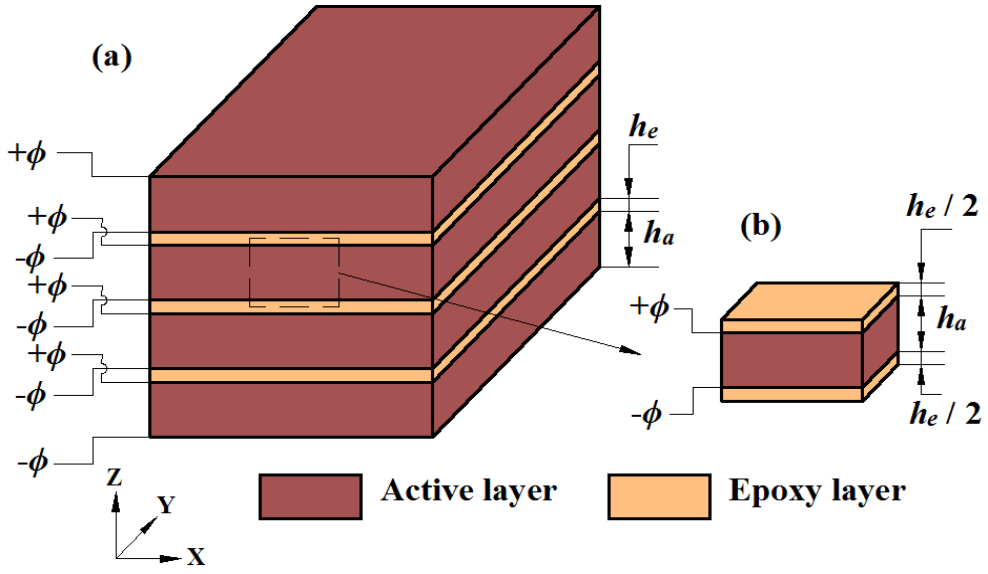

Fig. 5.2 (a) Laminate of shear piezoelectric actuator (active) layers and (b) the corresponding Representative Volume Element (RVE) ($+\phi$ / $-\phi$ is the positive/negative electric potential).

5.2 Shear actuator laminate and effective properties

For a specified applied transverse electric field across the top and bottom electrode surfaces of a piezoelectric actuator, the corresponding required voltage increases at a higher thickness of the actuator. So, the piezoelectric actuators would be of small thickness. But, a small thickness of a piezoelectric actuator

would cause its insufficient shear actuation force in an application. So, presently every shear actuator (BL-PFC, SAFC and monolithic shear piezoelectric actuator) is taken in the form of a laminate within a thickness (h_c) of application, where a number of the uniform actuator (active) layers of small thickness (h_a) are bonded through the thin (h_e) epoxy binder layers as shown in Fig. 5.2(a). The top and bottom surfaces of every actuator (active) layer are fully electrode surfaces, and the active layers within the laminate are considered to be activated by the uniform external electric field/voltage.

The electrodes over the top and bottom surfaces of every active layer are considered as the printed silver electrodes. As this kind of electrode usually appears with a thickness in nano-scale [396–398], its (electrode) contribution to the stiffness of the laminate is not accounted. So, the electrodes are presently assumed to provide isopotential surfaces only. Accordingly, the effective properties of the laminate are determined by defining a representative volume element (RVE) as shown in Fig. 5.2(b), where the active layer is made of either of the aforesaid actuator materials. The active layer of shear mode monolithic piezoelectric actuator (Fig. 5.1(b)) possesses homogeneous material properties, while the same layer made of BL-PFC or SAFC is also considered as a homogeneous layer according to its (BL-PFC or SAFC) asymptotically homogeneous properties. Consequently, the RVE becomes a volume of two-phase composite made of the layers of two homogeneous materials, and its effective properties are determined using the Uniform Field Method (UFM).

According to the aforesaid arrangement of electrodes in the laminate/RVE, the active (piezoelectric) layer is subjected to a dominant electric field (E_z) in the transverse (z) direction. This electric field is also always specified for the present use of the laminate as an actuator. So, the converse piezoelectric constitutive relation for the active (piezoelectric) layer and the similar constitutive relation for the epoxy layers can be written as,

$$\boldsymbol{\sigma}^p = \boldsymbol{C}^p\boldsymbol{\varepsilon}^p - \boldsymbol{e}^p E_z \text{ for } p=1 \text{ and } \boldsymbol{\sigma}^p = \boldsymbol{C}^p\boldsymbol{\varepsilon}^p \text{ for } p=2 \tag{5.1a}$$

where, p represents the active layer or epoxy layer as per its value as 1 or 2, respectively; $\boldsymbol{\sigma}^p / \boldsymbol{\varepsilon}^p$ is the stress/strain vector for p^{th} phase; $\boldsymbol{C}^p$ is the stiffness matrix of p^{th} phase; $\boldsymbol{e}^p$ is a vector of piezoelectric coefficients

associated with the electric field (E_z) in the p^{th} phase. Equation (5.1a) can also be written in terms of the phase volume-average field quantities as,

$$\bar{\boldsymbol{\sigma}}^p = \boldsymbol{C}^p \bar{\boldsymbol{\varepsilon}}^p - \boldsymbol{e}^p \bar{E}_z \text{ for } p=1 \text{ and}$$
$$\bar{\boldsymbol{\sigma}}^p = \boldsymbol{C}^p \bar{\boldsymbol{\varepsilon}}^p \text{ for } p=2$$
$$\bar{\boldsymbol{\sigma}}^p = \left\{ \bar{\sigma}_x^p \quad \bar{\sigma}_y^p \quad \bar{\sigma}_z^p \quad \bar{\tau}_{yz}^p \quad \bar{\tau}_{xz}^p \quad \bar{\tau}_{xy}^p \right\}^{\mathrm{T}},$$
$$\bar{\boldsymbol{\varepsilon}}^p = \left\{ \bar{\varepsilon}_x^p \quad \bar{\varepsilon}_y^p \quad \bar{\varepsilon}_z^p \quad \bar{\gamma}_{yz}^p \quad \bar{\gamma}_{xz}^p \quad \bar{\gamma}_{xy}^p \right\}^{\mathrm{T}} \tag{5.1b}$$

where, the over-bar indicates phase volume-average quantity; $\bar{\sigma}_x^p / \bar{\varepsilon}_x^p$, $\bar{\sigma}_y^p / \bar{\varepsilon}_y^p$ and $\bar{\sigma}_z^p / \bar{\varepsilon}_z^p$ are the average normal stress/strain components over the volume of p^{th} phase along the x, y and z directions, respectively; $\bar{\tau}_{yz}^p / \bar{\gamma}_{yz}^p$, $\bar{\tau}_{xz}^p / \bar{\gamma}_{xz}^p$ and $\bar{\tau}_{xy}^p / \bar{\gamma}_{xy}^p$ are the average shear stress/strain components over the volume of p^{th} phase in the yz, xz and xy planes, respectively.

For the asymptotically homogeneous volume of the RVE, the tractions at the inter-phase surfaces would be continuous field quantities as $\bar{\sigma}_z^1 = \bar{\sigma}_z^2 = \bar{\sigma}_z$, $\bar{\tau}_{xz}^1 = \bar{\tau}_{xz}^2 = \bar{\tau}_{xz}$, $\bar{\tau}_{yz}^1 = \bar{\tau}_{yz}^2 = \bar{\tau}_{yz}$, where $\bar{\sigma}_z$, $\bar{\tau}_{xz}$ and $\bar{\tau}_{yz}$ are the volume-average stress components over the volume of the RVE. Further, since the layers of two different phases are continuously distributed in the xy-plane (Fig. 5.2), the in-plane strain components are assumed to be uniform over both the phases as $\bar{\varepsilon}_x^1 = \bar{\varepsilon}_x^2 = \bar{\varepsilon}_x$, $\bar{\varepsilon}_y^1 = \bar{\varepsilon}_y^2 = \bar{\varepsilon}_y$, $\bar{\gamma}_{xy}^1 = \bar{\gamma}_{xy}^2 = \bar{\gamma}_{xy}$, where $\bar{\varepsilon}_x$, $\bar{\varepsilon}_y$ and $\bar{\gamma}_{xy}$ are the volume-average strain components over the volume of the RVE. These uniform field quantities over the volume of the RVE, and also the remaining phase volume-average stress and strain components can be written as,

$$\bar{\boldsymbol{\sigma}}_U^p = \left\{ \bar{\sigma}_x^p \quad \bar{\sigma}_y^p \quad \bar{\tau}_{xy}^p \right\}^{\mathrm{T}},$$
$$\bar{\boldsymbol{\sigma}}_N^p = \bar{\boldsymbol{\sigma}}_N,$$
$$\bar{\boldsymbol{\sigma}}_N = \left\{ \bar{\sigma}_z \quad \bar{\tau}_{yz} \quad \bar{\tau}_{xz} \right\}^{\mathrm{T}}$$
$$\bar{\boldsymbol{\varepsilon}}_U^p = \left\{ \bar{\varepsilon}_z^p \quad \bar{\gamma}_{yz}^p \quad \bar{\gamma}_{xz}^p \right\}^{\mathrm{T}},$$
$$\bar{\boldsymbol{\varepsilon}}_N^p = \bar{\boldsymbol{\varepsilon}}_N,$$
$$\bar{\boldsymbol{\varepsilon}}_N = \left\{ \bar{\varepsilon}_x \quad \bar{\varepsilon}_y \quad \bar{\gamma}_{xy} \right\}^{\mathrm{T}} \tag{5.2}$$

According to the expressions in Eq. (5.2), the constitutive relations (Eq. (5.1b)) for the phases ($p=1, 2$) can be expressed as,

$$\begin{Bmatrix} \bar{\boldsymbol{\sigma}}_N^p \\ \bar{\boldsymbol{\sigma}}_U^p \end{Bmatrix} = \begin{bmatrix} \boldsymbol{C}_{NN}^p & \boldsymbol{C}_{NU}^p \\ \boldsymbol{C}_{UN}^p & \boldsymbol{C}_{UU}^p \end{bmatrix} \begin{Bmatrix} \bar{\boldsymbol{\varepsilon}}_N^p \\ \bar{\boldsymbol{\varepsilon}}_U^p \end{Bmatrix} - \begin{Bmatrix} \boldsymbol{e}_N^p \\ \boldsymbol{e}_U^p \end{Bmatrix} \bar{E}_z \tag{5.3a}$$

Equation (5.3a) can also be arranged in the following form,

$$\begin{aligned} \boldsymbol{S}_U^p &= \left(\boldsymbol{Q}^p \boldsymbol{S}_N^p + \boldsymbol{R}^p \bar{E}_z \right), \; p = 1,2 \\ \boldsymbol{S}_U^p &= \begin{Bmatrix} \bar{\boldsymbol{\varepsilon}}_U^p \\ \bar{\boldsymbol{\sigma}}_U^p \end{Bmatrix}, \boldsymbol{S}_N^p = \begin{Bmatrix} \bar{\boldsymbol{\varepsilon}}_N^p \\ \bar{\boldsymbol{\sigma}}_N^p \end{Bmatrix}, \\ \boldsymbol{Q}^p &= \begin{bmatrix} \boldsymbol{C}_{NU}^p & \boldsymbol{0} \\ \boldsymbol{C}_{UU}^p & -\boldsymbol{I}_1 \end{bmatrix}^{-1} \begin{bmatrix} -\boldsymbol{C}_{NN}^p & \boldsymbol{I}_2 \\ -\boldsymbol{C}_{UN}^p & \boldsymbol{0} \end{bmatrix}, \\ \boldsymbol{R}^p &= \begin{bmatrix} \boldsymbol{C}_{NU}^p & \boldsymbol{0} \\ \boldsymbol{C}_{UU}^p & -\boldsymbol{I}_1 \end{bmatrix}^{-1} \begin{Bmatrix} \boldsymbol{e}_N^p \\ \boldsymbol{e}_U^p \end{Bmatrix} \end{aligned} \tag{5.3b}$$

In Eq. (5.3b), $\boldsymbol{R}^p = \boldsymbol{0}$ for $p=2$ and $\boldsymbol{I}_1 / \boldsymbol{I}_2$ is the unit matrix. According to the rule of mixture, the average field quantities ($\bar{\boldsymbol{\sigma}}_U$ and $\bar{\boldsymbol{\varepsilon}}_U$) over the volume of RVE can be assumed in terms of the similar phase-volume average field quantities ($\bar{\boldsymbol{\sigma}}_U^p$ and $\bar{\boldsymbol{\varepsilon}}_U^p$) as,

$$\begin{aligned} \boldsymbol{S}_U &= \left(v_1 \boldsymbol{S}_U^1 + v_2 \boldsymbol{S}_U^2 \right), \\ \boldsymbol{S}_U &= \left\{ \bar{\boldsymbol{\varepsilon}}_U{}^{\mathrm{T}} \quad \bar{\boldsymbol{\sigma}}_U{}^{\mathrm{T}} \right\}^{\mathrm{T}}, \\ \bar{\boldsymbol{\sigma}}_U &= \left\{ \bar{\sigma}_x \quad \bar{\sigma}_y \quad \bar{\tau}_{xy} \right\}^{\mathrm{T}}, \\ \bar{\boldsymbol{\varepsilon}}_U &= \left\{ \bar{\varepsilon}_z \quad \bar{\gamma}_{yz} \quad \bar{\gamma}_{xz} \right\}^{\mathrm{T}} \end{aligned} \tag{5.4}$$

where, v_p ($p=1, 2$) is the volume fraction of p^{th} phase. Substituting Eq. (5.3b) in Eq. (5.4), the following expression can be obtained,

$$\begin{aligned} \boldsymbol{S}_U &= \left(\boldsymbol{C}_R \boldsymbol{S}_N + \boldsymbol{e}_R \bar{E}_z \right), \\ \boldsymbol{S}_N &= \left\{ \bar{\boldsymbol{\varepsilon}}_N{}^{\mathrm{T}} \quad \bar{\boldsymbol{\sigma}}_N{}^{\mathrm{T}} \right\}^{\mathrm{T}}, \\ \boldsymbol{C}_R &= \left(v_1 \boldsymbol{Q}^1 + v_2 \boldsymbol{Q}^2 \right), \\ \boldsymbol{e}_R &= v_1 \boldsymbol{R}^1 \end{aligned} \tag{5.5}$$

Equation (5.5) can be arranged in a form similar to Eq. (5.1a) or (5.1b) in order to obtain the effective converse piezoelectric constitutive relation for the RVE/laminate as,

$$\bar{\boldsymbol{\sigma}} = \bar{\boldsymbol{C}} \bar{\boldsymbol{\varepsilon}} - \bar{\boldsymbol{e}} E_z \tag{5.6}$$

where, $\bar{C}$ and $\bar{e}$ are the effective stiffness and the vector of piezoelectric coefficients of the laminate, respectively; E_z is the electric field across the thickness of the active layers ($E_z = \bar{E}_z$).

5.3 Smart annular sandwich plate

For shear mode piezoelectric actuation of bending mode of deformation of a plate, the shear piezoelectric actuators are usually embedded around the middle plane of the plate [190]. So, the present annular sandwich plate is constructed by inserting the patches of the shear piezoelectric actuators at the core. The configuration of the overall annular plate appears similar to that presented in Fig. 3.2 and it is reproduced here for better readability.

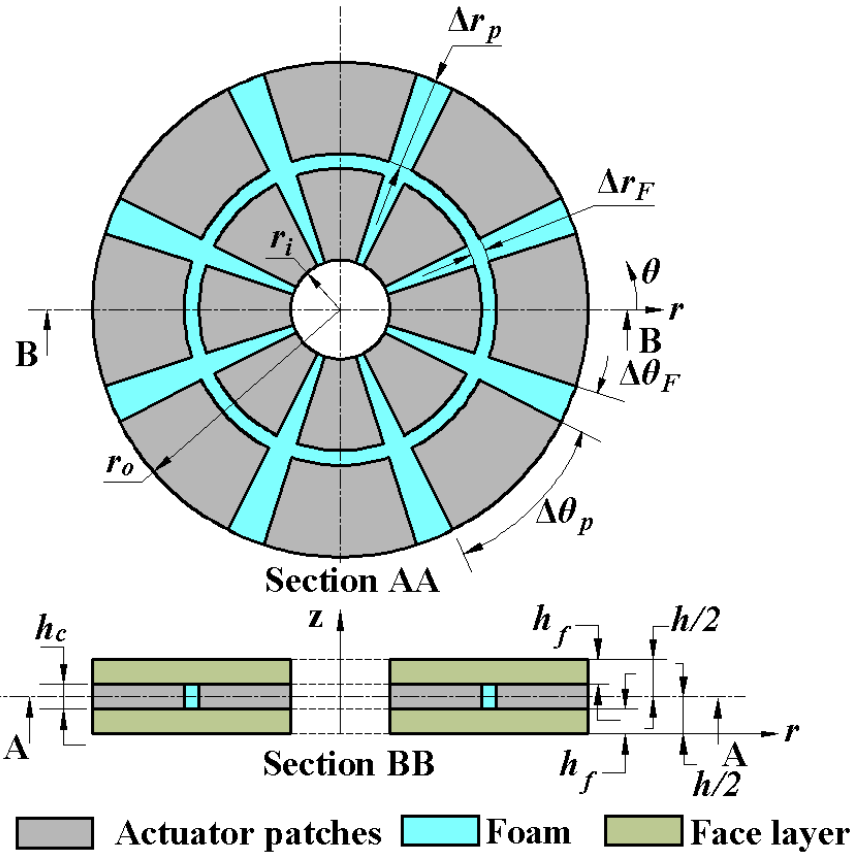

Fig. 3.2 Schematic diagram of the annular sandwich plate with the embedded shear actuator patches.

Since the laminate of a shear actuator (Fig. 5.2) is made in the form of a rectangular block with the Cartesian material coordinate system (xyz), the patches in the shape of the annular sector (Fig. 3.2) can be cut out from a block

of the laminate similar to that in Fig. 3.3, and the core layer of the sandwich plate can be constructed using these patches. The shear actuation force in every patch acts in the xz-plane of its Cartesian material coordinate system (xyz), and this shear actuation force is utilized in counteraction of the mechanically induced transverse shear stress (τ_{rz}) in the rz-plane of the annular sandwich plate. This mechanically induced transverse shear stress (τ_{rz}) changes its sign along the radial and circumferential directions of the annular plate as it is demonstrated in Figs. 3.4 for two typical bending modes of the annular plate. Following this variation of sign of the stress (τ_{rz}), the sign of the externally applied transverse electric field (E_z) is to be varied over the plane of the annular plate for effective shear actuation, and it is achieved by the variation the applied electric field (E_z) over the patches similar to the previous problem in Chapter 3.

5.4 Properties of constituent materials in the annular sandwich plate

Since the actuator patches possess Cartesian material coordinate system, their properties are transformed for their utilization in the reference cylindrical coordinate system as it is demonstrated in Chapter 3 through Fig. 3.5 and Eq. (3.2). However, for the use of the patches as actuators, the electric field in actuator patches is always specified. So, it may be observed from Eq. (3.13) that the electric displacement (D_z) has no effect on the motion of the overall annular plate since $\delta E_z = 0$ for the specified E_z at any instant of time. Therefore, the converse piezoelectric constitutive relation of the actuator patches would appear in the formulation of governing equation of the overall annular plate, and its aforesaid transformation with respect to the cylindrical coordinate system yields the following expression,

$$\begin{aligned} \boldsymbol{\sigma}^k &= (\boldsymbol{C}^k \boldsymbol{\varepsilon}^k - \boldsymbol{e}^k E_z), k = 2 \\ \boldsymbol{C}^k &= \boldsymbol{T}\bar{\boldsymbol{C}}\boldsymbol{T}^{\mathrm{T}}, \\ \boldsymbol{e}^k &= \boldsymbol{T}\bar{\boldsymbol{e}} \end{aligned} \tag{5.7}$$

where, k represents the bottom face layer, core layer and top face layer of the sandwich plate according to its value as 1, 2 and 3, respectively; $\boldsymbol{\sigma}^k$ / $\boldsymbol{\varepsilon}^k$ is the stress/strain vector at any point in the k^{th} layer; $\boldsymbol{C}^k$ is the stiffness matrix of the

k^{th} layer; $\boldsymbol{e}^k$ is the vector of piezoelectric coefficients associated with the transverse electric field (E_z) in the k^{th} layer; $\boldsymbol{T}$ is the transformation matrix. Besides the properties (Eq. (5.7)) of the actuator patches, the constitutive relations for the isotropic face layers ($k=1,3$) and the foam at the core ($k=2$) can be written similar to Eq. (3.3) as,

$$\boldsymbol{\sigma}^k = \boldsymbol{C}^k \boldsymbol{\varepsilon}^k, \; k=1,2,3$$

$$\boldsymbol{C} = \begin{bmatrix} C_s(1-v^k) & C_s v^k & C_s v^k & 0 & 0 & 0 \\ C_s v^k & C_s(1-v^k) & C_s v^k & 0 & 0 & 0 \\ C_s v^k & C_s v^k & C_s(1-v^k) & 0 & 0 & 0 \\ 0 & 0 & 0 & \dfrac{E^k}{2(1+v^k)} & 0 & 0 \\ 0 & 0 & 0 & 0 & \dfrac{E^k}{2(1+v^k)} & 0 \\ 0 & 0 & 0 & 0 & 0 & \dfrac{E^k}{2(1+v^k)} \end{bmatrix},$$

$$C_s = E^k / \left\langle (1+v^k)(1-2v^k) \right\rangle \tag{3.3}$$

where, E^k and v^k are Young's modulus and Poisson's ratio, respectively.

5.5 FE model of the annular sandwich plate

The bottom plane of the annular sandwich plate is taken as the reference plane and the origin of the reference cylindrical coordinate system ($r\theta z$) is located at the center of the reference annular plane. Within this reference cylindrical coordinate system, the kinematics of deformation of the overall annular plate is defined according to the layer-wise deformation theory as given in Eq. (3.4).

$$u^k(r,\theta,z,t) = u_0^k(r,\theta,t) + \sum_{i=1}^{3} z_i^k(z)\phi_i^k(r,\theta,t),$$

$$v^k(r,\theta,z,t) = v_0^k(r,\theta,t) + \sum_{i=1}^{3} z_i^k(z)\beta_i^k(r,\theta,t),$$

$$w^k(r,\theta,z,t) = w_0^k(r,\theta,t) + \sum_{i=1}^{3} z_i^k(z)\psi_i^k(r,\theta,t),$$

$$z_1^k = (z - z_0^k),$$

$$z_2^k = (z - z_0^k)^2,$$
$$z_3^k = (z - z_0^k)^3 \tag{3.4}$$

According to this displacement field, the FE model of the annular sandwich plate is derived following the same procedure as given in section 3.4, and the governing FE equations of motion of the annular sandwich plate can be obtained as,

$$\boldsymbol{M}\ddot{\boldsymbol{X}} + \boldsymbol{K}\boldsymbol{X} = \boldsymbol{P}_M + \sum_{s=1}^{n_p} \boldsymbol{P}_E^s E_z^s \tag{3.17}$$

For activating the shear actuator patches at the core of the annular sandwich plate, the electric field to an actuator patch (E_z^s for s^{th} patch) is supplied according to a shear-based feedback control strategy as proposed in section 3.5, where every shear actuator is activated by the feedback of the time-rate of change of the local slope of bending deformation (Eq. 3.18) of the overall annular plate and the corresponding mathematical expression for the applied electric field (E_z^s) arises as given in Eq. (3.19),

$$(\dot{\varphi}_r^s) = \frac{({}^o\dot{w}_0^s) - ({}^i\dot{w}_0^s)}{\Delta r^s},$$
$$\Delta r^s = (r_i^s - r_o^s) \tag{3.18}$$

$$E_z^s = -\frac{k_d^s}{\Delta r^s}\left\langle ({}^o\dot{w}_0^s) - ({}^i\dot{w}_0^s) \right\rangle \tag{3.19}$$

$$\left\langle ({}^o\dot{w}_0^s) - ({}^i\dot{w}_0^s) \right\rangle = N_T^s \dot{\boldsymbol{X}} \tag{3.20}$$

The transverse velocities at the sensing points are expressed in terms of the global nodal velocity vector ($\dot{\boldsymbol{X}}$) through a transformation row matrix (N_T^s) as given in Eq. (3.20), and then introducing Eqs. (3.19) and (3.20) in Eq. (3.17), the FE equations of motion of the annular sandwich plate can be obtained as given in Eq. (3.21).

$$\boldsymbol{M}\ddot{\boldsymbol{X}} + \boldsymbol{C}\dot{\boldsymbol{X}} + \boldsymbol{K}\boldsymbol{X} = \boldsymbol{P}_M(t),$$
$$\boldsymbol{C} = \sum_{s=1}^{n_p} \left\langle \boldsymbol{P}_E^s k_d^s N_T^s \right\rangle \tag{3.21}$$

Table 5.1 Effective properties of the PZT5H, BL-PFC and SAFC laminates.

PZT5H laminate										
C_{11} (GPa)	C_{22} (GPa)	C_{33} (GPa)	C_{12} (GPa)	C_{13} (GPa)	C_{23} (GPa)	C_{44} (GPa)	C_{55} (GPa)	C_{66} (GPa)	e_{35} (C/m^2)	ρ (kg/m^3)
82.9	95.4	56.2	53.0	36.8	34.9	13.0	12.8	22.1	9.164	7239.5
BL-PFC laminate ($\psi = 25^o$)										
C_{11} (GPa)	C_{22} (GPa)	C_{33} (GPa)	C_{12} (GPa)	C_{13} (GPa)	C_{23} (GPa)	C_{44} (GPa)	C_{55} (GPa)	C_{66} (GPa)	e_{35} (C/m^2)	ρ (kg/m^3)
16.7	42.2	29.1	8.03	9.97	13.6	8.40	6.70	4.80	5.921	5903.6
SAFC laminate										
C_{11} (GPa)	C_{22} (GPa)	C_{33} (GPa)	C_{12} (GPa)	C_{13} (GPa)	C_{23} (GPa)	C_{44} (GPa)	C_{55} (GPa)	C_{66} (GPa)	e_{35} (C/m^2)	ρ (kg/m^3)
14.6	54.0	37.6	8.88	6.94	14.0	11.3	3.83	4.13	2.114	5903.6

5.6 Results and discussions

5.6.1 Effective properties of the shear actuator laminate

The material for the shear mode monolithic piezoelectric actuator (Fig. 5.1(b)) is considered as PZT5H [391]. The same material (PZT5H) is also considered for the fibers of BL-PFC (Fig. 4.1) and SAFC (Fig. 5.1(a)) while the matrix phase of these PFCs is made of epoxy ($E = 2.9$ GPa, $\nu = 0.3$, $\rho = 1250$ kg/m^3). Using these constituent materials, the homogenized properties of the SAFC (Fig. 5.1(a)) are obtained following the micromechanics formulation in [73]. The effective properties of BL-PFC (Fig. 4.1) are computed according to the micromechanics formulation in section 4.2. Both the SAFC and BL-PFC are taken with a fiber volume fraction (v_f) of 0.777. According to these homogenized properties, SAFC and BL-PFC are treated as the homogeneous layers in the corresponding laminates (Fig. 5.2), and the effective properties of the laminates are determined. Presently, the actuator laminate comprising of the active layers of BL-PFC is denoted as BL-PFC laminate. A similar designation is also followed for the laminate with the active layers of SAFC/PZT5H as SAFC laminate/PZT5H laminate.

The thickness of any of the actuator laminates is considered as 2 mm while the thicknesses of the corresponding active layers and epoxy layers are taken as 480 μm and 10 μm, respectively. With these geometrical and material properties of the actuator laminates, their effective properties are computed using the micromechanics formulation as presented in section 5.2. The mass

densities of these actuator laminates are also computed using the rule of mixture. These results are presented in Table 5.1. It may be observed from Table 5.1 that all actuator laminates possess orthotropic material properties and they are capable to produce the shear actuation force in the xz-plane of the Cartesian material coordinate system (xyz) through the piezoelectric coefficient e_{35} when an electric field (E_z) is applied across the top and bottom surface electrodes of active layers.

5.6.2 Verification of the FE formulation

The verification of the FE formulation in handling the shear piezoelectric actuation force in the actuator patches at the core of the annular sandwich plate is carried out following the same procedure as given in section 3.6.1 (Chapter 3). But, unlike the previous verification results (Fig. 3.8(b)), the annular rings of shear piezoelectric actuators at the core of the axisymmetric annular sandwich plate (Fig. 3.8(a)) are presently activated by applying uniform transverse electric field. The corresponding axisymmetric bending deflections of the overall annular plate obtained through the present FE formulation and ANSYS model are illustrated in Fig. 5.3. Figure 5.3 shows a good agreement of the results through the present FE formulation with that obtained from the ANSYS model thus verifying the present FE formulation in handling the shear piezoelectric actuation force in the patches at the core of the annular sandwich plate.

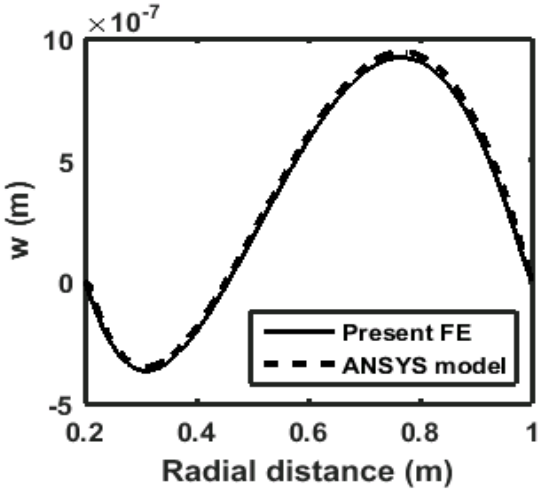

Fig. 5.3 Bending deflection (w) of the axisymmetric annular sandwich plate for an applied electric field across the thickness of the shear piezoelectric actuators in the core.

5.6.3 Analysis of shear-based active control of the annular sandwich plate

The annular sandwich plate is presently taken with the geometrical properties as r_i = 0.2 m, r_o = 1 m, h_c = 2 mm and h_f = 2 mm. The face layers are considered to be made of Aluminum ($E = 70$ GPa, $\nu = 0.33$, $\rho = 2700$ kg/m^3) and the properties of the foam at core are $E = 35.3$ MPa, ν = 0.383, ρ = 32 kg/m^3. The inner and outer edges of the overall annular plate are considered as the simply-supported edges ($w_0 = 0$, $\beta_i^k = 0$, $\psi_i^k = 0$). The transversely distributed harmonic load is considered as it is given in Eq. (2.46), where p_o and ω are the load-amplitude and operating frequency, respectively. The control gains (k_d^s, $s = 1,2,\ldots n_p$) over the shear actuator patches are taken with uniform value as, $k_d^s = k_d$ ($s = 1,2,\ldots n_p$).

$$p(r,\theta,t) = p_o(1+\cos\theta+\cos 2\theta+\cos 3\theta)e^{j\omega t} \tag{2.46}$$

For an initial study, the actuator patches are considered to be made of the PZT-5H laminate, and they (actuator patches) are arranged by $n_r = 2$, $n_\theta = 8$, Δr_F = 5 mm, $\Delta\theta_F = 2^o$ (Fig. 3.2). The corresponding controlled frequency responses of the overall annular plate under the harmonic load (Eq. (2.46)) are illustrated in Fig. 5.4(a) for different values of the control gain (k_d). The corresponding variations of the control voltage are also illustrated in Fig. 5.4(b). In these frequency responses (Fig. 5.4(a)), the maximum nodal transverse displacement-amplitude ($w_{\max}/h$) is plotted at every operating frequency (ω) while the maximum one ($V_{\max}$) among the control voltages over the actuator patches is presented (Fig. 5.4(b)) for the required control voltage. The bending modes at different resonant frequencies (Fig. 5.4(a)) are indicated by (m,n) where m and n are the radial and circumferential mode numbers, respectively. The results in Fig. 5.4 show that all resonant displacement amplitudes are attenuated in a uniform manner for an increase of the control gain (k_d). So, it is possible to control all modes of vibration using a single arrangement of shear actuator patches and velocity sensors. More importantly, an increase of the control gain (k_d) does not cause a significant change of the required control

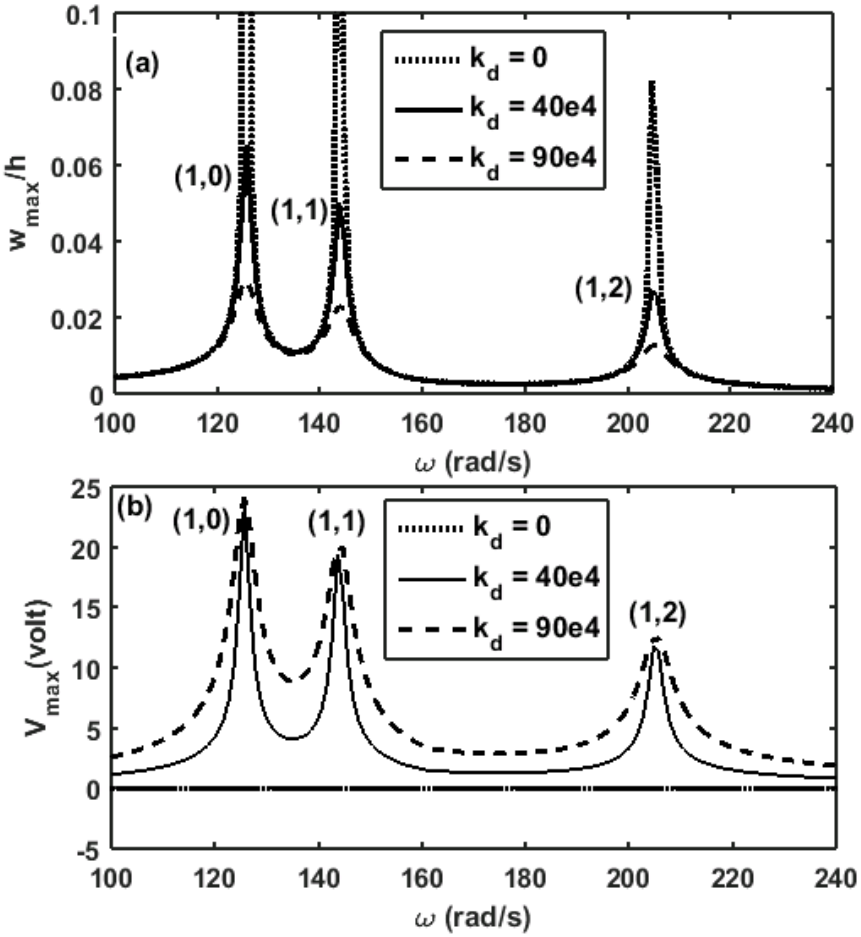

Fig. 5.4 Variations of (a) the maximum transverse displacement-amplitude ($w_{\max}/h$) of the annular sandwich plate and (b) the corresponding maximum control voltage with the operating frequency (ω) ($p_o = 1.6$ N/m²).

voltage at any resonant frequency while the corresponding displacement-amplitude is attenuated indicatively. So, a resonant displacement-amplitude can be attenuated to the desired mark by increasing the control gain without the additional expense of control voltage. These results infer the suitability of the arrangement of actuator patches and the associated shear-based feedback control strategy. It may be noted here that this kind of arrangement of actuator patches and the associated shear-based feedback control strategy were proposed in Chapter 3 in the use of an obliquely reinforced 1-3 PFC for shear-based active control of an annular plate. Although this obliquely reinforced 1-3 PFC possesses anisotropic material properties, the results in Figs. 5.4 and 3.10 indicate that the same arrangement of actuator patches, as well as the same

shear-based feedback control strategy, can fruitfully be used for the present shear-mode actuator laminates with orthotropic material properties.

5.6.4 Optimal arrangement of shear actuator patches

Although the fruitfulness of the present arrangement of the shear actuator patches at the core is implied through the previous result (Fig. 5.4), the corresponding geometrical dimensions (Δr_F, $\Delta\theta_F$, n_θ, n_r) can be taken in an optimal manner for achieving maximum shear-based attenuation of vibration of the annular sandwich plate. In this issue, n_r is already taken with the value of 2 for the convenience in supplying the external transverse electric field through the plate-edges. However, the other parameters (Δr_F, $\Delta\theta_F$ and n_θ) can be taken with their optimal values that may further appear differently for three different shear actuators (BL-PFC, SAFC and PZT5H laminates). So, the optimal values of these parameters (Δr_F, $\Delta\theta_F$, n_θ) are presently determined for every actuator.

An increase of the gap (Δr_F or $\Delta\theta_F$) may cause the reduction of shear actuation of the plate while a decrease of the same may result in difficulties in fabrication of the core layer. So, these gaps are presently considered with their reasonable values as $\Delta r_F =$ 5mm, $\Delta\theta_F = 2^o$ for any of the shear actuators. Now, the optimal value of n_θ may vary for different bending modes of vibration of the annular sandwich plate as its (n_θ) value is mainly dependent on the alteration of sign of the shear stress (τ_{rz}) along the circumferential direction. So, the mode-based optimal value of this parameter (n_θ) is determined at present for every actuator. It should be noted here that the fiber orientation angle (ϕ) of BL-PFC (Fig. 4.1) is an important parameter for its effective shear actuation capability as it is indicated in the previous chapter (Fig. 4.8, Chapter 4). So, the design variables for the mode-based optimal arrangement of the patches of BL-PFC laminate are taken as n_θ and ϕ, while the only one design variable for the patches of SAFC or PZT5H laminate is taken as n_θ.

Presently the mode-based optimal values of the design variables (n_θ, ϕ) are determined by taking every variable within the suitable bounds while the objective is to achieve maximum shear-based attenuation of resonant displacement-amplitude at a bending mode of vibration of interest. A low value of n_θ reduces the flexibility of the sandwich plate while a high value of the same

needs more number of velocity sensors according to the present shear-based feedback control strategy. Following these constraints, the lower and upper bounds of n_θ are considered as 8 and 12, respectively. Besides, similar limiting values for fiber orientation angle (ϕ) of BL-PFC (Fig. 4.1) are taken as 20^o and 40^o following the study in the previous chapter (Fig. 4.8). According to these bounds of the design variables (n_θ, ϕ), their mode-based optimal values for every actuator are decided using the Exhaustive Search Method [399] although other optimization methods can be employed for the same.

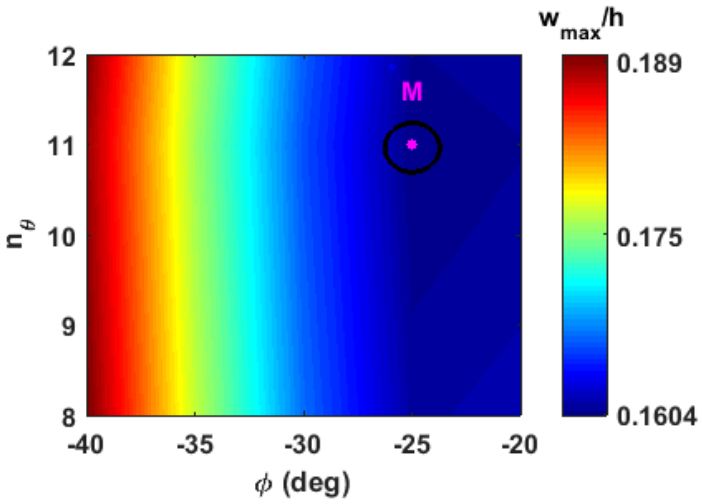

Fig. 5.5 Contour plot of resonant displacement-amplitude (w_{max}/h) at the fundamental mode of vibration of the annular plate within a two-dimensional domain of n_θ and ϕ where the patches are made of the BL-PFC laminate (p_o = 5 N/m², k_d = 40e4).

In case of the patches of BL-PFC laminate, the optimization method (Exhaustive Search Method) is implemented by taking a two-dimensional domain within the aforesaid bounds of the axial parameters (n_θ and ϕ). Within this two-dimensional domain, the grid points are generated in an even manner, and the resonant displacement-amplitude is evaluated at every grid point to obtain the variation of the resonant displacement-amplitude within this domain as illustrated through a contour plot in Fig. 5.5 for the fundamental mode ($m=1$, $n=0$) of vibration of the annular sandwich plate. From this contour plot (Fig. 5.5), the coordinates (n_θ, ϕ) of the point (M) of minimum resonant displacement-amplitude are the optimal values of the design variables (n_θ and ϕ). This

procedure is followed for every mode, and the corresponding optimal values of the design variables (n_θ and ϕ) are illustrated in Table 5.2.

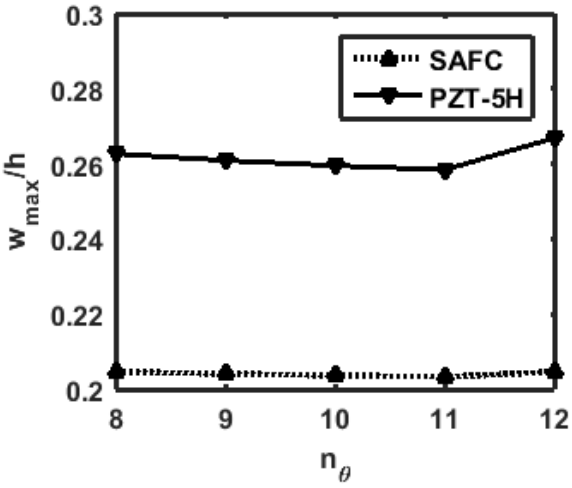

Fig. 5.6 Variation of the resonant displacement-amplitude ($w_{\max}/h$) at the fundamental mode of vibration of the annular plate with n_θ where the patches are made of the SAFC/PZT-5H laminate ($p_o = 5$ N/m², $k_d = 40e4$).

Table 5.2 Mode-based optimum values of the design variables (n_θ, ϕ) for the actuator patches of BL-PFC/SAFC/PZT5H laminate.

Shear actuator	Mode (m,n)	ϕ (deg)	n_r	n_θ
BL-PFC laminate	(1,0)	25	2	11
	(1,1)	25	2	11
SAFC laminate	(1,0)	-	2	11
	(1,1)	-	2	11
PZT5H laminate	(1,0)	-	2	11
	(1,1)	-	2	11

For the patches of SAFC/PZT5H laminate, there is only one design variable as n_θ. So, one-dimensional domain within the bounds of the axial parameter of n_θ is formed, and the variation of the resonant displacement-amplitude within this domain is evaluated as shown in Fig. 5.6 for the fundamental bending mode of vibration of the annular sandwich plate. From this result, the optimal value of the parameter (n_θ) for the maximum attenuation of resonant displacement-amplitude can be obtained. Repeating the same procedure for the first two bending modes of vibration, the corresponding mode-based optimal values of n_θ are presented in Table 5.2.

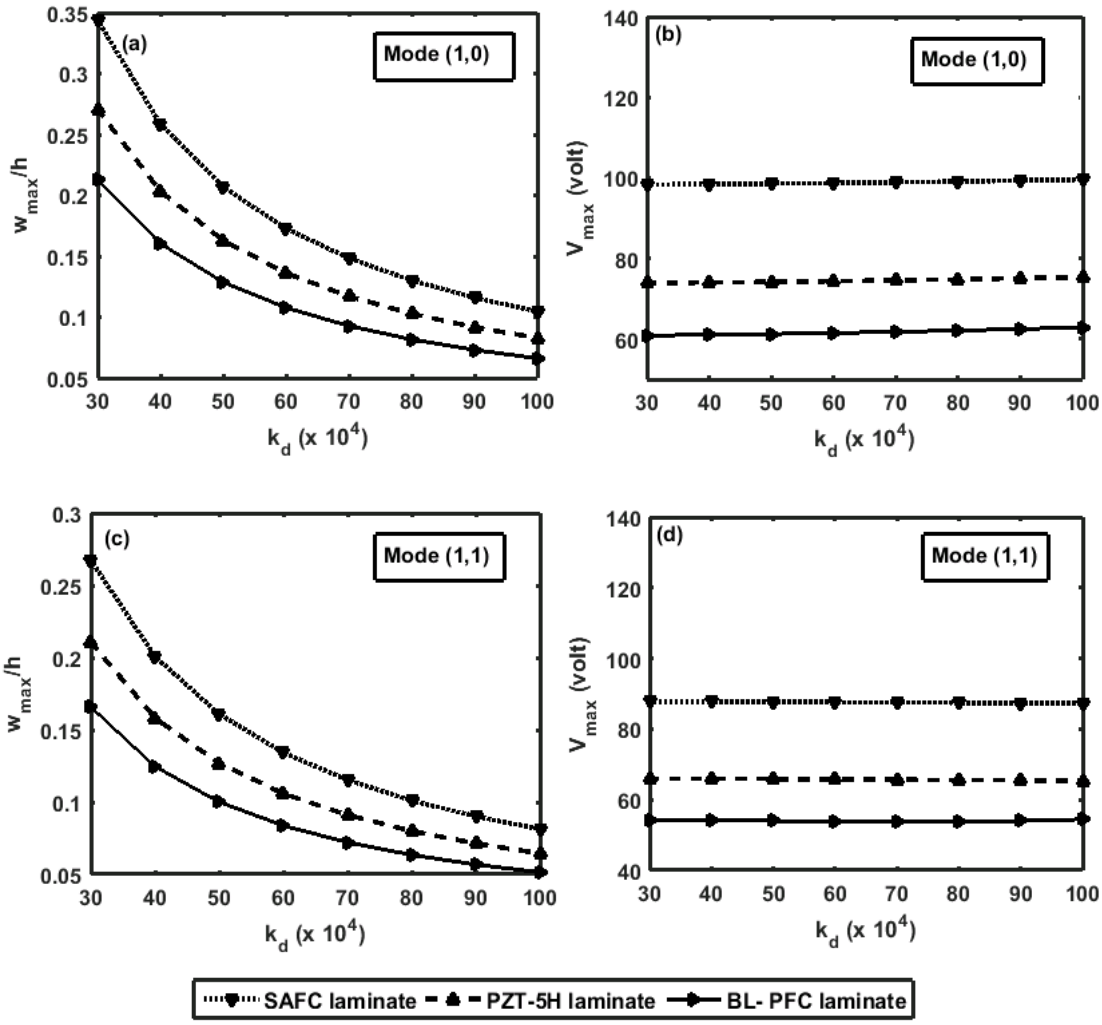

Fig. 5.7 Variations of the resonant displacement-amplitude (w_{max}/h) and the corresponding maximum control voltage (V_{max}) with the control-gain (k_d); w_{max}/h for (a) mode: $m=1$, $n=0$ and (c) mode: $m=1$, $n=1$; V_{max} for (b) mode: $m=1$, $n=0$ and (d) mode: $m=1$, $n=1$ (p_o = 5 N/m²).

5.6.5 Comparative study

According to the geometrical and effective material properties (Table 5.1) of the BL-PFC, SAFC and PZT5H laminates, all three shear actuators (Figs. 4.1, 5.1(a), 5.1(b)) are presently taken in a uniform manner. Further, the patches of each of the actuator laminates are optimally arranged (Table 5.2) at the core of the annular sandwich plate. On the basis of these arrangements of the three different actuators, their shear actuation capabilities in attenuation of vibration of the annular sandwich plate are assessed by evaluating the resonant displacement amplitudes at the first two bending modes of vibration for different

values of the control gain (k_d) under a constant load-amplitude (p_o, Eq. (2.46)). The corresponding maximum control voltage is also evaluated. These results are illustrated in Fig. 5.7. It may be observed from these results (Fig. 5.7) that every shear actuator indicatively attenuates the vibration of the sandwich plate in the expense of reasonable control voltage. However, the monolithic piezoelectric actuator (PZT5H) provides better shear-based actuation than that of the SAFC. The best one is the BL-PFC since this PFC provides maximum attenuation of resonant displacement-amplitude at any bending mode of vibration with the least expense of the required control voltage.

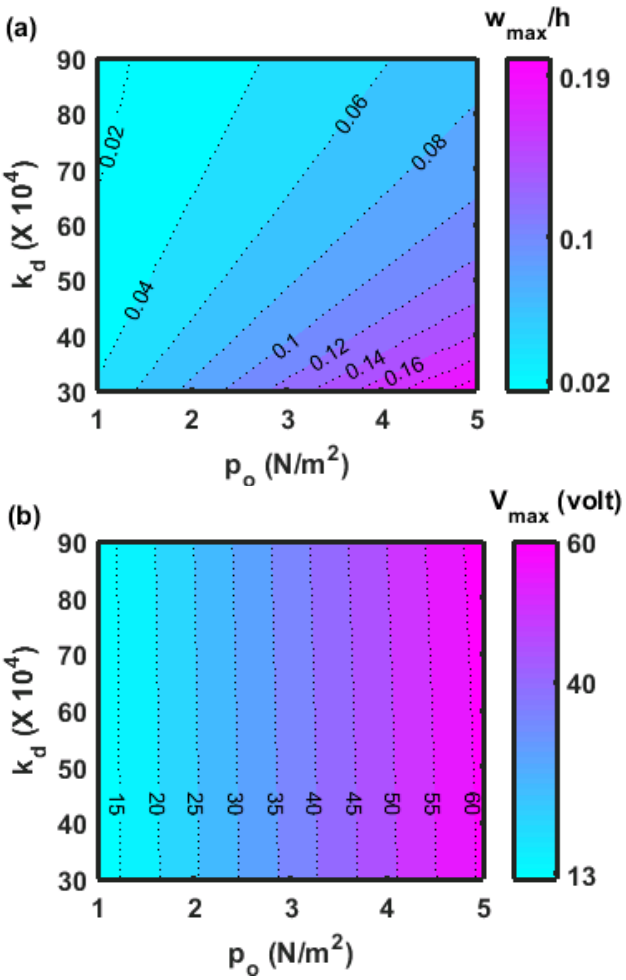

Fig. 5.8 Contour plots of (a) the resonant displacement-amplitude ($w_{\max}/h$) at the fundamental mode and (b) the corresponding maximum control voltage ($V_{\max}$) in the two-dimensional domain of the load-amplitude (p_o) and control-gain (k_d) for the patches of the BL-PFC laminate.

In the previous results (Fig. 5.7), the actuation capabilities of the three different shear actuators are compared considering a constant load-amplitude (

p_o). However, for the different values of the control-gain (k_d) and load-amplitude(p_o), the corresponding variations of the resonant-displacement amplitude and the maximum control voltage are illustrated in Figs. 5.8(a) and 5.8(b), respectively for the actuator patches made of the BL-PFC laminate. The results in Fig. 5.8(b) show an indicative variation of the control voltage with the load-amplitude (p_o) while the same parameter (voltage) remains almost constant for the variations of the control gain (k_d) at a constant load-amplitude (p_o). So, the application of the shear actuator is mainly limited to a certain load-amplitude where the applied electric field exceeds the permissible value for the piezoelectric actuator. Similar characteristics of shear actuation are also obtained for the other two shear mode actuators (PZT5H and SAFC), and thus the corresponding results (similar to Fig. 5.8) are not furnished here. However, for an increase of the control gain (k_d) at different load amplitudes (p_o), the corresponding decrease of the resonant displacement-amplitude and increase of the maximum control voltage are measured by defining the parameters $\Delta W(\%)$ and $\Delta V(\%)$ as given in Eqs. (3.24a) and (3.24b).

$$\Delta W(\%) = \frac{\left(w_{\max}/h\right)_1 - \left(w_{\max}/h\right)_2}{\left(w_{\max}/h\right)_1} \times 100 \tag{3.24a}$$

$$\Delta V(\%) = \frac{\left(V_{\max}\right)_2 - \left(V_{\max}\right)_1}{\left(V_{\max}\right)_1} \times 100 \tag{3.24b}$$

For an increase of the control gain from 30×10^4 to 90×10^4 at different load amplitudes (p_o), the corresponding values of these parameters ($\Delta W(\%)$ and $\Delta V(\%)$) are illustrated in Table 5.3 for three different shear actuator laminates. It may be observed from Table 5.3 that the rate of change of shear actuation with the control gain is almost independent of the load-amplitude for any actuator laminate. It also infers that all the shear actuator laminates act in a uniform manner for an increase of the control gain at any load-amplitude. But, the maximum attenuation of resonant displacement-amplitude occurs for the actuator patches of BL-PFC laminate as shown in Fig. 5.7. So, these results suggest BL-PFC as the best material for shear actuator in controlling the vibration of annular plates.

Table 5.3 Decrease of the resonant displacement-amplitude ($\Delta W(\%)$) at the fundamental mode and the corresponding increase of the maximum control voltage ($\Delta V(\%)$) for a change (from 30×10^4 to 90×10^4) of control gain (k_d) at different load amplitudes (p_o).

p_o	BL-PFC laminate		SAFC laminate		PZT5H laminate	
($\mathrm{N/m^2}$)	$\Delta W(\%)$	$\Delta V(\%)$	$\Delta W(\%)$	$\Delta V(\%)$	$\Delta W(\%)$	$\Delta V(\%)$
1	65.72	2.56	65.70	1.00	67.40	1.59
2	65.70	2.55	66.18	1.00	65.85	1.56
3	65.43	2.55	66.02	1.00	66.10	1.54
4	65.74	2.56	66.30	1.01	66.10	1.55
5	65.74	2.56	66.29	1.00	66.10	1.57

5.7 Summary

In this chapter, the shear-based attenuation of vibration of an annular sandwich plate is investigated using three different shear mode piezoelectric actuators namely BL-PFC, SAFC and monolithic piezoelectric actuators. Every shear mode actuator is used in the form of a laminate, where a number of shear actuator layers are stacked to provide transverse shear actuation force in the xz-plane of the Cartesian material coordinate system (xyz) of the laminate when a transverse electric field is applied across the top and bottom fully electrode surfaces of the actuator layers. The motivation in forming this actuator laminate is to achieve higher shear actuation force in the expense of a small applied voltage across the thickness of the actuator layers.

The patches of this shear actuator laminate are inserted at the core of the annular sandwich plate for shear-based attenuation of its (sandwich plate) bending modes of vibration by means of activating the actuator patches according to the velocity feedback control law. The shear-based attenuation of vibration of the annular plate is supposed to occur through the counteraction of the mechanically induced shear stress in the transverse plane of thickness and radial coordinates of the annular plate. In order to achieve it in an effective manner, the same arrangement of shear actuator patches as presented in Chapter 3 is followed, and the actuator patches are activated according to the velocity feedback control law as the corresponding shear-based feedback control strategy is illustrated in section 3.5.

For analyzing the shear-based attenuation of flexural vibration of the annular sandwich plate, first, the effective electro-elastic properties of the

actuator laminate are determined through a micromechanics formulation based on the Uniform Field Method (UFM). Next, a closed-loop FE model of the annular sandwich plate is derived following the same procedure as given in sections 3.4 and 3.5. Subsequently, an initial study on the characteristics of the controlled frequency responses of the annular sandwich plate is performed, and it reveals that the present arrangement of the shear actuator patches and the associated shear-based feedback control strategy are worthy for effective shear-based attenuation of any bending mode of vibration of the sandwich plate, where also a resonant displacement-amplitude can be attenuated to the desired mark by increasing the velocity feedback control gain without indicative change of the required control voltage. Owing to these advantages, the same closed-loop model of the annular sandwich plate is further utilized for a comparative study on the shear actuation capabilities of the three different shear actuators in attenuation of vibration of the sandwich plate.

This comparative study is carried out by taking the BL-PFC, SAFC and PZT5H laminates in a uniform manner. Every kind of shear actuator laminate is used through a mode-based optimal arrangement of its patches at the core of the annular sandwich plate. The corresponding results for the shear-based attenuation of resonant displacement amplitudes reveal that SAFC has lesser shear actuation capability than that of the PZT5H, while the BL-PFC possesses the maximum shear actuation capability in comparison to that for any of the other two shear actuators (SAFC and PZT5H). These observations recommend BL-PFC as the best material for shear-based attenuation of vibration of the annular sandwich plates.

Chapter 6

A design of shear actuated hybrid damping treatment for annular plates using balanced laminate of PFC and 0-3 viscoelastic composite

6.1 Introduction

In the context of passive damping of structural vibration, the viscoelastic materials (VEMs) have long been utilized due their excellent energy-dissipation property. These materials (VEMs) are extensively utilized in a particular case of passive control of flexural vibration of thin-walled structures, where VEM layers are attached to the host structures through the Unconstrained Layer Damping (UCLD) or Constrained Layer Damping (CLD) arrangements (section 1.5, Chapter 1). Among these two passive damping arrangements, the CLD treatment is preferred in most of the pertaining studies due to its superior damping capability, and in these applications of CLD treatment, the monolithic VEMs are utilized as the material of damping layer. Besides, the conventional monolithic VEMs, an advanced viscoelastic composite (VEC) damping material also emerged [400] for improved CLD treatment of flexural vibration of thin-walled structures. However, the CLD and UCLD treatment are usually incapable of providing good passive damping especially at a low operating frequency [282]. Moreover, these damping treatments are not adaptive to the change of vibration characteristics of a structure. In view of these shortcomings, the hybrid active-passive damping treatment emerged (section 1.5) where the piezoelectric actuators are added with the viscoelastic materials for achieving adaptive control of structural vibration in a wide range of operating frequency.

In these hybrid damping treatments, the active-passive damping appears by means of utilizing the actuation force of the piezoelectric actuator in the enhancement of energy dissipation capability of the associated viscoelastic material and also by imparting energy dissipation through active action of the actuator. So, a good piezoelectric actuator would provide better hybrid active-passive damping treatment, and it (actuator) may be chosen from the available studies on the development of piezoelectric actuators. In this concern, most of the available studies on the development of hybrid active-passive damping treatment have been

carried out utilizing the extension mode monolithic piezoelectric/PFC actuators along with the monolithic viscoelastic/VEC damping materials (section 1.5, Chapter 1). Besides, the research on the utilization of shear piezoelectric actuators for hybrid active-passive damping treatment is not yet matured as the corresponding literature survey in Chapter 1 shows a very few studies [332,333] on this subject using the shear mode monolithic piezoelectric actuators and pure viscoelastic materials (VEMs). Among these limited number of studies, the conclusion given by Batra and Geng [332] is an important one where it is stated that the energy dissipation through the hybrid damping treatment using shear piezoelectric actuator is higher than that for the similar damping treatment using extension mode piezoelectric actuator. According to this observation [332], the shear piezoelectric actuators may be potential ones for effective hybrid active-passive damping of structural vibration. But, with reference to the available studies on this subject (section 1.5, Chapter 1), there is a need of further research on the development of shear actuated hybrid active-passive damping treatment, and it may be carried out using the high-performing shear mode actuators and damping materials like the BL-PFC actuator developed in the previous chapter and 0-3 VEC developed in [400].

The study in this chapter is in this direction, where a new shear actuated hybrid active-passive damping treatment is proposed in layered construction for vibration control of the plane structures of revolution using the BL-PFC and a 0-3 VEC. The plane structure of revolution is considered here as the annular plate since it is extensively utilized in a variety of engineering structures (Chapter 1). Despite the wide application of the annular plates, a study on the active-passive control of a similar plate has not yet been addressed in the literature to the best knowledge of this author. It is attempted in this chapter towards the development of a fruitful design for shear actuated hybrid active-passive damping treatment using the present BL-PFC actuator and the 0-3 VEC.

The present design of a shear actuated hybrid active-passive damping treatment is carried out in three steps following the issues concerning the fruitful utilization of shear actuator (BL-PFC) and damping material (0-3 VEC) for control of annular plates. In the first step, an active layer in the shape of a thin annular disc is designed using the patches of BL-PFC. It is a piezo-foam composite disc similar to that designed for the core layer of the annular sandwich plate in the previous

chapter. In the second step, a thin annular disc of 0-3 VEC is designed, where the graphite wafers in the shape of the annular sector are periodically distributed in the cylindrical direction. Although the geometrical dimensions of this annular disc of 0-3 VEC (Fig. 6.2) is presently designed in an optimal manner, its constructional features are not identical to that of a rectangular one [400], where some essential features in regard to its (0-3 VEC) passive damping capacity have deviated due to the cylindrical coordinate frame instead of the rectangular one. However, the objective with the present design of a disc of 0-3 VEC is to investigate the utility of the concept of VEC in shear actuated hybrid active-passive damping treatment of annular plates where the disc of 0-3 VEC is utilized as a damping layer within a layered annular plate. This layered annular plate is designed in the last step using the active layer, passive layer and the layers of substrate material. Here, the difficulties arise in deciding the appropriate stacking sequence of different layers of the layered annular plate since the appropriate stacking sequence of the active layer coincides with that of the passive damping layer. However, an optimal layered configuration of the overall annular plate is presented towards the effective shear actuated hybrid active-passive damping treatment. The analysis of the active-passive damping characteristics of the layered annular plate is carried out by developing a closed-loop FE model. The results reveal fruitfulness of the present design of a shear actuated hybrid active-passive damping treatment for annular plates.

6.2 Annular piezo-foam composite disc using BL-PFC patches

As the shear actuation force in the BL-PFC (Fig. 4.1) appears in the rectangular coordinate system, it may not provide effective shear actuation where the actuation force is required in the cylindrical coordinates. This discrepancy appears due to the behaviour of BL-PFC as an anisotropic material in the reference cylindrical coordinate frame. In view of this shortcoming, an active layer is designed in the shape of the thin annular disc as shown in Fig. 6.1(a). It is a piezo-foam composite disc similar to the core layer of the annular sandwich plate in the previous chapter. Figure 6.1(b) shows the orientation of the Cartesian principal material coordinate system of the BL-PFC patches within the reference cylindrical coordinate system, where the patches are made from a rectangular block of BL-PFC (Fig. 4.1) to construct the piezo-foam composite disc or active layer. Every BL-PFC patch behaves as an anisotropic material in the cylindrical coordinates of the annular

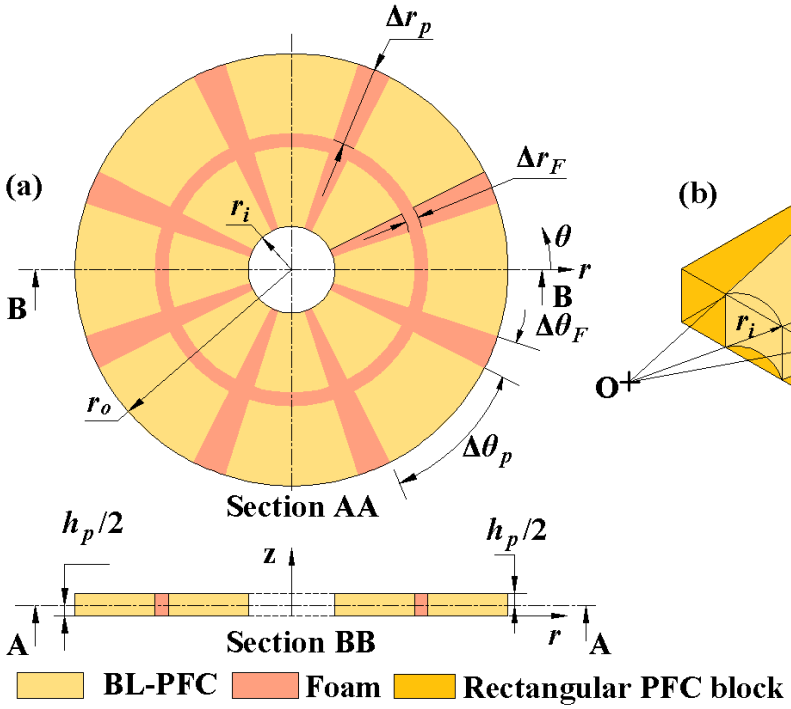

Fig. 6.1 (a) Schematic diagram of the active layer, (b) a block of BL-PFC used for making a typical row of actuator patches in the active layer.

composite disc. However, the shear actuation force in the xz -plane of every patch can be used in the rz -plane of the composite disc by taking the patches with their sufficiently narrow circumferential span $(\Delta\theta_p)$.

6.3 Design of an annular disc of 0-3 VEC

In the CLD treatment of rectangular plates, the damping layer is usually made of monolithic VEM. However, the damping capacity of the treatment can be enhanced indicatively through the replacement of VEM layer by a 0-3 VEC layer [400] as shown in Fig. 6.2(a). Now, to utilize a similar 0-3 VEC layer for improved passive damping in the CLD treatment of annular plates, the rectangular 0-3 VEC layer (Fig. 6.2(a)) can be constructed in the cylindrical coordinate frame resulting in a thin annular disc of 0-3 VEC as shown in Fig. 6.2(b). This disc of 0-3 VEC is comprised of a 2-2 VEC layer that is sandwiched between two identical monolithic VEM layers. The 2-2 VEC layer is comprised of an array of identical graphite wafers in the shape of the annular sector. The number of graphite wafers along the radial/circumferential direction is denoted by n_{rg} / $n_{\theta g}$. The thickness of the top

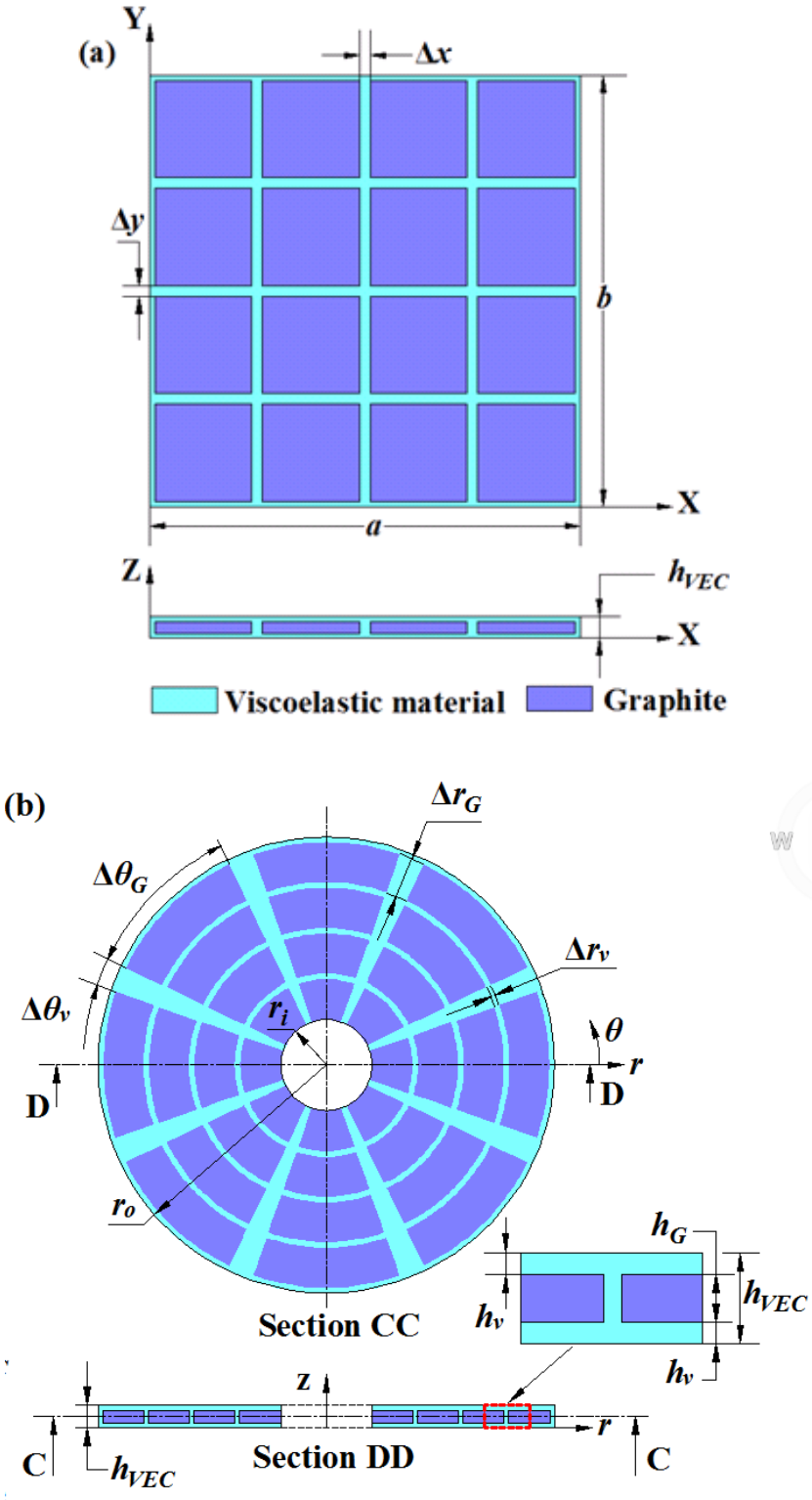

Fig. 6.2 Schematic diagrams of (a) a rectangular 0-3 VEC layer and (b) an annular disc of 0-3 VEC.

and bottom pure VEM layers is denoted by h_v while the same parameter for the overall VEC layer is denoted by h_{VEC}. The thickness of the 2-2 VEC layer is implied by h_v and h_{VEC}, and it is expressed by a ratio r_c ($r_c = h_v / h_{VEC}$). The other in-plane geometrical dimensions (Δr_v, Δr_G, $\Delta\theta_v$, $\Delta\theta_G$) of the annular disc of 0-3 VEC are illustrated in the corresponding figure (Fig. 6.2(b)). However, it is recommended in [400] that the graphite wafers are to be separated with a very small in-plane gap in micro-scale. But, the present conversion of geometry of the 0-3 VEC layer results in increasing circumferential gap ($\Delta\theta_v$) with radius, and thus this gap cannot be maintained in the recommended accuracy in micro-scale especially for the requirement of large radial span of the annular VEC disc. Although this shortcoming appears in the implementation of the concept of 0-3 VEC for passive damping of annular plates, the present investigation reveals the effectiveness of this disc of 0-3 VEC in the role of a passive damping layer within the shear actuated hybrid active-passive damping treatment for annular plates.

6.4 Design of a layered annular plate for shear actuated hybrid damping treatment

For CLD treatment of a plate, the constrained viscoelastic layer is usually located following the middle/top/bottom surface of the plate [401-403]. Accordingly, for CLD treatment of an annular plate, the plate can be taken in two different layered configurations as the corresponding cross sections of the overall annular plate are shown in Figs. 6.3(a)-(b). In Fig. 6.3(a), the viscoelastic layer is taken at the core of the overall annular plate. The same viscoelastic layer is divided through its middle surface, and the corresponding two identical viscoelastic layers are shifted symmetrically from the middle plane of the overall annular plate as shown in Fig. 6.3(b) in order to follow their (viscoelastic layers) locations towards the top and bottom surfaces of the overall plate.

In order to integrate shear actuators with the passive damping layer for achieving hybrid active-passive control of the annular plate, the active layer (Fig. 6.1(a)) is added in the former two configurations (Figs. 6.3(a)-(b)) of the annular plate as shown in Figs. 6.4(a)-(b). In Fig. 6.4(b), the active layer is added at the core of the overall annular plate, while, for the other configuration (Fig. 6.4(a)), the same active layer is divided through its middle surface, and the corresponding two

identical active layers are symmetrically located with respect to the passive damping layer at the core. The in-plane locations of the actuator patches in the upper active layer are considered to be identical to that of the similar patches in the lower active layer. Consequently, the in-plane area of an actuator patch is denoted

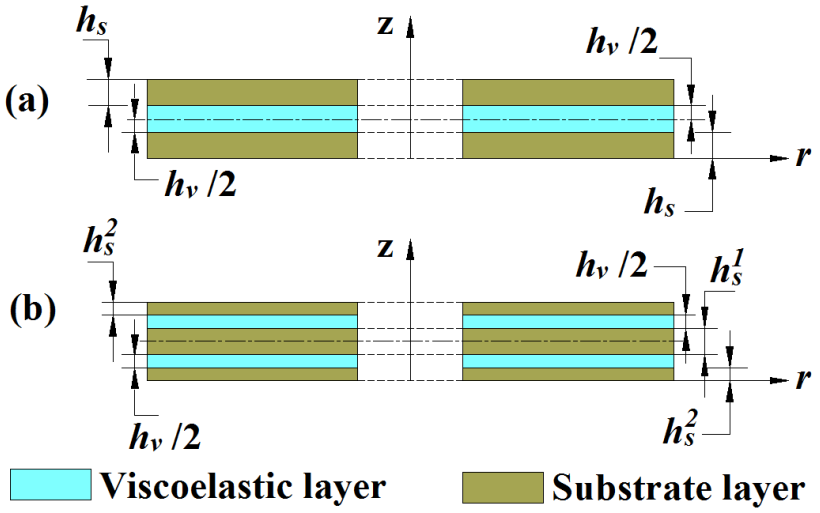

Fig. 6.3 Cross-section of the layered annular plate with (*a*) a VEM layer at the core or (*b*) two identical VEM layers symmetrically located with respect to the middle plane of the overall plate.

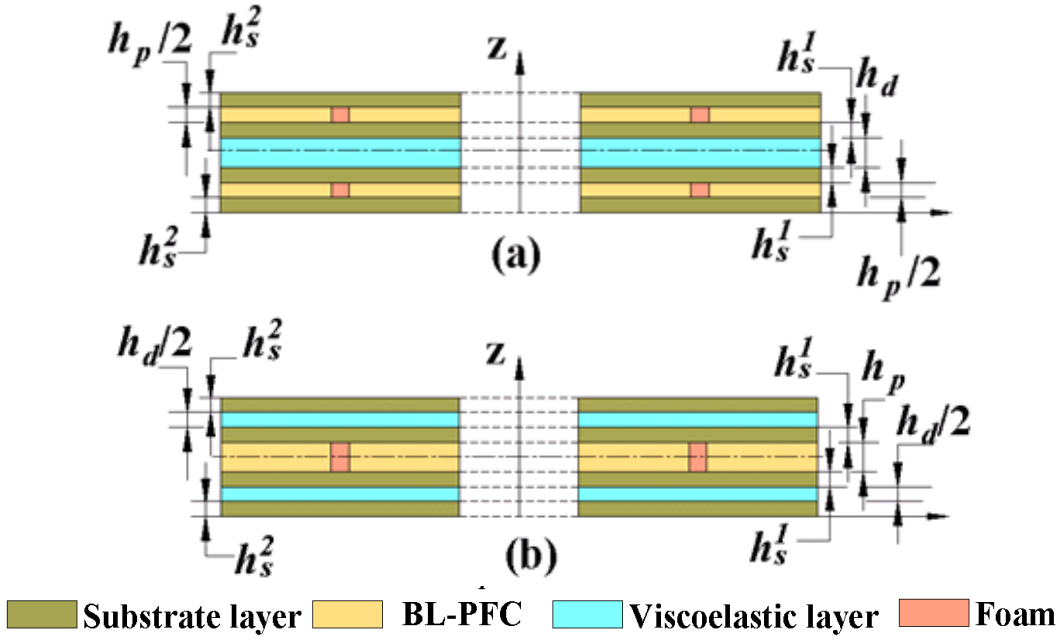

Fig. 6.4 Cross-section of the layered annular plate with (*a*) a VEM layer at the core and two identical active layers or (b) an active layer at the core and two identical VEM layers.

by an actuator zone over the plane of the plate, and the number (n_p) of the actuator zones over the plane of the annular plate is equal to that of the actuator patches in an active layer for any of the cases of single or double active layers.

For the utilization of the 0-3 VEC instead of the pure VEM, the VEM layers in the aforesaid configurations of the layered annular plate (Figs. 6.4(a)-(b)) are replaced by the disc of 0-3 VEC as shown in Figs. 6.5(a)-(b). In case of the use of two VEC layers (Fig. 6.5(b)), the in-plane locations of graphite wafers in the upper VEC layer are considered to be the same as the in-plane locations of the similar wafers in the lower VEC layer. The thickness of VEC layers in Fig. 6.5(b) is considered to be half of that of the VEC layer in Fig. 6.5(a), while the thicknesses of the pure VEM layers and 2-2 VEC layer in every VEC layer are taken with a constant value of r_c ($r_c = h_v / h_{VEC}$ (Fig. 6.2(b))).

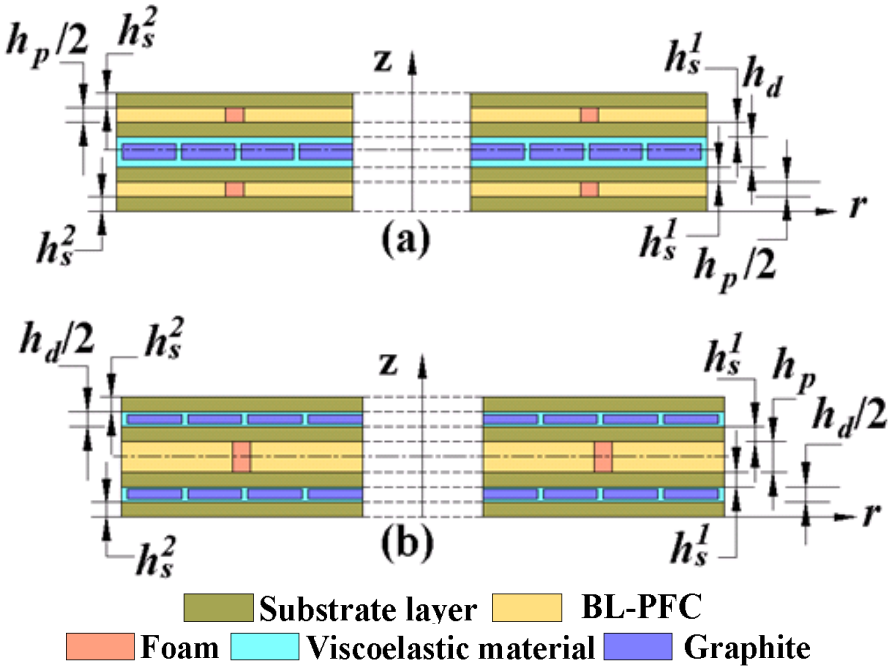

Fig. 6.5 Cross-section of the layered annular plate with (a) a VEC layer at the core and two identical active layers or (b) an active layer at the core and two identical VEC layers.

6.5 Properties of the constituent materials in the layered annular plate

The top and bottom surfaces of the shear actuator patches of BL-PFC are fully electrode surfaces, and the external transverse electric field (E_z) is applied across

these electrodes. So, the BL-PFC actuator patches are subjected to a dominant electric field (E_z)/electric displacement (D_z) in the transverse (z) direction, and thus its constitutive relations can be written as,

$$\boldsymbol{\sigma} = (\mathbf{C}\boldsymbol{\varepsilon} - \boldsymbol{e}_z E_z),$$

$$D_z = (\boldsymbol{e}_z{}^{\mathrm{T}}\boldsymbol{\varepsilon} + \in_{33} E_z) \tag{6.1}$$

where, $\boldsymbol{\sigma}$ / $\boldsymbol{\varepsilon}$ are the stress/strain vector; $\boldsymbol{C}$ is the stiffness matrix; $\boldsymbol{e}_z$ is a vector of piezoelectric coefficients associated with the transverse electric field (E_z); $\in_{33}$ is the permittivity coefficient associated with the transverse electric field (E_z).

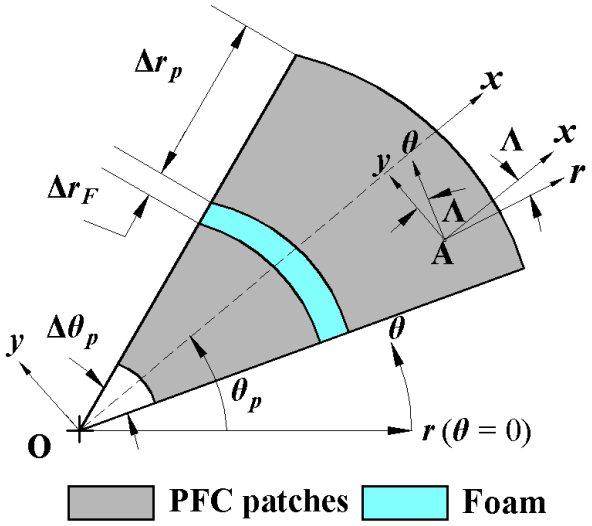

Fig. 3.5 Schematic diagram of a typical row of actuator patches in the $r\theta$-plane of the annular plate.

For a typical row of BL-PFC actuator patches within the active (piezo-foam) layer (Fig. 6.1) along the radial direction, the Cartesian material coordinate system (xyz) of BL-PFC patches and the reference cylindrical coordinate system ($r\theta z$) for the overall annular plate can be illustrated through Fig. 3.5 that is reproduced here for better readability. Accordingly, similar to that in section 3.3, the material properties at any point (r,θ) of a BL-PFC patch can be obtained in the reference cylindrical coordinate system ($r\theta z$) through a transformation of the properties (Eq. (6.1)) of BL-PFC for a rotation of x / y axis with respect to the z-axis at an angle of $\Lambda = (\theta_p - \theta)$ as,

$$\boldsymbol{\sigma}^p = (\boldsymbol{C}^p \boldsymbol{\varepsilon}^p - \boldsymbol{e}_z^p E_z),$$

$$D_z^p = \left\langle \left(\boldsymbol{e}_z^p\right)^{\mathrm{T}} \boldsymbol{\varepsilon}^p + \epsilon_{33}^p E_z \right\rangle, \; p = 2$$

$$\boldsymbol{C}^p = \boldsymbol{T}\boldsymbol{C}\boldsymbol{T}^{\mathrm{T}},$$

$$\boldsymbol{e}_z^p = \boldsymbol{T}\boldsymbol{e}_z, \; \epsilon_{33}^p = \epsilon_{33} \tag{6.2a}$$

where, the superscript p indicates the materials for substrate layer, actuator patches, foam, viscoelastic layer and wafers as per its values as 1, 2, 3, 4 and 5, respectively; $\boldsymbol{T}$ is the transformation matrix.

The present layered annular plate is considered as a thin plate, and its mathematical model is derived using the Equivalent Single Layer (ESL) theory where the transverse normal stress is usually neglected ([404]). Accordingly, the constitutive relations (Eq. (6.2a)) can be reduced as,

$$\boldsymbol{\sigma}_b^p = (\boldsymbol{C}_{bb}^p \boldsymbol{\varepsilon}_b^p + \boldsymbol{C}_{bs}^p \boldsymbol{\varepsilon}_s^p - \boldsymbol{e}_{zb}^p E_z),$$

$$\boldsymbol{\sigma}_s^p = (\boldsymbol{C}_{sb}^p \boldsymbol{\varepsilon}_b^p + \boldsymbol{C}_{ss}^p \boldsymbol{\varepsilon}_s^p - \boldsymbol{e}_{zs}^p E_z),$$

$$D_z^p = \left\langle \left(\boldsymbol{e}_{zb}^p\right)^{\mathrm{T}} \boldsymbol{\varepsilon}_b^p + \left(\boldsymbol{e}_{zs}^p\right)^{\mathrm{T}} \boldsymbol{\varepsilon}_s^p + \epsilon_{33}^p E_z \right\rangle, \; p = 2,$$

$$\boldsymbol{\varepsilon}_b^p = \left\{ \varepsilon_r^p \quad \varepsilon_\theta^p \quad \gamma_{r\theta}^p \right\}^{\mathrm{T}},$$

$$\boldsymbol{\varepsilon}_s^p = \left\{ \gamma_{\theta z}^p \quad \gamma_{rz}^p \right\}^{\mathrm{T}},$$

$$\boldsymbol{\sigma}_b^p = \left\{ \sigma_r^p \quad \sigma_\theta^p \quad \tau_{r\theta}^p \right\}^{\mathrm{T}},$$

$$\boldsymbol{\sigma}_s^p = \left\{ \tau_{\theta z}^p \quad \tau_{rz}^p \right\}^{\mathrm{T}},$$

$$\boldsymbol{C}_{bb}^p = \begin{bmatrix} \bar{C}_{11}^p & \bar{C}_{12}^p & \bar{C}_{16}^p \\ \bar{C}_{12}^p & \bar{C}_{22}^p & \bar{C}_{26}^p \\ \bar{C}_{16}^p & \bar{C}_{26}^p & \bar{C}_{66}^p \end{bmatrix}, \boldsymbol{C}_{bs}^p = \begin{bmatrix} \bar{C}_{14}^p & \bar{C}_{15}^p \\ \bar{C}_{24}^p & \bar{C}_{25}^p \\ \bar{C}_{46}^p & \bar{C}_{56}^p \end{bmatrix},$$

$$\boldsymbol{C}_{ss}^p = \begin{bmatrix} \bar{C}_{44}^p & \bar{C}_{45}^p \\ \bar{C}_{45}^p & \bar{C}_{55}^p \end{bmatrix}, \boldsymbol{e}_{zb}^p = \begin{Bmatrix} \bar{e}_{31}^p \\ \bar{e}_{32}^p \\ \bar{e}_{36}^p \end{Bmatrix}, \; \boldsymbol{e}_{zs}^p = \begin{Bmatrix} \bar{e}_{34}^p \\ \bar{e}_{35}^p \end{Bmatrix},$$

$$\boldsymbol{C}_{sb}^{p}=\left(\boldsymbol{C}_{bs}^{p}\right)^{\mathrm{T}},\ \bar{C}_{ij}^{p}=\left\langle C_{ij}^{p}-C_{i3}^{p}C_{3j}^{p}/C_{33}^{p}\right\rangle,$$
$$\bar{e}_{3j}^{p}=\left\langle e_{3j}^{p}-C_{3j}^{p}e_{33}^{p}/C_{33}^{p}\right\rangle, i,j=1,2,4,5,6 \quad (6.2b)$$

where, $\sigma_r^p / \varepsilon_r^p$ and $\sigma_\theta^p / \varepsilon_\theta^p$ are the normal stresses/strains along the radial and circumferential directions, respectively in the p^{th} constituent material; $\tau_{\theta z}^p / \gamma_{\theta z}^p$, $\tau_{r\theta}^p / \gamma_{r\theta}^p$ and $\tau_{rz}^p / \gamma_{rz}^p$ are the shear stresses/strains in the θz, $r\theta$ and rz planes, respectively within the p^{th} constituent material; C_{ij}^p and e_{ij}^p are the elements of $\boldsymbol{C}^p$ and $\boldsymbol{e}_z^p$, respectively. Similar constitutive relations of the isotropic materials for the substrate layers, foam, graphite wafers and viscoelastic phase can be written as,

$$\boldsymbol{\sigma}_b^p=\boldsymbol{C}_{bb}^p\boldsymbol{\varepsilon}_b^p,$$
$$\boldsymbol{\sigma}_s^p=\boldsymbol{C}_{ss}^p\boldsymbol{\varepsilon}_s^p,\ p=1,3,4,5$$
$$\boldsymbol{C}_{bb}^p=\begin{bmatrix} C_c & C_c\nu^p & 0 \\ C_c\nu^p & C_c & 0 \\ 0 & 0 & C_c\left(1-\nu^p\right) \end{bmatrix},$$
$$\boldsymbol{C}_{ss}^p=\begin{bmatrix} C_c\left(1-\nu^p\right) & 0 \\ 0 & C_c\left(1-\nu^p\right) \end{bmatrix},$$
$$C_c=E^p\Big/\left\langle 1-\left(\nu^p\right)^2\right\rangle \quad (6.3)$$

In Eq. (6.3), E^p and ν^p are Young's modulus and Poisson's ratio of the p^{th} material ($p=1$, 3, 4, 5), respectively. It should be noted here that the viscoelastic material is modelled according to the complex modulus approach, and thus E^p is a complex quantity for the viscoelastic material ($p=4$).

6.6 FE model of the overall annular plate

The bottom surface of the overall annular plate is considered as the reference plane, and the origin of the reference cylindrical coordinate system ($r\theta z$) is located

at the centre of this annular plane. The kinematics of deformation of the layered plate is defined according to the layer-wise theory [404] as,

$$u^k(r,\theta,z,t) = u_0(r,\theta,t) + \sum_{i=1}^{N_L} z_i^k(z)\,\alpha_i(r,\theta,t)\,,$$

$$v^k(r,\theta,z,t) = v_0(r,\theta,t) + \sum_{i=1}^{N_L} z_i^k(z)\,\beta_i(r,\theta,t)\,,$$

$$w^k(r,\theta,z,t) = w_0(r,\theta,t) \tag{6.4}$$

where, N_L is the total number of layers in the overall annular plate; k represents a layer as per its value as 1,2,.... N_L starting from the bottom layer; u^k / u_0, v^k / v_0 and w^k / w_0 are the displacements along the r, θ and z directions, respectively at any point within the k^{th} layer or reference plane; α_i / β_i is the rotation of the normal to the middle plane of i^{th} layer with respect to the θ / r axis; z_i^k is the thickness coordinate as given in Eq. (6.5) where h_k represents the thickness of k^{th} layer.

$$z_1^k = z \text{ or } h_1 \text{ for } k=1 \text{ or } k>1$$

$$z_2^k = 0 \text{ or } (z-h_1) \text{ or } h_2 \text{ for } k<2 \text{ or } k=2 \text{ or } k>2$$

$$z_3^k = 0 \text{ or } (z-h_1-h_2) \text{ or } h_3 \text{ for } k<3 \text{ or } k=3 \text{ or } k>3$$

.

.

$$z_{(N_L-1)}^k = 0 \text{ or } (z-h_1-h_2-h_3-....-h_{(N_L-2)}) \text{ or } h_{(N_L-1)} \text{ for}$$

$$k<(N_L-1) \text{ or } k=(N_L-1) \text{ or } k>(N_L-1)$$

$$z_{N_L}^k = 0 \text{ or } (z-h_1-h_2-h_3-....-h_{N_{L-1}}) \text{ for } k<N \text{ or } k=N_L \tag{6.5}$$

It may be noted here that the kinematics of deformation of every layer of the layered annular plate in this chapter is defined according to the first-order deformation theory (Eq. (6.4)) instead of the third-order theory (Eq. (3.4)) that is considered in the previous formulation (Chapter 3 and Chapter 5) of the annular sandwich plates. This change is made here based on an analysis of the corresponding difference in the results as it is presented in the later section (section 6.8.1) where a minimal difference in the results is observed while the computational cost decreases significantly for the reduced nodal degrees of freedom in the FE model of the

layered plate. However, according to the displacement field in Eq. (6.4), the displacement components (u^k, v^k, w^k) at any point within the k^{th} layer can be written as,

$$\boldsymbol{d}^k = (\boldsymbol{d}_t + \boldsymbol{Z}_r^k \boldsymbol{d}_r),$$

$$\boldsymbol{d}^k = \left\{u^k \quad v^k \quad w^k\right\}^{\mathrm{T}},$$

$$\boldsymbol{d}_t = \left\{u_0 \quad v_0 \quad w_0\right\}^{\mathrm{T}},$$

$$\boldsymbol{d}_r = \left\{\alpha_1 \quad \beta_1 \quad \alpha_2 \quad \beta_2 \quad . \quad . \quad . \quad \alpha_{N_L} \quad \beta_{N_L}\right\}^{\mathrm{T}},$$

$$\boldsymbol{Z}_r^k = \left[\boldsymbol{Z}_1^k \quad \boldsymbol{Z}_2^k \quad \boldsymbol{Z}_3^k \quad \ldots \quad \boldsymbol{Z}_{N_L}^k\right],$$

$$\boldsymbol{Z}_i^k = \begin{bmatrix} z_i^k & 0 & 0 \\ 0 & z_i^k & 0 \end{bmatrix}^{\mathrm{T}} \tag{6.6}$$

The displacement components can also be expressed in terms of a generalized displacement vector ($\boldsymbol{d}$) and the transformation matrices ($\boldsymbol{T}_t$ and $\boldsymbol{T}_r$) as,

$$\boldsymbol{d}^k = (\boldsymbol{T}_t + \boldsymbol{Z}_r^k \boldsymbol{T}_r)\boldsymbol{d},$$

$$\boldsymbol{d} = \left\{u_0 \quad v_0 \quad w_0 \quad \alpha_1 \quad \beta_1 \quad \alpha_2 \quad \beta_2 \quad \alpha_3 \quad \beta_3 \quad ..... \quad ..... \quad \alpha_{N_L} \quad \beta_{N_L}\right\}^{\mathrm{T}} \tag{6.7}$$

According to the displacement field (Eq. (6.4)) and the state of strain (Eqs. (6.2b)-(6.3)), the strain-displacement relations for k^{th} layer can be written as,

$$\boldsymbol{\varepsilon}_b^k = (\boldsymbol{\varepsilon}_{bL} + \boldsymbol{Z}_b^k \boldsymbol{\kappa}_b),$$

$$\boldsymbol{\varepsilon}_s^k = (\boldsymbol{\varepsilon}_{sL} + \boldsymbol{Z}_s^k \boldsymbol{\kappa}_s),$$

$$\boldsymbol{\kappa}_b = \left\{\boldsymbol{\kappa}_b^1 \quad \boldsymbol{\kappa}_b^2 \quad .... \quad \boldsymbol{\kappa}_b^{N_L}\right\}^{\mathrm{T}},$$

$$\boldsymbol{\kappa}_s = \left\{\boldsymbol{\kappa}_s^1 \quad \boldsymbol{\kappa}_s^2 \quad .... \quad \boldsymbol{\kappa}_s^{N_L}\right\}^{\mathrm{T}},$$

$$\boldsymbol{\varepsilon}_{bL} = \left\{\frac{\partial u_0}{\partial r} \quad \left(\frac{\partial v_0}{r\partial\theta} + \frac{u_0}{r}\right) \quad \left(\frac{\partial u_0}{r\partial\theta} + \frac{\partial v_0}{\partial r} - \frac{v_0}{r}\right)\right\}^{\mathrm{T}},$$

$$\boldsymbol{\varepsilon}_{sL} = \left\{\frac{\partial w_0}{r\partial\theta} \quad \frac{\partial w_0}{\partial r}\right\}^{\mathrm{T}},$$

$$\boldsymbol{\kappa}_b^i = \left\{ \frac{\partial \alpha_i}{\partial r} \quad \frac{\partial \beta_i}{r\partial \theta} \quad \left(\frac{\partial \alpha_i}{r\partial \theta} + \frac{\partial \beta_i}{\partial r} - \frac{\beta_i}{r} \right) \right\}^{\mathrm{T}},$$

$$\boldsymbol{\kappa}_s^i = \{ \beta_i \quad \alpha_i \}^{\mathrm{T}},$$

$$\boldsymbol{Z}_b^k = [\boldsymbol{z}_{b1}^k \quad \boldsymbol{z}_{b2}^k \quad .... \quad \boldsymbol{z}_{bN_L}^k],$$

$$\boldsymbol{Z}_s^k = [\boldsymbol{z}_{s1}^k \quad \boldsymbol{z}_{s2}^k \quad .... \quad \boldsymbol{z}_{sN_L}^k],$$

$$\boldsymbol{z}_{bi}^k = \boldsymbol{I}_{3\times 3} \otimes z_i^k, \; \boldsymbol{z}_{si}^k = \boldsymbol{I}_{2\times 2} \otimes (\partial z_i^k / \partial z) \tag{6.8}$$

where, $\boldsymbol{\varepsilon}_b^k / \boldsymbol{\varepsilon}_s^k$ is in the same form of $\boldsymbol{\varepsilon}_b^p / \boldsymbol{\varepsilon}_s^p$ (Eq. (6.2b)); $\otimes$ represents the Kronecker product; $\boldsymbol{I}_{3\times 3} / \boldsymbol{I}_{2\times 2}$ is the unit matrix of size $(3\times 3)/(2\times 2)$. The generalized strain vectors ($\boldsymbol{\varepsilon}_{bL}$, $\boldsymbol{\kappa}_b$, $\boldsymbol{\varepsilon}_{sL}$, $\boldsymbol{\kappa}_s$) appearing in Eq. (6.8) can also be written in terms of the operator matrices ($\boldsymbol{L}_{bL}$, $\boldsymbol{L}_{b\kappa}$, $\boldsymbol{L}_{sL}$, $\boldsymbol{L}_{s\kappa}$) as,

$$\boldsymbol{\varepsilon}_{bL} = \boldsymbol{L}_{bL}\boldsymbol{d}_t,$$

$$\boldsymbol{\kappa}_b = \boldsymbol{L}_{b\kappa}\boldsymbol{d}_r,$$

$$\boldsymbol{\varepsilon}_{sL} = \boldsymbol{L}_{sL}\boldsymbol{d}_t,$$

$$\boldsymbol{\kappa}_s = \boldsymbol{L}_{s\kappa}\boldsymbol{d}_r \tag{6.9}$$

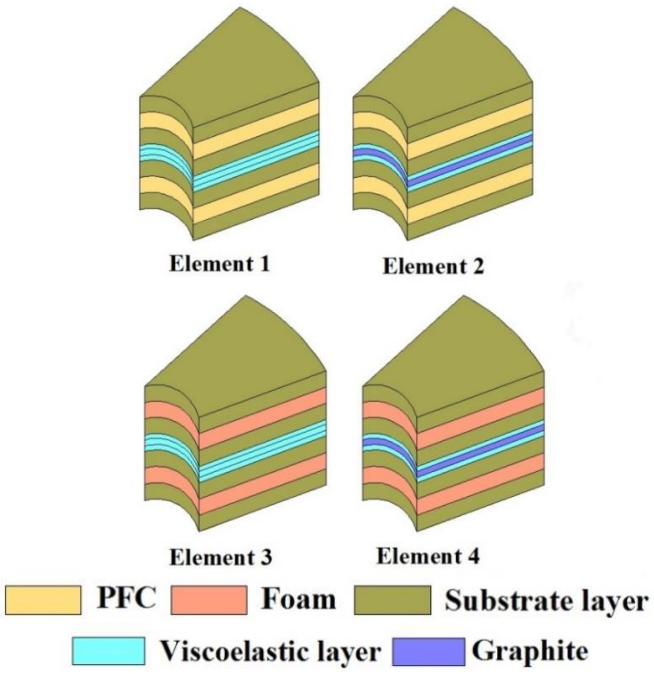

Fig. 6.6 Elemental stacking sequences in the FE mesh of the layered annular plate with the VEC core and two piezo-foam layers (Fig.6(a)).

In order to derive the FE model of the overall annular plate, its reference plane is discretized by 9-node quadrilateral elements in such a manner that every element is in the shape of the annular sector with its edges in parallel to the radial and circumferential axes of the reference cylindrical coordinate system. A typical element is considered to be made of the homogeneous layers although there are the VEC and active (piezo-foam composite) layers within the overall layered annular plate. It can be achieved by generating the FE mesh of the reference plane of the overall annular plate following the boundaries of the graphite wafers and actuator patches in the ($r\theta$) plane of the plate. Consequently, the elements in the FE mesh would appear with different elemental stacking sequences of the substrate, graphite, viscoelastic, foam and actuator layers according to the layered construction of the overall annular plate. For an example of the layered annular plate in Fig 6.5(a)), four types of elemental stacking sequences appear as shown in Fig. 6.6.

The generalized strain and displacement vectors (Eqs. (6.7) and (6.9)) at any point in a typical element can be expressed in terms of the shape function matrix ($\boldsymbol{N}$) and the elemental nodal displacement vector ($\boldsymbol{d}^e$) as follows,

$$\begin{aligned}
\boldsymbol{d} &= \boldsymbol{N}\,\boldsymbol{d}^e, \\
\boldsymbol{\varepsilon}_{bL} &= \boldsymbol{B}_{bL}\boldsymbol{d}^e, \\
\boldsymbol{\kappa}_b &= \boldsymbol{B}_{\kappa b}\boldsymbol{d}^e, \\
\boldsymbol{\varepsilon}_{sL} &= \boldsymbol{B}_{sL}\boldsymbol{d}^e, \\
\boldsymbol{\kappa}_s &= \boldsymbol{B}_{\kappa s}\boldsymbol{d}^e \\
\boldsymbol{B}_{bL} &= \boldsymbol{L}_{bL}\boldsymbol{T}_t\boldsymbol{N}, \\
\boldsymbol{B}_{\kappa b} &= \boldsymbol{L}_{b\kappa}\boldsymbol{T}_r\boldsymbol{N}, \\
\boldsymbol{B}_{sL} &= \boldsymbol{L}_{sL}\boldsymbol{T}_t\boldsymbol{N}, \\
\boldsymbol{B}_{\kappa s} &= \boldsymbol{L}_{s\kappa}\boldsymbol{T}_r\boldsymbol{N}
\end{aligned} \tag{6.10}$$

The overall annular plate is considered to be subjected to a transversely distributed harmonic load ($p(r,\theta,t)$) at its bottom surface ($z=0$). For the corresponding vibration of the overall plate, the first variations of the total potential

energy (δT_p^e) and the total kinetic energy (δT_k^e) of a typical element at an instant of time (t) can be written as,

$$\delta T_p^e = \int_{r_i^e}^{r_o^e}\int_{\theta_i^e}^{\theta_o^e}\left\{\sum_{k=1}^{N_L}\int_{h_{k-1}}^{h_{k+1}}\left[(\delta\boldsymbol{\varepsilon}_b^k)^{\mathrm{T}}\boldsymbol{\sigma}_b^k + (\delta\boldsymbol{\varepsilon}_s^k)^{\mathrm{T}}\boldsymbol{\sigma}_s^k - (\delta E_z)D_z^k\right]dz - Q_w\right\} rd\theta dr\,,$$

$$Q_w = \left\langle(\delta w_0)\, p(r,\theta,t)\right\rangle_{z=0} \tag{6.11}$$

$$\delta T_k^e = \int_{r_i^e}^{r_0^e}\int_{\theta_i^e}^{\theta_0^e}\left\langle\sum_{k=1}^{N_L}\int_{h_{k-1}}^{h_{k+1}}\left\{\delta\dot{u}^k \quad \delta\dot{v}^k \quad \delta\dot{w}^k\right\}\rho^k\left\{\dot{u}^k \quad \dot{v}^k \quad \dot{w}^k\right\}^{\mathrm{T}}dz\right\rangle rd\theta dr \tag{6.12}$$

where, h_{k-1} and h_{k+1} are the thickness coordinates at the bottom and top surfaces of k^{th} layer, respectively; ρ^k is the mass density of the k^{th} layer; r_i^e / θ_i^e and r_0^e / θ_0^e are the inner and outer radial/circumferential coordinates at the inner and outer boundaries of an element, respectively. It should be noted here that the term $(\delta E_z)D_z^k$ in Eq. (6.11) would remain only for the actuator layer within the stacking sequence of an element. Moreover, since the electric field (E_z) is specified at every instant of time through a control strategy, Eq. (6.11) can be reduced by $\delta E_z = 0$. Using Eqs.(6.2b), (6.3), (6.6), (6.8) and (6.10) in Eqs. (6.11) and (6.12), the simplified expressions of the first variations of total potential energy (δT_p^e) and total kinetic energy (δT_k^e) for a typical element can be obtained as,

$$\delta T_p^e = \left(\delta\boldsymbol{d}^e\right)^{\mathrm{T}}\left\langle\left(\boldsymbol{K}_b^e + \boldsymbol{K}_s^e\right)\boldsymbol{d}^e - \left(\boldsymbol{P}_{bE}^e + \boldsymbol{P}_{sE}^e\right)E_z - \boldsymbol{P}_M^e\right\rangle,$$

$$\delta T_k^e = (\delta\dot{\boldsymbol{d}}^e)^{\mathrm{T}}\boldsymbol{M}^e\dot{\boldsymbol{d}}^e\,,$$

$$\boldsymbol{K}_b^e = \int_{r_i^e}^{r_o^e}\int_{\theta_i^e}^{\theta_i^e}\left\langle\begin{array}{l}\left(\boldsymbol{B}_{bL}\right)^{\mathrm{T}}\left(\boldsymbol{A}_1\boldsymbol{B}_{bL} + \boldsymbol{B}_1\boldsymbol{B}_{\kappa b} + \boldsymbol{A}_2\boldsymbol{B}_{sL} + \boldsymbol{B}_2\boldsymbol{B}_{\kappa s}\right)\\ +\left(\boldsymbol{B}_{\kappa b}\right)^{\mathrm{T}}\left(\boldsymbol{B}_3\boldsymbol{B}_{bL} + \boldsymbol{D}_1\boldsymbol{B}_{\kappa b} + \boldsymbol{B}_4\boldsymbol{B}_{sL} + \boldsymbol{D}_2\boldsymbol{B}_{\kappa s}\right)\end{array}\right\rangle rd\theta dr\,,$$

$$\boldsymbol{K}_s^e = \int_{r_i^e}^{r_o^e}\int_{\theta_i^e}^{\theta_i^e}\left\langle\begin{array}{l}\left(\boldsymbol{B}_{sL}\right)^{\mathrm{T}}\left(\boldsymbol{A}_3\boldsymbol{B}_{bL} + \boldsymbol{B}_5\boldsymbol{B}_{\kappa b} + \boldsymbol{A}_4\boldsymbol{B}_{sL} + \boldsymbol{B}_6\boldsymbol{B}_{\kappa s}\right)\\ +\left(\boldsymbol{B}_{\kappa s}\right)^{\mathrm{T}}\left(\boldsymbol{B}_7\boldsymbol{B}_{bL} + \boldsymbol{D}_3\boldsymbol{B}_{\kappa b} + \boldsymbol{B}_8\boldsymbol{B}_{sL} + \boldsymbol{D}_4\boldsymbol{B}_{\kappa s}\right)\end{array}\right\rangle rd\theta dr\,,$$

$$\boldsymbol{M}^e = \int_{r_i^e}^{r_o^e}\int_{\theta_i^e}^{\theta_i^e}\left\langle\boldsymbol{N}^{\mathrm{T}}\left\langle(\boldsymbol{T}_t)^{\mathrm{T}}m_1\boldsymbol{T}_t + (\boldsymbol{T}_t)^{\mathrm{T}}\boldsymbol{m}_2\boldsymbol{T}_r + (\boldsymbol{T}_r)^{\mathrm{T}}\boldsymbol{m}_3\boldsymbol{T}_t + (\boldsymbol{T}_r)^{\mathrm{T}}\boldsymbol{m}_4\boldsymbol{T}_r\right\rangle\boldsymbol{N}\right\rangle rd\theta dr\,,$$

$$\boldsymbol{P}_M^e = \int_{r_i^e}^{r_o^e}\int_{\theta_i^e}^{\theta_i^e} \left\langle \boldsymbol{N}^{\mathrm{T}} \boldsymbol{T}_p{}^{\mathrm{T}}\, p(r,\theta,t) \right\rangle r\,d\theta\,dr\,,$$

$$\boldsymbol{P}_{bE}^e = \int_{r_i^e}^{r_o^e}\int_{\theta_i^e}^{\theta_i^e} \left\langle (\boldsymbol{B}_{bL})^{\mathrm{T}} \boldsymbol{A}_{bE} + (\boldsymbol{B}_{\kappa b})^{\mathrm{T}} \boldsymbol{B}_{bE} \right\rangle r\,d\theta\,dr\,,$$

$$\boldsymbol{P}_{sE}^e = \int_{r_i^e}^{r_o^e}\int_{\theta_i^e}^{\theta_i^e} \left\langle (\boldsymbol{B}_{sL})^{\mathrm{T}} \boldsymbol{A}_{sE} + (\boldsymbol{B}_{\kappa s})^{\mathrm{T}} \boldsymbol{B}_{sE} \right\rangle r\,d\theta\,dr \qquad (6.13)$$

where, $\boldsymbol{K}_b^e$ and $\boldsymbol{K}_s^e$ are the elemental bending and shear stiffness matrices, respectively; $\boldsymbol{M}^e$ is the elemental mass matrix; $\boldsymbol{P}_{bE}^e$ and $\boldsymbol{P}_{sE}^e$ are the elemental nodal electro-elastic coefficient vectors; $\boldsymbol{P}_M^e$ is the elemental nodal mechanical load vector; $\boldsymbol{T}_p$ is a row matrix that specifies the work-conjugate displacement (w_0) for the applied transverse distributed load ($p(r,\theta,t)$) at the bottom surface ($z=0$) of the overall annular plate. The different rigidity matrices, electro-elastic coupling vectors and mass matrix per unit area in Eq. (6.13) are computed according to the expressions in Eq. (6.14), where it is important to follow the stacking sequence of different layers in an element for assigning the layer-wise material properties.

$$\boldsymbol{A}_1 = \sum_{k=1}^{N_L}\int_{h_{k-1}}^{h_{k+1}} \boldsymbol{C}_{bb}^k dz\,,$$

$$\boldsymbol{B}_1 = \sum_{k=1}^{N_L}\int_{h_{k-1}}^{h_{k+1}} \boldsymbol{C}_{bb}^k \boldsymbol{Z}_b^k dz\,,$$

$$\boldsymbol{A}_2 = \sum_{k=1}^{N_L}\int_{h_{k-1}}^{h_{k+1}} \boldsymbol{C}_{bs}^k dz\,,$$

$$\boldsymbol{B}_2 = \sum_{k=1}^{N_L}\int_{h_{k-1}}^{h_{k+1}} \boldsymbol{C}_{bs}^k \boldsymbol{Z}_s^k dz\,,$$

$$\boldsymbol{B}_3 = \sum_{k=1}^{N_L}\int_{h_{k-1}}^{h_{k+1}} \left(\boldsymbol{Z}_b^k\right)^{\mathrm{T}} \boldsymbol{C}_{bb}^k dz\,,$$

$$\boldsymbol{D}_1 = \sum_{k=1}^{N_L}\int_{h_{k-1}}^{h_{k+1}} \left(\boldsymbol{Z}_b^k\right)^{\mathrm{T}} \boldsymbol{C}_{bb}^k \boldsymbol{Z}_b^k dz\,,$$

$$\boldsymbol{B}_4 = \sum_{k=1}^{N_L}\int_{h_{k-1}}^{h_{k+1}} \left(\boldsymbol{Z}_b^k\right)^{\mathrm{T}} \boldsymbol{C}_{bs}^k dz\,,$$

$$\boldsymbol{D}_2 = \sum_{k=1}^{N_L} \int_{h_{k-1}}^{h_{k+1}} \left(\boldsymbol{Z}_b^k\right)^{\mathrm{T}} \boldsymbol{C}_{bs}^k \boldsymbol{Z}_s^k \, dz \,,$$

$$\boldsymbol{A}_3 = \sum_{k=1}^{N_L} \int_{h_{k-1}}^{h_{k+1}} \boldsymbol{C}_{sb}^k \, dz \,,$$

$$\boldsymbol{B}_5 = \sum_{k=1}^{N_L} \int_{h_{k-1}}^{h_{k+1}} \boldsymbol{C}_{sb}^k \boldsymbol{Z}_b^k \, dz \,,$$

$$\boldsymbol{A}_4 = \sum_{k=1}^{N_L} \int_{h_{k-1}}^{h_{k+1}} \boldsymbol{C}_{ss}^k \, dz \,,$$

$$\boldsymbol{B}_6 = \sum_{k=1}^{N_L} \int_{h_{k-1}}^{h_{k+1}} \boldsymbol{C}_{ss}^k \boldsymbol{Z}_s^k \, dz \,,$$

$$\boldsymbol{B}_7 = \sum_{k=1}^{N_L} \int_{h_{k-1}}^{h_{k+1}} \left(\boldsymbol{Z}_s^k\right)^{\mathrm{T}} \boldsymbol{C}_{sb}^k \, dz \,,$$

$$\boldsymbol{D}_3 = \sum_{k=1}^{N_L} \int_{h_{k-1}}^{h_{k+1}} \left(\boldsymbol{Z}_s^k\right)^{\mathrm{T}} \boldsymbol{C}_{sb}^k \boldsymbol{Z}_b^k \, dz \,,$$

$$\boldsymbol{B}_8 = \sum_{k=1}^{N_L} \int_{h_{k-1}}^{h_{k+1}} \left(\boldsymbol{Z}_s^k\right)^{\mathrm{T}} \boldsymbol{C}_{ss}^k \, dz \,,$$

$$\boldsymbol{D}_4 = \sum_{k=1}^{N_L} \int_{h_{k-1}}^{h_{k+1}} \left(\boldsymbol{Z}_s^k\right)^{\mathrm{T}} \boldsymbol{C}_{ss}^k \boldsymbol{Z}_s^k \, dz \,,$$

$$m_1 = \sum_{k=1}^{N_L} \int_{h_{k-1}}^{h_{k+1}} \rho^k \, dz \,,$$

$$\boldsymbol{m}_2 = \sum_{k=1}^{N_L} \int_{h_{k-1}}^{h_{k+1}} \rho^k \boldsymbol{Z}_r^k \, dz \,,$$

$$\boldsymbol{m}_3 = \sum_{k=1}^{N_L} \int_{h_{k-1}}^{h_{k+1}} \left(\boldsymbol{Z}_r^k\right)^{\mathrm{T}} \rho^k \, dz \,,$$

$$\boldsymbol{m}_4 = \sum_{k=1}^{N_L} \int_{h_{k-1}}^{h_{k+1}} \left(\boldsymbol{Z}_r^k\right)^{\mathrm{T}} \rho^k \boldsymbol{Z}_r^k \, dz \,,$$

$$\boldsymbol{A}_{bE} = \sum_{k=1}^{N_L} \int_{h_{k-1}}^{h_{k+1}} \boldsymbol{e}_b^k \, dz \,,$$

$$\boldsymbol{B}_{bE} = \sum_{k=1}^{N_L} \int_{h_{k-1}}^{h_{k+1}} \left(\boldsymbol{Z}_b^k \right)^{\mathrm{T}} \boldsymbol{e}_b^k \, dz \,,$$

$$\boldsymbol{A}_{sE} = \sum_{k=1}^{N_L} \int_{h_{k-1}}^{h_{k+1}} \boldsymbol{e}_s^k \, dz \,,$$

$$\boldsymbol{B}_{sE} = \sum_{k=1}^{N_L} \int_{h_{k-1}}^{h_{k+1}} \left(\boldsymbol{Z}_s^k \right)^{\mathrm{T}} \boldsymbol{e}_s^k \, dz \qquad (6.14)$$

In Eq. (6.13), the shear and bending counterparts of the elemental stiffness matrix and electro-elastic coefficient vector are formulated separately so that the selective integration can be implemented in a straightforward manner. It may be noted here that the elemental electro-elastic coefficient vector is a null vector for an element without any actuator layer.

The matrices and vectors in Eq. (6.13) are generated by the numerical integration according to the full (3×3)/reduced (2×2) Gauss quadrature rule (selective integration for 9-node plane element). The properties of the BL-PFC actuator (Eq. (6.1)) are originally defined in its Cartesian material coordinate system (xyz). So, for an element with BL-PFC actuator layer, first, the properties of the actuator layer are computed at every Gauss point within the element according to Eq. (6.2a), and then the quantities in Eq. (6.14) are computed at the same Gauss points in order to generate the matrices and vectors in Eq. (6.13) for that element as per the full (3×3)/reduced (2×2) Gauss quadrature rule. For an element without actuator (BL-PFC) layer, the full (3×3)/reduced (2×2) Gauss quadrature rule is implemented in a straightforward manner since the layers of that element are made of isotropic materials. The governing equations of motion of the overall annular plate are obtained employing extended Hamilton's principle (2.35).

Using Eq. (6.13) in Eq. (2.35), the elemental governing equations of motion can be obtained, and the assemblage of these elemental equations in the global space yields the governing equations of motion for the overall layered annular plate as follows,

$$\boldsymbol{M}\ddot{\boldsymbol{X}} + \boldsymbol{K}\boldsymbol{X} = \boldsymbol{P}_M + \sum_{s=1}^{n_p} \boldsymbol{P}_E^s E_z^s \,,$$

$$\boldsymbol{K} = (\boldsymbol{K}_b + \boldsymbol{K}_s)\,,$$

$$\boldsymbol{P}_E^s = (\boldsymbol{P}_{bE}^s + \boldsymbol{P}_{sE}^s) \tag{6.15}$$

where, $\boldsymbol{M}$ is the global mass matrix; $\boldsymbol{K}_b$ and $\boldsymbol{K}_s$ are the bending and shear counterparts of the global stiffness matrix ($\boldsymbol{K}$), respectively; $\boldsymbol{X}$ is the global nodal displacement vector; $\boldsymbol{P}_M$ is the global nodal mechanical load vector; n_p is the number of actuator zones over the plane of the annular plate as defined in the earlier section; $\boldsymbol{P}_{bE}^s$ and $\boldsymbol{P}_{sE}^s$ are the bending and shear counterparts of the global nodal electro-elastic coefficient vector ($\boldsymbol{P}_E^s$), respectively for s^{th} actuator zone and that ($\boldsymbol{P}_{bE}^s$, $\boldsymbol{P}_{sE}^s$) are obtained through the assemblage of elemental nodal electro-elastic coefficient vectors ($\boldsymbol{P}_{bE}^e$, $\boldsymbol{P}_{sE}^e$) for the elements within the s^{th} actuator zone; E_z^s is the applied transverse electric field across the thickness of the actuator patches in the s^{th} actuator zone.

6.7 Shear-based active control strategy

According to the constructional features of the active layer (Fig. 6.1), the patches of BL-PFC are presently used mainly to counteract the mechanically induced transverse shear stress (τ_{rz}) in the overall annular plate. This mechanically induced shear stress (τ_{rz}) changes its sign over the plane of the annular plate for its any bending mode-shape of vibration. So, for effective actuation, the actuator patches in every actuator zone are considered to be activated by the feedback of their local requirement in counteraction of the mechanically induced shear stress (τ_{rz}), and it is presently achieved by the feedback of the time-rate of change of local slope of bending deformation of the plate in the rz -plane similar to the shear-based control strategy as presented in section 3.5.

For the implementation of this shear-based control strategy, the velocity sensors are used, and those are located over the top surface of the overall annular plate following the radial boundaries of the actuators zones in the plane of the plate as shown in Fig. 6.7. It may be noted here that a similar arrangement of the

velocity sensors is shown in Fig. 3.7 in the analysis of the annular sandwich plate having the actuator patches of obliquely reinforced 1-3 PFC at the core. The difference here lies only in consideration of actuator zones in the plane of the plate as shown in Fig. 6.7. However, the transverse velocities sensed by the velocity sensors are used to estimate the time-rate of change of slope (in the rz-plane) around an actuator zone as the corresponding mathematical expression can be written according to Eq. (3.18) where the superscript s is now taken as a typical actuator zone.

$$(\dot{\varphi}_r^s) = \frac{({}^o\dot{w}_0^s) - ({}^i\dot{w}_0^s)}{\Delta r^s}, \quad \Delta r^s = (r_i^s - r_o^s) \tag{3.18}$$

The time-rate of change of estimated slope (Eq. (3.18)) around an actuator zone is fed back in the form of the transverse electric field across the thickness of the actuator patches within that zone according to the velocity feedback control law, and it can be expressed by Eq. (3.19).

$$E_z^s = -\frac{k_d^s}{\Delta r^s}\left\langle ({}^o\dot{w}_0^s) - ({}^i\dot{w}_0^s)\right\rangle \tag{3.19}$$

Expressing the transverse velocities at the sensing points in terms of the global nodal velocity vector ($\dot{\boldsymbol{X}}$) and a transformation row matrix ($\boldsymbol{N}_T^s$) by Eq. 3.20, and then using Eqs. (3.19) and (3.20) in Eq. (6.15), the closed-loop FE equations of motion of the layered annular plate can be obtained in a similar form as given in Eq. (3.21).

$$\begin{aligned} &\left\langle ({}^o\dot{w}_0^s) - ({}^i\dot{w}_0^s)\right\rangle = N_T^s \dot{\boldsymbol{X}} \\ &\boldsymbol{M}\ddot{\boldsymbol{X}} + \boldsymbol{C}\dot{\boldsymbol{X}} + \boldsymbol{K}\boldsymbol{X} = \boldsymbol{P}_M(t), \end{aligned} \tag{3.20}$$

$$\boldsymbol{C} = \sum_{s=1}^{n_p}\left\langle \boldsymbol{P}_E^s k_d^s N_T^s \right\rangle \tag{3.21}$$

6.8 Results and discussions

For the configurations of the layered annular plate as shown in Figs. 6.4 and 6.5, the inner (r_i) and outer (r_o) radii are considered as 0.2 m and 1 m, respectively. The total thickness ($h_s = 2(h_s^1 + h_s^2)$) of the substrate layers is taken as 4 mm. The total thickness (h_p) of the active (piezo-foam) layers and the total thickness (h_d) of

the damping (VEC/VEM) layers are considered as equal with a value of 2 mm. So, the thickness (h) of the overall layered annular plate arises as 8 mm. All geometrical dimensions (r_c, Δr_v, Δr_G, $\Delta\theta_v$, $\Delta\theta_G$, n_{rg}, $n_{\theta g}$ (Fig. 6.2(b)) in the arrangement of graphite wafers within the VEC layers are taken in an optimal manner. For active (piezo-foam, Fig. 6.1(a)) layers, the gaps Δr_F and $\Delta\theta_F$ are taken as 10 mm and 5^0, respectively. With these gaps ($\Delta r_F = 10$ mm, $\Delta\theta_F = 5^0$),two actuator patches are considered along the radial direction ($n_r = 2$) for the convenience in application of external transverse electric field through the edges of the layered annular plate, while the number (n_θ) of actuator patches along the circumferential direction is taken optimally based on the requirement of narrow circumferential span ($\Delta\theta_p$) of patches (section 6.2) as well as the bending modes of vibration of the annular plate under study (section 3.2).

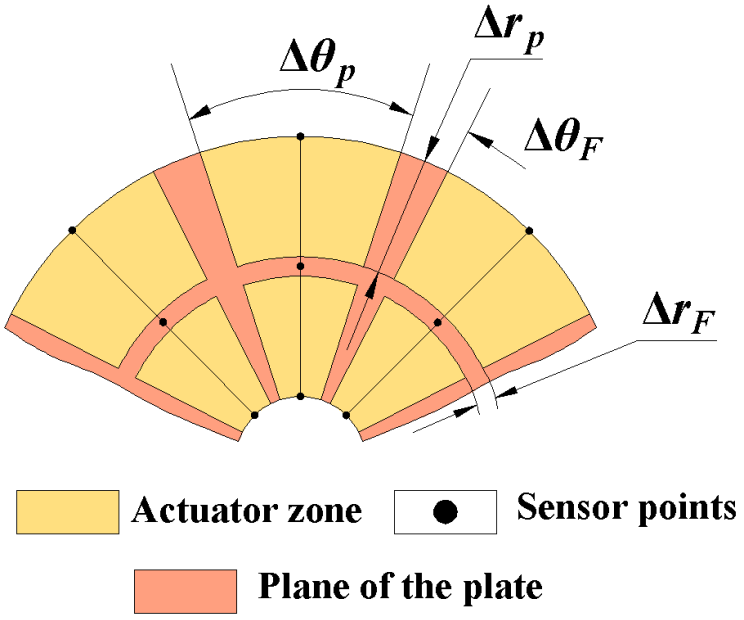

Fig. 6.7 Actuator zones and the corresponding locations of the velocity sensors over the plane of the annular plate.

The substrate layers are considered to be made of Aluminium (E = 70 GPa, ν = 0.3, ρ = 2700 kg/m^3). The material properties of the foam at the core are taken as considered in the analysis of the annular sandwich plates in Chapter 3 (E = 35.3 MPa, G = 12.76 MPa, ρ = 32 kg/m^3). The viscoelastic material is considered

to have the properties of $E = 11.75(1+0.3i)$ MPa, $\nu = 0.49$, $\rho =$ 920 kg/m^3. The properties of the graphite wafers are, $E =$ 250 GPa, $\nu =$ 0.3, $\rho =$ 1400 kg/m^3. The actuator of BL-PFC is considered to be made of the fibers of PZT5H [391] and epoxy matrix ($E =$ 2.9 GPa, $\nu =$ 0.3, $\rho =$ 1250 kg/m^3), and its (BL-PFC) properties are obtained from the micromechanics formulation in section 4.2 for the fiber orientation angle (ϕ) and fiber volume fraction as 25^0 and 0.776, respectively. These properties of BL-PFC are, $C_{11} = 16.76$ GPa, $C_{22} =$ 42.20 GPa, $C_{33} = 29.18$ GPa, $C_{12} = 8.03$ GPa, $C_{13} =$ 9.97 GPa, $C_{23} =$ 13.68 GPa, $C_{44} =$ 8.40 GPa, $C_{55} =$ 6.70 GPa, $C_{66} =$ 4.80 GPa, $e_{35} =$ 5.92 C/m^2, $\rho =$ 5903.67 kg/m^3.

The inner and outer edges of the overall annular plate are considered as the simply-supported edges ($w_0 = 0$, $v_0 = 0$, $\beta_i = 0$ at $r = r_o$ and r_i) while the transversely distributed harmonic load is considered in a form as given in Eq. (2.46).

$$p(r,\theta,t) = (1 + \cos\theta + \cos 2\theta + \cos 3\theta)\, p_o e^{i\omega t} \tag{2.46}$$

The feedback control gains (k_d^s) over the actuator zones ($s = 1,2,\ldots.. n_p$) are taken with the uniform value ($k_d^s = k_d$). In the present results, the controlled frequency response of the layered annular plate under the harmonic load (Eq. (2.46)) is presented by the maximum nodal transverse displacement-amplitude ($w_{\max} / h$) at every frequency (ω). The corresponding required control voltage is presented as the maximum one ($V_{\max}$) among the control voltages over the actuator zones.

6.8.1 Verification of present FE formulation

For verification of the present FE formulation, first, the layered annular plate is taken as an isotropic annular plate considering negligibly thin active ($h_p \approx 0$) and VEM/VEC ($h_d \approx 0$) layers. The fundamental natural frequency of this annular plate is computed for different boundary conditions. These results are illustrated in Table 6.1 together with similar results for an identical annular plate analysed in [388]. It may be observed from Table 6.1 that the present results are in good agreement with the similar results available in [388]. This comparison verifies the present FE formulation for handling the vibration of the annular plate.

Table 6.1 Comparison of dimensionless ($\lambda = \omega r_o^2 \sqrt{\rho h / D}$, $D = Eh^3/12(1-\nu^2)$) natural frequency for the isotropic annular plate (CC/SS implies clamped/simply-supported inner and outer edges of the isotropic annular plate).

Source	BCs	λ		
		$r_i / r_o = 0.2$	$r_i / r_o = 0.4$	$r_i / r_o = 0.6$
Present	CC	34.64	61.89	139.47
Ref. [388]		34.61	61.87	139.60
Present	SS	16.78	28.12	62.13
Ref. [388]		16.72	28.08	62.12

For further verification of the present FE formulation in handling the shear mode piezoelectric actuation, the layered annular plate in Fig. 6.4(b) is taken in the form of an annular sandwich plate with the active (piezo-foam) layer at the core and negligibly thin ($h_d \approx 0$) VEM layers. The circumferential gaps among the actuator patches in the piezo-foam layer are removed ($\Delta\theta_F = 0$) retaining the radial gaps ($\Delta r_F \neq 0$) so that two annular actuators appear at the inner and outer edges of the sandwich annular plate. The material of these annular actuators is taken as PZT5H [391] that is considered to be poled along the radial direction, and thus an axisymmetric configuration of the annular sandwich plate arises. For an applied transverse electric field (E_z) across the thickness of the annular actuators at the core, the shear actuation force in the rz-plane appears and the corresponding electro-elastic deformation of the annular sandwich plate with the fixed inner and outer edges is computed using the present FE formulation. The corresponding axisymmetric bending deflection of the annular sandwich plate is plotted in Fig. 6.8 along with the similar results for an identical plate as given in Fig. 5.3. It may be observed from Fig. 6.8 that the results through the present FE formulation are in good agreement with those obtained from the ANSYS model. Moreover, the results remain almost the same for the present consideration of the layer-wise first order deformation theory instead of the previous consideration of the layer-wise higher order deformation theory (Chapter 5). This may be due to the thinness of component layers of the annular sandwich plate. However, this comparison (Fig. 6.8) verifies the FE formulation in this chapter for handling the shear piezoelectric actuation in control of annular plates.

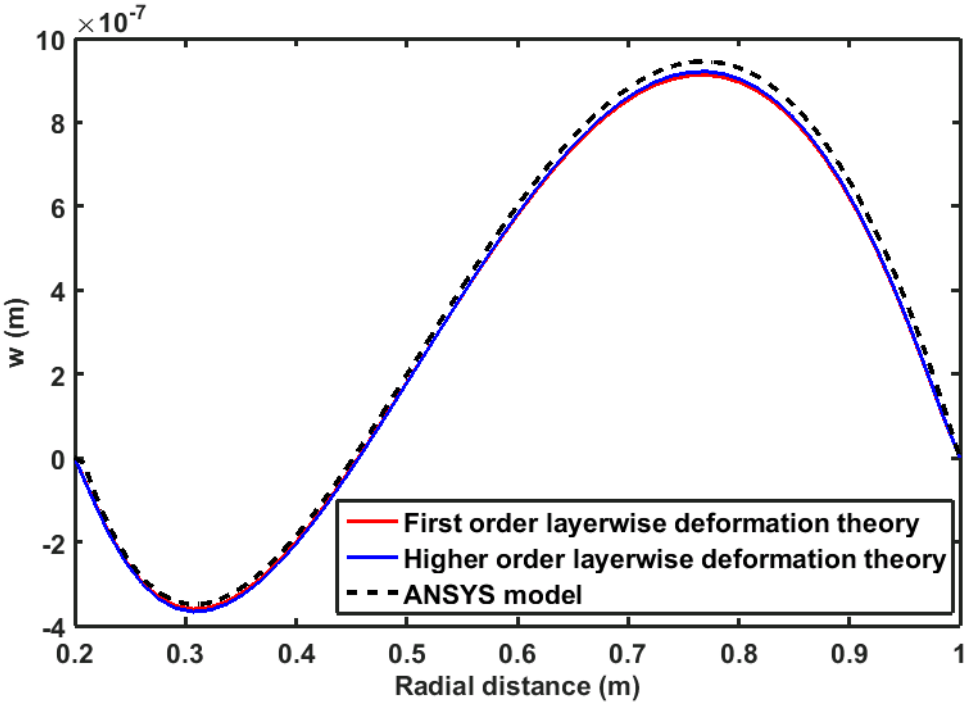

Fig. 6.8 Bending deflection comparison of the axisymmetric annular sandwich plate across its radial span (w is the transverse deflection).

The present layered annular plate (Figs. 6.4 and 6.5) appears with a little complex geometric configuration particularly for the macroscopic inclusions of graphite wafers and shear actuator patches. However, for a verification of the corresponding (present) FE code in accounting the inclusions correctly according to their specified geometrical locations, the distributions of the transverse shear strain (γ_{rz}) over the top surfaces of the VEC layers and active (piezo-foam) layers are computed for the fundamental bending mode-shape of the overall annular plate. This computation is carried out for all configurations of the layered annular plate as shown in Figs.6.4 and 6.5, however, it is illustrated in Figs. 6.9(a)-(b) for one configuration (Fig. 6.5(b)) of the layered annular plate. Here, the in-plane locations of the graphite wafers in the VEC layers are considered as, $n_{rg}=4$, $n_{\theta g}=8$, $\Delta r_v=$ 20 mm and $\Delta\theta_v=5^o$. The similar locations of actuator patches in the active (piezo-foam) layers is taken as, $n_r=2$, $n_\theta=8$, $\Delta r_F=$ 40 mm and $\Delta\theta_F=10^o$ .It may be observed from Figs. 6.9(a)-(b) that the strain (γ_{rz}) appears according to these specified locations of the inclusions, and these results infer the reality of the FE code in accounting the inclusions/patches as per their specified geometrical configurations.

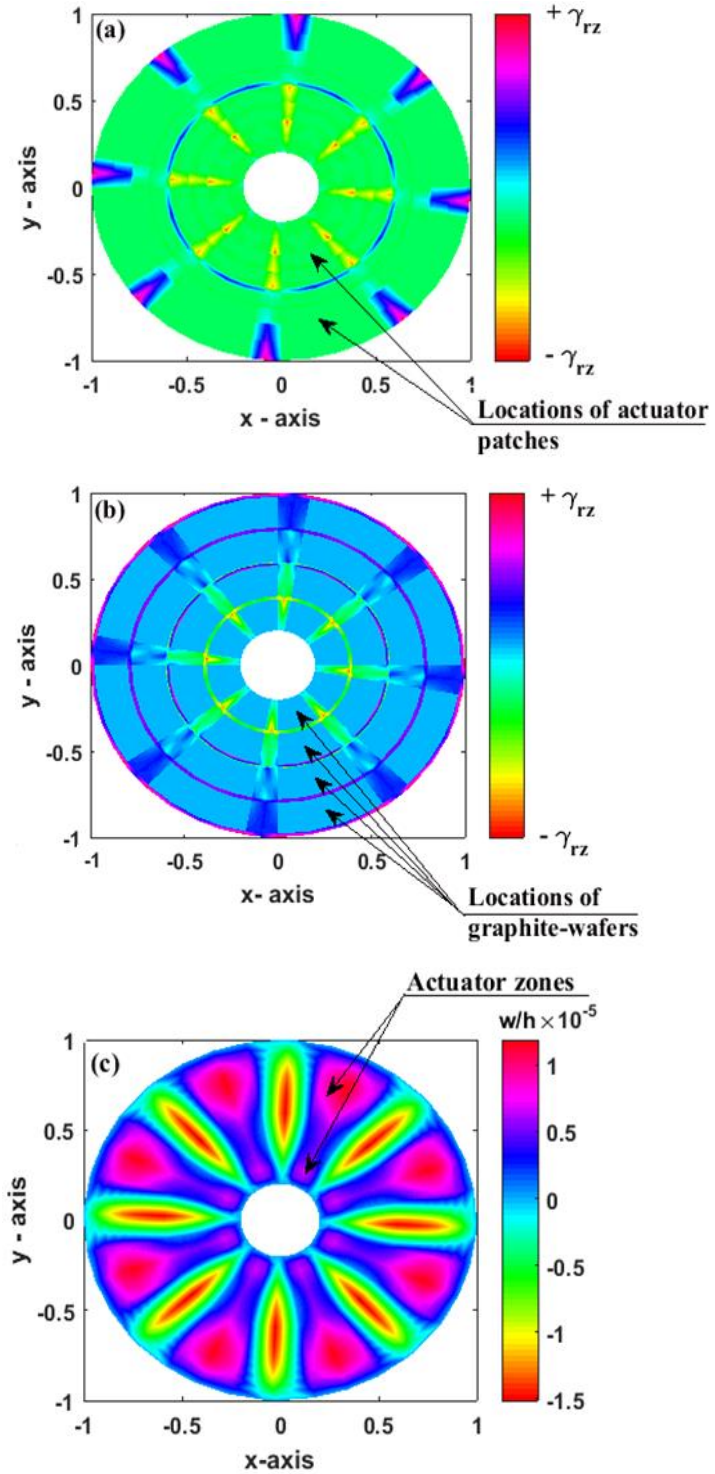

Fig. 6.9 Distributions of transverse shear strain (γ_{rz}) over the top surfaces of the (a) active (piezo-foam layer) and (b) VEC layer of the layered annular plate (Fig. 6.5(b)); (c) bending deflection of the overall annular plate (Fig. 6.5(b)) for a transversely applied electric field over the actuator patches.

The electro-elastic coupling effect of the actuator patches is presently accounted by means of computing the electro-elastic coupling vectors ($\boldsymbol{P}_E^s$, $s = 1,2,\ldots n_p$, Eq. (6.15)) corresponding to the actuator zones. In order to verify the present FE code in computation of this electro-elastic coupling vector according to a given configuration of the actuator patches or zones, the applied transverse electric field (E_z^s) is taken uniformly for all the actuator zones, and the corresponding transverse deflection of the layered annular plate is computed for each of its configurations (Figs. 6.4 and 6.5). This result is illustrated in Fig. 6.9(c) for one configuration of the layered annular plate (Fig. 6.5(b)). The locations of the actuator patches and the graphite wafers in the active and VEC layers, respectively, are considered as those are taken for the results in Figs. 6.9(a)-(b). It may be observed from Fig. 6.9(c) that the shear actuated bending deflection appears following the specified locations of the actuator zones ($n_p = 16$ ($2 \times n_r$)). The deflections over the inner or outer actuator zones arise uniformly due to the uniform applied transverse electric field (E_z^s). As the result for a similar plate is not available in the literature, this result (Fig. 6.9(c)) may be considered for a verification of the present FE code in computation of the electro-elastic coupling vectors ($\boldsymbol{P}_E^s$, $s = 1,2,\ldots n_p$) corresponding to a given configuration of actuator zones.

6.8.2 Shear-based active control of annular plates

The active layer in Fig. 6.1(a) is designed similar to the piezo-foam composite layer at the core of the annular sandwich plate in the previous chapters (Chapter 3 and Chapter 5). In shear mode active control of vibration of an annular plate, the fruitfulness of this design of a piezo-foam composite layer or active layer associated with a shear-based control strategy (section 3.5) is substantiated in the previous results (Figs. 3.10 and 5.4). The BL-PFC actuator can also be used effectively through this piezo-foam composite disc or active layer for shear actuation of annular plates as it is illustrated in the previous chapter (Chapter 5), where optimal angle (ϕ) of BL-PFC and the optimal number (n_θ) of BL-PFC patches along the circumferential direction were obtained as 25^0 and 11, respectively (Table 5.2). However, from the earlier results in Fig. 5.5, it may be observed that the shear-

based control of the annular plate primarily depends on ϕ whereas the value of n_θ does not appear as an indicative parameter within the specified range (8 to 12) although its (n_θ) optimal value appears as 11. So, the same value (25^0) of ϕ of BL-PFC is considered for the active layer of the layered annular plate in this chapter. But, an appropriate value of n_θ may appear less than 8 as it seems from the results in Fig. 5.5, and it facilities to construct the overall annular plate with less number of velocity sensors as well as reduced geometrical complexity. In doing so, the present layered annular plate (Fig. 6.4(b)) with the active (piezo-foam) layer at the core is considered without viscoelastic layers ($h_d \approx 0$), and the resonant displacement amplitudes ($w_{\max}/h$) for different values of n_θ are computed for first four bending modes of vibration of the plate under the constant values of control gain (k_d) and load-amplitude (p_o).

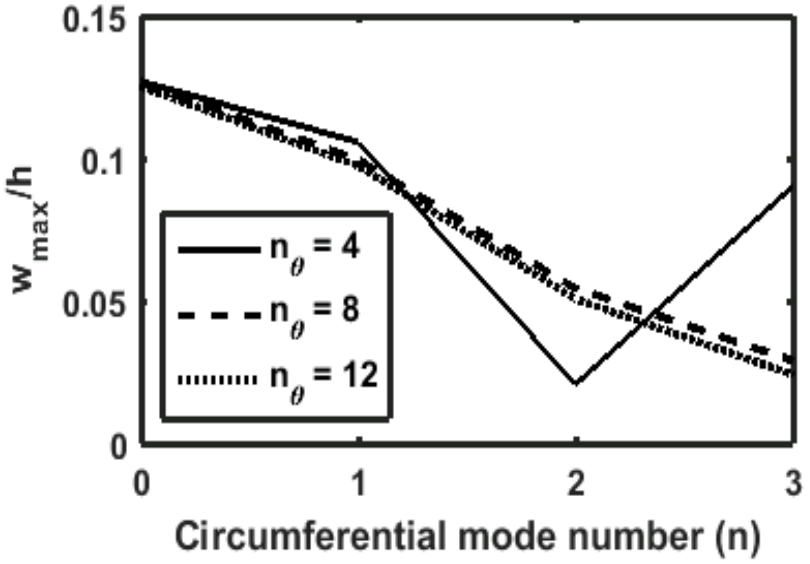

Fig. 6.10 Resonant transverse displacement amplitudes at the first four bending modes ($n=0,1,2,3;\ m=1$) of the annular sandwich plate for different values of n_θ ($p_o = 5$ N/m^2, $k_d = 50e4$).

This result is illustrated in Fig. 6.10, and it may be observed from this result that all the modes of vibration are attenuated in a uniform manner when the value of n_θ is greater than or equal to 8. It is also clear from the corresponding ($n_\theta = 8$) frequency responses and the variation of maximum control voltage as shown in

Figs. 6.11(a) and (b), respectively, where it is clear that all the modes of vibration are attenuated in a uniform manner by the BL-PFC patches for an increase of the control gain (k_d). So, although the optimal value of n_θ was obtained as 11 (Table 5.2), the value of the same parameter may be taken as 8 with a minimal decrease in attenuation of the resonant displacement amplitudes as it is observed from Fig. 6.10. As the lesser value of n_θ requires reduced number of velocity sensors along with the reduced complexity of the overall plate, the active layer in the layered annular plate in this chapter is considered to be made of 8 patches of BL-PFC along the circumferential direction while the other dimensions of the same active layer is considered as mentioned at the beginning of section 6.8.

6.8.3 Active-passive control of the annular plate using active and VEM layers

In this section, the characteristics of the present hybrid active-passive damping treatment of the layered annular plate are investigated by taking the active (piezo-foam) layer and the VEM layer. For any bending-mode of deformation of the layered annular plate, the mechanically induced transverse shear stress in the plate appears with its maximum value around the middle plane of the overall plate. So, the location of the VEM layer within the layered plate is preferred around the middle plane of the overall plate since it is a known fact that the passive damping through a constrained VEM layer mainly arises by means of transverse shear deformation of the same (VEM) layer. However, the middle plane of the overall plate is also important location for the shear actuator (active/piezo-foam composite layer) in achieving effective shear-based active control of the layered annular plate. So, it is difficult to decide an appropriate stacking sequence of the component layers of the layered annular plate for its effective hybrid active-passive damping treatment. However, if the passive damping is prioritized over the shear-mode actuation, the VEM layer is to be located at the core of the overall plate as shown by the configuration of the layered annular plate in Fig. 6.4(a). Conversely, if the shear-mode actuation is prioritized, then the active layer is to be located at the core as shown by the configuration of the layered annular plate in Fig. 6.4(b). These two configurations of the layered annular plate are presently denoted by PFC-VEM#1 (Fig. 6.4(a)) and PFC-VEM#2 (Fig. 6.4(b)).

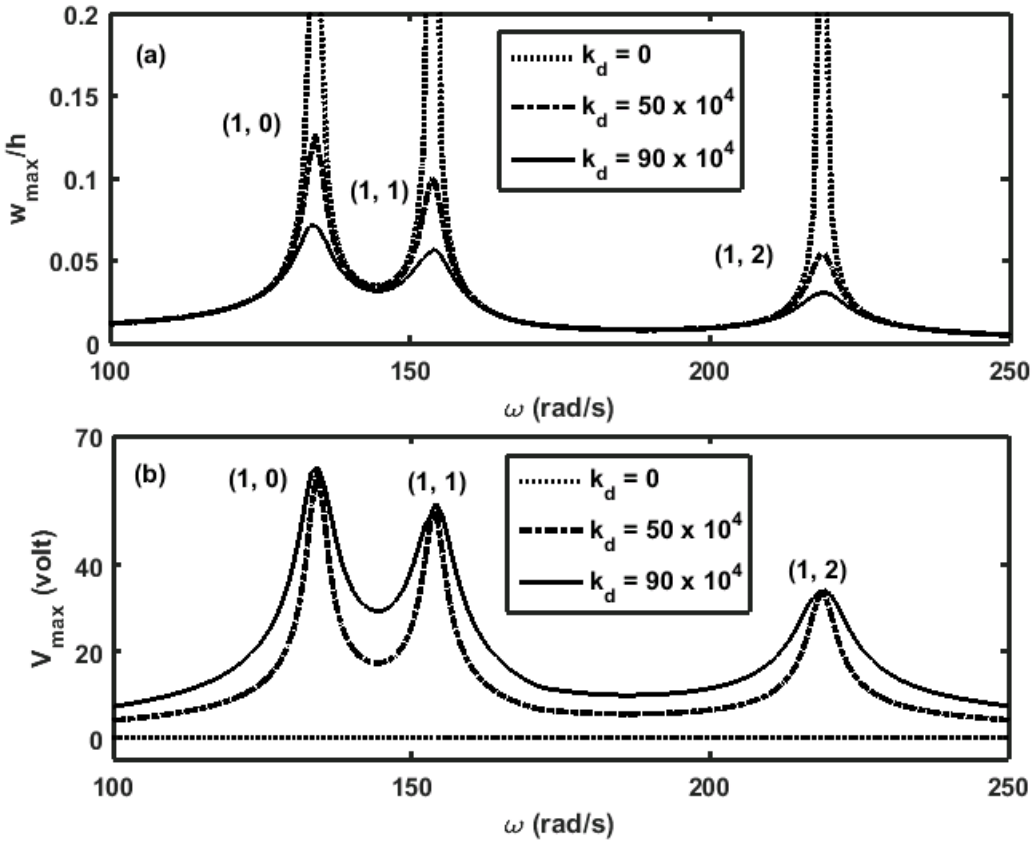

Fig. 6.11 (a) Frequency responses of the layered annular plate (Fig. 6.4(b), $h_d \approx 0$) with the active (piezo-foam) layer at the core and (b) the corresponding variations of the maximum control voltage ($V_{\max}$) for different values of the control gain (k_d) ($p_o = 5$ N/m^2).

For each of these configurations (PFC-VEM#1 and PFC-VEM#2), the thickness (h_s^1) of the inner substrate layers is varied from its zero value while the total thickness ($h_s = 2(h_s^1 + h_s^2)$) of the substrate layers is considered to remain the same along with no change of the active and VEM layers. The corresponding variations of the resonant displacement-amplitude ($w_{\max}/h$, $m=0$, $n=1$) and the maximum control voltage ($V_{\max}$) are illustrated in Figs. 6.12(a) and (b), respectively, for the specified values of control gain (k_d) and load-amplitude (p_o). It may be observed from Fig. 6.12(a) that the configuration PFC-VEM#1 (Fig. 6.4(a)) provides better active-passive control of the layered annular plate, where the VEM layer lies at the core and the maximum attenuation of vibration of the overall plate appears for

$h_s^1 = 0$ ($h_s = 2h_s^2$) i.e. when the active layers are stacked over the top and bottom surfaces of the VEM layer at the core and the substrate layers act as the face

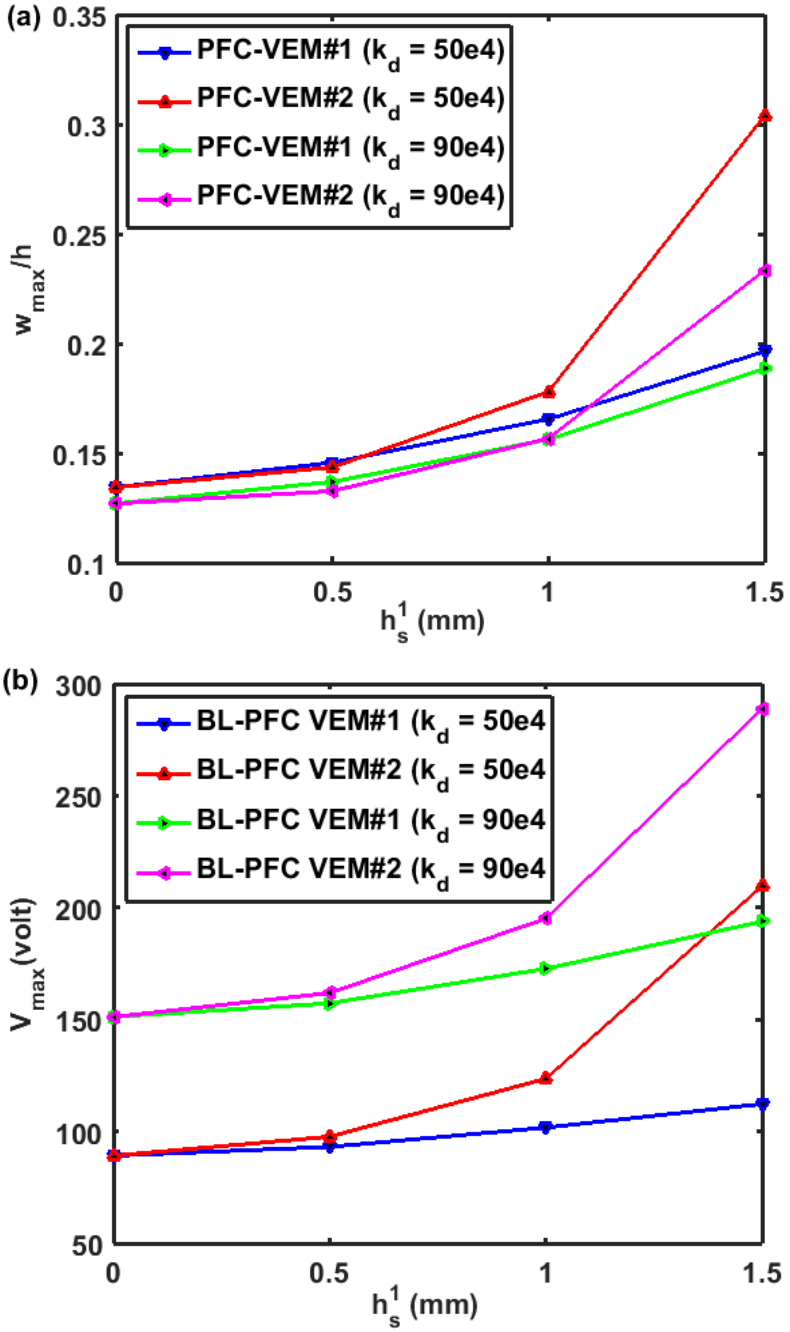

Fig. 6.12 (a) Variations of the resonant displacement-amplitude ($w_{\max}/h$, $m=0$, $n=1$) with the thickness (h_s^1) of the inner substrate layers in the configurations (PFC-VEM#1 and PFC-VEM#2) of the layered annular plate; (b) corresponding variations of the maximum control voltage ($V_{\max}$) ($p_o = 40$ N/m^2).

layers. Corresponding to this configuration (PFC-VEM#1, $h_s^1 = 0$), it may be observed from Fig. 6.12(a) that a negligibly small increase of attenuation of the resonant displacement-amplitude appears for a rise in control-gain from 50e4 to 90e4 while the maximum control voltage increases indicatively (Fig. 6.12(b)). It implies that the shear actuators (active layer) cannot be utilized fruitfully although the VEM and active layers are stacked appropriately within the layered annular plate. In view of this shortcoming, the VEC layer (Fig. 6.2(b)) is used instead of the VEM layer as shown in Figs. 6.5(a)-(b), and the corresponding active-passive control of the layered annular plate is investigated in the following section.

6.8.4 Active-passive control of the annular plate using active and VEC layers

The configurations above namely PFC-VEM#1 and PFC-VEM#2 are modified using present 0-3 VEC layers (Fig. 6.2(b)) in place of the VEM layers. The corresponding configurations of the layered annular plate are shown in Figs. 6.5(a) and 6.5(b) that are denoted by PFC-VEC#1 and PFC-VEC#2, respectively. In the 0-3 VEC layers, the circumferential gap ($\Delta\theta_v$) between the graphite wafers is considered as, $\Delta\theta_v = \Delta r_v / r_m$ ($r_m = (r_o + r_i)/2$) while other geometrical parameters (r_c, Δr_v, n_{rg}, $n_{\theta g}$) in the arrangement of the wafers are taken optimally for effective active-passive control of the overall annular plate. Accordingly, the geometrical parameters (r_c, Δr_v, n_{rg}, $n_{\theta g}$) are considered as the design variables, and their optimal values are determined for the maximum attenuation of resonant displacement-amplitude ($w_{\max}/h$, $m=0$, $n=1$) of the overall annular plate.

First, the layered annular plate with the configuration PFC-VEC#2 (Fig. 6.5(b)) is considered where the VEC layers are taken as the constrained damping layers ($h_s^2 \neq 0$) and the thickness (h_s^1) of the inner substrate layers is varied from its (h_s^1) zero value without alteration of the total thickness ($h_s = 2(h_s^1 + h_s^2)$) of the substrate layers. The thicknesses of the active and VEC layers are considered to remain with their constant values. The objective here is to locate the constrained VEC layers at an optimal vertical distance (h_s^1) from the top and bottom surfaces of the active

layer at the core. So, one more design variable (h_s^1) is added to the previous ones (r_c , Δr_v , n_{rg} , $n_{\theta g}$).

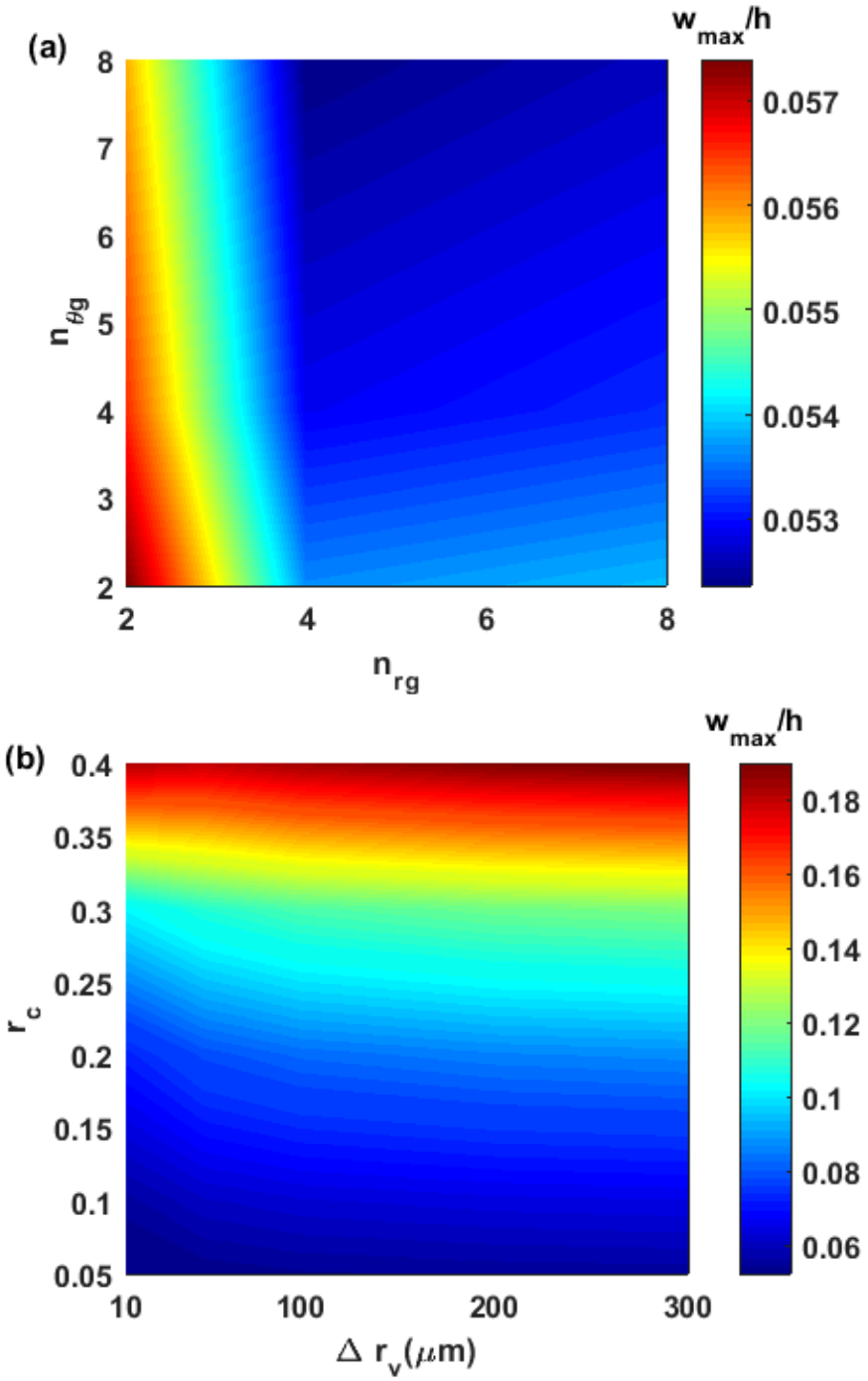

Fig. 6.13 Contour plots of ($w_{\max} / h$) in the two-dimensional domains of (*a*) n_{rg} and $n_{\theta g}$, (*b*) r_c and Δr_v .

Although any optimization algorithm can be employed, the Exhaustive Search Method [399] is used here considering the bounds of the design variables as, ($0.05 \le r_c \le 0.4$), ($2 \le n_{rg} \le 8$), ($2 \le n_{\theta g} \le 8$), ($10\ \mu m \le \Delta r_v \le 300\ \mu m$) and ($1\ \text{mm} \le h_s^1 \le 1.95\text{mm}$). With these bounds of the design variables, a five-dimensional domain with the coordinate axes of the design variables is assumed and the grid points are generated in an even manner within the axial bounds (bounds of design variables). Subsequently, the resonant displacement-amplitude ($w_{\max}/h$, $m=0$, $n=1$) is computed at every grid point for the specified values of control-gain (k_d) and load-amplitude (p_o) as 50×10^4 and 40 N/m^2, respectively. This result provides the nature of variation of the displacement-amplitude ($w_{\max}/h$) within the domain, and the point of minimum value of ($w_{\max}/h$) indicates the optimal values of the design variables as those are presently obtained as $h_s^1 = 1.95$ mm, $\Delta r_v = 10\ \mu m$, $r_c = 0.05$, $n_{rg} = 4$, $n_{\theta g} = 8$.

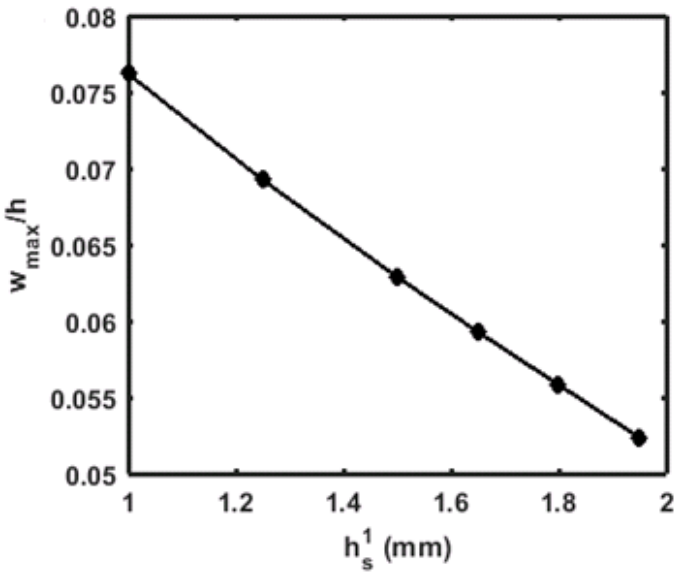

Fig. 6.14 Variation of ($w_{\max}/h$) with the thickness (h_s^1) of the inner substrate layers.

For an illustration of the effects of different geometrical parameters (r_c, Δr_v, n_{rg}, $n_{\theta g}$ and h_s^1) on the attenuation of the resonant displacement-amplitude ($w_{\max}/h$), the contour plot of ($w_{\max}/h$) in the two-dimensional domain of n_{rg} and $n_{\theta g}$ is shown in Fig. 6.13(a) while the other design variables (r_c, Δr_v, h_s^1) are taken

with their aforesaid optimal values. Similarly, the contour plot of ($w_{\max}/h$) in the two-dimensional domain of r_c and Δr_v is shown in Fig. 6.13(b) for the aforesaid optimal values of other design variables (n_{rg}, $n_{\theta g}$, h_s^1). Also, the variation of ($w_{\max}/h$) with the thickness (h_s^1) of the inner substrate layers is illustrated in Fig. 6.14 where the other design variables (r_c, Δr_v, n_{rg}, $n_{\theta g}$) are taken with their aforesaid optimal values. It may be observed from Figs. 6.13(a) and 6.13(b) that the attenuation of vibration of the layered annular plate is weakly dependent on $n_{\theta g}$ and Δr_v while the dominant parameters are n_{rg} and r_c. More importantly, it may be observed from Fig. 6.14 that the locations of the VEC layers within the thickness of the overall annular plate play an important role in having effective hybrid active-passive damping treatment of the overall annular plate.

The layered annular plate with the configuration PFC-VEC#1 (Fig. 6.5(a)) is also optimized in the similar manner. However, in this case, it is observed that the insertion of graphite wafers within the VEM layer at the core indicatively affects the active-passive control of vibration of the overall annular plate. This may be due to the fact that the important location of VEM is the middle plane of the overall annular plate. But, the volume of VEM at the same location (middle plane) reduces due to the inclusion of the graphite wafers. So, the VEC layer cannot provide a good hybrid active-passive damping treatment when the passive damping is prioritized over the shear actuation by means of locating the passive damping layer at the core of the overall annular plate.

6.8.5 Comparative study

The component layers of the layered annular plate are stacked in two different sequences on the basis of prioritizing passive damping over the shear actuation and vice versa. However, in case of the priority of passive damping, the aforesaid analysis of the corresponding configurations namely PFC-VEM#1 (Fig. 6.4(a)) and PFC-VEC#1 (Fig. 6.5(a)) reveals that the configuration PFC-VEM#1 provides better active-passive control of the overall annular plate where the active layers are to be attached to the top and bottom surfaces of the VEM layer at the core of the overall annular plate (for $h_s^1 = 0$ in Fig. 6.12(a)). In parallel, for the case of the priority of

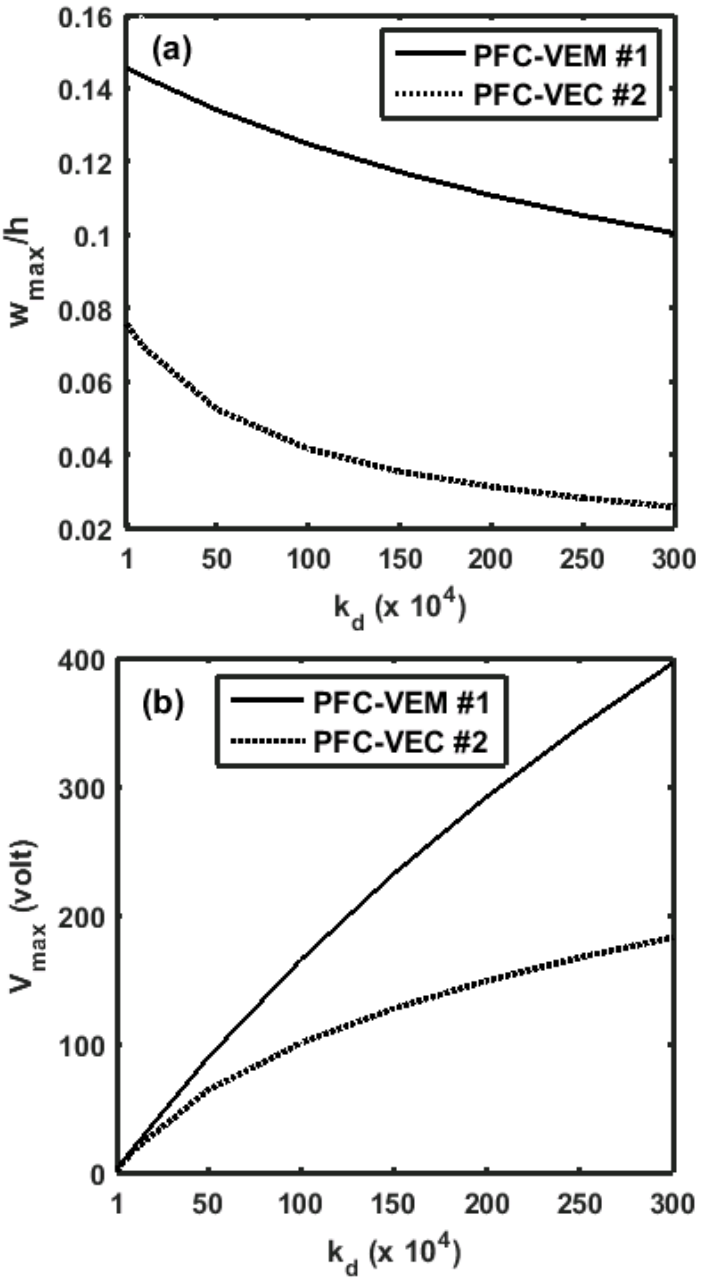

Fig. 6.15 Variations of (a) the resonant displacement-amplitude ($w_{\max}/h$) and (b) the maximum control voltage ($V_{\max}$) with the control gain (k_d) for the configurations PFC-VEM#1 and PFC-VEC#2 of the overall annular plate ($p_o = 40$ N/m^2).

shear actuation over the passive damping, the aforesaid results for the corresponding configurations namely PFC-VEM#2 (Fig. 6.4(b)) and PFC-VEC#2 (Fig. 6.5(b)) show that the better active-passive control of the overall annular plate

appears for the configuration PFC-VEC#2. So, the configuration PFC-VEM#1 (Fig. 6.4(a), passive priority) provides better active-passive control of the annular plate in case of the use of pure VEM layer whereas the fruitful use of the VEC layer lies through the configuration PFC-VEC#2 (Fig. 6.5(b), active priority). Now, a comparative study on the effectiveness of these two configurations (PFC-VEM#1and PFC-VEC#2) of the overall annular plate is performed.

Both the configurations (PFC-VEM#1 and PFC-VEC#2) are taken with their aforesaid optimal geometrical properties, and the corresponding variations of the resonant displacement-amplitude ($w_{\max}/h$, $m=0$, $n=1$) and maximum control voltage ($V_{\max}$) with the control gain (k_d) are illustrated in Figs. 6.15(a) and 6.15(b), respectively. It may be observed from Fig. 6.15(a) that the configuration PFC-VEC#2 provides indicatively higher active-passive control of the overall annular plate in comparison to that for the configuration PFC-VEM#1. The configuration PFC-VEC#2 also requires lesser control voltage especially when a high attenuation of the displacement-amplitude is required by increasing the control-gain (Fig. 6.15(b)). These observations infer the fruitfulness of the present design and utilization of a VEC layer (disc of 0-3 VEC) for shear actuated hybrid active-passive damping treatment of annular plates.

Figures 6.16(a) and 6.16(b) illustrate the controlled frequency responses of the layered annular plate for its configurations PFC-VEM#1 and PFC-VEC#2, respectively. For every configuration, the responses are evaluated with ($\eta \neq 0$) or without ($\eta = 0$) considering the loss factor (η) of the viscoelastic material so that the active-passive ($\eta \neq 0$) or shear-based active ($\eta = 0$) control of the overall plate arises. In Fig. 6.16(a), the response for $\eta = 0$ infers that the active (piezo-foam) layers cannot be utilized in an effective manner through the configuration PFC-VEM#1 where the active-passive control ($\eta \neq 0$) mainly appears due to the viscoelastic damping. In contrast, Fig. 6.16(b) shows an indicative shear-based active control ($\eta = 0$) of the overall annular plate through the configuration PFC-VEC#2, and the addition of passive damping ($\eta \neq 0$) further enhances the attenuation of vibration of the overall plate. As a result, an indicatively higher active-passive control of the overall annular plate arises through its configuration PFC-VEC#2.

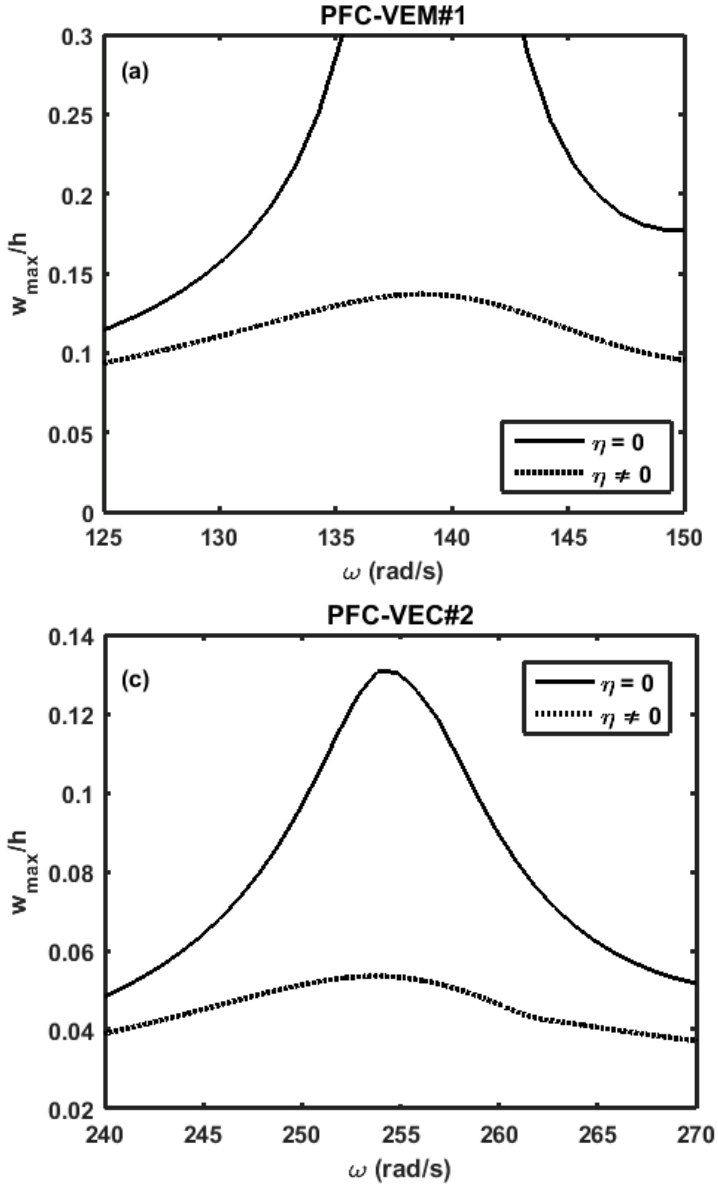

Fig. 6.16 Frequency responses ($w_{\max}/h, m=0, n=1$) of the layered annular plate for its different configurations (a) PFC-VEM#1 (Fig. 6.4(a)) and (b) PFC-VEC#2 (Fig. 6.5(b)) ($p_0 = 40$ N/m^2, $k_d = 40\times10^4$).

For quantification of attenuation of vibration of the layered annular plate, the attenuation $(\Delta W(\%))$ and the corresponding increase of maximum control voltage $(\Delta V(\%))$ for an increase of the control gain (k_d) are defined in Eqs. (3.22a) and (3.22b).

$$\Delta W(\%) = \frac{(w_{\max}/h)_1 - (w_{\max}/h)_2}{(w_{\max}/h)_1} \times 100 \tag{3.22a}$$

$$\Delta V(\%) = \frac{(V_{\max})_2 - (V_{\max})_1}{(V_{\max})_1} \times 100 \tag{3.22b}$$

According to these expressions (Eqs. (3.22a) and (3.22b)), the attenuation ($\Delta W(\%)$) of the resonant displacement amplitude at the fundamental mode and the corresponding increase ($\Delta V(\%)$) of the maximum control voltage for an increase of the control gain from 10×10^4 to 500×10^4 are illustrated in Table 6.2 for different values of the load-amplitude (p_o). It may be observed from Table 6.2 that the rate of attenuation ($\Delta W(\%)$) and the corresponding rate of increase of control voltage ($\Delta V(\%)$) are almost independent of the load-amplitude (p_o). However, it is important to observe (Table 6.2) that the rate of attenuation ($\Delta W(\%)$) through the configuration PFC-VEC#2 is indicatively higher than that through the configuration PFC-VEM#1. The results for PFC-VEC#2 in Table 6.2 also indicates a high attenuation of the resonant displacement-amplitude of the overall annular plate, and it infers the fruitfulness of the present design of a shear actuated hybrid active-passive damping treatment using BL-PFC actuator and 0-3 VEC.

Table 6.2 Attenuation ($\Delta W(\%)$) of the resonant displacement-amplitude ($w_{\max}/h$, $m=0$, $n=1$) and the corresponding increase ($\Delta V(\%)$) of the control voltage for an increase (from 10×10^4 to 500×10^4) of control gain (k_d) at load-amplitudes (p_o).

p_o (N/m^2)	PFC-VEC#2		PFC-VEM#1	
	$\Delta W(\%)$	$\Delta V(\%)$	$\Delta W(\%)$	$\Delta V(\%)$
10	72.41	92.45	39.66	96.58
20	72.04	92.45	39.66	96.58
30	72.16	92.45	39.69	96.58
40	72.08	92.45	39.69	96.58
50	72.15	92.44	39.69	96.58

6.9 Summary

In this chapter, a shear actuated hybrid active-passive damping treatment is designed for vibration control of annular plates using the BL-PFC and a 0-3 VEC. In order to utilize BL-PFC actuator for hybrid active-passive damping treatment of

annular plates, an active layer in the shape of the thin annular disc is designed similar to the piezo-foam composite layer at the core of annular sandwich plate analysed in Chapter 3 and Chapter 5. The shear actuation force mainly arises in the transverse plane of radial and thickness coordinates of the piezo-foam composite disc for an externally applied transverse electric field across the thickness of the BL-PFC patches within that disc.

The 0-3 VEC is an advanced viscoelastic composite damping material that is comprised of graphite wafers embedded within the viscoelastic matrix. For its utilization as a passive damping layer in the hybrid active-passive damping treatment of annular plates, a thin annular disc of 0-3 VEC is designed where the graphite wafers in the shape of the annular sector are periodically distributed in the cylindrical coordinates of the composite disc.

These active and passive damping layers are embedded in a host annular plate for achieving shear actuated hybrid active-passive damping of the overall annular plate, where a layered annular plate is composed using active (piezo-foam composite disc) layer, passive damping (0-3 VEC disc) layer and the layers of substrate material. Since both the passive damping and shear-mode actuation arise through the transverse shear strains, the appropriate stacking sequence of the active layer (shear actuator) coincides with that of the passive damping layer. So, the layered annular plate is composed with two different configurations by prioritizing passive damping over the shear actuation and vice versa. The damping characteristics of the layered annular plate are then analysed by developing a closed-loop FE model, where the shear actuators (BL-PFC) are activated by the feedback of the time-rate of change of the local slope of bending deformation of the overall annular plate.

The BL-PFC patches within the active layer or piezo-foam composite disc are first configured optimally. Subsequently, this piezo-foam composite disc is used along with the 0-3 VEC or VEM disc for the active-passive control of the layered annular plate, where the graphite wafers within the 0-3 VEC disc are configured optimally. The corresponding results reveal an indicative shear actuated hybrid active-passive control of the layered annular plate. If the layered annular plate is composed based on the priority of passive damping, then the present results suggest VEM instead of VEC for good active-passive control of the plate. On the other hand, if the layered annular plate is composed based on the priority of shear

actuation, superior control of the plate arises for the use of 0-3 VEC in place of VEM. Between these two cases, the later one (using VEC with shear actuation priority) provides indicatively higher active-passive damping than that by the former one (using VEM with passive damping priority).

Chapter 7

Conclusions and scope of future work

7.1 Conclusions

This dissertation deals with the active and active-passive control of annular plates through the design of two new piezoelectric fiber composite (PFC) actuators and a shear actuated hybrid damping treatment. First, an extension mode piezoelectric fiber composite (PFC) actuator with cylindrically periodic microstructure is designed especially for directional actuation of plane structures of revolution. The PFC actuator is designed in the form of a thin annular disc where the continuous piezoelectric fibers are periodically distributed along the circumferential direction to yield the directional actuation along the radial direction in the cylindrical principal material coordinate system. This kind of microstructure of the annular PFC actuator yields its radially varying electromechanical properties that are determined through the segmentation of its (PFC) volume into a large number of micro-volumes of different fiber volume fractions. The closed-form expressions for the effective electromechanical coefficients of the micro-volumes are derived, and the corresponding verification is carried out through the numerical homogenization using FE procedure. As the properties of this annular PFC actuator vary in the radial coordinate, the effect of the same coordinate on its electromechanical coupling coefficients is investigated by redesigning it in different radial segments within a radial span of application. This radial span of application is considered as that of a substrate annular plate where the annular PFC actuator is attached to the top surface of the substrate plate with different radial spans, and the active control of flexural vibration of the smart annular plate is studied by activating the actuator according to the velocity feedback control law. The corresponding results are evaluated by deriving a closed-loop FE model of the smart annular plate especially for a demonstration of the actuation capability of the annular PFC actuator as well as its effective utilization with an appropriate geometric configuration in the radial coordinate.

Besides the aforesaid extension-mode annular PFC actuator, an obliquely reinforced 1-3 PFC is introduced for shear-based active control of annular plates.

This study is carried out by constructing an annular sandwich plate where the patches of the 1-3 PFC in the shape of the annular sector are embedded within the core of foam. A typical patch of the obliquely reinforced 1-3 PFC are comprised of longitudinally poled piezoelectric fibers that are obliquely reinforced in a vertical plane of the Cartesian material coordinate system for producing the shear actuation force in the same vertical plane in response to an applied transverse electric field. This shear actuation force is used in the plane of radial and transverse coordinates of the annular plate for actuation of its (plate) bending mode of deformation/vibration. In this concern, a fruitful arrangement of the shear actuator patches at the core of the annular sandwich plate is presented. Accordingly, an electro-elastic FE model of the annular sandwich plate is developed based on the layer-wise shear deformation theory. Using this FE model, the mechanism of shear actuation of the annular sandwich plate with the embedded patches of the obliquely reinforced 1-3 PFC is first analysed, and then the effectiveness of the 1-3 PFC patches in shear-mode active control of flexural vibration of the annular sandwich plate is studied by developing a closed-loop FE model of the smart plate. In developing this closed-loop FE model of the shear actuated annular sandwich plate, a shear-based feedback control strategy is proposed for activating the shear actuator patches according to the velocity feedback control law, where every shear actuator patch is activated by the feedback of the time-rate of change of the local slope of bending deformation of the overall annular plate.

In a quest of modification of constructional features of the obliquely reinforced 1-3 PFC towards its improved shear actuation capability, a novel balanced laminate of PFC (BL-PFC) is proposed. It is designed by taking an even number of vertically reinforced 2-2 PFC layers of identical geometrical and material properties. The vertically reinforced 2-2 PFC layers in the BL-PFC are bonded through the epoxy binder layers while their thickness is taken in micro-scale. So, the investigation on the shear actuation capability of the balanced laminate of PFC is carried out by evaluating its (laminate) effective properties through a micromechanics formulation. With these effective properties, the BL-PFC is utilized as a material of the actuator patches at the core of a sandwich beam, while the patches of the obliquely reinforced 1-3 PFC or the shear-mode monolithic piezoelectric actuator (PZT5H) are

also used separately in place of the patches of BL-PFC. For each of the cases (1-3 PFC, BL-PFC and monolithic piezoelectric actuator), the shear actuated deformation of the sandwich beam is studied to clarify the shear actuation characteristics of the BL-PFC in comparison to that of the obliquely reinforced 1-3 PFC or shear-mode monolithic piezoelectric actuator.

Further study on the shear actuation capability of the BL-PFC actuator is carried out in active control of flexural vibration of annular plates, where two different shear mode PFC actuators namely SAFC and BL-PFC are utilized separately. The conventional shear mode monolithic piezoelectric (PZT5H) actuator is also used separately, and a comparative study on the shear actuation capabilities of all three shear actuators is performed to address the best one for shear-based control of the annular sandwich plate. Every actuator is used in the form of an actuator laminate for achieving higher shear actuation force in expense of lesser applied control voltage. The patches of this actuator laminate are placed instead of the patches of obliquely reinforced 1-3 PFC within the core of the earlier annular sandwich plate and the analysis of the overall annular plate is carried out for the patches of each of the laminates of three different shear actuators. First, the effective properties of the actuator laminates are evaluated using the Uniform Field Method. Next, a closed-loop FE model of the annular sandwich plate is developed based on the layer-wise shear deformation theory. Using this FE model, the arrangement of the actuator patches at the core is optimized for every shear actuator, and the corresponding shear actuated resonant displacement-amplitudes of the sandwich plate are evaluated to identify the best actuator for shear-based attenuation of vibration of the annular sandwich plate.

Finally, the shear actuation capability of the BL-PFC in a shear actuated hybrid active-passive damping treatment is investigated in vibration control of annular plates. A layered annular plate is designed with the stack of active layer, passive damping layer and the layers of substrate material. The active layer is comprised of BL-PFC patches embedded within the foam layer in an optimal manner with 2-2 phase connectivity. The passive damping layer is initially made of a viscoelastic material (VEM), however, the graphite wafers are inserted within it (VEM) in an optimal manner with 0-3 phase connectivity resulting in a 0-3 VEC layer. On the basis of prioritizing shear actuation over passive damping and vice

versa, two different layered configurations of the hybrid damping treatment are designed optimally. The corresponding active-passive damping characteristics are investigated by developing a closed-loop FE model of the overall annular plate, where the aforesaid (presently proposed) shear-based feedback control strategy is utilized for activating the shear actuator patches according to the velocity feedback control law.

The following main observations are obtained from the aforesaid studies in this thesis,

(1) The results for the radially varying effective electro-elastic properties of the present annular PFC actuator reveal an indicative difference between the magnitudes of the effective piezoelectric coefficients ($\bar{e}_{31}$ and $\bar{e}_{32}$, $\bar{e}_{31} > \bar{e}_{32}$) that provide the actuation forces along the in-plane axes of the cylindrical principal material coordinate system. So, the annular PFC is capable of providing primary/directional actuation along the radial direction through the coefficient $\bar{e}_{31}$.

(2) The effective piezoelectric coefficient ($\bar{e}_{31}$) of the present annular PFC actuator appears with an indicative magnitude at its inner radius, but this magnitude decreases indicatively with the increasing radius. So, the annular PFC actuator is redesigned in small radial segments within a radial span of application. The corresponding results reveal indicative improvement of the magnitude of the coefficient ($\bar{e}_{31}$) at any radius within the radial span of application.

(3) The actuation capability of the annular PFC actuator in active vibration control of flexural vibration of annular plates is close to that of the monolithic piezoelectric actuator, where the annular PFC actuator is to be used with small radial segments within a large radial span of application.

(4) The study on the mechanism of shear actuation of the annular sandwich plate with the embedded patches of the obliquely reinforced 1-3 PFC reveals that the shear actuated bending deformation of the annular plate appears through two main piezoelectric coefficients as e_{33} and e_{35}. Both the coefficients (e_{33} and e_{35}) provide the primary shear actuation forces in the same transverse plane of the annular plate. But, the shear actuation by e_{33} is

opposite to that by e_{35}. So, the total actuation of the annular sandwich plate decreases, where the actuation through e_{35} is reduced by that through e_{33}. Despite this fact, a good shear actuated bending deformation of the annular sandwich plate is observed.

(5) On the basis of the observation as given in point (4), the study on the effectiveness of the actuator patches of the obliquely reinforced 1-3 PFC in shear-based active control of bending modes of vibration of the annular plate is carried out. The corresponding controlled frequency responses of the annular sandwich plate under a transverse harmonic load exhibit indicative shear mode actuation capability of the actuator patches made of the obliquely reinforced 1-3 PFC, where also the required control voltage remains within the reasonable range. It is observed that a higher attenuation of resonant displacement amplitude through an increase of the velocity feedback control gain does not require much increase of the control voltage. The increase of the required control voltage mainly appears for the higher amplitude of the applied harmonic load, and thus the application of the 1-3 PFC as a material of shear actuator is mainly limited to the load-amplitude where the applied electric field exceeds its permissible value. It is also observed that the rate of attenuation of the resonant displacement amplitude with the increase of the control gain is almost independent of the amplitude of the applied harmonic load. These observations infer a good shear mode actuation capability of the obliquely reinforced 1-3 PFC and also the suitability of the present arrangement of the shear actuator patches at the core of the annular sandwich plate along with the present shear-based control strategy.

(6) The study on the shear-mode actuation of a sandwich beam with the embedded patches of BL-PFC or obliquely reinforced 1-3 PFC or shear-mode monolithic piezoelectric actuator (PZT5H) reveals an indicatively higher shear actuation capability of the BL-PFC than that of the obliquely reinforced 1-3 PFC or the traditional monolithic shear piezoelectric actuator.

(7) The shear actuation capability of the BL-PFC indicatively depends on its fiber orientation angle that is to be taken with an optimal value in an application.

(8) The study on the characteristics of the controlled frequency responses of the annular sandwich plate with the embedded patches of the laminate of shear-

mode monolithic piezoelectric actuator reveals that the present strategy for the arrangement of the shear actuator patches and the selection of the output parameter (local slope of bending) for feedback control are worthy for effective shear-based attenuation of any bending mode of vibration of the sandwich plate, where also a resonant displacement-amplitude can be attenuated to the desired mark by increasing the velocity feedback control gain without indicative change of the required control voltage.

(9) The comparative study on the shear actuation capabilities of three different actuators (BL-PFC, SAFC and PZT5H laminates) reveals that the mode-based optimal arrangement of the actuator patches at the core of the annular sandwich plate remains almost the same for all three different kinds of shear-mode actuators. However, SAFC has lesser shear actuation capability than that of the PZT5H, while the BL-PFC possesses the maximum shear actuation capability in comparison to that for any of the other two shear actuators (SAFC and PZT5H).

(10) The present design and analysis of a shear actuated hybrid active-passive damping treatment of annular plates reveals an indicative shear actuated hybrid active-passive control of the corresponding layered annular plate. If the layered annular plate is composed based on the priority of passive damping over the shear actuation, then the present results suggest VEM instead of VEC for a good active-passive control of the overall plate, where the shear actuators are to be located over the top and bottom surfaces of the VEM layer at the core and the substrate layers act as the face layers. Here, the shear actuators cannot be used in a fruitful manner although the configuration of the layered annular plate is taken in an optimal manner for achieving maximum attenuation of resonant displacement amplitudes.

(11) If the layered annular plate is composed based on the priority of shear actuation over the passive damping, superior control of the plate arises for the use of 0-3 VEC in place of VEM, where the active layer containing shear actuator patches is to be kept at the core and the 0-3 VEC layers are to be located towards the top and bottom surfaces of the overall layered annular plate. In this case, the shear actuators can be utilized fruitfully in attenuation of vibration of the overall annular plate while the addition of the

viscoelastic damping through the 0-3 VEC layer causes an effective hybrid active-passive damping of vibration of the overall annular plate.

(12) Between these two cases as furnished in points (10) and (11), the later one (using VEC with shear actuation priority, point (11)) provides indicatively higher active-passive damping than that by the former one (using VEM with passive damping priority, point (10)).

7.2 Scope of future work

Although preceding chapters of this thesis fulfil the objectives of the present research, further study may still be carried out for improvement of shear-mode/extension-mode PFC actuators and shear actuated hybrid active-passive damping treatment of structural vibration. Some of the future works which may be readily undertaken in line with the present work are as follows,

(1) The experimental verification of the active and active-passive damping models designed in this dissertation.

(2) Performance of the present annular PFC actuator in active-passive control of vibration of annular plates. This work may be carried out by taking the damping layer as the 0-3 VEC disc/layer.

(3) Design and analysis of a hybrid active-passive damping treatment of annular plates using shear-mode BL-PFC actuator, extension-mode PFC actuator and 0-3 VEC.

(4) Applications of the BL-PFC actuator for shear actuation of other kinds of thin-walled flexible structures.

References

[1] Tzou HS, Lee H-J, Arnold SM. Smart materials, precision sensors/actuators, smart structures, and structronic systems. Mech Adv Mater Struct 2004;11:367–93.

[2] Chaudhry Z, Rogers C. Actuators for smart structures. Fiber Opt Smart Struct 95-34976 09-39), New York, NY, John Wiley Sons, Inc(Wiley Ser Pure Appl Opt 1995, 1995:497–536.

[3] Chee CYK. Static shape control of laminated composite plate smart structure using piezoelectric actuators. PhD thesis, The University of Sydney; 2000.

[4] Newnham RE, Skinner DP, Cross LE. Connectivity and piezoelectric-pyroelectric composites. Mater Res Bull 1978; 13:525-36.

[5] Chan HLW, Unsworth J. Simple model for piezoelectric ceramic/polymer 1-3 composites used in ultrasonic transducer applications. IEEE Trans Ultrason Ferroelectr Freq Control 1989;36:434–41.

[6] Gururaja TR, Cross LE, Newnham RE, Auld BA, Wang YJ, Schulze WA. Piezoelectric Composite Materials for Ultrasonic Transducer Applications. Part I: Resonant Modes of Vibration of PZT Rod-Polymer Composites. IEEE Trans Sonics Ultrason 1985;32:481-98.

[7] Gururaja TR, Cross LE, Newnham RE, Schulze WA. Piezoelectric Composite Materials for Ultrasonic Transducer Applications. Part II: Evaluation of Ultrasonic Medical Applications. IEEE Trans Sonics Ultrason 1985;32:499-513.

[8] Newnham RE, Bowen LJ, Klicker KA, Cross LE. Composite piezoelectric transducers. Mater Des 1980;2:93-106.

[9] Safari A, Newnham RE, Cross LE, Schulze WA. Perforated pzt-polymer composites for piezoelectric transducer applications. Ferroelectrics 1982;41:197-205.

[10] Savakus HP, Klicker KA, Newnham RE. PZT-epoxy piezoelectric transducers: A simplified fabrication procedure. Mater Res Bull 1981;16:677-80.

[11] Smith WA, Shaulov AA, Singer BM. Properties of composite piezoelectric materials for ultrasonic transducers. IEEE 1984 Ultrason. Symp., 1984, p. 539–44.

[12] Smith WA, Shaulov A, Auld BA. Tailoring the properties of composite

piezoelectric materials for medical ultrasonic transducers. IEEE 1985 Ultrason. Symp., 1985, p. 642–7.

[13] Smith WA, Auld BA. Modeling 1–3 Composite Piezoelectrics: Thickness-Mode Oscillations. IEEE Trans Ultrason Ferroelectr Freq Control 1991;38:40-7.

[14] Hagood N, Bent A. Development of piezoelectric fiber composites for structural actuation. 34th Struct. Struct. Dyn. Mater. Conf., 1993.

[15] Bent AA, Hagood NW. Piezoelectric fiber composites with interdigitated electrodes. J Intell Mater Syst Struct 1997;11:903-19.

[16] High JW, Wilkie WK. Method of fabricating NASA-standard macro-fiber composite piezoelectric actuators NASA/TM-2003-212427, ARL-TR-2833, 2003.

[17] Mallik N, Ray MC. Effective coefficients of piezoelectric fiber-reinforced composites. AIAA J 2003;41:704–10.

[18] Ray MC. Micromechanics of piezoelectric composites with improved effective piezoelectric constant. Int J Mech Mater Des 2006;3:361-71.

[19] Benveniste Y, Dvorak GJ. Uniform fields and universal relations in piezoelectric composites. J Mech Phys Solids 1992;40:1295-312.

[20] Wang B. Three-dimensional analysis of an ellipsoidal inclusion in a piezoelectric material. Int J Solids Struct 1992;29:293-308.

[21] Dunn ML, Taya M. Micromechanics predictions of the effective electroelastic moduli of piezoelectric composites. Int J Solids Struct 1993;30:161-75.

[22] Benveniste Y. Universal Relations in piezoelectric composites with eigenstress and polarization fields, Part I: Binary Media—Local fields and effective behavior. J Appl Mech 1993;60:265–9.

[23] Benveniste Y. On the micromechanics of fibrous piezoelectric composites. Mech Mater 1994;18:183-93.

[24] Huang JH, Kuo WS. Micromechanics determination of the effective properties of piezoelectric composites containing spatially oriented short fibers. Acta Mater 1996;44:4889-98.

[25] Kuo WS, Huang JH. On the effective electroelastic properties of piezoelectric composites containing spatially oriented inclusions. Int J Solids Struct 1997;34:2445-61.

[26] Yu N. On overall properties of smart piezoelectric composites. Compos

Part B Eng 1999;30:709-12.

[27] Sabina FJ, Rodríguez-Ramos R, Bravo-Castillero J, Guinovart-Díaz R. Closed-form expressions for the effective coefficients of a fibre-reinforced composite with transversely isotropic constituents. II: Piezoelectric and hexagonal symmetry. J Mech Phys Solids 2001;49:1445-62.

[28] Tan P, Tong L. Micromechanics models for non-linear behavior of piezo-electric fiber reinforced composite materials. Int J Solids Struct 2001;38:8999-9032.

[29] Tan P, Tong L. Micro-electromechanics models for piezoelectric-fiber-reinforced composite materials. Compos Sci Technol 2001;61:759-69.

[30] Bowen CR, Perry A, Kara H, Mahon SW. Analytical modelling of 3-3 piezoelectric composites. J Eur Ceram Soc 2001;21:1463-7.

[31] Bowen CR, Kara H. Pore anisotropy in 3-3 piezoelectric composites. Mater. Chem. Phys., 2002;75:45-9.

[32] Ruan X, Chou TW, Safari A, Danforth SC. A 3-D connectivity model for effective piezoelectric properties of yarn composites. J Compos Mater 2002;36:1693-1708.

[33] Kar-Gupta R, Venkatesh TA. Electromechanical response of 1-3 piezoelectric composites: Effect of poling characteristics. J Appl Phys 2005;98:054102.

[34] Kar-Gupta R, Venkatesh TA. Electromechanical response of 1-3 piezoelectric composites: An analytical model. Acta Mater 2007;55:1093-108.

[35] Kar-Gupta R, Venkatesh TA. Electromechanical response of 1-3 piezoelectric composites: A numerical model to assess the effects of fiber distribution. Acta Mater 2007;55:1275-92.

[36] Della CN, Shu D. On the performance of 1-3 piezoelectric composites with a passive and active matrix. Sensors Actuators, A Phys 2007;140:200-6.

[37] Della CN, Shu D. The performance of 1-3 piezoelectric composites with a porous non-piezoelectric matrix. Acta Mater 2008;56:754-61.

[38] Challagulla KS, Venkatesh TA. Electromechanical response of 2-2 layered piezoelectric composites: A micromechanical model based on the asymptotic homogenization method. Philos Mag 2009;89:1197-222.

[39] Deraemaeker A, Nasser H, Benjeddou A, Preumont A. Mixing rules for the piezoelectric properties of macro fiber composites. J Intell Mater Syst

Struct 2009;20:1475-82.

[40] Sakthivel M, Arockiarajan A. An analytical model for predicting thermo-electro-mechanical response of 1-3 piezoelectric composites. Comput Mater Sci 2010;48:759-67.

[41] Nasser H, Biscani F, Belouettar S. Effect of matrix properties on the overall piezoelectric constants of piezocomposite transducers. Mech. Adv. Mater. Struct., 2011;18:531-9.

[42] Brenner R, Bravo-Castillero J, Léon DM. Investigation of the effective response of 2-1-2 piezoelectric composites. Procedia IUTAM 2012;3:292–300.

[43] Brenner R, Bravo-Castillero J, Léon DM. Investigation of the effective response of 2-1-2 piezoelectric composites. Procedia IUTAM, 2012;3:288-96.

[44] Sakthivel M, Arockiarajan A. An effective matrix poling characteristics of 1-3-2 piezoelectric composites. Sensors Actuators, A Phys 2011;167:34-43.

[45] Sakthivel M, Arockiarajan A. Thermo-electro-mechanical response of 1-3-2 piezoelectric composites: Effect of fiber orientations. Acta Mech 2012;223:1353-69.

[46] Kalamkarov AL, Savi MA. Micromechanical modeling and effective properties of the smart grid-reinforced composites. J Brazilian Soc Mech Sci Eng 2012;34:343–51.

[47] Sreenivasa Prasath S, Arockiarajan A. Effective electromechanical response of macro-fiber composite (MFC): Analytical and numerical models. Int J Mech Sci 2013;77:98-106.

[48] Kar-Gupta R, Venkatesh TA. Electromechanical response of (2-2) layered piezoelectric composites. Smart Mater Struct 2013;22:25035.

[49] Iyer S, Venkatesh TA. Electromechanical response of (3-0, 3-1) particulate, fibrous, and porous piezoelectric composites with anisotropic constituents: A model based on the homogenization method. Int J Solids Struct 2014;51:1221-34.

[50] Eynbeygi M, Aghdam MM. A micromechanical study on the electro-elastic behavior of piezoelectric fiber-reinforced composites using the element-free Galerkin method. Acta Mech 2015;226:3177-94.

[51] Poizat C, Sester M. Effective properties of composites with embedded

piezoelectric fibres. Comput Mater Sci 1999;16:89-97.

[52] Pettermann HE, Suresh S. A comprehensive unit cell model: A study of coupled effects in piezoelectric 1-3 composites. Int J Solids Struct 2000;37:5447-64.

[53] Qin Q. Micromechanics-BEM analysis for piezoelectric composites. Tsinghua Sci Technol 2005;10:30-4.

[54] Berger H, Kari S, Gabbert U, Rodriguez-Ramos R, Guinovart R, Otero JA, et al. An analytical and numerical approach for calculating effective material coefficients of piezoelectric fiber composites. Int. J. Solids Struct., 2005;42:5692-714.

[55] Berger H, Kari S, Gabbert U, Rodríguez-Ramos R, Bravo-Castillero J, Guinovart-Díaz R. A comprehensive numerical homogenisation technique for calculating effective coefficients of uniaxial piezoelectric fibre composites. Mater Sci Eng A 2005;412:53-60.

[56] Berger H, Kari S, Gabbert U, Rodriguez-Ramos R, Bravo-Castillero J, Guinovart-Diaz R. Calculation of effective coefficients for piezoelectric fiber composites based on a general numerical homogenization technique. Compos Struct 2005;71:397-400.

[57] Berger H, Kari S, Gabbert U, Rodriguez-Ramos R, Bravo-Castillero J, Guinovart-Diaz R, et al. Unit cell models of piezoelectric fiber composites for numerical and analytical calculation of effective properties. Smart Mater Struct 2006;15: 451.

[58] Kari S, Berger H, Rodriguez-Ramos R, Gabbert U. Numerical evaluation of effective material properties of transversely randomly distributed unidirectional piezoelectric fiber composites. J Intell Mater Syst Struct 2007;18:361-72.

[59] Deraemaeker A, Benelechi S, Benjeddou A, Preumont A. Analytical and Numerical Computation of Homogenized Properties of MFCS: Application to a Composite Boom with MFC Actuators and Sensors. Proc. III ECCOMAS Themat. Conf. Smart Struct. Mater., 2007.

[60] Kar-Gupta R, Venkatesh TA. Electromechanical response of piezoelectric composites: Effects of geometric connectivity and grain size. Acta Mater 2008;56:3810-23.

[61] Deraemaeker A, Nasser H. Numerical evaluation of the equivalent properties of Macro Fiber Composite (MFC) transducers using periodic

homogenization. Int J Solids Struct 2010;47:3272-85.

[62] Li Y, Zheng H, Long S, Wu L. Effects of the piezoelectric phase's geometric properties on effective coefficients of 1-3 piezoelectric composites. Comput Mater Sci 2011;50:2135-41.

[63] Trindade MA, Benjeddou A. Finite element characterisation of multilayer d_{31} piezoelectric macro-fibre composites. Compos Struct 2016;151:47-57.

[64] Zhen Y, Li J-F, Zhang H. Electrical and elastic properties of 1-3 PZT/epoxy piezoelectric composites. J Electroceramics 2008;21:410–3.

[65] Shindo Y, Narita F, Watanabe T. Nonlinear electromechanical fields and localized polarization switching of 1-3 piezoelectric/polymer composites. Eur J Mech A/Solids 2010;29:647-53.

[66] Zhou M, Sun M, Li M, Xie S, Huang S. Fabrication and properties of 1-3-2 multi-element piezoelectric composite. J Electroceramics 2012;28:139–43.

[67] Jayendiran R, Arockiarajan A. Non-linear electromechanical response of 1-3 type piezocomposites. Int J Solids Struct 2013;50:2259-70.

[68] Xu D, Du P, Wang J, Hou P, Huang S, Cheng X. Design and properties of Gaussian-type 1-3 piezoelectric composites. Compos Struct 2016;140:213–6.

[69] Geng B, Xu D, Yi S, Gao G, Xu H, Cheng X. Design and properties 1–3 multi-element piezoelectric composite with low crosstalk effects. Ceram Int 2017;43:15167-72.

[70] Mi X, Qin L, Liao Q, Wang L. Electromechanical coupling coefficient and acoustic impedance of 1-1-3 piezoelectric composites. Ceram Int 2017;43:7374–7.

[71] Mi X, Qin L, Liao Q, Wang L. Electromechanical coupling coefficient and acoustic impedance of 1-1-3 piezoelectric composites. Ceram Int 2017;43:7374-7.

[72] Yi S, Zhang W, Gao G, Xu H, Xu D. Structural design and properties of fine scale 2-2-2 PZT/epoxy piezoelectric composites for high frequency application. Ceram Int 2018;44:10940–4.

[73] Raja S, Ikeda T. Concept and electro-elastic modeling of shear actuated fiber composite using micro-mechanics approach. J Intell Mater Syst Struct 2008;19:1173–83.

[74] Benjeddou A, Al-Ajmi M. Analytical homogenizations of piezoceramic d 15 shear macro-fibre composites. IUTAM Symp. Multiscale Model. Fatigue,

Damage Fract. Smart Mater., 2011, p. 229–42.

[75] Trindade MA, Benjeddou A. Finite element homogenization technique for the characterization of d_{15} shear piezoelectric macro-fibre composites. Smart Mater Struct 2011;20:075012.

[76] Trindade MA, Benjeddou A. Parametric analysis of effective material properties of thickness-shear piezoelectric macro-fibre composites. J Brazilian Soc Mech Sci Eng 2012;34:352–61.

[77] Kranz B, Benjeddou A, Drossel WG. Numerical and experimental characterizations of longitudinally polarized piezoelectric d 15 shear macro-fiber composites. Acta Mech 2013;224:2471-87.

[78] Kranz B, Benjeddou A, Drossel WG. Enthalpy - Based homogenization procedure for composite piezoelectric modules with integrated electrodes. Smart Struct Syst 2013;12:579-94.

[79] Trindade MA, Benjeddou A. Finite element characterization and parametric analysis of the nonlinear behaviour of an actual d_{15} shear MFC. Acta Mech 2013;224:2489-503.

[80] Yuan X, Chen Z, Wu M, Luo H, Chen C, Zhou K, et al. A novel thickness polarized d_{15} shear piezoelectric fiber composites. Sensors Actuators, A Phys 2017;260:185-90.

[81] Bailey T, Hubbard JE. Distributed piezoelectric-polymer active vibration control of a cantilever beam. J Guid Control Dyn 1985;8:605-11.

[82] Burke SE, Hubbard JE. Active Vibration Control of a Simply Supported Beam Using a Spatially Distributed Actuator. IEEE Control Syst Mag 1987;7:25-30.

[83] Clauser HR. From Static to Dynamic Materials in Design. ASME J Mech Eng 1975;97.

[84] Clauser HR. Concepts-modern materials concepts make structure key to progress. Mater Eng 1968;68:38.

[85] Crawley EF, De Luis J. Use of piezoelectric actuators as elements of intelligent structures. AIAA J 1987;25:1373-85.

[86] Baz AM. Static deflection control of flexible beams by piezo-electric actuators. 1986.

[87] Plump JM, Hubbard JE, Bailey T. Nonlinear Control of a Distributed System: Simulation and Experimental Results. J Dyn Syst Meas Control 1987;109:133-9.

[88] Baz A, Poh S. Performance of an active control system with piezoelectric actuators. J Sound Vib 1988;126:327-43.

[89] Crawley EF, De Luis J, Hagood NW, Anderson EH. Development of piezoelectric technology for applications in control of intelligent structures. 1988 Am. Control Conf., 1988, p. 1890–6.

[90] Crawley EF, Anderson EH. Detailed models of piezoceramic actuation of beams. J Intell Mater Syst Struct 1990;1:4–25.

[91] Miller SE, Hubbard J. Observability of a Bernoulli-Euler beam using PVF 2 as a distributed sensor. Dyn Control Large Struct 1988:375–90.

[92] Im S, Atluri SN. Effects of a piezo-actuator on a finitely deformed beam subjected togeneral loading. AIAA J 1989;27:1801–7.

[93] Baz A, Poh S. Experimental implementation of the modified independent modal space control method. J Sound Vib 1990;139:133–49.

[94] Hanagud S, Obal MW, Calise AJ. Optimal vibration control by the use of piezoceramic sensors and actuators. J Guid Control Dyn 1992;15:1199–206.

[95] Dosch JJ, Inman DJ, Garcia E. A self-sensing piezoelectric actuator for collocated control. J Intell Mater Syst Struct 1992;3:166–85.

[96] Rao S, Sunar M. Analysis of distributed thermopiezoelectric sensors and actuators inadvanced intelligent structures. AIAA J 1993;31:1280–6.

[97] Tzou HS, Ye R. Piezothermoelasticity and precision control of piezoelectric systems: theory and finite element analysis. J Vib Acoust 1994;116:489–95.

[98] Shen NH. Analysis of beams containing piezoelectric sensors and actuators. Smart Mater Struct 1994;3:439.

[99] Chattopadhyay A, Seeley CE. A multiobjective design optimization procedure for control of structures using piezoelectric materials. J Intell Mater Syst Struct 1994;5:403–11.

[100] Saravanos DA, Heyliger PR. Coupled layerwise analysis of composite beams with embedded piezoelectric sensors and actuators. J Intell Mater Syst Struct 1995;6:350–63.

[101] Kim SJ, Jones JD. Influence of piezo-actuator thickness on the active vibration control of a cantilever beam. J Intell Mater Syst Struct 1995;6:610–23.

[102] Gopinathan M, Pajunen GA. Model reference control of vibrations in

flexible smart structures. Proc. 1995 34th IEEE Conf. Decis. Control, vol. 4, 1995, p. 3551–6.

[103] Chang-Qing C, Xiao-Ming W, Ya-Peng S. Finite element approach of vibration control using self-sensing piezoelectric actuators. Comput Struct 1996;60:505–12.

[104] Aldraihem OJ, Wetherhold RC, Singh T. A comparison of the Timoshenko theory and the Euler-Bernoulli theory for control of laminated beams. ASME Aerosp. Div. Int. Mech. Eng. Congr. Expo. Atlanta, GA, 1996, p. 455–62.

[105] Aldraihem OJ, Wetherhold RC, Singh T. Distributed control of laminated beams: Timoshenko theory vs. Euler-Bernoulli theory. J Intell Mater Syst Struct 1997;8:149–57.

[106] Chandrashekhara K, Varadarajan S. Adaptive shape control of composite beams with piezoelectric actuators. J Intell Mater Syst Struct 1997;8:112–24.

[107] Seshu P, Naganathan NG. Finite-element analysis of strain transfer in an induced strain actuator. Smart Mater Struct 1997;6:76.

[108] Smyser CP, Chandrashekhara K. Robust vibration control of composite beams using piezoelectric devices and neural networks. Smart Mater Struct 1997;6:178.

[109] Peng XQ, Lam KY, Liu GR. Active vibration control of composite beams with piezoelectrics: a finite element model with third order theory. J Sound Vib 1998;209:635–50.

[110] Raja S, Rohwer K, Rose M. Piezothermoelastic modeling and active vibration control of laminated composite beams. J Intell Mater Syst Struct 1999;10:890–9.

[111] Chee CYK, Tong L, Steven GP. A mixed model for composite beams with piezoelectric actuators and sensors. Smart Mater Struct 1999;8:417.

[112] Agrawal BN, Treanor KE. Shape control of a beam using piezoelectric actuators. Smart Mater Struct 1999;8:729.

[113] Bruant I, Coffignal G, Lene F, Verge M. Active control of beam structures with piezoelectric actuators and sensors: modeling and simulation. Smart Mater Struct 2001;10:404.

[114] Gosavi S V, Kelkar AG. Modelling, identification, and passivity-based robust control of piezo-actuated flexible beam. J Vib Acoust

2004;126:260–71.

[115] Ganapathi M, Patel BP, Touratier M. A C1 finite element for flexural and torsional analysis of rectangular piezoelectric laminated/sandwich composite beams. Int J Numer Methods Eng 2004;61:584–610.

[116] Gardonio P, Elliott SJ. Modal response of a beam with a sensor-actuator pair for the implementation of velocity feedback control. J Sound Vib 2005;284:1–22.

[117] Plagianakos TS, Saravanos DA. Coupled High-Order Shear Layerwise Analysis of Adaptive Sandwich Piezoelectric Composite Beams. AIAA J 2005;43:885–94.

[118] Cai G-P, Yang SX. A discrete optimal control method for a flexible cantilever beam with time delay. J Vib Control 2006;12:509–26.

[119] Zemčik R, Rolfes R, Rose M, Teßmer J. High-performance four-node shell element with piezoelectric coupling for the analysis of smart laminated structures. Int J Numer Methods Eng 2007;70:934–61.

[120] Kumar KR, Narayanan S. Active vibration control of beams with optimal placement of piezoelectric sensor/actuator pairs. Smart Mater Struct 2008;17:55008.

[121] Rao AK, Natesan K, Seetharama Bhat M, Ganguli R. Experimental demonstration of H∞ control based active vibration suppression in composite fin-tip of aircraft using optimally placed piezoelectric patch actuators. J Intell Mater Syst Struct 2008;19:651–69.

[122] Qiu Z, Zhang X, Wang Y, Wu Z, others. Active vibration control of a flexible beam using a non-collocated acceleration sensor and piezoelectric patch actuator. J Sound Vib 2009;326:438–55.

[123] Neto MA, Yu W, Roy S. Two finite elements for general composite beams with piezoelectric actuators and sensors. Finite Elem Anal Des 2009;45:295–304.

[124] Kapuria S, Yasin MY. Active vibration control of piezoelectric laminated beams with electroded actuators and sensors using an efficient finite element involving an electric node. Smart Mater Struct 2010;19:45019.

[125] Elshafei MA, Alraiess F. Modeling and analysis of smart piezoelectric beams using simple higher order shear deformation theory. Smart Mater Struct 2013;22:35006.

[126] Ray MC, Dong L, Atluri SN. Simple efficient smart finite elements for the

analysis of smart composite beams. Comput Model Eng Sci 2016;111:437–71.

[127] Sulbhewar LN, Raveendranath P. A consistently efficient and accurate higher order shear deformation theory based finite element to model extension mode piezoelectric smart beams. J Intell Mater Syst Struct 2016;27:1231–49.

[128] Tzou HS, Gadre M. Active vibration isolation by polymeric piezoelectret with variable feedback gains. AIAA J 1988;26:1014–7.

[129] Tzou HS, Tseng CI. Distributed piezoelectric sensor/actuator design for dynamic measurement/control of distributed parameter systems: A piezoelectric finite element approach. J Sound Vib 1990;138:17-34.

[130] Crawley EF, Lazarus KB. Induced strain actuation of isotropic and anisotropic plates. AIAA J 1991;29:944–51.

[131] Tauchert TR. Piezothermoelastic behavior of a laminated plate. J Therm Stress 1992;15:25–37.

[132] Ha SK, Keilers C, Chang F-K. Finite element analysis of composite structures containing distributed piezoceramic sensors and actuators. AIAA J 1992;30:772–80.

[133] Ray MC, Bhattacharya R, Samanta B. Exact solutions for static analysis of intelligent structures. AIAA J 1993;31:1684–91.

[134] Chandrashekhara K, Agarwal AN. Active vibration control of laminated composite plates using piezoelectric devices: a finite element approach. J Intell Mater Syst Struct 1993;4:496–508.

[135] Hwang W-S, Park HC. Finite element modeling of piezoelectric sensors and actuators. AIAA J 1993;31:930–7.

[136] Heyliger P. Static behavior of laminated elastic/piezoelectric plates. AIAA J 1994;32:2481–4.

[137] Suleman A, Venkayya VB. A simple finite element formulation for a laminated composite plate with piezoelectric layers. J Intell Mater Syst Struct 1995;6:776–82.

[138] Heyliger P, Saravanos DA. Exact free-vibration analysis of laminated plates with embedded piezoelectric layers. J Acoust Soc Am 1995;98:1547–57.

[139] Chandrashekhara K, Tenneti R. Thermally induced vibration suppression of laminated plates with piezoelectric sensors and actuators. Smart Mater

Struct 1995;4:281.

[140] Batra RC, Liang XQ, Yang JS. The vibration of a simply supported rectangular elastic plate due to piezoelectric actuators. Int J Solids Struct 1996;33:1597–618.

[141] Lazarus KB, Crawley EF, Lin CY. Multivariable high-authority control of plate-like active structures. J Guid Control Dyn 1996;19:1357–63.

[142] Robbins Jr DH, Reddy JN. An efficient computational model for the stress analysis of smart plate structures. Smart Mater Struct 1996;5:353.

[143] Saravanos DA, Heyliger PR, Hopkins DA. Layerwise mechanics and finite element for the dynamic analysis of piezoelectric composite plates. Int J Solids Struct 1997;34:359–78.

[144] Ling-Hui H. Axisymmetric response of circular plates with piezoelectric layers: an exact solution. Int J Mech Sci 1998;40:1265–79.

[145] Ray MC, Bhattacharya R, Samanta B. Exact solutions for dynamic analysis of composite plates with distributed piezoelectric layers. Comput Struct 1998;66:737–43.

[146] Ray MC. Optimal control of laminated plate with piezoelectric sensor and actuator layers. AIAA J 1998;36:2204–8.

[147] Vel SS, Batra RC. Three-dimensional analytical solution for hybrid multilayered piezoelectric plates. J Appl Mech 2000;67:558–67.

[148] Vel SS, Batra RC. Analysis of piezoelectric bimorphs and plates with segmented actuators. Thin-Walled Struct 2001;39:23–44.

[149] Tylikowski A. Control of circular plate vibrations via piezoelectric actuators shunted with a capacitive circuit. Thin-Walled Struct 2001;39:83–94.

[150] Görnandt A, Gabbert U. Finite element analysis of thermopiezoelectric smart structures. Acta Mech 2002;154:129–40.

[151] Sekouri EM, Hu Y-R, Ngo AD. Modeling of a circular plate with piezoelectric actuators. Mechatronics 2004;14:1007–20.

[152] Duan WH, Quek ST, Wang Q. Free vibration analysis of piezoelectric coupled thin and thick annular plate. J Sound Vib 2005;281:119–39.

[153] Fox CHJ, Chen X, McWilliam S. Analysis of the deflection of a circular plate with an annular piezoelectric actuator. Sensors Actuators A Phys 2007;133:180–94.

[154] Jiang JP, Li DX. Finite element formulations for thermopiezoelastic

laminated composite plates. Smart Mater Struct 2008.

[155] Ebrahimi F, Rastgoo A. Free vibration analysis of smart annular FGM plates integrated with piezoelectric layers. Smart Mater Struct 2008;17:15044.

[156] Ebrahimi F, Rastgoo A, Atai AA. A theoretical analysis of smart moderately thick shear deformable annular functionally graded plate. Eur J Mech A/Solids 2009;28:962-73.

[157] Wu N, Wang Q, Quek ST. Free vibration analysis of piezoelectric coupled circular plate with open circuit. J Sound Vib 2010;329:1126-36.

[158] Hosseini-Hashemi S, Es'haghi M, Rokni Damavandi Taher H. An exact analytical solution for freely vibrating piezoelectric coupled circular/annular thick plates using Reddy plate theory. Compos Struct 2010;92:1333-51.

[159] Hosseini-Hashemi S, Khorshidi K, Es'haghi M, Fadaee M, Karimi M. On the effects of coupling between in-plane and out-of-plane vibrating modes of smart functionally graded circular/annular plates. Appl Math Model 2012;36:1132-47.

[160] Khorshidi K, Rezaei E, Ghadimi AA, Pagoli M. Active vibration control of circular plates coupled with piezoelectric layers excited by plane sound wave. Appl Math Model 2015;39:1217-28.

[161] Alibeigloo A. Thermo elasticity solution of functionally graded, solid, circular, and annular plates integrated with piezoelectric layers using the differential quadrature method. Mech Adv Mater Struct 2018;25:766-84.

[162] Forward RL. Electronic damping of orthogonal bending modes in a cylindrical mast-experiment. J Spacecr Rockets 1981;18:11–7.

[163] Tzou HS, Gadre M. Theoretical analysis of a multi-layered thin shell coupled with piezoelectric shell actuators for distributed vibration controls. J Sound Vib 1989;132:433–50.

[164] Banks HT, Smith RC, Wang Y. The modeling of piezoceramic patch interactions with shells, plates, and beams. Q Appl Math 1995;53:353–81.

[165] Dube GP, Kapuria S, Dumir PC. Exact piezothermoelastic solution of simply-supported orthotropic circular cylindrical panel in cylindrical bending. Arch Appl Mech 1996;66:537–54.

[166] Dube GP, Kapuria S, Dumir PC. Exact piezothermoelastic solution of simply-supported orthotropic flat panel in cylindrical bending. Int J Mech

Sci 1996;38:1161–77.

[167] Heyliger P, Pei KC, Saravanos D. Layerwise mechanics and finite element model for laminated piezoelectric shells. AIAA J 1996;34:2353–60.

[168] Saravanos DA. Mixed laminate theory and finite element for smart piezoelectric composite shell structures. AIAA J 1997;35:1327–33.

[169] Chen C-Q, Shen Y-P. Three-dimensional analysis for the free vibration of finite-length orthotropic piezoelectric circular cylindrical shells. J Vib Acoust 1998;120:194–8.

[170] Lee H-J, Saravanos DA. A mixed multi-field finite element formulation for thermopiezoelectric composite shells. Int J Solids Struct 2000;37:4949–67.

[171] Zhou Y-H, Tzou HS. Active control of nonlinear piezoelectric circular shallow spherical shells. Int J Solids Struct 2000;37:1663–77.

[172] Balamurugan V, Narayanan S. Shell finite element for smart piezoelectric composite plate/shell structures and its application to the study of active vibration control. Finite Elem Anal Des 2001;37:713–38.

[173] Narayanan S, Balamurugan V. Finite element modelling of piezolaminated smart structures for active vibration control with distributed sensors and actuators. J Sound Vib 2003;262:529–62.

[174] Liew KM, He XQ, Kitipornchai S. Finite element method for the feedback control of FGM shells in the frequency domain via piezoelectric sensors and actuators. Comput Methods Appl Mech Eng 2004;193:257–73.

[175] Kumar R, Mishra BK, Jain SC. Static and dynamic analysis of smart cylindrical shell. Finite Elem Anal Des 2008;45:13–24.

[176] Khdeir AA, Aldraihem OJ. Exact analysis for static response of cross ply laminated smart shells. Compos Struct 2011;94:92–101.

[177] Schulz K, Klinkel S, Wagner W. A finite element formulation for piezoelectric shell structures considering geometrical and material non-linearities. Int J Numer Methods Eng 2011;87:491–520.

[178] Rao MN, Tarun S, Schmidt R, Schröder KU. Finite element modeling and analysis of piezo-integrated composite structures under large applied electric fields. Smart Mater Struct 2016;25:55044.

[179] Rao MN, Schmidt R, Schröder KU. Static and dynamic FE analysis of piezolaminated composite shells considering electric field nonlinearity under thermo-electro-mechanical loads. Acta Mech 2018;229:5093–120.

[180] Mukherjee A, Chaudhuri AS. Exact solutions for instability control of piezolaminated imperfect struts. AIAA J 2004;42:857–9.

[181] Ghasemi-Nejhad MN, Pourjalali S, Uyema M, Yousefpour A. Finite element method for active vibration suppression of smart composite structures using piezoelectric materials. J Thermoplast Compos Mater 2006;19:309–52.

[182] Liu T. Classical flutter and active control of wind turbine blade based on piezoelectric actuation. Shock Vib 2015;1-13.

[183] Chróścielewski J, Schmidt R, Eremeyev VA. Nonlinear finite element modeling of vibration control of plane rod-type structural members with integrated piezoelectric patches. Contin Mech Thermodyn 2019;31:147–88.

[184] Koganezawa S, Uematsu Y, Yamada T, Nakano H, Inoue J, Suzuki T. Dual-stage actuator system for magnetic disk drives using a shear mode piezoelectric microactuator. IEEE Trans Magn 1999;35:988–92.

[185] Koganezawa S, HARA T. Development of shear-mode piezoelectric microactuator for precise head positioning. Fujitsu Sci Tech J 2001;37:212–9.

[186] Dong S, Kim HW, Strauss MT, Uchino K, Viehland D. A piezoelectric shear-shear mode ultrasonic motor. Proc. 8th Int. Conf. new actuators, 2002, p. 126–9.

[187] Zhang Z, Grishin A. Characterization of piezoelectric shear mode inkjet actuator. Integr Ferroelectr 2005;69:401–15.

[188] Brünahl J, Grishin AM. Piezoelectric shear mode drop-on-demand inkjet actuator. Sensors Actuators A Phys 2002;101:371–82.

[189] Sun CT, Zhang XD. Use of thickness-shear mode in adaptive sandwich structures. Smart Mater Struct 1995;4:202.

[190] Zhang XD, Sun CT. Analysis of a sandwich plate containing a piezoelectric core. Smart Mater Struct 1999;8:31.

[191] Benjeddou A, Trindade MA, Ohayon R. New Shear Actuated Smart Structure Beam Finite Element. AIAA J 1999;37:378-83.

[192] Trindade MA, Benjeddou A, Ohayon R. Parametric analysis of the vibration control of sandwich beams through shear-based piezoelectric actuation. J Intell Mater Syst Struct 1999;10:377–85.

[193] Aldraihem OJ, Khdeir AA. Smart beams with extension and thickness-

shear piezoelectric actuators. Smart Mater Struct 2000;9:1.

[194] Khdeir AA, Aldraihem OJ. Deflection analysis of beams with extension and shear piezoelectric patches using discontinuity functions. Smart Mater Struct 2001;10:212.

[195] Raja S, Prathap G, Sinha PK. Active vibration control of composite sandwich beams with piezoelectric extension-bending and shear actuators. Smart Mater Struct 2002;11:63.

[196] Aldraihem OJ, Khdeir AA. Exact deflection solutions of beams with shear piezoelectric actuators. Int J Solids Struct 2003;40:1–12.

[197] Edery-Azulay L, Abramovich H. Piezoelectric actuation and sensing mechanisms—closed form solutions. Compos Struct 2004;64:443–53.

[198] Raja S, Sreedeep R, Prathap G. Bending behavior of hybrid-actuated piezoelectric sandwich beams. J Intell Mater Syst Struct 2004;15:611–9.

[199] Parashar SK, Von Wagner U, Hagedorn P. A modified Timoshenko beam theory for nonlinear shear-induced flexural vibrations of piezoceramic continua. Nonlinear Dyn 2004;37:181–205.

[200] Parashar SK, von Wagner U, Hagedorn P. Nonlinear shear-induced flexural vibrations of piezoceramic actuators: experiments and modeling. J Sound Vib 2005;285:989–1014.

[201] Baillargeon BP, Vel SS. Active vibration suppression of sandwich beams using piezoelectric shear actuators: experiments and numerical simulations. J Intell Mater Syst Struct 2005;16:517–30.

[202] Poizat C, Benjeddou A. On analytical and finite element modelling of piezoelectric extension and shear bimorphs. Comput Struct 2006;84:1426–37.

[203] Trindade MA, Benjeddou A. On higher-order modelling of smart beams with embedded shear-mode piezoceramic actuators and sensors. Mech Adv Mater Struct 2006;13:357–69.

[204] Trindade MA. Simultaneous extension and shear piezoelectric actuation for active vibration control of sandwich beams. J Intell Mater Syst Struct 2007;18:591–600.

[205] Kapuria S, Hagedorn P. Unified efficient layerwise theory for smart beams with segmented extension/shear mode, piezoelectric actuators and sensors. J Mech Mater Struct 2007;2:1267–98.

[206] Trindade MA, Maio CEB. Multimodal passive vibration control of sandwich

beams with shunted shear piezoelectric materials. Smart Mater Struct 2008;17:55015.

[207] Sharma P, Parashar SK. Free vibration analysis of shear-induced flexural vibration of FGPM annular plate using generalized differential quadrature method. Compos Struct 2016;155:213–22.

[208] Lezgy-Nazargah M. Efficient coupled refined finite element for dynamic analysis of sandwich beams containing embedded shear-mode piezoelectric layers. Mech Adv Mater Struct 2016;23:337–52.

[209] Vel SS, Batra RC. Exact solution for rectangular sandwich plates with embedded piezoelectric shear actuators. AIAA J 2001;39:1363–73.

[210] Vel SS, Batra RC. Exact solution for the cylindrical bending of laminated plates with embedded piezoelectric shear actuators. Smart Mater Struct 2001;10:240.

[211] Benjeddou A, Deu J-F. Piezoelectric transverse shear actuation and sensing of plates, Part 1: A three-dimensional mixed state space formulation. J Intell Mater Syst Struct 2001;12:435–49.

[212] Benjeddou A, Deu J-F. Piezoelectric transverse shear actuation and sensing of plates, Part 2: Application and analysis. J Intell Mater Syst Struct 2001;12:451–67.

[213] Deü J-F, Benjeddou A. Free-vibration analysis of laminated plates with embedded shear-mode piezoceramic layers. Int J Solids Struct 2005;42:2059–88.

[214] Baillargeon BP, Vel SS. Exact solution for the vibration and active damping of composite plates with piezoelectric shear actuators. J Sound Vib 2005;282:781–804.

[215] Parashar SK, DasGupta A, von Wagner U, Hagedorn P. Non-linear shear vibrations of piezoceramic actuators. Int J Non Linear Mech 2005;40:429–43.

[216] D'Ottavio M, Wallmersperger T, Kröplin B. Classical and advanced models for laminated plates with piezoelectric layers actuated in shear mode. Mech Adv Mater Struct 2008;15:167–81.

[217] Parashar SK. Modeling and analysis of shear-induced flexural vibrations of annular piezoceramic actuators. J Intell Mater Syst Struct 2013;24:1572–82.

[218] Sharma TK, Parashar SK. Investigation of free vibration analysis of

functionally graded annular piezoelectric plate using COMSOL. AIP Conf. Proc., vol. 1953, 2018, p. 140084.

[219] Gao X, Xin X, Wu J, Chu Z, Dong S. A multilayered-cylindrical piezoelectric shear actuator operating in shear d_{15} mode. Appl Phys Lett 2018;112:152902.

[220] Benjeddou A, Gorge V, Ohayon R. Use of piezoelectric shear response in adaptive sandwich shells of revolution-Part 2: Finite element implementation. J Intell Mater Syst Struct 2001;12:247–57.

[221] Benjeddou A, Gorge V, Ohayon R. Use of piezoelectric shear response in adaptive sandwich shells of revolution-Part 1: Theoretical formulation. J Intell Mater Syst Struct 2001;12:235–45.

[222] Vel SS, Baillargeon BP. Analysis of static deformation, vibration and active damping of cylindrical composite shells with piezoelectric shear actuators. J Vib Acoust 2005;127:395–407.

[223] Li H, Yang Y. Dynamic response and active control of a composite cylindrical shell with piezoelectric shear actuators. Smart Mater Struct 2007;16:909.

[224] Khdeir AA, Aldraihem OJ. Analysis of smart cross ply laminated shells with shear piezoelectric actuators. Smart Mater Struct 2011;20:105030.

[225] Centolanza LR, Smith EC, Munsky B. Induced-shear piezoelectric actuators for rotor blade trailing edge flaps. Smart Mater Struct 2002;11:24.

[226] Thakkar D, Ganguli R. Helicopter vibration reduction in forward flight with induced-shear based piezoceramic actuation. Smart Mater Struct 2004;13:599.

[227] Khdeir AA, Aldraihem OJ. Analytical investigation of laminated arches with extension and shear piezoelectric actuators. Eur J Mech 2013;37:185–92.

[228] Aldraihem OJ, Wetherhold RC. Mechanics and control of coupled bending and twisting vibration of laminated beams. Smart Mater Struct 1997;6:123.

[229] Mahut T, Agbossou A, Pastor J. Dynamic analysis of piezoelectric fiber composite in an active beam using homogenization and finite element methods. J Intell Mater Syst Struct 1998;9:1009–16.

[230] Cesnik CES, Shin S. On the modeling of integrally actuated helicopter

blades. Int J Solids Struct 2001;38:1765–89.

[231] Sodano HA, Park G, Inman DJ. An investigation into the performance of macro-fiber composites for sensing and structural vibration applications. Mech Syst Signal Process 2004;18:683–97.

[232] Wickramasinghe VK, Hagood NW. Durability characterization of active fiber composite actuators for helicopter rotor blade applications. J Aircr 2004;41:931–7.

[233] Wickramasinghe VK, Hagood NW. Material characterization of active fiber composites for integral twist-actuated rotor blade application. Smart Mater Struct 2004;13:1155.

[234] Park J-S, Kim J-H. Analytical development of single crystal macro fiber composite actuators for active twist rotor blades. Smart Mater Struct 2005;14:745.

[235] Brockmann TH, Lammering R. Beam finite elements for rotating piezoelectric fiber composite structures. J Intell Mater Syst Struct 2006;17:431–48.

[236] Guennam AE, Luccioni BM. FE modeling of a closed box beam with piezoelectric fiber composite patches. Smart Mater Struct 2006;15:1605.

[237] Nguyen C-H, Kornmann X. A comparison of dynamic piezoactuation of fiber-based actuators and conventional PZT patches. J Intell Mater Syst Struct 2006;17:45–55.

[238] Choi S-C, Park J-S, Kim J-H. Active damping of rotating composite thin-walled beams using MFC actuators and PVDF sensors. Compos Struct 2006;76:362–74.

[239] Choi S-C, Park J-S, Kim J-H. Vibration control of pre-twisted rotating composite thin-walled beams with piezoelectric fiber composites. J Sound Vib 2007;300:176–96.

[240] Cook AC, Vel SS. Multiscale analysis of laminated plates with integrated piezoelectric fiber composite actuators. Compos Struct 2012;94:322–36.

[241] Azzouz MS, Mei C, Bevan JS, Ro JJ. Finite element modeling of MFC/AFC actuators and performance of MFC. J Intell Mater Syst Struct 2001;12:601–12.

[242] Mallik N, Ray MC. Exact solutions for the analysis of piezoelectric fiber reinforced composites as distributed actuators for smart composite plates. Int J Mech Mater Des 2004;1:347–64.

[243] Ray MC, Mallik N. Finite element analysis of smart structures containing piezoelectric fiber-reinforced composite actuator. AIAA J 2004;42:1398–405.

[244] Park J-S, Kim J-H. Suppression of aero-thermal large deflections and snap-through behaviors of composite panels using macro fiber composite actuators. Smart Mater Struct 2004;13:1448.

[245] Panda S, Ray MC. Nonlinear analysis of smart functionally graded plates integrated with a layer of piezoelectric fiber reinforced composite. Smart Mater Struct 2006;15:1595.

[246] Ray MC, Sachade HM. Finite element analysis of smart functionally graded plates. Int J Solids Struct 2006;43:5468–84.

[247] Ray MC, Sachade HM. Exact solutions for the functionally graded plates integrated with a layer of piezoelectric fiber-reinforced composite. J Appl Mech 2006;73:622–32.

[248] Reddy BA, Ray MC. Optimal control of smart functionally graded plates using piezoelectric fiber reinforced composites. J Vib Control 2007;13:795–814.

[249] Panda S, Ray MC. Nonlinear finite element analysis of functionally graded plates integrated with patches of piezoelectric fiber reinforced composite. Finite Elem Anal Des 2008;44:493–504.

[250] Zhang HY, Shen YP. Vibration suppression of laminated plates with 1-3 piezoelectric fiber-reinforced composite layers equipped with interdigitated electrodes. Compos Struct 2007;79:220–8.

[251] Dano ML, Julliere B. Active control of thermally induced distortion in composite structures using macro fiber composite actuators. Smart Mater Struct 2007;16:2315.

[252] Mahato PK, Maiti DK. Aeroelastic analysis of smart composite structures in hygro-thermal environment. Compos Struct 2010;92:1027–38.

[253] Panda S. Non-linear analysis of smart annular plates using cylindrically orthotropic piezoelectric fiber-reinforced composite. J Intell Mater Syst Struct 2011;22:1789–801.

[254] Panda S, Sopan GG. Nonlinear analysis of smart functionally graded annular sector plates using cylindrically orthotropic piezoelectric fiber reinforced composite. Int J Mech Mater Des 2013;9:35–53.

[255] Kapuria S, Yasin MY. Active vibration control of smart plates using

directional actuation and sensing capability of piezoelectric composites. Acta Mech 2013;224:1185–99.

[256] Kumar A, Panda S, Chakraborty D. Harmonically exited nonlinear vibration of heated functionally graded plates integrated with piezoelectric composite actuator. J Intell Mater Syst Struct 2015;26:931–51.

[257] Zhang S-Q, Li Y-X, Schmidt R. Modeling and simulation of macro-fiber composite layered smart structures. Compos Struct 2015;126:89–100.

[258] Zippo A, Ferrari G, Amabili M, Barbieri M, Pellicano F. Active vibration control of a composite sandwich plate. Compos Struct 2015;128:100–14.

[259] Kumar ASP, Panda S, Reddy NH. A comparative study on the smart damping capabilities of cylindrically orthotropic piezoelectric fiber-reinforced composite actuators in vibration control of simply supported/fully clamped isotropic annular plate. J Intell Mater Syst Struct 2017;28:1839–59.

[260] Pandey A, Arockiarajan A. Performance studies on Macro fiber composite (MFC) under thermal condition using Kirchhoff and Mindlin plate theories. Int J Mech Sci 2017;130:416–25.

[261] Wang X, Zhou W, Xun G, Wu Z. Dynamic shape control of piezocomposite-actuated morphing wings with vibration suppression. J Intell Mater Syst Struct 2018;29:358–70.

[262] Rouzegar J, Abbasi A. A refined finite element method for bending analysis of laminated plates integrated with piezoelectric fiber-reinforced composite actuators. Acta Mech Sin 2018;34:689–705.

[263] Kwak MK, Heo S, Jeong M. Dynamic modelling and active vibration controller design for a cylindrical shell equipped with piezoelectric sensors and actuators. J Sound Vib 2009;321:510–24.

[264] Sohn JW, Choi S-B, Kim HS. Vibration control of smart hull structure with optimally placed piezoelectric composite actuators. Int J Mech Sci 2011;53:647–59.

[265] Sohn JW, Choi S-B, Lee C-H. Active vibration control of smart hull structure using piezoelectric composite actuators. Smart Mater Struct 2009;18:74004.

[266] Kim HS, Sohn JW, Choi S-B. Vibration control of a cylindrical shell structure using macro fiber composite actuators. Mech Based Des Struct Mach 2011;39:491–506.

[267] Panda S. Performance of a short piezoelectric fiber-reinforced composite actuator in vibration control of functionally graded circular cylindrical shell. J Intell Mater Syst Struct 2016;27:2774–94.

[268] Panda SP, Panda S. Micromechanical finite element analysis of effective properties of a unidirectional short piezoelectric fiber reinforced composite. Int J Mech Mater Des 2015;11:41–57.

[269] Guo X, Liu D, Zhang W, Sun L, Chen S. Nonlinear dynamic analysis of macrofiber composites laminated shells. Adv Mater Sci Eng 2017;1-17.

[270] Tarazaga PA, Inman DJ, Wilkie WK. Control of a space rigidizable inflatable boom using macro-fiber composite actuators. J Vib Control 2007;13:935–50.

[271] Park S, Inman DJ, Yun C-B. An outlier analysis of MFC-based impedance sensing data for wireless structural health monitoring of railroad tracks. Eng Struct 2008;30:2792–9.

[272] Barkanov E, Gluhih S, Kovalov A. Optimal design of the active twist for helicopter rotor blades with C-spar. Mech Adv Mater Struct 2008;15:325–34.

[273] Bilgen O, Kochersberger KB, Inman DJ, Ohanian III OJ. Macro-fiber composite actuated simply supported thin airfoils. Smart Mater Struct 2010;19:55010.

[274] Bilgen O, De Marqui jr C, Kochersberger KB, Inman DJ. Macro-fiber composite actuators for flow control of a variable camber airfoil. J Intell Mater Syst Struct 2011;22:81–91.

[275] Wang X, Zhou W, Wu Z, Xing J. Tracking control system design for roll maneuver via active wings using macro fiber composites. AIAA Model. Simul. Technol. Conf., 2016, p. 4012.

[276] Raja S, Ikeda T, Dwarakanathan D. Deflection and vibration control of laminated plates using extension and shear actuated fiber composites. Smart Mater Res 2011;1-15.

[277] Gopinath T, Raja S, Ikeda T. Active flutter control of composite plate with embedded and surface bonded piezoelectric composites. Act. Passiv. Smart Struct. Integr. Syst. 2011, vol. 7977, 2011, p. 797706.

[278] Gopinath T, Raja S, Ikeda T. Finite element formulation of laminated plate with flexible piezoelectric actuators and vibration control analysis. Act. Passiv. Smart Struct. Integr. Syst. 2011, vol. 7977, 2011, p. 797707.

[279] Ungar EE, Kerwin Jr EM. Plate damping due to thickness deformations in attached viscoelastic layers. J Acoust Soc Am 1964;36:386–92.

[280] Grootenhuis P. The control of vibrations with viscoelastic materials. J Sound Vib 1970;11:421-33.

[281] Lu YP, Killian JW, Everstine GC. Vibrations of three layered damped sandwich plate composites. J Sound Vib 1979;64:63-71.

[282] Shi Y, Hua H, Sol H. The finite element analysis and experimental study of beams with active constrained layer damping treatments. J Sound Vib 2004;278:343–63.

[283] Huang SC, Inman DJ, Austin EM. Some design considerations for active and passive constrained layer damping treatments. Smart Mater Struct 1996;5:301.

[284] Jeung YS, Shen IY. Development of isoparametric, degenerate constrained layer element for plate and shell structures. AIAA J 2001;39:1997-2005.

[285] Chantalakhana C, Stanway R. Active constrained layer damping of clamped-clamped plate vibrations. J Sound Vib 2001;241:755-77.

[286] Trindade MA, Benjeddou A. Hybrid active-passive damping treatments using viscoelastic and piezoelectric materials: Review and assessment. JVC/Journal Vib Control 2002;8:699-745.

[287] Ray MC, Pradhan AK. On the use of vertically reinforced 1-3 piezoelectric composites for hybrid damping of laminated composite plates. Mech Adv Mater Struct 2007;14:245-61.

[288] Plump JM, Hubbard JE. Modeling of an active constrained layer damper. Twelves Intl. Congr. Acoust., 1986, p. 24–31.

[289] Hagood NW, von Flotow A. Damping of structural vibrations with piezoelectric materials and passive electrical networks. J Sound Vib 1991;146:243–68.

[290] Ghoneim H. Application of the Electromechanical Surface Damping to the Vibration Control of a Cantilever Plate. J Vib Acoust 1996;118:551-7.

[291] Gentilman RL, Fiore DF, Pham HT, French KW, Bowen LJ. Fabrication and properties of 1-3 PZT-polymer composites. Ceramic Trans 1994; 43:239-47.

[292] Arafa M, Baz A. Dynamics of active piezoelectric damping composites. Compos Part B Eng 2000;31:255–64.

[293] Agnes G, Napolitano K. Active constrained layer viscoelastic damping.

34th Struct. Struct. Dyn. Mater. Conf., 1993, p. 1702.

[294] Yellin JM, Shen IY. A self-sensing active constrained layer damping treatment for a Euler-Bernoulli beam. Smart Mater Struct 1996;5:628.

[295] Baz A, Ro J. Partial treatment of flexible beams with active constrained layer damping. ASME Appl Mech Div 1993;167:61.

[296] Baz A, Ro J. Optimum Design and Control of Active Constrained Layer Damping. J Mech Des 1995;117:135-44.

[297] Veley DE, Rao SS. A comparison of active, passive and hybrid damping in structural design. Smart Mater Struct 1996;5:660.

[298] Baz A. Robust control of active constrained layer damping. J Sound Vib 1998;211:467–80.

[299] Kapadia RK, Kawiecki G. Experimental evaluation of segmented active constrained layer damping treatments. J Intell Mater Syst Struct 1997;8:103–11.

[300] Azvine B, Tomlinson GR, Wynne R, Sensburg O. Vibration suppression of flexible structures using active damping. Proc. 4th Int. Conf. Adapt. Struct. Tech., Technomic Pub. Co., Lancaster, 1993, p. 340–56.

[301] Rongong JA, Wright JR, Wynne RJ, Tomlinson GR. Modelling of a hybrid constrained layer/piezoceramic approach to active damping. J Vib Acoust 1997;119:120–30.

[302] Liao WH, Wang KW. A new active constrained layer configuration with enhanced boundary actions. Smart Mater Struct 1996;5:638.

[303] Varadan V V, Lim Y-H, Varadan VK. Closed loop finite-element modeling of active/passive damping in structural vibration control. Smart Mater Struct 1996;5:685.

[304] Badre-Alam A, Wang KW, Gandhi F. Optimization of enhanced active constrained layer (EACL) treatment on helicopter flexbeams for aeromechanical stability augmentation. Smart Mater Struct 1999;8:182.

[305] Liu Y, Wang K-W. Enhanced active constrained layer damping treatment with symmetrically and nonsymmetrically distributed edge elements. Smart Struct. Mater. 1998 Passiv. Damping Isol., vol. 3327, 1998, p. 61–73.

[306] Crassidis JL, Baz A, Wereley N. H∞ control of active constrained layer damping. J Vib Control 2000;6:113–36.

[307] Chen T-H, Baz AM. Performance characteristics of active constrained layer

damping versus passive constrained layer damping with active control. Smart Struct. Mater. 1996 Math. Control Smart Struct., vol. 2715, 1996, p. 256–69.

[308] Lam MJ, Inman DJ, Saunders WR. Vibration control through passive constrained layer damping and active control. J Intell Mater Syst Struct 1997;8:663–77.

[309] Lam MJ, Inman DJ, Saunders WR. Variations of hybrid damping Passive Damping and Isolation. Proc. SPIE 5th Annu. Symp. Smart Struct. Mater., 1998.

[310] Baz A, Ro J. Vibration control of plates with active constrained layer damping. Smart Mater Struct 1996;5:272.

[311] Ray MC, Baz A. Optimization of energy dissipation of active constrained layer damping treatments of plates. J Sound Vib 1997;208:391–406.

[312] Park CH, Baz A. Comparison between finite element formulations of active constrained layer damping using classical and layer-wise laminate theory. Finite Elem Anal Des 2001;37:35–56.

[313] Ro J, Baz A. Optimum placement and control of active constrained layer damping using modal strain energy approach. Modal Anal 2002;8:861–76.

[314] Liu T, Hua H, Zhang Z. Robust control of plate vibration via active constrained layer damping. Thin-Walled Struct 2004;42:427–48.

[315] Boudaoud H, Belouettar S, Daya EM, Potier-Ferry M. A shell finite element for active-passive vibration control of composite structures with piezoelectric and viscoelastic layers. Mech Adv Mater Struct 2008;15:208–19.

[316] Araújo AL, Mota Soares CM, Mota Soares CA. Finite element model for hybrid active-passive damping analysis of anisotropic laminated sandwich structures. J Sandw Struct Mater 2010;12:397–419.

[317] Moita JS, Araújo AL, Martins PG, Soares CMM, Soares CAM. Analysis of active-passive plate structures using a simple and efficient finite element model. Mech Adv Mater Struct 2011;18:159–69.

[318] Moita JS, Araújo AL, Martins P, Soares CMM, Soares CAM. A finite element model for the analysis of viscoelastic sandwich structures. Comput Struct 2011;89:1874–81.

[319] Araújo AL, Carvalho VS, Soares CMM, Belinha J, Ferreira AJM. Vibration analysis of laminated soft core sandwich plates with piezoelectric sensors

and actuators. Compos Struct 2016;151:91–8.

[320] Plattenburg J, Dreyer JT, Singh R. Active and passive damping patches on a thin rectangular plate: a refined analytical model with experimental validation. J Sound Vib 2015;353:75–95.

[321] Lu J, Wang P, Zhan Z. Active vibration control of thin-plate structures with partial SCLD treatment. Mech Syst Signal Process 2017;84:531–50.

[322] Luis NF, Madeira JFA, Araújo AL, Ferreira AJM. Active vibration attenuation in viscoelastic laminated composite panels using multiobjective optimization. Compos Part B Eng 2017;128:53–66.

[323] Moita JS, Araújo AL, Correia VF, Soares CMM, Herskovits J. Active-passive damping in functionally graded sandwich plate/shell structures. Compos Struct 2018;202:324–32.

[324] Lu J, Zhan Z, Liu X, Wang P. Numerical modeling and model updating for smart laminated structures with viscoelastic damping. Smart Mater Struct 2018;27:75038.

[325] Kumar A, Panda S, Kumar A, Narsaria V. Performance of a graphite wafer-reinforced viscoelastic composite layer for active-passive damping of plate vibration. Compos Struct 2018; 186: 303-14.

[326] Shen IY. Active constrained layer damping treatments for shell structures: A deep-shell theory, some intuitive results, and an energy analysis. Smart Mater Struct 1997;6:89.

[327] Baz A, Chen T. Control of axi-symmetric vibrations of cylindrical shells using active constrained layer damping. Thin-Walled Struct 2000;36:1–20.

[328] Ray MC, Oh J, Baz A. Active constrained layer damping of thin cylindrical shells. J Sound Vib 2001;240:921–35.

[329] Ray MC, Reddy JN. Optimal control of thin circular cylindrical laminated composite shells using active constrained layer damping treatment. Smart Mater Struct 2003;13:64.

[330] Zheng L, Zhang D, Wang Y. Vibration and damping characteristics of cylindrical shells with active constrained layer damping treatments. Smart Mater Struct 2011;20:25008.

[331] Kumar N, Singh SP. Vibration control of curved panel using smart damping. Mech Syst Signal Process 2012;30:232–47.

[332] Batra RC, Geng TS. Comparison of active constrained layer damping by using extension and shear mode piezoceramic actuators. J Intell Mater

Syst Struct 2002;13:349–67.

[333] Trindade MA. Experimental analysis of active-passive vibration control using viscoelastic materials and extension and shear piezoelectric actuators. JVC/Journal Vib Control 2011;17:917-29.

[334] Ray MC, Mallik N. Active control of laminated composite beams using a piezoelectric fiber reinforced composite layer. Smart Mater Struct 2003;13:146.

[335] Ray MC, Pradhan AK. The performance of vertically reinforced 1-3 piezoelectric composites in active damping of smart structures. Smart Mater Struct 2006;15:631.

[336] Sarangi SK, Ray MC. Smart damping of geometrically nonlinear vibrations of laminated composite beams using vertically reinforced 1-3 piezoelectric composites. Smart Mater Struct 2010;19:75020.

[337] Biswas D, Ray MC. Active constrained layer damping of geometrically nonlinear vibration of rotating composite beams using 1-3 piezoelectric composite. Int J Mech Mater Des 2013;9:83–104.

[338] Ghosh S, Agrawal S, Pradhan AK, Pandit MK. Performance of vertically reinforced 1-3 piezo composites for active damping of smart sandwich beams. J Sandw Struct Mater 2015;17:258–77.

[339] Sahoo SR, Ray MC. Analysis of smart damping of laminated composite beams using mesh free method. Int J Mech Mater Des 2018;14:359–74.

[340] Ray MC, Reddy JN. Performance of piezoelectric fiber-reinforced composites for active structural-acoustic control of laminated composite plates. IEEE Trans Ultrason Ferroelectr Freq Control 2004;51:1477–90.

[341] Ray MC. Hybrid damping of smart, functionally graded plates using piezoelectric, fiber-reinforced composites. IEEE Trans Ultrason Ferroelectr Freq Control 2006;53:2152–65.

[342] Panda S, Ray MC. Active constrained layer damping of geometrically nonlinear vibrations of functionally graded plates using piezoelectric fiber-reinforced composites. Smart Mater Struct 2008;17:025012.

[343] Panda S, Ray MC. Active control of geometrically nonlinear vibrations of functionally graded laminated composite plates using piezoelectric fiber reinforced composites. J Sound Vib 2009;325:186–205.

[344] Ray MC, Faye A. Active structural-acoustic control of laminated composite plates using vertically/obliquely reinforced 1-3 piezoelectric composite

patch. Int J Mech Mater Des 2009;5:123.

[345] Kumar RS, Ray MC. Active constrained layer damping of geometrically nonlinear vibrations of smart laminated composite sandwich plates using 1-3 piezoelectric composites. Int J Mech Mater Des 2012;8:359–80.

[346] Li J, Narita Y. Vibration suppression for laminated composite plates with arbitrary boundary conditions. Mech Compos Mater 2013;49:519–30.

[347] Kanasogi RM, Ray MC. Control of geometrically nonlinear vibrations of skew laminated composite plates using skew or rectangular 1-3 piezoelectric patches. Int J Mech Mater Des 2013;9:325–54.

[348] Kanasogi RM, Ray MC. Active constrained layer damping of smart skew laminated composite plates using 1-3 piezoelectric composites. J Compos 2013;2013.

[349] Kumar RS, Ray MC. Smart damping of geometrically nonlinear vibrations of functionally graded sandwich plates using 1-3 piezoelectric composites. Mech Adv Mater Struct 2016;23:652–69.

[350] Kumar AMS, Panda S, Chakraborty D. Piezo-viscoelastically damped nonlinear frequency response of functionally graded plates with a heated plate-surface. J Vib Control 2016;22:320–43.

[351] Kattimani SC, Ray MC. Smart damping of geometrically nonlinear vibrations of magneto-electro-elastic plates. Compos Struct 2014;114:51–63.

[352] Kattimani SC, Ray MC. Control of geometrically nonlinear vibrations of functionally graded magneto-electro-elastic plates. Int J Mech Sci 2015;99:154–67.

[353] Kattimani SC, Ray MC. Vibration control of multiferroic fibrous composite plates using active constrained layer damping. Mech Syst Signal Process 2018;106:334–54.

[354] Sahoo SR, Ray MC. Active control of laminated composite plates using elliptical smart constrained layer damping treatment. Compos Struct 2019;211:376–89.

[355] Vinyas M. Vibration control of skew magneto-electro-elastic plates using active constrained layer damping. Compos Struct 2019;208:600–17.

[356] Ray MC, Reddy JN. Active control of laminated cylindrical shells using piezoelectric fiber reinforced composites. Compos Sci Technol 2005;65:1226–36.

[357] Ray MC, Balaji R. Active structural-acoustic control of laminated cylindrical panels using smart damping treatment. Int J Mech Sci 2007;49:1001–17.

[358] Ray MC. Smart damping of laminated thin cylindrical panels using piezoelectric fiber reinforced composites. Int J Solids Struct 2007;44:587–602.

[359] Ray MC, Pradhan AK. Performance of vertically and obliquely reinforced 1-3 piezoelectric composites for active damping of laminated composite shells. J Sound Vib 2008;315:816–35.

[360] Ray MC, Pradhan AK. Active damping of laminated thin cylindrical composite panels using vertically/obliquely reinforced 1-3 piezoelectric composites. Acta Mech 2010;209:201–18.

[361] Sarangi SK, Ray MC. Active damping of geometrically nonlinear vibrations of doubly curved laminated composite shells. Compos Struct 2011;93:3216–28.

[362] Kumar RS, Ray MC. Active control of geometrically nonlinear vibrations of doubly curved smart sandwich shells using 1-3 piezoelectric composites. Compos Struct 2013;105:173–87.

[363] Datta P, Ray MC. Smart damping of geometrically nonlinear vibrations of composite shells using fractional order derivative viscoelastic constitutive relations. Mech Adv Mater Struct 2018;25:62–78.

[364] Sarangi SK, Ray MC. Active damping of geometrically nonlinear vibrations of laminated composite plates using vertically reinforced 1-3 piezoelectric composites. Acta Mech 2011;222:363–80.

[365] Sarangi SK, Ray MC. Smart control of nonlinear vibrations of doubly curved functionally graded laminated composite shells under a thermal environment using 1-3 piezoelectric composites. Int J Mech Mater Des 2013;9:253–80.

[366] Shah PH, Ray MC. Active control of laminated composite truncated conical shells using vertically and obliquely reinforced 1-3 piezoelectric composites. Eur J Mech 2012;32:1–12.

[367] Shah PH, Ray MC. Active structural-acoustic control of laminated composite truncated conical shells using smart damping treatment. J Vib Acoust 2013;135:21001.

[368] Kumar A, Ray MC. Control of smart rotating laminated composite

truncated conical shell using ACLD treatment. Int J Mech Sci 2014;89:123–41.

[369] Li J, Narita Y. Vibration suppression for laminated cylindrical panels with arbitrary edge conditions. J Vib Control 2013;19:626–40.

[370] Shivakumar J, Ashok MH, Ray MC. Active control of geometrically nonlinear transient vibrations of laminated composite cylindrical panels using piezoelectric fiber reinforced composite. Acta Mech 2013;224:1–15.

[371] Vadiraja DN, Sahasrabudhe AD. Vibration analysis and optimal control of rotating pre-twisted thin-walled beams using MFC actuators and sensors. Thin-Walled Struct 2009;47:555–67.

[372] Cao L, Mantell S, Polla D. Design and simulation of an implantable medical drug delivery system using microelectromechanical systems technology. Sensors Actuators A Phys 2001;94:117–25.

[373] Kim YH, Ha SK. Analysis of a disk-type stator for the piezoelectric ultrasonic motor using impedance matrix. J Sound Vib 2003;263:643–63.

[374] Cha Y, Abdolhamidi S, Porfiri M. Energy harvesting from underwater vibration of an annular ionic polymer metal composite. Meccanica 2015;50:2675–90.

[375] Sergienko VP, Bukharov SN, Kupreev A V. Noise and vibration in brake systems of vehicles. Part 1: experimental procedures. J Frict Wear 2008;29:234–41.

[376] Bambill D V, La Malfa S, Rossit CA, Laura PAA. Analytical and experimental investigation on transverse vibrations of solid, circular and annular plates carrying a concentrated mass at an arbitrary position with marine applications. Ocean Eng 2004;31:127–38.

[377] Shi L, Shuai J, Wang X, Xu K. Experimental and numerical investigation of stress in a large-scale steel tank with a floating roof. Thin-Walled Struct 2017;117:25–34.

[378] Buffum D, Fleeter S. Aerodynamic performance of an annular flat plate airfoil cascade with nonuniform inlet velocity. AIAA J 1986;24:270–7.

[379] Lin X, Huang S, Zhou K, Zhang D. The influence of structural parameters on the actuation performance of piezoelectric fiber composites. Mater Des 2016;107:123–9.

[380] Reiter T, Dvorak GJ, Tvergaard V. Micromechanical models for graded composite materials. J Mech Phys Solids 1997;45:1281–302.

[381] Cady WG. Piezoelectricity: an introduction to the theory and applications of electromechanical phenomena in crystals. McGraw-Hill; 1946.

[382] Trindade MA, Benjeddou A. Finite element homogenization technique for the characterization of d_{15} shear piezoelectric macro-fibre composites. Smart Mater Struct 2011;20:075012.

[383] Aboudi J, Arnold SM, Bednarcyk BA. Micromechanics of composite materials: a generalized multiscale analysis approach. Elsevier, Oxford; 2013.

[384] Tiersten HF. Linear piezoelectric plate vibrations. Plenum Press, New York; 2013.

[385] Deraemaeker A, Nasser H, Benjeddou A, Preumont A. Mixing rules for the piezoelectric properties of macro fiber composites. J Intell Mater Syst Struct 2009;20:1475–82.

[386] Trindade MA, Benjeddou A. Finite element characterisation of multilayer d_{31} piezoelectric macro-fibre composites. Compos Struct 2016;151:47–57.

[387] Odegard GM. Constitutive modeling of piezoelectric polymer composites. Acta Mater 2004;52:5315–30.

[388] Singh B, Chakraverty S. Transverse vibration of annular circular and elliptic plates using the characteristic orthogonal polynomials in two dimensions. J Sound Vib 1993;162:537–46.

[389] Dong S, Uchino K, Li L, Viehland D. Analytical solutions for the transverse deflection of a piezoelectric circular axisymmetric unimorph actuator. IEEE Trans Ultrason Ferroelectr Freq Control 2007;54:1240–9.

[390] Reddy JN, Robbins DH. Theories and computational models for composite laminates. Appl Mech Rev 1994;47:147–69.

[391] Erturk A, Inman DJ. Piezoelectric energy harvesting. John Wiley & Sons; 2011.

[392] Daniel IM, Ishai O, Daniel IM, Daniel I. Engineering mechanics of composite materials. New York : Oxford university press; 1994.

[393] Ikeda T. Fundamentals of Piezoelectricity. Oxford University Press; 1990.

[394] Hill R. Elastic properties of reinforced solids: some theoretical principles. J Mech Phys Solids 1963;11:357–72.

[395] Biscani F, Nasser H, Belouettar S, Carrera E. Equivalent electro-elastic properties of Macro Fiber Composite (MFC) transducers using asymptotic expansion approach. Compos Part B Eng 2011;42:444–55.

[396] Pabst O, Perelaer J, Beckert E, et al. All inkjet-printed piezoelectric polymer actuators: Characterization and applications for micropumps in lab-on-a-chip systems. Org Electron 2013; 14: 3423–3429.

[397] Fukuda K, Hikichi K, Sekine T, et al. Strain sensitivity and durability in p-type and n-type organic thin-film transistors with printed silver electrodes. Sci Rep 2013; 3: 2048.

[398] Low S-H, Lau G-K. Bi-axially crumpled silver thin-film electrodes for dielectric elastomer actuators. Smart Mater Struct 2014; 23: 125021.

[399] Deb K. Optimization for engineering design: Algorithms and examples. PHI Learning Pvt. Ltd.; 2012.

[400] Kumar A, Panda S, Narsaria V, Kumar A. Augmented constrained layer damping in plates through the optimal design of a 0-3 viscoelastic composite layer. Journal Vib Control 2018; 24: 5514-24.

[401] Yan M-J, Dowell EH. Governing Equations for Vibrating Constrained-Layer Damping Sandwich Plates and Beams. J Appl Mech 1972; 39: 1041-46.

[402] Moreira RAS, Dias Rodrigues J. A layerwise model for thin soft core sandwich plates. Comput Struct 2006; 84: 1256-63.

[403] Filippi M, Carrera E, Valvano S. Analysis of multilayered structures embedding viscoelastic layers by higher-order, and zig-zag plate elements. Compos Part B Eng 2018; 154: 77-89.

[404] Reddy JN. Mechanics of Laminated Composite Plates and Shells: Theory and Analysis. CRC press; 2004.

[405] Aboudi, J., Pindera, M.J. and Arnold, S.M., 1994. Elastic response of metal matrix composites with tailored microstructures to thermal gradients. International journal of solids and structures, 31(10), pp.1393-1428.

[406] Kumar, M.A., Panda, S. and Chakraborty, D., 2015. Design and analysis of a smart graded fiber-reinforced composite laminated plate. Composite Structures, 124, pp.176-195.

List of Publications

The work presented in this thesis has led to the following research papers published and being under review in peer reviewed journals.

1. Dubey MK, Panda S. Electromechanical properties and actuation capability of an extension mode piezoelectric fiber composite actuator with cylindrically periodic microstructure. Archive of Applied Mechanics. 2018. 88(12): 2261-2281.
2. Panda S, Dubey MK. A balanced laminate of piezoelectric fiber composite for improved shear piezoelectric actuation of beams. Mechanics of Advanced Materials and Structures. 2018: 1-13.

3. Dubey MK, Panda S. Shear-based vibration control of annular sandwich plates using different piezoelectric fiber composites: a comparative study. Journal of Sandwich Structures and Materials. 2019: 1099636219838446.

4. Dubey MK, Panda S. Shear actuation mechanism and shear-based actuation capability of an obliquely reinforced PFC in active control of annular plates. Journal of Intelligent Material Systems and Structures. 30(16): 2447-2463.

5. Dubey MK, Panda S. A design of shear actuated hybrid damping treatment for annular plates using balanced laminate of PFC and 0-3 viscoelastic composite. (Manuscript is prepared to submit in the peer reviewed international journal).